ISBN 82-553-1257-9
ISSN 0809-4403
Mechanics and Applied Mathematics Series, No. 7, October 2000

Proceedings of the
13TH NORDIC SEMINAR ON COMPUTATIONAL MECHANICS (NSCM-13)

Oslo, 20-21 October, 2000

Jostein Hellesland, Harald Osnes and Geir Skeie (editors)

Mechanics Division, Department of Mathematics,
University of Oslo

Avdeling for mekanikk
Matematisk institutt, Universitetet i Oslo

ISSN: 0809-4403
ISBN: 82-553-1257-9

Mechanics and Applied Mathematics Series

No 7, October 2000

Produsert av Unipub forlag
Trykk og innbinding: GCSM AS, Oslo 2000

Unipub forlag er en avdeling i Akademika AS, som eies av Studentsamskipnaden i Oslo.

Preface

These proceedings contain the papers presented at the *Thirteenth Nordic Seminar on Computational Mechanics*, held at the University of Oslo, Oslo, Norway, 20-21 October, 2000.

The Nordic Seminars on Computational Mechanics represent a major activity of the Nordic Association for Computational Mechanics (NoACM). The NoACM was founded in 1988 with the objective to stimulate and promote research and practice in computational mechanics, to foster the interchange of ideas among the various fields contributing to computational mechanics, and to provide forums and meetings for dissemination of knowledge in computational mechanics. Younger researchers, including doctorate students etc., are especially encouraged to partake at these seminars. The member countries of NoACM are the Nordic countries (Denmark, Finland, Iceland, Norway and Sweden) and the Baltic countries (Estonia, Latvia and Lithuania). NoACM is a subchapter of the International Organization for Computational Mechanics (IACM) and the European Community on Computational Methods in Applied Sciences (ECCOMAS).

The responsibility for organizing this year's seminar was assigned by NoACM to the Mechanics Division of the Department of Mathematics, University of Oslo (UiO), in cooperation with Det Norske Veritas (DNV).

On behalf of the organizers, sincere appreciations are extended to all contributors at the seminar, not least to the invited lecturers and to the other speakers for their efforts in preparing talks and papers (extended abstracts). The latter is for practical reasons issued as a volume in the Mechanics and Applied Mathematics Series at the University of Oslo.

The financial support provided by the Research Council of Norway (Norges forskningsråd) and Det Norske Veritas is gratefully acknowledged.

Oslo, 10 October, 2000

The editors

Nordic Association for Computational Mechanics (NoACM)

Organizing Committee

- **Dr. Jostein Hellesland**, Chairman,
  Professor, Mechanics Division, University of Oslo (UiO)
- **Dr. Hans Petter Langtangen**,
  Professor, Dept. of Informatics, UiO
- **Dr. Harald Osnes**,
  Assoc. Professor, Mechanics Division, UiO
- **Dr. Geir Skeie**,
  Principal Engineer, Det Norske Veritas, and Adjunct Assoc. Professor, Mechanics Division, UiO
- **Dr. Pål G. Bergan**,
  Vice President, Det Norske Veritas, and Professor, Norwegian University of Science and Technology (NTNU)

Program Committee

- **Dr. Pål G. Bergan**, Norway
- **Dr. Lars Damkilde**, Denmark
- **Dr. Jaan Lellep**, Estonia
- **Dr. Martti Mikkola**, Finland
- **Dr. Nils-Erik Wiberg** , Sweden

NSCM-13 Seminar Secretariat

- Mechanics Division, Dept. of Mathematics, University of Oslo (UiO) P.O. Box 1053 - Blindern, N-0316 Oslo, Norway
- Telephone: +47 2285 5950/+47 2285 5888; Telefax: +47 2285 4349; E-mail: NSCM13@math.uio.no; URL: www.math.uio.no/NSCM13/

Financial Support

- The Research Council of Norway (Norges forskningsråd (NFR))
- Det Norske Veritas (DNV)

Content

Failure in structural impact – experimental and numerical studies

Odd Sture Hopperstad, Tore Børvik and Magnus Langseth

Structural Impact Laboratory (SIMLab), Department of Structural Engineering,
Norwegian University of Science and Technology, N-7491 Trondheim, Norway.
Phone: + 47 73 59 47 00; Fax: + 47 73 59 47 01; E-mail: odd.hopperstad@bygg.ntnu.no

Introduction

Plates struck normally by free-flying objects with different nose shapes and velocities constitute a generic problem in structural impact. It is a problem ideally suited for investigations of mechanisms for energy absorption and failure under impact loading conditions. In a research project currently running at SIMLab, we are studying this problem using experiments, metallurgical investigations, constitutive modelling and finite element simulations (Refs. [1]-[7]). Some results will be summarised in this paper.

Materials

The target plates were made of Weldox 460 E steel. We performed different types of tensile tests with axisymmetric specimens to identify the mechanical properties (strength and ductility) of the plate material [6]. These were quasi-static tests with smooth and notched specimens at room temperature, high strain-rate tests with smooth specimens at room temperature, and quasi-static tests with smooth specimens at elevated temperatures. All specimens were taken parallel to the rolling direction of the steel plate and tested in the as-received condition. From the experiments we found that Weldox 460 E steel exhibits strong strain-hardening, moderate strain-rate hardening (more or less unaffected by the level of plastic strain), and complex temperature softening (caused by the "blue brittle" effect for carbon steels). We further confirmed that the ductility (measured as strain to fracture) decreases markedly with increasing stress triaxiality. Strain rate was found to be less important, but some reduction in ductility was observed with increasing strain rate. As the temperature increases, the main trend is that the ductility increases, but the relation is complex due to the "blue brittle" effect.

Projectiles were manufactured from Arne tool steel. After machining, they were oil-hardened to a Rockwell C value of 53 ($\sigma_y \approx 1900$ MPa) in order to minimise plastic deformations during impact. The mechanical properties of the projectile were obtained through quasi-static tensile test [6]. These tests verified the high strength of the projectile material and further revealed that both strain-hardening capacity and ductility are very low.

Impact tests

We used a compressed gas gun to perform the impact tests (Refs. [1]-[4]). The projectile is accelerated through a barrel and strikes the target after about 2 m of free flight. During testing, the initial velocity of the projectile and the residual velocities of the projectile and plug were measured using different laser and photocell systems. In addition, we used a computer-operated digital high-speed camera system to photograph the penetration process. The target plates had a free span diameter of 500 mm and were clamped in a circular frame by pre-stressed bolts. The nominal hardness, diameter (20 mm) and mass (0.197 kg) of the cylindrical projectiles were constant in all tests, while the length varied between 80 and 98 mm.

The test programme was divided into two parts. First, we varied the plate thickness and the impact velocity of the projectile, while the shape of the projectile was constant [1][2]. A blunt projectile was used in these tests. Second, we kept the plate thickness constant and varied the projectile's nose shape and impact velocity [3][4]. The nose shapes of the projectile were hemispherical and conical – in addition to the already used blunt shape. Results from the tests, given as diagrams of impact velocity against residual velocity of the projectile, are presented in Figure 1.

Metallurgical studies

A metallurgical study was undertaken for some plates partly penetrated by the projectile [5]. For blunt projectiles, the plugging process was controlled by a combination of localised shear, bending and tension for the thinnest plates (less than 10 mm). For plates with thickness between 10 and 16 mm, adiabatic shear bands were detected. These shear bands were only deformed; i.e. no phase-transformed material was found in the shear zones. However, clear evidence of transformed adiabatic shear bands (causing extreme strains, strain rates and temperatures) was found in plates equal to or thicker than 20 mm. Also, elliptical cavities were found along the localised shear zones in front of the projectile, showing that microvoids nucleate, grow and coalesce in front of the crack tip to form the macrocrack. Adiabatic shear bands were not found for hemispherical and conical projectiles. Instead the projectile penetrated the target mainly by pushing the material in front of the projectile aside.

Constitutive relation and failure criterion

The tensile tests of the plate material show that the constitutive relation needs to include strain hardening, strain-rate hardening and temperature softening, while the failure criterion should take into account the influence of stress triaxiality, strain rate and temperature. Johnson and Cook [9][10] have proposed a constitutive equation and a failure criterion having these features based on an extensive set of experimental data. In this study, slightly modified versions of the constitutive relation and failure criterion of Johnson and Cook have been adopted in a coupled model of viscoplasticity and ductile damage [6]. The coupling of damage into the constitutive equations is done within the framework proposed by Lemaitre [11], and this allows accounting for softening effects of microvoids and microcracks. The model has been implemented in LS-DYNA [6][8]. Fracture is simulated by employing element erosion when the damage reaches a critical level. The calibration of the model was based on data from the different tensile tests described above and analytical formulas [6]. The calibration results were verified through finite element simulations of the tensile tests, but no inverse modelling has been used.

The projectile was modelled as elastic-plastic [6]. No failure criterion was used for the projectile material in this study.

Finite element analysis

In the first set of simulations, we investigated the effect of varying the target plate thickness between 4 and 30 mm [2]. We used a fixed mesh of 4-node axisymmetric elements with one-point integration and stiffness-based hourglass control. The smallest element in the impact region was 0.125 x 0.1 mm^2 in all simulations for target thickness equal to or less than 12 mm, while it was increased to 0.25 x 0.2 mm^2 for thicker plates to reduce the CPU time.

In the second set of simulations, we studied the effects of changing the projectile nose shape for target plates with 12 mm thickness [3][4]. Numerical problems occurred for the fixed mesh for conical projectiles due to mesh distortions and unacceptable small time steps, and we found it necessary to adopt rezoning. We ran all adaptive simulations with a characteristic element size of 0.3x0.375 mm^2, giving 40 elements over the target thickness. For blunt projectiles about 10 adaptive refinements were used in each run, while for hemispherical and conical projectiles many more refinements were required–as many as 100 were used in some of the simulations.

Figure 2 shows plots of the initial configuration for the different projectiles. Numerical results are presented in Figure 3 for comparison with the experimental results in Figure 1. Figure 4a compares the experimental and computed capacity of the plates, in terms of the impact velocity just giving complete perforation of the plates – the ballistic limit velocity. The mesh sensitivity observed for blunt projectiles is shown in Figure 4b.

Concluding remarks

The use of computer codes to solve transient dynamic problems is today commonplace, and a large number of commercial FE codes exist. It thus becomes increasingly important to validate the FE codes against precise experimental data. In this work, more than 150 different numerical simulations have been conducted and compared with more than 100 different high-precision, large-scale impact tests. In general, good correlation between numerical and experimental results is achieved, and the correct mechanisms for energy absorption and failure are predicted numerically.

References

[1] T. Børvik, M. Langseth, O.S. Hopperstad and K.A. Malo, Ballistic Penetration of Steel Plates, *Int. J. Impact Engng.*, Vol. 22, No. 9-10, pp. 855-887, 1999.

[2] T. Børvik, O.S. Hopperstad, M. Langseth and K.A. Malo, Effect of Target Thickness in Blunt-Nose Projectile Penetration in Weldox 460 E Steel Plates, *in progress*, 2000.

[3] T. Børvik, M. Langseth, O.S. Hopperstad and K.A. Malo, Effect of projectile nose shape in structural impact, Part I: Experimental study, *submitted for publication*, 2000.

[4] T. Børvik, O.S. Hopperstad, T. Berstad and M. Langseth, Effect of projectile nose shape in structural impact, Part II: Numerical Simulations, *submitted for publication*, 2000

[5] T. Børvik, J.R. Leinum, J.K. Solberg, O.S. Hopperstad and M. Langseth, Shear Plug Formation in Weldox 460 E Steel Plates Impacted by Blunt-Nosed Projectiles, *submitted for publication*, 2000.

[6] T. Børvik, O.S. Hopperstad, T. Berstad and M. Langseth, Computational Model of Viscoplasticity and Ductile Damage for Projectile Impact, *submitted for publication*, 2000.

[7] T. Børvik, O.S. Hopperstad, T. Berstad and M. Langseth, Numerical Simulation of Plugging Failure in Ballistic Penetration, *accepted for publication in the Int. J. Solids and Structures*, 2000.

[8] LS-DYNA User's Manual, Version 950, Livermore Software Technology Corporation, 1999.

[9] G.R. Johnson and W.H. Cook, A Constitutive Model and Data for Metals Subjected to Large Strains, High Strain Rates and High Temperatures, *Proc. of Seventh Int. Symposium on Ballistics*, The Hague, 1983.

[10] G.R. Johnson and W.H. Cook, Fracture Characteristics of Three Metals Subjected to Various Strains, Strain Rates, Temperatures, and Pressures, *Int. J. Engng. Fracture Mechanics,* Vol. 21, pp. 31-48, 1985.

[11] J. Lemaitre, A Short Course in Damage Mechanics, *Springer-Verlag*, 1992.

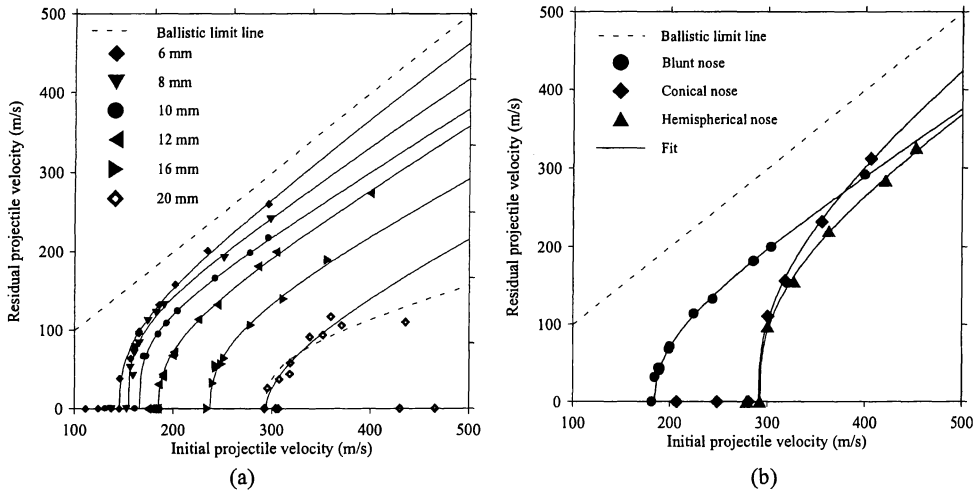

Figure 1. Experimental results for (a) different target thicknesses and (b) projectile nose shapes.

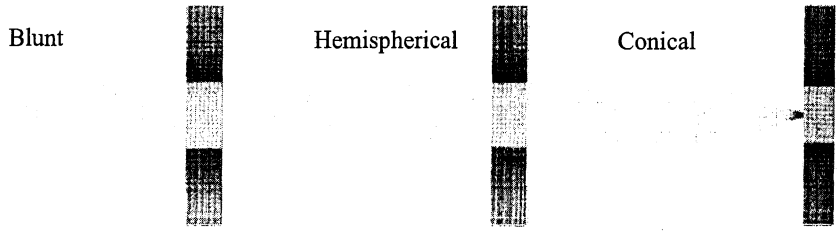

Figure 2. Plots of initial configuration showing the different projectiles and a section of the target.

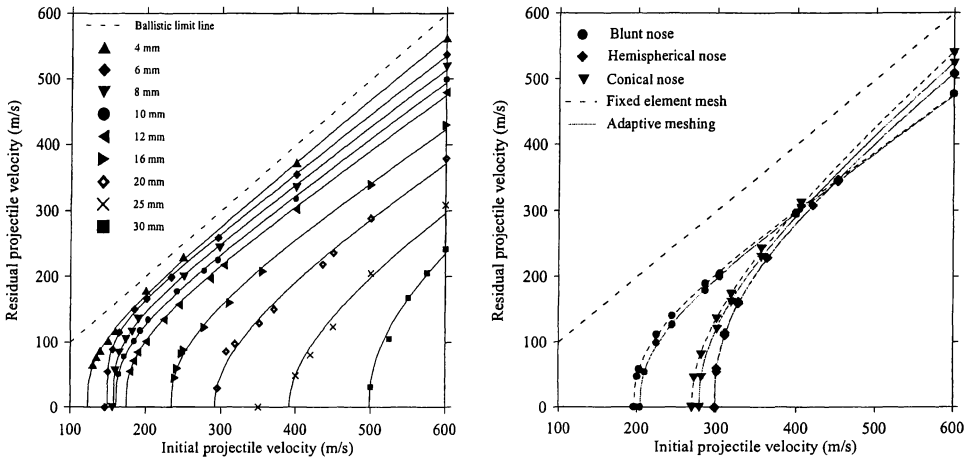

(a) (b)

Figure 3. Computed ballistic limit curves for different (a) target thicknesses and (b) projectile nose shapes.

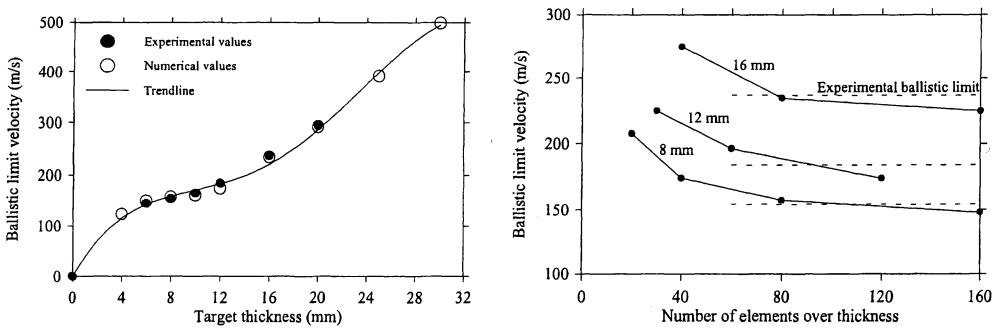

(a) (b)

Figure 4. (a) Comparison between measured and computed ballistic limit velocities versus target thickness. (b) The effect of mesh density on the ballistic limit velocity for targets of different thickness in simulations with blunt projectiles.

On finite element simulations in roadside safety design

Larsgunnar Nilsson

Div. of Solid Mechanics,
Linköping University,
S-581 83 Linköping,
Sweden

Stabilized finite element methods for Reissner-Mindlin plates

Mikko Lyly
Center for Scientific Computing
P.O. Box 405
FIN-02101 Espoo, Finland

Rolf Stenberg
Department of Mathematics
Tampere University of Technology
P.O. Box 692
FIN-33101 Tampere, Finland

1 Introduction

In this communication we will give a short review of the stabilized finite element methods we have developed for the Reissner-Mindlin plate equations. We only present a triangular and a quadrilateral family and refer to our paper [9] for the complete discussion.

The advantages of the stabilized plate elements are:

- They employ standard basis functions, equal for the rotation and the deflection. No special "bubble" degrees of freedom are needed.
- They contain stable and optimally convergent methods with linear (or bilinear) basis functions.
- They give rise to well conditioned stiffness methods which is an advantage for iterative solvers.

2 The plate model

Let $\Omega \subset \mathbb{R}^2$ be the midsurface of the plate and suppose that the plate is clamped along the boundary part Γ_C and free along the complementary part Γ_F. The variational formulation of the (appropriately scaled, cf. e.g. [3]) Reissner-Mindlin model is: find the deflection $w \in W$ and the rotation vector $\boldsymbol{\beta} = (\beta_x, \beta_y) \in \boldsymbol{V}$ such that

$$a(\boldsymbol{\beta}, \boldsymbol{\eta}) + t^{-2}(\nabla w - \boldsymbol{\beta}, \nabla v - \boldsymbol{\eta}) = (g, v) \quad \forall (v, \boldsymbol{\eta}) \in W \times \boldsymbol{V}. \tag{2.1}$$

Here t is the thickness of the plate and g is the (scaled) transverse load. The bilinear form a represents bending energy and is defined as

$$a(\boldsymbol{\beta}, \boldsymbol{\eta}) = \frac{1}{6}\Big\{(\boldsymbol{\varepsilon}(\boldsymbol{\beta}), \boldsymbol{\varepsilon}(\boldsymbol{\eta})) + \frac{\nu}{1-\nu}(\operatorname{div}\boldsymbol{\beta}, \operatorname{div}\boldsymbol{\eta})\Big\}, \tag{2.2}$$

where ν is the Poisson ratio, $\boldsymbol{\varepsilon}(\cdot)$ is the small strain tensor and "div" stands for the divergence, viz.

$$\boldsymbol{\varepsilon}(\boldsymbol{\beta}) = \frac{1}{2}\Big\{\nabla\boldsymbol{\beta} + (\nabla\boldsymbol{\beta})^T\Big\}, \tag{2.3}$$

$$\operatorname{div}\boldsymbol{\beta} = \frac{\partial\beta_x}{\partial x} + \frac{\partial\beta_y}{\partial y}. \tag{2.4}$$

The spaces for the deflection and rotation are

$$W = \{\, v \in H^1(\Omega) \mid v_{|\Gamma_C} = 0 \,\} \quad \text{and} \quad \boldsymbol{V} = \{\, \boldsymbol{\eta} \in [H^1(\Omega)]^2 \mid \boldsymbol{\eta}_{|\Gamma_C} = \boldsymbol{0} \,\}, \tag{2.5}$$

respectively. We use standard mathematical notation. For $D \subset \mathbb{R}^2$ we define the Sobolev spaces $H^s(D)$, with $s \geq 0$, in the usual way by interpolation [7]. The norms and seminorms will be denoted by $\|\cdot\|_{s,D}$ and $|\cdot|_{s,D}$, respectively. The L_2-inner products in $L_2(D)$, $[L_2(D)]^2$ or $[L_2(D)]^{2\times 2}$ are denoted by $(\cdot,\cdot)_D$. The subscript D will be dropped when $D = \Omega$.

By taking the (scaled) shear force

$$\boldsymbol{q} = t^{-2}(\nabla w - \boldsymbol{\beta}) \tag{2.6}$$

as an independent unknown in $\boldsymbol{S} = [L_2(\Omega)]^2$ one gets the following mixed formulation: find $(w, \boldsymbol{\beta}, \boldsymbol{q}) \in W \times \boldsymbol{V} \times \boldsymbol{S}$ such that

$$\begin{aligned} a(\boldsymbol{\beta}, \boldsymbol{\eta}) + (\boldsymbol{q}, \nabla v - \boldsymbol{\eta}) &= (g, v) \quad \forall (v, \boldsymbol{\eta}) \in W \times \boldsymbol{V}, \\ (\nabla w - \boldsymbol{\beta}, \boldsymbol{s}) - t^2(\boldsymbol{q}, \boldsymbol{s}) &= 0 \qquad \forall \boldsymbol{s} \in \boldsymbol{S}. \end{aligned} \tag{2.7}$$

The differential equations of this system are obtained by integrating by parts:

$$\begin{aligned} \boldsymbol{L}\boldsymbol{\beta} + \boldsymbol{q} &= \boldsymbol{0} \quad \text{in } \Omega, \\ -\operatorname{div} \boldsymbol{q} &= g \quad \text{in } \Omega, \\ -t^2\boldsymbol{q} + \nabla w - \boldsymbol{\beta} &= \boldsymbol{0} \quad \text{in } \Omega, \\ w = 0,\ \boldsymbol{\beta} &= \boldsymbol{0} \quad \text{on } \Gamma_C, \\ \boldsymbol{m} \cdot \boldsymbol{n} = \boldsymbol{0},\ \boldsymbol{q} \cdot \boldsymbol{n} &= 0 \quad \text{on } \Gamma_F. \end{aligned} \tag{2.8}$$

Here the differential operator $\boldsymbol{L}$ is defined from

$$\boldsymbol{L}\boldsymbol{\eta} = \frac{1}{6}\mathbf{div}\left\{\boldsymbol{\varepsilon}(\boldsymbol{\eta}) + \frac{\nu}{1-\nu}\operatorname{div}\boldsymbol{\eta}\boldsymbol{I}\right\} \tag{2.9}$$

and $\boldsymbol{m}$ is the (scaled) bending moment tensor:

$$\boldsymbol{m} = \frac{1}{6}\left\{\boldsymbol{\varepsilon}(\boldsymbol{\beta}) + \frac{\nu}{1-\nu}\operatorname{div}\boldsymbol{\beta}\boldsymbol{I}\right\}. \tag{2.10}$$

The notation **div** stands for the divergence of second order tensors:

$$\mathbf{div}\, \boldsymbol{r} = \left(\frac{\partial r_{xx}}{\partial x} + \frac{\partial r_{xy}}{\partial y}, \frac{\partial r_{yx}}{\partial x} + \frac{\partial r_{yy}}{\partial y}\right). \tag{2.11}$$

The first two equations in (2.8) are the local equilibrium equations between the moment, shear force and load. The third equation is the constitutive relation between the shear strain and shear force.

3 The stabilized methods

Let $\mathcal{C}_h$ be a partitioning of $\bar{\Omega}$ into triangular or quadrilateral finite elements of size h. The elements $K \in \mathcal{C}_h$ are images of the reference element $\hat{K}$ under the (bi)linear mapping $\boldsymbol{F}_K : \hat{K} \to K$. The discrete solution spaces are defined with the index $k \geq 1$ as

$$W_h = \{v \in W \mid v_{|K} \in R_k(K),\ \forall K \in \mathcal{C}_h\}, \tag{3.1}$$

$$\boldsymbol{V}_h = \{\boldsymbol{\eta} \in \boldsymbol{V} \mid \boldsymbol{\eta}_{|K} \in [R_k(K)]^2,\ \forall K \in \mathcal{C}_h\}, \tag{3.2}$$

and

$$\boldsymbol{S}_h = \{\boldsymbol{s} \in \boldsymbol{S} \mid \boldsymbol{s}_{|K} \in \boldsymbol{S}_k(K),\ \forall K \in \mathcal{C}_h\}, \tag{3.3}$$

where

$$R_k(K) = \begin{cases} P_m(K) & \text{when } K \text{ is a triangle,} \\ Q_k(K) & \text{when } K \text{ is a quadrilateral,} \end{cases} \tag{3.4}$$

and

$$\boldsymbol{S}_k(K) = \{\boldsymbol{\eta} = \boldsymbol{J}_K^{-T}\hat{\boldsymbol{\eta}} \circ \boldsymbol{F}_K^{-1} \mid \hat{\boldsymbol{\eta}} \in \boldsymbol{S}_k(\hat{K})\}. \tag{3.5}$$

Here $P_k(K)$ and $Q_k(K)$ are the usual polynomial spaces defined on K. $\boldsymbol{J}_K$ is the Jacobian matrix of $\boldsymbol{F}_K$ and $\boldsymbol{J}_K^{-T}$ is the transpose of $\boldsymbol{J}_K^{-1}$. The space $\boldsymbol{S}_k(\hat{K})$ will be defined later.

The methods are all defined as follows: find the approximate deflection $w_h \in W_h$ and the rotation vector $\boldsymbol{\beta}_h \in \boldsymbol{V}_h$ such that

$$\mathcal{B}_h(w_h, \boldsymbol{\beta}_h; v, \boldsymbol{\eta}) = (g, v) \quad \forall (v, \boldsymbol{\eta}) \in W_h \times \boldsymbol{V}_h, \tag{3.6}$$

with

$$\mathcal{B}_h(z, \boldsymbol{\phi}; v, \boldsymbol{\eta}) = a(\boldsymbol{\phi}, \boldsymbol{\eta}) - \sum_{K \in \mathcal{C}_h} \alpha_K h_K^2 (\boldsymbol{L}\boldsymbol{\phi}, \boldsymbol{L}\boldsymbol{\eta})_K \tag{3.7}$$

$$+ \sum_{K \in \mathcal{C}_h} (t^2 + \alpha_K h_K^2)^{-1} (\boldsymbol{R}_K(\nabla z - \boldsymbol{\phi}) - \alpha_K h_K^2 \boldsymbol{L}\boldsymbol{\phi}, \boldsymbol{R}_K(\nabla v - \boldsymbol{\eta}) - \alpha_K h_K^2 \boldsymbol{L}\boldsymbol{\eta})_K.$$

The approximate shear is computed from

$$\boldsymbol{q}_{h|K} = (t^2 + \alpha_K h_K^2)^{-1} (\boldsymbol{R}_K(\nabla w_h - \boldsymbol{\beta}_h) - \alpha_K h_K^2 \boldsymbol{L}\boldsymbol{\beta}_h)_{|K},\ \forall K \in \mathcal{C}_h. \tag{3.8}$$

Here $\alpha_K > 0$ is a numerical parameter, h_K is the size of K and $\boldsymbol{R}_K : [H^1(K)]^2 \to \boldsymbol{S}_k(K)$ is the MITC reduction operator. It is defined from the operator $\boldsymbol{R}_{\hat{K}} : [H^1(\hat{K})]^2 \to \boldsymbol{S}_k(\hat{K})$ on the reference element by a covariant transformation through the equation

$$\boldsymbol{R}_K \boldsymbol{\eta} = \boldsymbol{J}_K^{-T} \boldsymbol{R}_{\hat{K}} \boldsymbol{J}_K^T \boldsymbol{\eta}. \tag{3.9}$$

The different methods are finally specified by defining the operator $\boldsymbol{R}_{\hat{K}}$ together with the space $\boldsymbol{S}_k(\hat{K})$. In this paper we will consider the following two choices.

Triangular elements. *For a triangle K we choose*

$$\boldsymbol{S}_k(\hat{K}) = [P_{k-1}(\hat{K})]^2 \oplus (\eta, -\xi)\widetilde{P}_{k-1}(\hat{K}), \tag{3.10}$$

where $\widetilde{P}_{k-1}(\hat{K})$ is space of homogeneous polynomials of degree $k-1$. ξ and η are the coordinates of $\hat{K}$ (i.e. the natural coordinates of K). This is the 90-degrees rotated Raviart-Thomas space [11] .

The reduction operator $\boldsymbol{R}_{\hat{K}}$ is defined through the conditions

$$\int_{\hat{E}} [(\boldsymbol{R}_{\hat{K}}\hat{\boldsymbol{\eta}} - \hat{\boldsymbol{\eta}}) \cdot \hat{\tau}]\hat{v}\, d\hat{s} = 0,\ \forall \hat{v} \in P_{k-1}(\hat{E}),\ \textit{for every edge } \hat{E} \text{ of } \hat{K}, \tag{3.11}$$

and

$$\int_{\hat{K}} (\boldsymbol{R}_{\hat{K}}\hat{\boldsymbol{\eta}} - \hat{\boldsymbol{\eta}}) \cdot \hat{\boldsymbol{s}}\, d\xi d\eta = 0,\ \forall \hat{\boldsymbol{s}} \in [P_{k-2}(\hat{K})]^2, \tag{3.12}$$

where $\hat{\tau}$ is the unit tangent to the edge.

Remark 3.1 When $k = 1$, it holds

$$\boldsymbol{L}\boldsymbol{\eta}_{|K} = \mathbf{0}, \quad \forall K \in \mathcal{C}_h, \ \forall \boldsymbol{\eta} \in \boldsymbol{V}_h, \tag{3.13}$$

and the bilinear form $\mathcal{B}_h$ reduces to

$$\mathcal{B}_h(z, \boldsymbol{\phi}; v, \boldsymbol{\eta}) = a(\boldsymbol{\phi}, \boldsymbol{\eta}) + \sum_{K \in \mathcal{C}_h} (t^2 + \alpha_K h_K^2)^{-1} (\boldsymbol{R}_K(\nabla z - \boldsymbol{\phi}), \boldsymbol{R}_K(\nabla v - \boldsymbol{\eta}))_K. \tag{3.14}$$

This gives the linear element introduced and analyzed in [5]. In [8] it has been shown that this element is essentially equivalent to an element introduced by Hughes and Tessler [13]. Later, it has been rediscovered in [14, 2, 12].

Quadrilateral elements. *For a quadrilateral K we choose*

$$\boldsymbol{S}_k(\hat{K}) = P_{k-1,k}(\hat{K}) \times P_{k,k-1}(\hat{K}), \tag{3.15}$$

which is the 90-degrees rotated rectangular Raviart-Thomas space [11].

The reduction operator is defined through the conditions

$$\int_{\hat{E}} [(\boldsymbol{R}_{\hat{K}}\hat{\boldsymbol{\eta}} \ - \hat{\boldsymbol{\eta}} \ ) \cdot \hat{\boldsymbol{\tau}}] \hat{v} \ d\hat{s} = 0, \ \forall \hat{v} \in P_{k-1}(\hat{E}), \ \textit{for every edge } \hat{E} \textit{ of } \hat{K}, \tag{3.16}$$

and

$$\int_{\hat{K}} (\boldsymbol{R}_{\hat{K}}\hat{\boldsymbol{\eta}} \ - \hat{\boldsymbol{\eta}} \ ) \cdot \hat{\boldsymbol{s}} \ d\xi d\eta = 0, \ \forall \hat{\boldsymbol{s}} \in P_{k-1,k-2}(\hat{K}) \times P_{k-2,k-1}(\hat{K}). \tag{3.17}$$

Remark 3.2 The MITC4 element of Bathe and Dvorkin [4] is obtained from the family of quadrilateral elements by taking $k = 1$ and $\alpha = 0$.

4 Stability and error analysis

Let us next outline the error analysis of the methods. A detailed theoretical discussion can be found from [9], where it was shown that the methods are stable and optimally convergent with respect to h and k, uniformly in t, provided that appropriate boundary layer refinements have been performed.

To begin with, let us denote by $C_I > 0$ the biggest constant in the inverse inequality

$$C_I \sum_{K \in \mathcal{C}_h} h_K^2 \|\boldsymbol{L}\,\boldsymbol{\eta}\|_{0,K}^2 \le a(\boldsymbol{\eta}, \boldsymbol{\eta}), \qquad \forall \boldsymbol{\eta} \in \boldsymbol{V}_h, \tag{4.1}$$

which is valid as $\boldsymbol{V}_h$ consists of continuous piecewise polynomial functions (cf. e.g. [6]).

For the discrete solution space $W_h \times \boldsymbol{V}_h$ we define the mesh dependent norm

$$|||(v, \boldsymbol{\eta})|||_h = \|v\|_1 + \|\boldsymbol{\eta}\|_1 + \Big(\sum_{K \in \mathcal{C}_h} (t^2 + h_K^2)^{-1} \|\boldsymbol{R}_K(\nabla v - \boldsymbol{\eta})\|_{0,K}^2 \Big)^{1/2}. \tag{4.2}$$

The stability follows then from the Poincaré and Korn inequalities [8, Theorem 4.1]:

Theorem 4.1 *There exists a constant $C > 0$ such that for $0 < \alpha < C_I$ it holds*

$$\mathcal{B}_h(v, \eta; v, \eta) \geq C|||(v, \eta)|||_h^2 \quad \forall (v, \eta) \in W_h \times \boldsymbol{V}_h. \quad \square$$

In the convergence analysis we use a regularity result by Arnold and Liu [1] for clamped polygonal plates. The analysis in [1] reveals that the exact solution has a strong irregular boundary layer in a small neighborhood of $\partial\Omega$. In the interior part of the midsurface the regularity is dictated by the smoothness of the load.

To measure the size of the elements in the interior region Ω_i and the boundary region $\Omega_b = \Omega \setminus \Omega_i$ we introduce the mesh parameters

$$h_i = \max_{K \subset \Omega_i} h_K, \quad h_b = \max_{K \not\subset \Omega_i} h_K. \tag{4.3}$$

We then have [8, Theorem 4.3]:

Theorem 4.2 *Suppose that $g \in H^{k-1}(\Omega)$ and $0 < \alpha < C_I$ for all $K \in \mathcal{C}_h$. Then it holds*

$$\|w - w_h\|_1 + \|\beta - \beta_h\|_1 + \Big(\sum_{K \in \mathcal{C}_h} (t^2 + h_K^2) \|\boldsymbol{q} - \boldsymbol{q}_h\|_{0,K}^2 \Big)^{1/2}$$
$$\leq C \Big\{ h_i^k (\|g\|_{k-2} + t\|g\|_{k-1}) + h_b (\|g\|_{-1} + t\|g\|_0) \Big\}. \quad \square$$

According to the result the methods are optimally convergent for all $t > 0$ provided that the mesh is refined towards the boundary such that $h_b = \mathcal{O}(h_i^k)$. Furthermore, it suffices to use (bi)linear elements with $k = 1$ in Ω_b. The boundary layer is then resolved within the same accuracy as the smooth component in Ω_i using higher order elements with $k \geq 1$. The grading and transition between different polynomial degrees can be performed by appropriate restrictions on the inter element boundaries.

5 Numerical examples

In [9, 10] we showed by numerical experiments that our stabilized methods with $k = 1, 2, 3$, are stable and converge as predicted by the theory. The numerical results indicated that the accuracy of the (bi)linear elements is rather insensitive to the choice of the stabilization parameter in the range $0.1 \leq \alpha \leq 0.5$. The best compromise value for different boundary conditions etc. was found to be $\alpha = 0.2$ for the quadrilateral elements and $\alpha = 0.4$ for the triangular elements. For higher order methods with $k \geq 2$ the optimal value can be determined numerically from small local eigenvalue problems.

In this paper we study the spectral condition number of the stiffness matrix with respect to α for different values of t and h. The purpose of the experiments is to show that the condition number is of order $\mathcal{O}(h^{-4})$ for all $t > 0$ The theoretically predicted estimate for standard plate elements is $\mathcal{O}(t^{-2}h^{-2})$, which meanins that the system becomes ill conditioned as $t \to 0$. The stabilized methods do not suffer from this defect. We also show that stabilization can significantly speed up the iterative solution of the equations.

The numerical results will be given for a uniformly loaded clamped square plate with $\bar{\Omega} = [0, 1] \times [0, 1]$ and $0.001 \leq t \leq 0.1$. The material parameters are taken to be $E = 1$ and $\nu = 0.3$. We will consider the linear and bilienear elements with $k = 1$ and $0 < \alpha \leq 1/2$. The midsurface of the plate is divided uniformly into $N \times N$ quadrilateral and $2N \times N$ triangular elements, see Figure 1.

In Figure 2 we have plotted the condition number of the stiffness matrix with respect to the mesh parameter $h = 1/N$ for $0 < \alpha \leq 1/2$ with $t = 0.01$ fixed. In Figure 3 we plot the condition number with respect to $0.0001 \leq t \leq 0.1$ for $0 < \alpha \leq 1/2$ with $h = 1/8$ fixed.

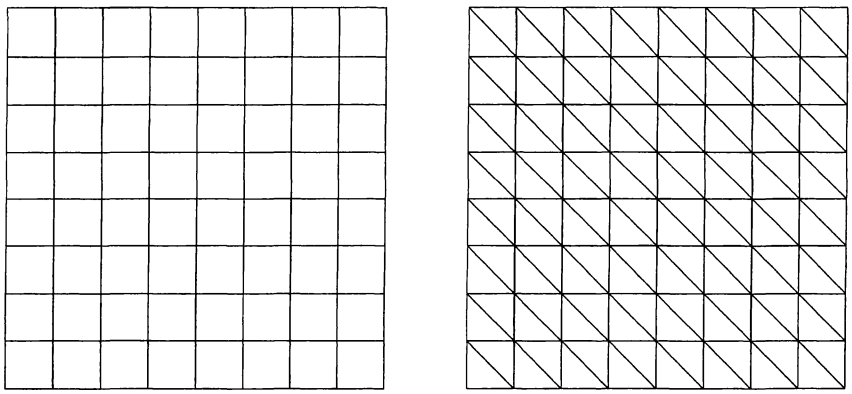

Figure 1. The quadrilateral and triangular finite element meshes for $N = 8$.

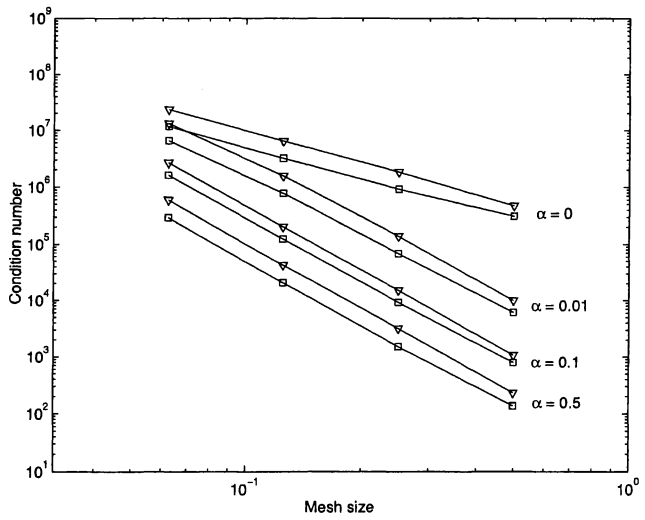

Figure 2. Condition number of the stiffness matrix for $t = 0.01$ with $\frac{1}{16} \leq h \leq \frac{1}{2}$ and $0 \leq \alpha \leq 0.5$. The symbols $\bigtriangledown$ and $\square$ denote the linear and bilinear elements, respectively.

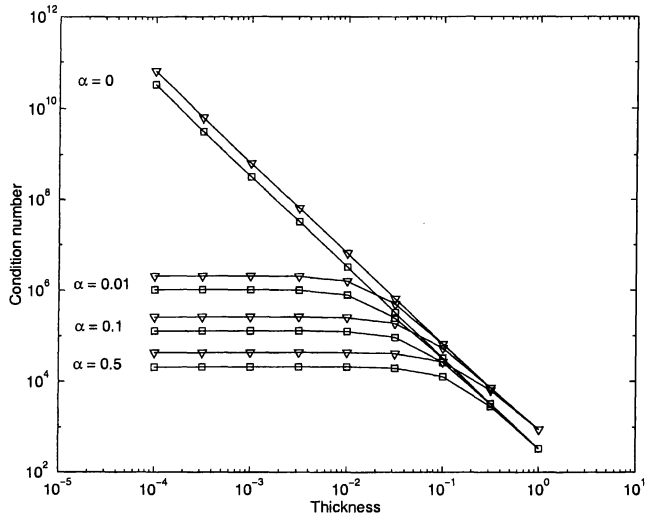

Figure 3. Condition number of the stiffness matrix for $h = 1/8$ with $0.0001 \leq t \leq 1$ and $0 \leq \alpha \leq 0.5$. The symbols $\bigtriangledown$ and $\square$ denote the linear and bilinear elements, respectively.

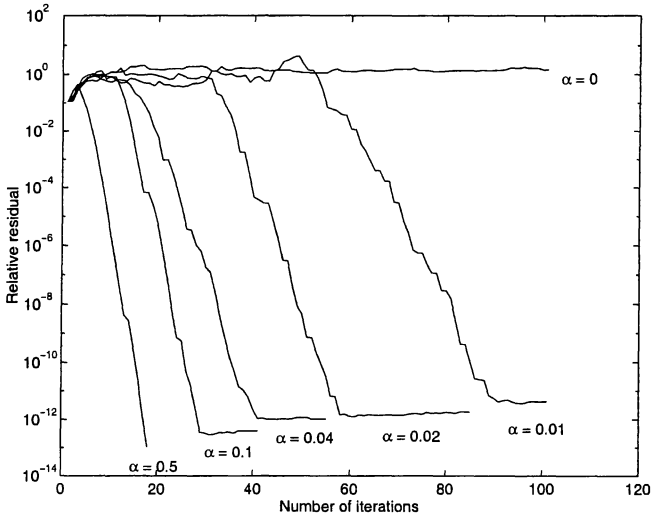

Figure 4. Relative residual of the preconditioned conjugate gradient solution.

The figures show that the condition number for the original MITC4 element with $\alpha = 0$ is proportional to t^{-2} and h^{-2}. For the stabilized methods with $\alpha > 0$, the condition number is proportional to h^{-4}, i.e. it is independent of the thickness of the plate. When iterative solution methods are considered, this can be a great advantage.

Let us finally consider the numerical solution of the equilibrium equations by the preconditioned conjugate gradient method. The results are given for the triangular elemenet with $k = 1$. Figure 4 shows the relative residual of the pcg-algorithm of MATLAB with

respect to the number of iterations. The thickness of the plate was $t = 0.01$ and mesh parameter $h = 1/8$. The equations were preconditioned by an incomplete Cholesky factorization of the stiffness matrix. The results show that stabilization improves dramatically the convergence speed of the method.

References

[1] D.N. Arnold and X. Liu. Interior estimates for a low order finite element method for the Reissner-Mindlin plate model. *Adv. Comp. Math.*, 7:337–360, 1997.

[2] F. Auricchio and R.L. Taylor. A triangular thick plate finite element with an exact thin limit. *Finite Elements in Analysis and Design*, 19:57–68, 1995.

[3] K.J. Bathe, F. Brezzi, and M. Fortin. Mixed-interpolated elements for Reissner-Mindlin plates. *Int. J. Num. Meths. Eng.*, 28:1787–1801, 1989.

[4] K.J. Bathe and E. Dvorkin. A four node plate bending element based on Mindlin-Reissner plate theory and mixed interpolation. *Int. J. Num. Meths. Eng.*, 21:367–383, 1985.

[5] F. Brezzi, M. Fortin, and R. Stenberg. Error analysis of mixed-interpolated elements for Reissner-Mindlin plates. *Mathematical Models and Methods in Applied Sciences*, 1:125–151, 1991.

[6] P.G. Ciarlet. *The Finite Element Method for Elliptic Problems.* North - Holland, 1978.

[7] J. L. Lions and E. Magenes. *Non-homogeneous Boundary Value Problems and Applications I.* Springer-Verlag, Berlin, Heidelberg, New York, 1972.

[8] M. Lyly. On the connection between some linear triangular Reissner-Mindlin plate bending elements. *Numer. Math.*, 85:77–107, 2000.

[9] M. Lyly and R. Stenberg. Stabilized finite element methods for Reissner-Mindlin plates. *Universität Innsbruck, Institut für Mathematik und Geometrie. Forschungsbericht 4-1999. 40 pp.*

[10] M. Lyly, R. Stenberg, and T. Vihinen. A stable bilinear element for Reissner-Mindlin plates. *Comp. Meths. in Appl. Mech. Engrg.*, 110:343–357, 1993.

[11] P.A. Raviart and J.M. Thomas. A mixed finite element method for second order elliptic problems. In *Mathematical Aspects of the Finite Element Method. Lecture Notes in Math. 606*, pages 292–315. Springer-Verlag, 1977.

[12] R.L. Taylor and F. Auricchio. Linked interpolation for Reissner-Mindlin plate elements. *Int. J. Num. Meths. Eng.*, 36:3057–3066, 1993.

[13] A. Tessler and T.J.R. Hughes. A three node mindlin plate element with improved transverse shear. *Comp. Meths. Appl. Mech. Engrg.*, 50:71–101, 1985.

[14] Z. Xu. A thick-thin triangular plate element. *Int. J. Num. Meths. Eng.*, 33:963–973, 1992.

Radiation Boundary Conditions for Acoustic and Elastic Waves

Steen Krenk

Department of Structural Engineering and Materials
Technical University of Denmark, DK-2800 Lyngby, Denmark

Abstract. An overview of radiation boundary conditions for acoustic and elastic waves is presented. When the waves at the boundary come from a limited region local boundary conditions may be used, consisting of an impedance relation for plane waves, and an additional stiffness term for diverging waves. Wide-angle radiation boundary conditions are obtained for acoustic waves by introducing an approximate representation of the angle of incidence in terms of derivatives in the surface. The use of Padé approximations or a rational interpolation scheme corresponding to multi-directional transmission is discussed. A formulation in terms of fictitious surface layers is described, and it is demonstrated that radiation through corners can be described accurately by introducing radiation boundary conditions for the fictitious surface layers at the corners. An extension of this formulation from acoustic to elastic waves is indicated.

1. Introduction

Many problems of elastic wave propagation involve infinite domains, and solution of such problems by finite element or finite difference methods must therefore account for the existence of an infinite medium beyond the finite part included in the mesh and bounded by a radiation boundary, introduced in the model, Fig. 1. Different methods exist for representing the influence of the infinite medium beyond the radiation boundary such as infinite elements, coupling to a boundary element representation of the infinite domain, and the use of radiation boundary conditions.

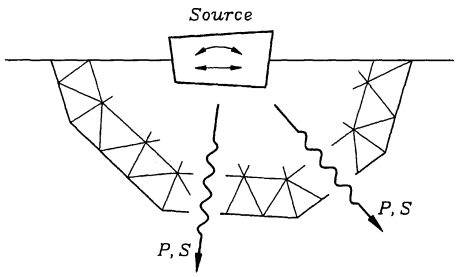

Figure 1. Radiation or scattering of elastic waves.

The elastic wave propagation problem is governed by the equations of motion

$$\boldsymbol{\nabla}\cdot\boldsymbol{\sigma} \;-\; \rho\,\ddot{\mathbf{u}} \;+\; \mathbf{f} \;=\; \mathbf{0} \tag{1}$$

where $\boldsymbol{\sigma}$ is the stress tensor, $\mathbf{u}$ the displacement vector, and ρ the mass density. $\boldsymbol{\nabla}$ is the gradient or divergence operator and a dot over a symbol indicates time differentiation. In a variational setting the form of the boundary conditions follows from multiplication of the field equations by a virtual displacement vector $\tilde{\mathbf{u}}$, integration over the material volume, and use of the divergence theorem. The result is

$$\int_S \tilde{\mathbf{u}}\cdot(\hat{\mathbf{n}}\cdot\boldsymbol{\sigma})\,dS \;-\; \int_V \big(\tilde{\boldsymbol{\varepsilon}}:\boldsymbol{\sigma} \;+\; \rho\,\tilde{\mathbf{u}}\cdot\ddot{\mathbf{u}} \;-\; \tilde{\mathbf{u}}\cdot\mathbf{f}\big)\,dV \;=\; 0 \tag{2}$$

The boundary conditions are identified from the surface integral in first term. Within a variational formulation a radiation boundary condition must similarly enable evaluation of the contribution to the boundary integral from the radiation boundary. This amounts to the establishment of an expression for the boundary stress vector $\boldsymbol{\tau}$ in terms of the displacement and velocity vector fields $\mathbf{u}$ and $\dot{\mathbf{u}}$, representing radiation *from* the boundary.

2. Local Radiation Boundary Condition

The simplest kind of radiation condition consists of a relation between the stress vector $\boldsymbol{\tau}$ and the velocity $\dot{\mathbf{u}}$. This relation, originating in acoustics as the impedance condition, was used for elastic waves by Lysmer & Kuhlemeyer (1969) in the form of an analogy. In a similar ad hoc fashion the effect of wave spreading was introduced by Kellezi (1999), assuming the type of attenuation representative of two-dimensional spreading. A rigorous theory, presented by Krenk & Kirkegaard (2000), is summarized in this section. The extension to moving loads has been presented by Krenk et al. (1999). The much simpler acoustic case follows in a similar way. A discussion of current finite element procedures for radiating boundary conditions is given by Wolf & Song (1996).

2.1. Plane wave condition – Impedance form.

Figure 2a illustrates a plane elastic wave field propagating in the direction of the unit vector $\hat{\mathbf{r}}$. The corresponding displacement field can be written as the sum of a primary compression wave field $\mathbf{u}_P$ and a secondary shear wave field $\mathbf{u}_S$,

$$\mathbf{u} \;=\; \mathbf{u}_P \;+\; \mathbf{u}_S \tag{3}$$

The P-wave consists of displacements in the direction $\hat{\mathbf{r}}$, propagating with wave speed c_P, while the S-wave consists of transverse motion, here assumed to be in the transverse direction defined by the unit vector $\hat{\mathbf{t}}$, propagating with wave speed c_S,

$$\mathbf{u}_P \;=\; \hat{\mathbf{r}}\,u_P(t-r/c_P) \qquad , \qquad \mathbf{u}_S \;=\; \hat{\mathbf{t}}\,u_S(t-r/c_S) \tag{4}$$

The wave speeds are given in terms of the Lame constants and the density as

$$c_P^2 \;=\; \frac{\lambda+2\mu}{\rho} \qquad , \qquad c_S^2 \;=\; \frac{\mu}{\rho} \tag{5}$$

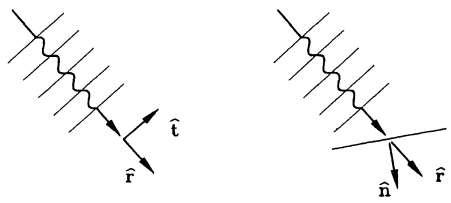

FIGURE 2. Plane elastic wave field propagating in direction $\hat{\mathbf{r}}$.

The particular form (4) of the primary and secondary wave fields leads to the plane wave identities,

$$\Big(\frac{\partial}{\partial t} + c_P\frac{\partial}{\partial r}\Big)\mathbf{u}_P = \mathbf{0} \quad , \quad \Big(\frac{\partial}{\partial t} + c_S\frac{\partial}{\partial r}\Big)\mathbf{u}_S = \mathbf{0} \tag{6}$$

These identities contain the information to be expressed in the local plane wave radiation condition.

The radiation condition for plane elastic waves is obtained by separating the wave field into P- and S-components, and then using the identities (6) to express spatial displacement derivatives in the stress vector in terms of the time derivative. This leads to a tensor relation between the stress vector on an arbitrarily oriented section with outward normal vector $\hat{\mathbf{n}}$ and the velocity vector $\dot{\mathbf{u}}$. The stress contributions from the compression and shear waves are derived separately and then combined to yield the radiation condition as a tensor relation between the total stress vector and the total velocity, Krenk & Kirkegaard (2000).

$$\boldsymbol{\tau} = -(\mathbf{Z}_P + \mathbf{Z}_S)\cdot\dot{\mathbf{u}} = -\mathbf{Z}\cdot\dot{\mathbf{u}} \tag{7}$$

where the impedance tensor $\mathbf{Z}$ of a plane wave field propagating in the direction $\hat{\mathbf{r}}$ is given by

$$\mathbf{Z} = \frac{2\mu}{c_P}(\hat{\mathbf{n}}\cdot\hat{\mathbf{r}})\,\hat{\mathbf{r}}\hat{\mathbf{r}} + \frac{\mu}{c_S}(\hat{\mathbf{n}}\cdot\hat{\mathbf{r}})\,(\mathbf{1} - 2\hat{\mathbf{r}}\hat{\mathbf{r}}) + \frac{\lambda}{c_P}\hat{\mathbf{n}}\hat{\mathbf{r}} + \frac{\mu}{c_S}\hat{\mathbf{r}}\hat{\mathbf{n}} \tag{8}$$

Symmetry of the impedance tensor is only obtained for normal incidence of the waves on the section considered, or for a special material parameter combination, $\lambda = 2\mu$.

In the special case of normal incidence, $\hat{\mathbf{n}} = \hat{\mathbf{r}}$, the impedance tensor simplifies considerably,

$$\mathbf{Z} = \rho c_P\hat{\mathbf{r}}\hat{\mathbf{r}} + \rho c_S(\mathbf{1} - \hat{\mathbf{r}}\hat{\mathbf{r}}) \tag{9}$$

The first term is identified as a projection on the direction of propagation multiplied by the scalar impedance ρc_P of compression waves, and the second term is a projection on a transverse plane multiplied by the scalar impedance ρc_S of shear waves.

2.2. **Diverging wave condition – Additional stiffness.** In the case of spherical waves the displacement fields $\mathbf{u}_P$ and $\mathbf{u}_S$ satisfy the identities

$$\Big(\frac{\partial}{\partial t} + \frac{c_P}{r}\frac{\partial}{\partial r}r\Big)\mathbf{u}_P = \mathbf{0} \quad , \quad \Big(\frac{\partial}{\partial t} + \frac{c_S}{r}\frac{\partial}{\partial r}r\Big)\mathbf{u}_S = \mathbf{0} \tag{10}$$

Where the only difference from the plane wave identities is the inclusion of the coordinate r inside the spatial differential operator. This introduces an additional term $r^{-1}\mathbf{u}$ into the impedance relation (7).

When gradients along the wave front are neglected the stress vector generated by the compression and shear waves from a point source can be expressed in terms of the local total velocity and displacement vectors in the form

$$\boldsymbol{\tau} = -\mathbf{Z}\cdot\dot{\mathbf{u}} - \mathbf{R}\cdot\mathbf{u} \tag{11}$$

where $\mathbf{R}$ is an apparent stiffness tensor, generated by the spreading of the waves. The impedance tensor $\mathbf{Z}$ is identical to (8) corresponding to plane waves. The stiffness tensor $\mathbf{R}$ is given as the sum of P- and S-wave contributions as

$$\mathbf{R} = \mathbf{R}_P + \mathbf{R}_S = -\frac{\lambda+2\mu}{r}\hat{\mathbf{n}}\hat{\mathbf{r}} + \frac{2\mu}{r}\Big[\hat{\mathbf{r}}\hat{\mathbf{n}} + (\hat{\mathbf{n}}\cdot\hat{\mathbf{r}})\,\mathbf{1}\Big] \tag{12}$$

The stiffness decreases with distance from the source as r^{-1} for a spherical source.

2.3. **Example.** The local tensor boundary condition (11) has been tested by the concentrated force problem illustrated in Fig. 6. Ideally the force $\mathbf{f}(t)$ located at the origin of the coordinate system is assumed to act in an infinite isotropic elastic continuum. The model consists of a finite element discretization of the first octant with side length $L = 25\,\mathrm{m}$ using simple 8-node elements with linear displacement interpolation and side length $h = 1\,\mathrm{m}$. In both types of analysis the material was specified with wave speeds $c_P = 2c_S = 20\,\mathrm{m/s}$, corresponding to the special case of symmetric impedance matrix.

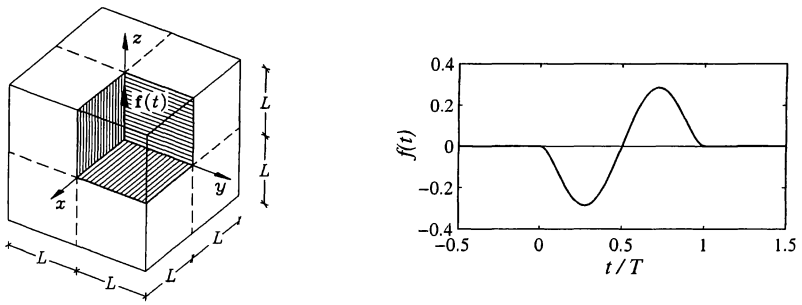

FIGURE 3. a) Elastic cube with side length $2L$, b) Time history of force pulse, $n = 2$.

The pulse shape was selected from the polynomial family defined by

$$f(t) = \tau\left(1-\tau^2\right)^n \quad , \quad -1 < \tau < 1 \tag{13}$$

with $\tau = 2t/T - 1$. The total duration of the pulse is T, and the integer n leads to vanishing derivatives of order $0, 1, n-1$ at the ends of the pulse.

The progress of the waves through the cube for a pulse duration of $T = 2\,\mathrm{s}$ is illustrated in Figs. 4 and 5, showing the strain energy density of the P-waves and the S-waves, respectively, at times $t = 1.25, 2.5, 4.0\,\mathrm{s}$. Figures 4a and b clearly show the angular variation of the P-wave field, while the P-wave has nearly left the cube in Fig. 4c. The circular wave front pattern of the S-waves in the transverse plane is illustrated in Fig. 5, where Fig. 4c shows the undisturbed passage of the radiating boundary without visible reflections.

FIGURE 4. P-wave strain energy density in xz-plane, a) $t = 1.25\,\mathrm{s}$, b) $t = 2.5\,\mathrm{s}$, c) $t = 4.0\,\mathrm{s}$.

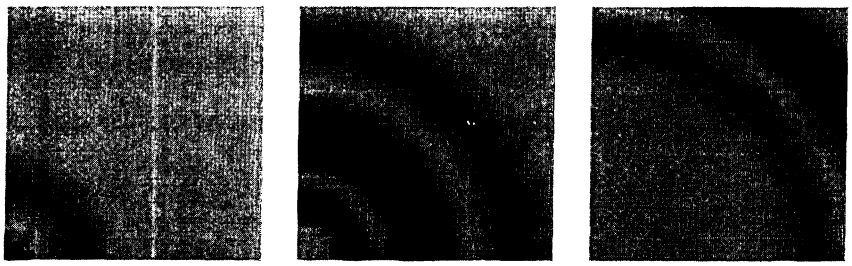

FIGURE 5. S-wave strain energy density in xy-plane, a) $t = 1.25\,\mathrm{s}$, b) $t = 2.5\,\mathrm{s}$, c) $t = 4.0\,\mathrm{s}$.

3. Wide-angle boundary conditions – Acoustic case

While the local radiation boundary condition described above has the advantage of simplicity, it is restricted by the need for a known representative direction of wave propagation at the boundary. This restriction can be overcome – or at least relaxed considerably – by using additional information of the wave field on the radiating boundary. This approach is described for acoustic waves in this section, Krenk (2000a), while a generalization to elastic waves is briefly sketched in Section 4, Krenk (2000b) .

For acoustic waves a potential function $\varphi(\mathbf{x})$ satisfies the wave equation

$$\nabla^2\varphi \;-\; \frac{1}{c^2}\frac{\partial^2\varphi}{\partial t^2} \;+\; f \;=\; 0 \tag{14}$$

When using a variational formulation it is seen that on the radiating part of the boundary a relation must be specified for the normal derivative $\partial\varphi/\partial n$ in terms of the potential φ or its time or spatial derivatives on the boundary.

3.1. **Padé approximation and fictitious layers.** A convenient basis for the development of radiation boundary conditions is the representation as a sum of plane waves of different direction, but all propagating outward through the radiating boundary surface. A plane wave with wave number vector $\mathbf{k}$ and angular frequency ω has a representation of the form

$$\varphi \;\propto\; \exp\, i\big(\omega t - \mathbf{k}\cdot\mathbf{x}\big) \tag{15}$$

Each plane wave satisfies the first order wave propagation equation

$$\nabla\varphi \;+\; \frac{\mathbf{k}}{\omega}\frac{\partial\varphi}{\partial t} \;=\; 0 \tag{16}$$

This vector equation produces a scalar radiation boundary condition by projection on the boundary surface normal $\mathbf{n}$,

$$\frac{\partial\varphi}{\partial n} \;+\; \frac{\cos\theta}{c}\frac{\partial\varphi}{\partial t} \;=\; 0 \tag{17}$$

where θ is the angle between the direction of propagation $\mathbf{k}$ and the outward normal $\mathbf{n}$.

In the general wave equation problem the angle θ is not known, and indeed wave components with any angle θ in the interval $-\frac{1}{2}\pi < \theta < \frac{1}{2}\pi$ are typically present. Thus the factor $\cos\theta$ in (17) must be expressed in a form not involving the angle explicitly. This task can be solved by expressing $\cos\theta$ approximately in terms of $\sin^2\theta$, because this term can be expressed directly by the Laplace operator in the radiating surface. A particular choice is the Padé approximation

$$\cos\theta \;=\; 1 \;-\; \cfrac{\sin^2\theta}{2 \;-\; \cfrac{\sin^2\theta}{2 \;-\; \cfrac{\sin^2\theta}{2 \;-\; \cdots}}} \qquad , \quad 0 \le \cos\theta \le 1 \tag{18}$$

where each additional term matches another term in the Taylor expansion around $\theta = 0$. This is a particular instance of a rational approximation of the form

$$\cos\theta \simeq \alpha_0 - \sum_{m=1}^{M} \frac{\alpha_m \sin^2\theta}{1 - \beta_m \sin^2\theta} \quad , \quad 0 \leq \cos\theta \leq 1 \tag{19}$$

The parameter α_0 is the value of the approximation at $\theta = 0$, and each unit fraction contains two parameters, α_m and β_m. In the continued fraction expansion (18) $\alpha_0 = 1$, corresponding to exact representation of normal incidence. When the rational approximation (19) is substituted into the plane wave boundary condition (17), it takes the form

$$\left(\frac{\partial}{\partial n} + \frac{\alpha_0}{c}\frac{\partial}{\partial t}\right)\varphi = \sum_{m=1}^{M} \frac{1}{c}\frac{\partial \psi_m}{\partial t} \quad , \quad \mathbf{x} \in S_\infty \tag{20}$$

where the terms ψ_m represent boundary densities defined as

$$\psi_m = \frac{\alpha_m \sin^2\theta}{1 - \beta_m \sin^2\theta}\,\varphi \quad , \quad \mathbf{x} \in S_\infty \tag{21}$$

This definition of the boundary density ψ_m can be recast into the form of a second order partial differential equation

$$\left[\frac{1}{c^2}\frac{\partial^2}{\partial t^2} - \beta_m \nabla_\perp^2\right]\psi_m = \alpha_m \nabla_\perp^2 \varphi \quad , \quad \mathbf{x} \in S_\infty \tag{22}$$

where $\nabla_\perp^2$ is the Laplace operator *in* the radiating surface, corresponding to the wave number $k_\perp = \sin\theta\, k$. Thus, the radiation boundary condition has been represented in terms of the first order relation (20) between the normal derivative $\partial\varphi/\partial n$, the time derivative of φ and M surface densities ψ_m, defined on the radiating surface S_∞ and governed by the wave equations (22) defined on this surface. This formulation is illustrated in Fig. 6.

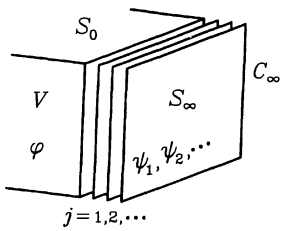

FIGURE 6. Radiation boundary condition as fictitious surface densities.

The boundary conditions (20)–(21) are a modified form of those proposed by Lindman (1975), while Enquist & Majda (1997,1999) used a similar technique to derive higher order boundary conditions. The present form arises naturally from the weak formulation by which an expression must be prescribed for the the normal derivative $\partial\varphi/\partial n$ on the radiating boundary surface. The present form of the boundary condition is ideally suited for finite element formulation by using the divergence theorem on the boundary integral.

3.2. **Multi-directional transmission.** An alternative and intuitively appealing way of constructing radiation boundary conditions was proposed by Higdon (1987,1990). The idea is to build a higher order boundary condition by forming products of the simple condition (17) with ideal transmission for selected angles $\theta_1, \theta_2, \cdots, \theta_J$.

$$\prod_{j=1}^{J} \Big(\frac{\partial}{\partial n} + \frac{\cos\theta_j}{c} \frac{\partial}{\partial t} \Big) \varphi \;=\; 0 \quad , \quad \mathbf{x} \in S_\infty \tag{23}$$

This boundary condition is a higher order operator, requiring special measures when implemented directly in finite difference or finite element codes. However, as demonstrated in the following, the multi-directional transmission condition (23) can be formulated in terms of fictitious surface densities in the form of (20) and (22). Indeed, the selection of angles $\theta_1, \cdots, \theta_J$ of ideal transmission is an effective way of obtaining desirable properties of the boundary condition, no matter what computational format is chosen subsequently.

The properties of the multi-directional boundary condition can be characterized in relation to a plane wave of the form (15), giving the simple product format

$$\prod_{j=1}^{J} \big(\cos\theta_j - \cos\theta \big) \, \varphi \;=\; 0 \tag{24}$$

When all terms with odd powers of $\cos\theta$ are collected, and $\cos\theta$ is extracted as a common factor to these terms, the polynomial takes the form

$$\begin{aligned} \prod_{j=1}^{J} \big(\cos\theta_j - \cos\theta \big) \;=\; & \big[\{\cos\theta_j\}_J^J + \{\cos\theta_j\}_{J-2}^J \cos^2\theta + \cdots \big] \\ & - \cos\theta \big[\{\cos\theta_j\}_{J-1}^J + \{\cos\theta_j\}_{J-3}^J \cos^2\theta + \cdots \big] \end{aligned} \tag{25}$$

The product boundary condition (24) is identical to the boundary condition obtained by substitution of (25) and division by the second bracket.

$$\Big(\cos\theta \;-\; \frac{\{\cos\theta_j\}_J^J + \{\cos\theta_j\}_{J-2}^J \cos^2\theta + \cdots}{\{\cos\theta_j\}_{J-1}^J + \{\cos\theta_j\}_{J-3}^J \cos^2\theta + \cdots} \Big) \varphi \;=\; 0 \tag{26}$$

It follows from the equation (25) that the term in the parenthesis of (26) vanishes for $\theta = \theta_j, j = 1, 2, \cdots$. Thus, the rational function interpolates $\cos\theta$ between these angles.

The rational function interpolation

$$\cos\theta \;\simeq\; \frac{\{\cos\theta_j\}_J^J + \{\cos\theta_j\}_{J-2}^J \cos^2\theta + \cdots}{\{\cos\theta_j\}_{J-1}^J + \{\cos\theta_j\}_{J-3}^J \cos^2\theta + \cdots} \quad , \quad 0 \le \cos\theta \le 1 \tag{27}$$

is a generalization of the Padé representation (18). In fact, the Padé representation corresponds to the particular case in which $\theta_1 = \theta_2 = \cdots = \theta_J = 0$, i.e. the case where the product format (22) is simply the normal incidence condition raised to the power J. This case corresponds to the limit of arbitrarily close interpolation points, each contributing by matching one more derivative at $\theta = 0$.

The quality of the radiation boundary condition can be evaluated from the reflection coefficient,

$$R \;=\; \frac{\Phi_r}{\Phi_i} \;=\; -\frac{\prod_{j=1}^{J}\big(\cos\theta_j - \cos\theta\big)}{\prod_{j=1}^{J}\big(\cos\theta_j + \cos\theta\big)} \tag{28}$$

which gives the amplitude of the reflected wave relative to the incident wave. This formula clearly indicates the perfect transmission at the angles θ_j. Numerical results indicate that equally spaced ideal transmission angles over the interval $0 \le \theta_j < \frac{1}{2}\pi$ give near-optimal properties of the boundary condition.

The rational interpolation representation (27) can be expressed in terms of unit fractions in the form

$$\cos\theta \;\simeq\; a_0 \;+\; \sum_{m=1}^{M} \frac{a_m \cos^2\theta}{1 \;+\; b_m \cos^2\theta} \quad , \quad 0 \le \cos\theta \le 1 \tag{29}$$

This form is equivalent to the unit fraction representation (19) used to identify the fictitious surface density format of the radiation boundary condition. Substitution of $\cos^2\theta = 1 - \sin^2\theta$ into (29) leads to the following expressions for the boundary condition parameters

$$\alpha_0 \;=\; a_0 + \sum_{m=1}^{M} \frac{a_m}{1+b_m} \quad , \quad \alpha_m \;=\; \frac{a_m}{(1+b_m)^2} \quad , \quad \beta_m \;=\; \frac{b_m}{1+b_m} \tag{30}$$

Expansions with one or two unit fractions are easily calculated analytically, but for higher order expansions numerical methods are needed. A simple procedure is available in the MATLAB program package, where the coefficients $\{\cos\theta_j\}_k^J$ can be evaluated by the function `poly`, and after a split in even and odd degree coefficients the unit fraction expansion coefficients a_0, a_m and b_m are evaluated by use of the function `residue`.

3.3. **Surface density boundary conditions.** The radiating boundary condition consists of the modified wave transmission equation (20) and the m wave equations (22) for the surface densities ψ_m. Variational equations for the surface densities ψ_m are obtained from the wave equations (22) *on the radiating surface* via multiplication by the virtual densities $\tilde{\psi}_m$, followed by integration over the radiating surface S_∞. After use of the divergence theorem on the surface Laplacian, these equations take the form

$$\begin{aligned} \int_{S_\infty} \Big[\frac{\tilde{\psi}_m}{c^2}\frac{\partial^2\psi_m}{\partial t^2} \;+\; \beta_m \nabla_\perp\tilde{\psi}_m \cdot \nabla_\perp\psi_m \;+\; \alpha_m \nabla_\perp\tilde{\psi}_m \cdot \nabla_\perp\varphi \Big]\, dS \\ - \int_{C_\infty} \tilde{\psi}_m \Big[\beta_m \frac{\partial\psi_m}{\partial n_\perp} \;+\; \alpha_m \frac{\partial\varphi}{\partial n_\perp} \Big]\, ds \;=\; 0 \end{aligned} \tag{31}$$

The surface densities may contain discontinuities or discontinuous derivatives at edges, and therefore the contour C_∞ must be considered as surrounding all individual continuous patches of the radiating surface S_∞.

The terms in (31) associated with the contour(s) C_∞ resembles the boundary term in the original problem, but now in a space of reduced dimension as the integral over S_∞ is replaced by an integral over its boundary C_∞, illustrated in Fig. 6. For a three-dimensional wave problem the boundary will be a two-dimensional surface, and an edge between two parts of the radiating surface will then be associated with additional line densities according to the theory presented above. For a two-dimensional wave problem the boundary is a contour, and parts of the radiating contour can meet at a corner. At such a corner each fictitious density ψ_m must be permitted to be discontinuous, and each part must satisfy the one-dimensional radiation condition corresponding to the wave velocity $c_m = c\sqrt{\beta_m}$ of the layer,

$$\frac{\partial \psi_m}{\partial n_\perp} + \frac{1}{c_m}\frac{\partial \psi_m}{\partial t} = 0 \tag{32}$$

Note the similarity with the normal transmission condition of the original problem.

At a radiating edge or corner the gradient term $\partial\varphi/\partial n_\perp$ would correspond to a concentrated load. The physics of the problem does not permit waves from this load to be sent back along the fictitious layer, and thus this term is absorbed into the radiation condition and disappears.

3.4. **Example.** The numerical performance of the fictitious surface density radiation boundary conditions is illustrated by considering a harmonic point source in an infinite plane at $(x, y) = (0, 0)$. Symmetry conditions are imposed along the axes, and the source intensity in the quarter-plane is selected as unity, whereby the analytical solution is expressed in terms of the Hankel function $\mathrm{H}_0^{(2)}(\,)$ as

$$\varphi = -i\,\mathrm{H}_0^{(2)}\Big(\frac{r\omega}{c}\Big)\,\mathrm{e}^{i\omega t} \tag{33}$$

The angular frequency is $\omega = 2\pi$ and the wave speed $c = 1$, whereby the wave length is $\lambda = 1$. A rectangular area in the first quadrant with dimensions $b \times h = 3.0 \times 1.0$ is modeled, Fig. 6. The area is discretized by use of bi-linear elements on a 45×15 mesh, corresponding to 15 elements per wavelength.

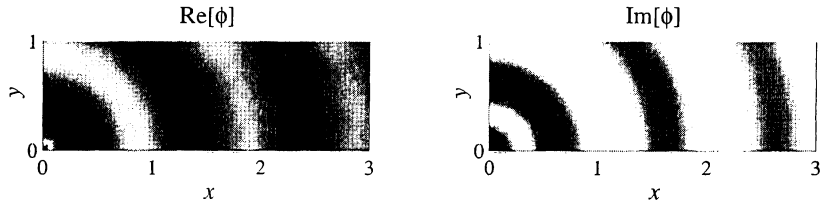

FIGURE 7. Wave field distribution for 1-layer condition.

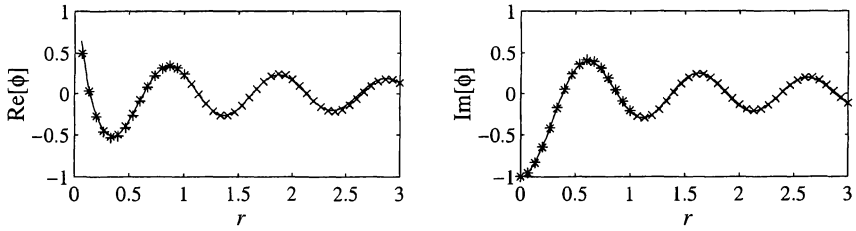

FIGURE 8. Wave field along axes, 1-layer: $\times$ x-axis, $+$ y-axis.

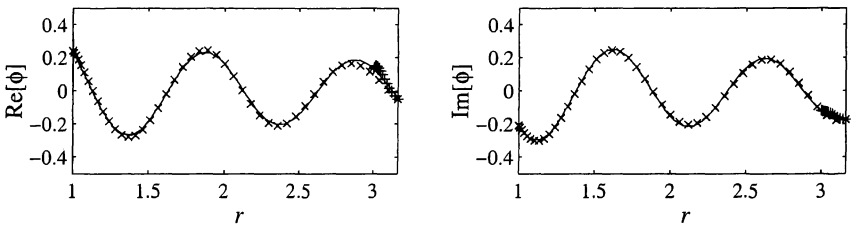

FIGURE 9. Wave field along sides, 1-layer: $\times$ at top $y = h$, $+$ at side $x = b$.

The assembled system equations can be written symbolically as

$$\begin{bmatrix} \mathbf{K}_{\varphi\varphi} - \omega^2\mathbf{M}_{\varphi\varphi} + i\omega\mathbf{C}_{\varphi\varphi} & -i\omega\mathbf{C}_{\varphi m} \\ \mathbf{K}_{m\varphi} & \mathbf{K}_{mm} - \omega^2\mathbf{M}_{mm} + i\omega\mathbf{C}_{mm} \end{bmatrix} \begin{bmatrix} \boldsymbol{\varphi} \\ \boldsymbol{\psi} \end{bmatrix} = \begin{bmatrix} \mathbf{f} + \mathbf{g} \\ \mathbf{0} \end{bmatrix} \tag{34}$$

where the vector $\boldsymbol{\psi}$ represents one or more fictitious surface density layers. In the present example the loading conditions are a unit load at the node $(x, y) = (0, 0)$. Radiation conditions are imposed along the sides $x = b$ and $y = h$, and each of these parts are associated with surface densities ψ_m, that are discontinuous at the radiating corner $(x, y) = (b, h)$, where radiation conditions of the form (32) are applied to each part separately.

The results are shown in Figs. 7-9 for a single fictitious surface layer. Figure 7 shows the real and imaginary fields, while Fig. 8 shows a comparison between the analytical solution (33) and the numerical results along the axes, and Fig. 9 shows similar results along the sides. The agreement is very good except in an area around the corner, where the angle of incidence is larger than the 61°, for which the reflection coefficient practically vanishes. With two layers the angle of incidence covered by the boundary is increased to 72°, and the results are very good in the whole domain, Krenk (2000a).

4. Wide-angle boundary condition for elastic waves

In the acoustic wave propagation problem the boundary condition (17) for oblique incidence could be used to obtain a general boundary condition by expressing the factor $\cos\theta$ by a rational function of $\sin^2\theta$. In the elastic problem the boundary condition is of tensor form as discussed in Section 2, and there are two angles due to P- and S-waves, respectively. In the elastic case it may therefore be convenient to use a somewhat more general approach associated with a split of the wave equation operator into two factors. This procedure is first outlined for acoustic waves, and the resulting elastic boundary condition is then given.

4.1. **Operator splitting.** The basic problem of development of radiation boundary conditions can be illustrated by the following simple argument, in which curvature is neglected for simplicity. Let n be a coordinate along the outward surface normal $\mathbf{n}$. The Laplace operator can then be split additively in the form

$$\nabla^2 = \frac{\partial^2}{\partial n^2} + \nabla_\perp^2 \tag{35}$$

where $\nabla_\perp^2$ is the Laplace operator on the boundary surface. Upon substitution of this representation, the acoustic wave equation (14) can be written in the form

$$\Big(\frac{\partial}{\partial n} - \frac{1}{c}\frac{\partial}{\partial t}\Big)\Big(\frac{\partial}{\partial n} + \frac{1}{c}\frac{\partial}{\partial t}\Big)\varphi = -\nabla_\perp^2\varphi \tag{36}$$

Formally, this is equivalent to

$$\Big(\frac{\partial}{\partial n} + \frac{1}{c}\frac{\partial}{\partial t}\Big)\varphi = \Big(\frac{1}{c}\frac{\partial}{\partial t} - \frac{\partial}{\partial n}\Big)^{-1}\nabla_\perp^2\varphi \tag{37}$$

For normal incidence the wave fronts coincide with the surface, whereby $\nabla_\perp^2\varphi = 0$. For non-normal incidence or combined wave fields an approximation of the right hand side must be obtained. If the problem is transformed into wave-number and frequency space, the Padé approximation can be considered as a sequence of approximations obtained by continued back substitution of the previous approximation into the right hand side of the equation.

4.2. **Elastic radiation conditions.** The elastodynamic field equation for an isotropic medium is

$$(\lambda+\mu)\nabla(\nabla\cdot\mathbf{u}) + \mu\nabla^2\mathbf{u} - \rho\,\partial_t^2\mathbf{u} = \mathbf{0} \tag{38}$$

The first step is to write this vector equation in a block format that separates normal and in-plane components,

$$\begin{bmatrix} (\lambda+2\mu)\partial_n^2 - \rho\partial_t^2 & \\ & \mu\partial_n^2 - \rho\partial_t^2 \end{bmatrix}\begin{bmatrix} u_n \\ \mathbf{u}_\perp \end{bmatrix} = -\begin{bmatrix} \mu\nabla_\perp^2 & (\lambda+\mu)\partial_n\nabla_\perp\cdot \\ (\lambda+\mu)\nabla_\perp\partial_n & (\lambda+\mu)\nabla_\perp\nabla_\perp\cdot + \mu\nabla_\perp^2 \end{bmatrix}\begin{bmatrix} u_n \\ \mathbf{u}_\perp \end{bmatrix} \tag{39}$$

These equations are now divided by the density ρ, and the left hand side factored into in- and out-going waves similar to (36),

$$\begin{bmatrix} c_P\partial_n + \partial_t & \\ & c_S\partial_n + \partial_t \end{bmatrix} \begin{bmatrix} u_n \\ \mathbf{u}_\perp \end{bmatrix} \tag{40}$$

$$= \begin{bmatrix} \partial_t - c_P\partial_n & \\ & \partial_t - c_S\partial_n \end{bmatrix}^{-1} \begin{bmatrix} c_S^2\nabla_\perp^2 & (c_P^2 - c_S^2)\partial_n\nabla_\perp\cdot \\ (c_P^2 - c_S^2)\nabla_\perp\partial_n & (c_P^2 - c_S^2)\nabla_\perp\nabla_\perp\cdot + c_S^2\nabla_\perp^2 \end{bmatrix} \begin{bmatrix} u_n \\ \mathbf{u}_\perp \end{bmatrix}$$

The normal derivatives ∂_n on the right side are eliminated by addition and subtraction of ∂_t. Finally an asymptotic solution is obtained, starting from normal incidence, by back substituting the previous result into the right side of the equation. The first order solution can be expressed in a form similar to that of the acoustic problem, namely a set of boundary conditions

$$\tau_n + \rho c_P\,\partial_t u_n + \mu\,\nabla_\perp\cdot\,\mathbf{u}_\perp = \rho c_P\,\partial_t\psi_n \tag{41}$$

$$\boldsymbol{\tau}_\perp + \rho c_S\,\partial_t\mathbf{u}_\perp + \lambda\,\nabla_\perp u_n = \rho c_S\,\partial_t\boldsymbol{\psi}_\perp \tag{42}$$

with additional terms from the boundary densities ψ_n and $\boldsymbol{\psi}_\perp$. The boundary densities in turn are governed by the second order field equations

$$\begin{aligned}[\rho\,\partial_t^2 - \tfrac{1}{4}\mu\nabla_\perp^2]\psi_n + \tfrac{1}{4}(\lambda+\mu)c_P^{-1}\partial_t\nabla_\perp\cdot\,\boldsymbol{\psi}_\perp \\ = \tfrac{1}{2}\mu\nabla_\perp^2 u_n + \tfrac{1}{2}(\lambda+\mu)c_P^{-1}\partial_t\nabla_\perp\cdot\mathbf{u}_\perp\end{aligned} \tag{43}$$

and

$$\begin{aligned}\tfrac{1}{4}(\lambda+\mu)c_S^{-1}\nabla_\perp\partial_t\psi_n + [\rho\,\partial_t^2 - \tfrac{1}{4}((\lambda+\mu)\nabla_\perp\nabla_\perp\cdot + \mu\,\nabla_\perp^2)]\boldsymbol{\psi}_\perp \\ = \tfrac{1}{2}(\lambda+\mu)c_S^{-1}\nabla_\perp\partial_t u_n + \tfrac{1}{2}[(\lambda+\mu)\nabla_\perp\nabla_\perp\cdot + \mu\,\nabla_\perp^2]\mathbf{u}_\perp\end{aligned} \tag{44}$$

corresponding to an elastic layer with transverse displacements ψ_n and an elastic layer with in-plane displacements $\boldsymbol{\psi}_\perp$. This formulation is a generalization of the Padé formulation of the acoustic problem, described in Section 3.1. Implementation of the elastodynamic boundary conditions is currently under way, Krenk (2000b).

5. Conclusions

Two types of radiation boundary conditions for the wave equation and elastodynamics in the time domain have been presented: a local impedance-stiffness condition, and a family of boundary conditions formulated in terms of fictitious surface layers. While the first requires the direction of incidence to be fairly well defined and known, the second type is valid within a certain angle around normal incidence. For the acoustic problem a single layer gives an angle around 60°, while two layers give 72°. A general technique for splitting the field equation into in- and out-going wave operators is used to extend the results to elastodynamics, leading to a surface shear layer and a layer with in-plane deformation. At

the intersection of two radiating surfaces it has been demonstrated that each part should be considered independent, and a radiation condition prescribed in the radiating surface.

Acknowledgment. This work has been supported by the Danish Technical Research Council.

REFERENCES

Enquist, B. and Majda, A. (1977), Absorbing boundary conditions for the numerical simulation of waves, *Mathematics of Computation*, Vol. 31, pp. 629-651.

Enquist, B. and Majda, A. (1979), Radiation boundary conditions for acoustic and elastic wave calculations, *Communications on Pure and Applied Mathematics*, Vol. 32, pp. 313-357.

Higdon, R.L. (1987), Numerical absorbing boundary conditions for the wave equation, *Mathematics of Computation*, Vol. 49, pp. 65-90.

Higdon, R.L. (1990), Radiation boundary conditions for elastic wave propagation, *SIAM Journal of Numerical Analysis*, Vol. 27, pp. 831-870.

Kellezi, L.X. (1999) *Dynamic Soil-Structure-Interaction, Transmitting Boundary for Transient Analysis*, Ph.D. Thesis, Department of Structural Engineering and Materials, Technical University of Denmark.

Krenk, S. (2000), Unified formulation of radiation conditions for the wave equation, *Danish Center for Applied Mathematics and Mechanics*, Report No. 634. (to be published)

Krenk, S. (2000), Asymptotic Elastic Wave Radiation Condition as a Boundary Layer, Technical University of Denmark. (in preparation)

Krenk, S., Kellezi, L., Nielsen, S.R.K. and Kirkegaard, P.H. (1999), Finite elements and transmitting boundary conditions for moving loads, *Structural Dynamics, Eurodyn '99*, Balkema, Rotterdam, Vol. 1, 447-452.

Krenk, S. and P.H. Kirkegaard (2000), Local tensor radiation conditions for elastic waves, Technical University of Denmark. (to be published)

Lindman, E.L. (1975), 'Free-Space' boundary conditions for the time dependent wave equation, *Journal of Computational Physics*, Vol. 18, pp. 66-78.

Lysmer, J. and Kuhlemeyer, R.L. (1969), Finite dynamic model for infinite media, *Journal of Engineering Mechanics, ASCE*, Vol. 95, pp. 859-877.

Wolf, J.P. and Song, C. (1996), *Finite Element Modelling of Unbounded Media.* Wiley, New York.

Non-linear Behaviour of Elastic and Viscoelastic Shells

Janis Brauns
Professor of Civil Engineering, Dr. Habil. Sc. Eng.

Department of Structural Engineering, LUA
19 Academia St., Jelgava, LV-3001, LATVIA
E-mail: braun@acad.latnet.lv

Introduction

The present tendencies toward using the strength reserves of construction materials to the very limit, the design of shell constructions of minimum weight, and other requirements make it essential to analyse non-linear mechanical and geometrical effects in structures. Advanced materials such as those on the polymer base behave complicated on loading, and in general the time dependence of their deformation fails to obey the linear equations of viscoelastic theory. There are three important characteristics of nonelastic behaviour: buckling that occurs in the course of creep, large displacements, and the redistribution of the stresses with respect to the initial elastic state.

An investigation of the initial imperfections and buckling modes of shells has been the subject of many experimental and theoretical studies [1-4]. On the basis of analysing of the forms of equilibrium it is possible to determine the stability of a shell on the whole [5, 6], especially if a statistical analysis is used [7]. The radial displacement field of shells characterises the stress state of the shell [2, 8].

1. Experimental investigation of viscoelastic shells

Since the mechanical properties of polymeric materials differ from those of metals, it is not possible to transfer these results to the behaviour of shells made by using polymeric materials. In order to study the behaviour of shells composed of a creep-prone material under load, series of experiments on the axial compression of circular cylindrical model shells have been performed. The samples were made from polyethylene, a material possessing the property of non-linear creep, and the mechanical properties of this material under long-time loading have been thoroughly investigated. The geometrical dimensions of the samples were: length L = 200 mm, outer diameter D = 105 mm, thickness h = 2, 3, 4, 5, and 6 mm. The shells were loaded uniformly at a constant rate of 50 N/sec to $q = q_{cr}$ (0.60 – 0.85), where q_{cr} is the instantaneous critical load. The load q was maintained until time when the stability was lost.

During the experiments we used a radial displacement gage to measure the changes in displacement $\tilde{w}(x,y,t_j)$ as a result of the loading process over the whole surface of the shell. The recording was carried out with loop oscillograph, and the time required for the continuous measurement at 12 levels along the length of the shell was 5 sec.

In order to find the characteristic buckling modes as function of time, at every discrete instant t_j the deformed surface was approximated by means of a Fourier series in the complex form:

$$w(x,y,t_j) = \sum_{m=-M}^{M} \sum_{n=-N}^{N} \alpha_{mn}(t_j) e^{i\left(\frac{m\pi x}{L} + \frac{ny}{R}\right)}, \qquad (1)$$

where m is the number of half waves along the generatrix, n is the number of waves around the circumference of the shell, R is the radius of the shell; axes x and y are directed along the generatrix and the circumference. The complex coefficients of the series $\alpha_{mn}(t_j)$ are determined

by integrating the experimental displacement function $\tilde{w}(x,y,t_j)$ taking into account the principle of the least square deviation:

$$\alpha_{mn}(i_j)=\frac{1}{2\pi RL}\int_0^{2\pi R}\int_0^{L}\tilde{w}(x,y,t_j)e^{-i\left(\frac{m\pi x}{L}+\frac{ny}{R}\right)}dxdy. \qquad (2)$$

The form (1) of the expansion for the displacement function is convenient for calculating the stresses in the shell wall, but fails to give any clear representation to kinetics of the buckling process. In order to analyse the changes in individual harmonics with time and also to determine the shape distribution as a function of the wall thickness, the coefficients of a double Fourier series in trigonometric form were used:

$$w(x,y,t_j)=\lambda_{mn}\left(\sum_{m=0}^{M}\sum_{n=0}^{N}a_{mn}(t_j)\cos\frac{m\pi x}{L}\cos\frac{ny}{R}+\sum_{m=0}^{M}\sum_{n=0}^{N}b_{mn}(t_j)\sin\frac{m\pi x}{L}\cos\frac{ny}{R}+\right.$$
$$\left.+\sum_{m=0}^{M}\sum_{n=0}^{N}c_{mn}\cos\frac{m\pi x}{L}\sin\frac{ny}{R}+\sum_{m=0}^{M}\sum_{n=0}^{N}d_{mn}\sin\frac{m\pi x}{L}\sin\frac{ny}{R}\right). \qquad (3)$$

The experimental results showed that, at the beginning of the loading process, the Poisson's effect resulted in a tendency toward transverse expansion of the shell; the median surface assumed a barrel-like form. In Fig. 1, curves show the change of the coefficients characterising the axisymmetrical and asymmetrical buckling shapes for shells with R/h = 8.3 (1, 4), 12.5 (2, 5), and 25.0 (3, 6). The change in coefficients is taking place with increasing load and time. By spectral (harmonic) analysis of the experimental data, it is determined that, during the loading period and initial period of constant load the coefficients leading to the axisymmetrical form develop most sharply. The rate of growth of these coefficients diminishes, but the values of the nonaxially symmetrical coefficients increase at the accelerating rate.

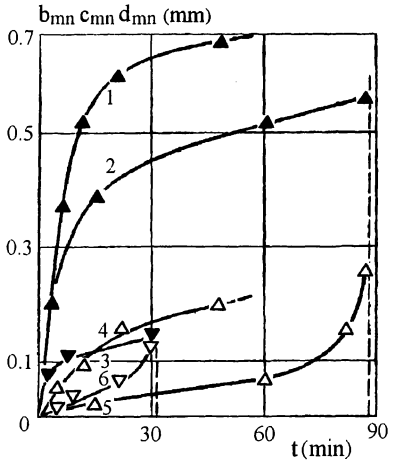

Fig. 1. Time change in the axisymmetrical coefficients c_{30} (1, 2, 3) and asymmetrical coefficients c_{02} (4), b_{23} (5), d_{34} (6).

By using the results of a spectral analysis of the field of displacements, it is possible to make a qualitative estimation of the range of harmonics giving rise to the buckling of shells of various thickness and explain the deformation of shell during loading process. By way of example, the

appearance the coefficient a_{00} is associated with the transverse deformation of the shell wall. The coefficients $\hat{a}_{01}$ and $\hat{a}_{11}$ carry information as to the lack of coincidence between the axes of the shell and radial-displacement gage.

The buckling process exhibits certain peculiarities under creep conditions not found under short-term loading. The nonuniformity of the field of deformation causes the development of an asymmetrical shape. The buckles take the form of depression drown out along the circumferential co-ordinate y. The range of distribution of the essential asymmetrical coefficients varies considerably with increasing thickness parameter. Whereas for shells with R/h = 10 the asymmetrical buckling is mainly characterised by second harmonic, for R/h = 25 the range of buckling shapes embraces the third, fourth, and fifth harmonics. Hence in exact calculations of thin-walled shells a number of other harmonics should be taken into account in addition to the fundamental harmonic, corresponding to the nominal shell size.

In order to study behaviour of composite shells the experimental investigation of the initial imperfections and buckling modes of glass-reinforced plastic cylindrical shells under hydrostatic pressure were performed. The behaviour of reinforced plastics, which, in addition to the anisotropy of mechanical properties, is also characterised by considerable shear creep. The shells tested were with an inside diameter D = 300 mm, nominal lengths L = 300 and 600 mm, and a wall thickness h that varied from 3.0 to 6.0 mm. The composition of the test shells was based on polyester resin. As a reinforcement of shells satin-weave glass fabric and glass fiber reinforcement made by winding method was used. The elastic mechanical characteristics of the shells were determined beforehand.

In order to investigate the process of buckling under short-term and long-term action of hydrostatic pressure an apparatus consisting of three basic units was used. In the control unit hydrostatic load of up to 25 atm was created. The second unit was a pressure chamber in which this load was transmitted to the shell. The third unit was used to measure the radial deflections (RD). The deflections and initial imperfections were measured at three levels every 15° around the perimeter.

For the shells with R/L = 0.60 and R/h = 43 there were initial imperfections with four circumferential waves, for the shells with R/L = 0.29 and R/h = 25 – tree waves. In Fig. 2 the development of the fundamental buckling mode for shell with R/L = 0.6 is shown. The dashed line represents the shape of initial imperfections, curve 1 corresponds to the load level 3.25 atm, curve 2 to a load of 4.0 atm. During loading the basic four-wave shape of the initial imperfections is transformed into a shape with five circumferencial waves. For such shells a theoretical calculation based on the linear theory with allowance for transverse shear predicts a five-wave shape. Along the generatrix the shells buckle in a single half-wave.

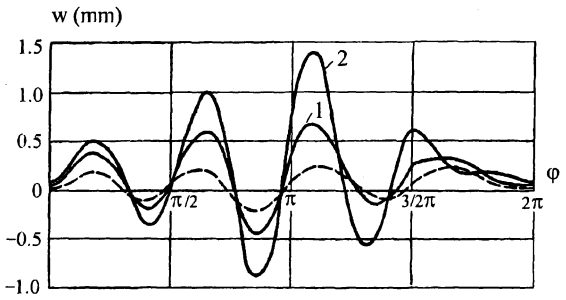

Fig. 2. Deformation of glass fabric reinforced shell under hydrostatic loading.

With the shells subjected to a long-term constant load the RD unit was used to record the changes in buckled shape with time. The variation of the characteristic coefficients of the

Fourier series for shell with R/L = 0.60 is shown in Fig. 3. It should be noted that the four-wave shape changes and a mode with five and six circumferential waves becomes dominant. The coefficients of the fifth and sixth harmonics d_{51} and d_{61} increase with time. This indicates that the deflections develop with time chiefly owing to shear creep strains, i.e., a nonaxisymemetric buckled shape develops.

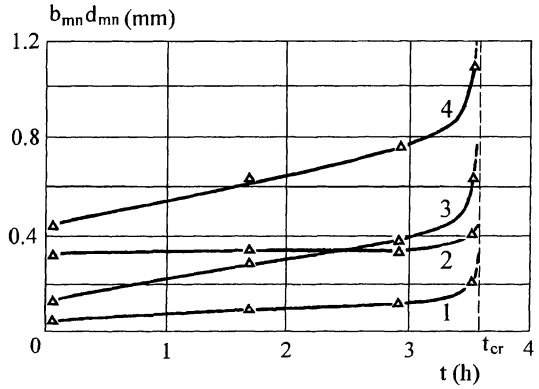

Fig. 3. Variation of characteristic coefficients of glass fabric reinforced shell: $b_{51}(1)$; $b_{01}(2)$; $d_{51}(3)$; $d_{61}(4)$.

2. Modelling of asymmetrical deformation of viscoelastic shell

The experimentally observed axisymmetric – nonaxisymmetric transformation of shapes can be described theoretically by an approach developed in [9]. We shall consider a cylindrical shell prepared from an isotropic and incompressible viscoelastic material. The physical relationships for the general cubic theory of viscoelasticity are written in the form

$$\varepsilon_{ij}(t)=\frac{1}{2G}\left\{s_{ij}(t)+\int_0^t K_1(t-\tau)s_{ij}(\tau)d\tau+\int_0^t K_3(t-\tau)s_{ij}(\tau)s_{kl}(\tau)s_{kl}(\tau)d\tau\right\}; \quad (4)$$

$s_{ij}=\sigma_{ij}-\sigma\delta_{ij}$; i, j, k, l = 1, 2.

For radial deflection function w and the Airy stress function Φ an approximation were introduced in the following form

$$w(x,y,t)=\sum_{m=-M}^{M}\sum_{n=-N}^{N}[\alpha_{mn}(t)-\alpha_{mn}{}^{0}]\Psi_{mn}(x,y); \quad (5)$$

$$\Phi(x,y,t)=\sum_{m=-M}^{M}\sum_{n=-N}^{N}\varphi_{mn}(t)\Psi_{mn}(m,n)-\frac{q_x y^2}{2}, \quad (6)$$

where $\Psi_{mn}(x,y)=e^{\left(\frac{m\pi x}{L}+\frac{ny}{R}\right)}$ are functions satisfying the given boundary conditions. The coefficients $\alpha_{mn}{}^{0}$ correspond to the function of initial irregularities in the geometry of the shell.

Taking into account the Kirchhoff–Love kinematic hypothesis, and by introducing (4), (5) and (6) into equations of equilibrium and compatibility of cylindrical shell resolving equations can be formed [9]. By integrating the system of resolving equations according to the Bubnov–Galerkin method there is possibility to pass from a system of non-linear integrodifferential equations to a system of non-linear integral equations. The system of equations of a mixed type

with unknown coefficients for expanding of the deflections function $\alpha_{mn}(t)$ and the stress function $\varphi_{mn}(t)$ is written as

$$A_{mn}\left\{\varphi_{mn}(t)+\breve{K}_1\varphi_{mn}\right\}+\frac{1}{3}\breve{K}_3\left\{\sum_{i=1}^{5}\sum_{l,u=-M}^{M}\sum_{k,v=-N}^{N}C_i f_i(m,n,l,k,u,v)\varphi_{mn}^{(3)}\right\}+$$
$$3G\left\{d_{mn}(t)+\sum_{l=-M}^{M}\sum_{k=-N}^{N}d_{lk}^{(12)}d_{m-l,n-k}^{(12)}\alpha_{mn}^{(2)}(t)-\sum_{l=-M}^{M}\sum_{k=-N}^{N}d_l^{(1)}d_k^{(2)}\alpha_{mn}^{(2)}(t)\right\}=0; \quad (7)$$

$$\frac{h^3}{6}B_{mn}\left\{G\alpha_{mn}(t)-\breve{\Gamma}_1\alpha_{mn}\right\}-\frac{h^5}{80}\breve{\Gamma}_3\left\{\sum_{i-1}^{5}\sum_{l,u=-M}^{M}\sum_{k,v=-N}^{N}C_i g_i(m,n,l,k,u,v)\alpha_{mn}^{(3)}\right\}-$$
$$-\frac{h}{R}c_m\varphi_{mn}(t)-h\sum_{l=-M}^{M}\sum_{k=-N}^{N}b_i^{(1)}b_k^{(2)}\alpha_{lk}(t)\varphi_{m-l,n-k}(t)+hq_x c_m\alpha_{mn}(t)=0, \quad (8)$$

where $\breve{K}_1,\breve{K}_3,\breve{\Gamma}_1,\breve{\Gamma}_3$ are integral operators with respect to time. The coefficients A, B, $b^{(1)}$, $b^{(2)}$, C, c, d, $d^{(1)}$, $d^{(2)}$, $d^{(12)}$ are formed by differentiation of functions (5) and (6), and trough wave-formation parameters express also the geometrical dimensions of the shell; f_i and g_i are functions of the wave -formation parameters only. The unknowns entering nonlinearity into (7) and (8) are expressed as

$$\alpha_{mn}^{(3)}=\sum_{l,u=-M}^{M}\sum_{k,v=-N}^{N}\alpha_{lk}\alpha_{m-l-u,n-k-v}\alpha_{uv};\ \alpha_{mn}^{(2)}=\sum_{l=-M}^{M}\sum_{k=-N}^{N}\alpha_{lk}\alpha_{m-l,n-k};$$
$$\varphi_{mn}^{(3)}=\sum_{l,u=-M}^{M}\sum_{k,v=-N}^{N}\varphi_{lk}\varphi_{m-l-u,n-k-v}\varphi_{uv}. \quad (9)$$

The solution of the system (7) and (8) can be built up only by approximation. For this purpose we shall restate it as

$$d_m\alpha_{mn}(t_{j+1})-\frac{1}{3G}A_{mn}\varphi_{mn}(t_{j+1})=\frac{1}{3G}A_{mn}\breve{K}_1\varphi_{mn}+\frac{1}{9G}\breve{K}_3\tilde{\varphi}_{mn}^{(3)}+$$
$$+\sum_{l,k}d_{lk}^{(12)}d_{m-l,n-k}^{(12)}\alpha_{mn}^{(2)}(t_j)-\sum_{l,k}d_l^{(1)}d_k^{(2)}\alpha_{mn}^{(2)}(t_j); \quad (10)$$

$$\left(\frac{h^3}{6}GB_{mn}+hq_x c_m\right)\alpha_{mn}(t_{j+1})-\frac{h}{R}c_m\varphi_{mn}(t_{j+1})=\frac{h^3}{6}B_{mn}\breve{\Gamma}_1\alpha_{mn}+$$
$$+\frac{h^5}{80}\breve{\Gamma}_3\tilde{\alpha}_{mn}^{(3)}+h\sum_{l,k}b_l^{(1)}b_k^{(2)}\alpha_{lk}(t_j)\varphi_{m-l,n-k}(t_j). \quad (11)$$

Here, $\tilde{\alpha}_{mn}^{(3)}$ and $\tilde{\varphi}_{mn}^{(3)}$ are non-linear under the integral expression.

The terms in system of Eqs (10) and (11) containing integrals with respect to time take into account the history of deformation (transformation of the form and changes in the stressed state) of the shell, starting from the time t = 0. If the integrals are substituted by numerical quadrature and the deformation process is considered in discrete moments of time, then the values of the integral terms with respect to the instant t_{j+1} are known. Thus, the system (10) – (11) at time t_{j+1} is a system of linear algebraic equations with respect to unknown $\alpha_{mn}(t_{j+1})$ and $\varphi_{mn}(t_{j+1})$. In Fig. 4 theoretical relationships for individual harmonics of Fourier series in the trigonometric form with dimensionless time $\hat{t}$ are shown.

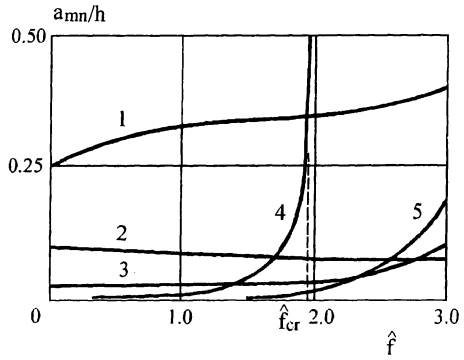

Fig. 4. The change of individual harmonics with dimensionless time: $a_{90}(1)$; $a_{80}(2)$; $a_{10}(3)$; $a_{14}(4)$; $a_{13}(5)$.

3. Deformation of viscoelastic shell in the post-critical stage

In view of the unavoidable initial imperfections, in the elastic stage of loading real shells immediately begin to deform and at a certain value of the load, as a result of snap-trough, go over into a new post-critical equilibrium shape. In the presence of creep the results depend on the nature of the creep. If the creep is not damped, then there is a critical time or deflection accumulation period which ends in snap-through, characterised by a high rate of deflections growth. In most cases the stability of imperfect viscoelastic shells has been investigated by the quasistatic method and the critical time determined; the post-critical behaviour of the shells has received relatively little attention. It is established that beyond the critical time the quasistatic theory ceases to give a solution.

Below it is shown that the quasistatic method can describe the post-critical behaviour of a viscoelastic shell. By taking into account the dynamic terms it is possible to describe the oscillations about the quasistatic solution. With this approach the buckled shapes can also be investigated in the post-critical stage. As our experiments have shown, after snap-through the material of thick composite shells begins to fail.

Cylindrical shell-panel composed of an isotropic material with linear creep and subjected to an axial load were considered. Using the physical relations and taking inertia forces into account in the transverse direction only, for the shell with an initial deflections $w^{\circ}(x, y)$ compressed along the generatrix the equation of motion of the shell was fixed in the following form

$$\frac{D}{h}\left\{\nabla^4 w(t)\int_0^t \Gamma(t-\tau)\nabla^4 w(\tau)d\tau\right\} = L[w(t)+w^0,\Phi(t)]+k_y\Phi(t)_{,xx}-\rho\ddot{w}(t), \qquad (12)$$

where D is cylindrical stiffness of shell.

By substituting the physical relations and the stress function in the middle-surface strain equation , for the case in question we obtain

$$\frac{1}{E}\nabla^4\Phi(t)+\int_0^t K(t-\tau)\nabla^4\Phi(\tau)d\tau = -\frac{1}{2}L[w(t)+2w^0,w(t)]-k_y w(t)_{,xx}. \qquad (13)$$

Here ∇ and L are differential operators; k_y is curvature.

In considering a cylindrical panel, as an approximation for the shell-panel deflection function the following expression were used

$$w(x,y,t) = f(t)\sin\frac{m\pi x}{a}\sin\frac{n\pi y}{b}. \qquad (14)$$

The expression (14) satisfies the boundary conditions corresponding to hinged supports. It is specified that transition from the pre-critical to the post-critical shape involves the formation of a single half-wave along the generatrix and along the arc.

Considering that the static boundary conditions at the edges are integrally equal to the given conditions, after integrating system (12) – (13) in accordance with the Bubnov–Galerkin method a single resolving expression is obtained in the following form

$$A\left[f^3(t)+3f^2(t)f_0+2f(t)f_0^2\right]-B\left[\frac{5}{6}f^2(t)+f(t)f_0\right]+(C+D)f(t)$$

$$-Fq_x\left[f(t)+f_0\right]-A\left[f(t)+f_0\right]\check{K}\left(f^2+2ff_0\right)+\frac{2}{3}B\left[f(t)+f_0\right]\check{K}f+ \qquad (15)$$

$$+\frac{1}{6}B\check{K}\left(f^2+2ff_0\right)-C\check{K}f-D\check{\Gamma}f-G\ddot{f}(t)=0,$$

where A,B, C, D, F and G are coefficients expressed in terms of the physical and geometric parameters of the shell; q_x is the load.

In the numerical solution of non-linear integral equation for the peak value of the deflection f = f(t) the integrals taking into account the history of deformation are evaluated by means of the trapezoidal rule. Thus, equation (15) for the given moment is a non-linear algebraic equation. The real solutions (all real roots) are shown in Fig. 5.

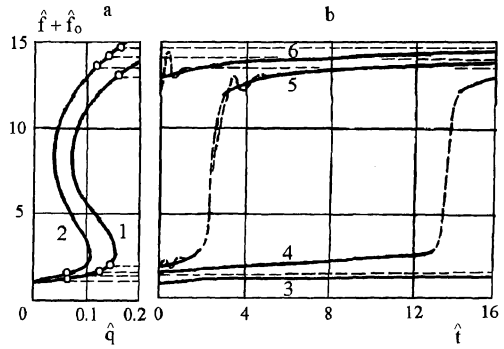

Fig. 5. Deformation of shell-panel in elastic state (a) and viscoelastic state (post-critical stage) (b).

In Fig. 5a the elastic solution is represented: curve 1 – with allowance for the instantaneous, curve 2 – with allowance for the long-time modulus of elasticity. The dimensionless initial peak deflection is $\hat{f}_0 = f_0 / h = 1$ (h is the thickness of the shell). In Fig. 5b three types of shell deformation curves at constant load $\hat{q} = q / q_{cr}$ are plotted. For loading to a load bellow the long-term critical load the deformation is damped (curve 3). If the load level is above the long-term critical load, but bellow the instantaneous critical load, then after a certain time the shell buckles (curves 4 and 5). Taking the inertial terms into account, the method gives a solution with damped oscillations about the static deformation curve. The numerical results were obtained when the second derivative with respect to time of the deflection function being expressed by finite difference.

During experiments on thicker glass reinforced plastic shells obtained by winding which were loaded with external hydrostatic pressure, the transition from the pre-critical to the post critical shape was realised by "snap-trough" (Fig. 6). It should be noted that in the post-critical stage part of the wall has already failed by debonding.

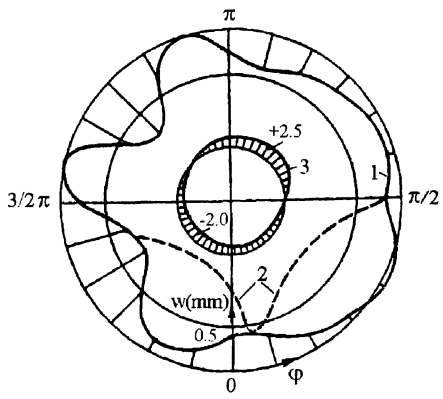

Fig. 6. Pre-critical (1) and post-critical (2) shapes of glass fiber plastic shell; relative variation of shell thickness in percents (3).

Conclusions

1. The analysis of experimental data obtained by testing isotropic and anisotropic shells provides a qualitative characteristic of buckling modes in case of short-term and long-term loading. It has been found that during loading of cylindrical shell, the form of initial deflections is transformed, and the shell buckles in a way different from initial imperfections.
2. Under short-term loading the basic buckling mode of glass-fiber reinforced shell coincides with or is similar to that predicted from the linear theory. In the case of long-term buckling at high load levels it is characteristic that, in addition to the fundamental characteristic, an important part is played by the harmonic n + 1, whose amplitude reaches its greatest value at the critical time.
3. The results of analytical modelling of buckling process qualitatively correspond to the experimental data. By using non-linear equations of thin slope shells and the approach developed, it is possible to describe the time dependent buckling of viscoelastic shells including the post-critical stage.

References

1. B.O. Almroth, A.M. Holmes and D.O. Brush, Exptl. Mech., No. 9 (1964) 69.
2. J.A. Brauns and R.B. Rikards, Polym. Mech., No. 4 (1972) 575.
3. P. Montague, Mech. Eng. Sci., No. 11 (1969) 103.
4. H. Showkati and P. Ansourian, J. Constr. Steel Res., No. 1 (1996) 53.
5. W. Flügge, Stresses in Shells, (1973), Berlin: Springer-Verlag.
6. H. M. Jensen, Collapse of Hydrostatically Loaded Cylindrical Shells, (1986), Lyngby, Technical University of Denmark.
7. B.P. Makarov, Mech. Solids (in Russian), No. 1 (1970) 97.
8. J. A. Brauns, Polym. Mech., No. 1 (1974) 83.
9. J.A. Brauns and G. A.Teters, Polym. Mech., No. 6 (1974) 928.

Generation of large-amplitude internal waves in the ocean

John Grue

Mechanics Division, Department of Mathematics, University of Oslo, Norway

This paper focuses on the generation of internal waves in the ocean. This is a topic that receives current international interest. It is well accepted that tidal flow over topography respresents the dominant source for generation of internal waves in the ocean. Another indirect cause may be wind acting on the ocean surface. Generation of internal waves in the ocean is one of several topics of the Stractegic University Programme 'General Analysis of Realistic Ocean Waves' at the University of Oslo. The investigations on internal waves are motivated by practical needs in the offshore industry, among others. It is of interest to know the currents induced by internal waves and eventual loads which may act on equipment like cables and risers. Further, internal waves may transport water particles, nutrients, small-sized species and pollution. There are also many other areas where understanding of internal waves are important.

We shall consider a simplified two-layer model valid for flows in two-dimensions. The model is capable for simulations of transient, fully nonlinear motion of a thin pycnocline (thermocline) that separates two fluids of slightly different densities (Grue et al. 1997). The lower layer has thickness h_1 and constant density ρ_1, and the upper layer has thickness h_2 and constant density $\rho_2 < \rho_1$ (figure 1). The free surface is modelled by a rigid lid, which is a valid approximation since the accelerations of the waves are small compared to the acceleration of gravity. A coordinate system $O-xy$ is introduced, with the x-axis along the interface at rest and the y-axis pointing upwards. We model the flow in each of the layers by potential theory. A Lagrangian method is adopted, where pseudo Lagrangian particles are introduced on the interface, each with a weighted velocity defined by $\mathbf{v}_\times = (1-\alpha)\mathbf{v}_1 + \alpha\mathbf{v}_2$, where $\mathbf{v}_1$ and $\mathbf{v}_2$ denote the fluid velocities in the respective layers, and $0 \leq \alpha \leq 1$.

The prognostic equations are obtained from the kinematic and dynamic boundary conditions at the interface, i.e.

$$D_\times(x,y)/dt = \mathbf{v}_\times,$$
$$D_\times(\phi_1 - \mu\phi_2)/dt = \mathbf{v}_\times \cdot (\mathbf{v}_1 - \mu\mathbf{v}_2) - (1/2)(\mathbf{v}_1^2 - \mu\mathbf{v}_2^2) - (1-\mu)gy,$$

where $\mu = \rho_2/\rho_1$, $D_\times/dt = \partial/\partial t + \mathbf{v}_\times \cdot \nabla$ and the gravity g acts downwards. The prognostic equations are expanded in Taylor series, keeping several terms, in order to obtain an efficient scheme. Accurate solution of the Laplace equation is crucial to an algoritm for computing interfacial flows, and we here apply complex theory and Cauchy's integral theorem for this purpose.

For interfacial waves with finite amplitude the physical Kelvin-Helmholtz instability is inevitably included in the theoretical model. This represents a difficulty since the space discretization cannot be too fine. Instability is removed by a regridding procedure and smoothing. We are, however, able to document convergence of the method and accuracy in all cases considered.

Tidal generated waves at a fixed bottom topography is simulated by moving the topography with an appropriate speed in fluid which is at rest in the far-field. If the lower layer is thinner than the upper layer, it is obvious that the moving topography will block fluid of the lower layer. A transcritical regime is identified when the speed of the moving geometry (or flow) is comparable to the linear long wave speed of the two-fluid system. In the transcritical regime an undulating bore will propagate upstream, in general. For speed of topography slightly exceeding the linear long wave speed, a train of solitary waves are generated. The amplitude of the waves are always comparable to the thickness of the thinner layer (figure 2, from Grue et al. 1997).

It is of interest to study how solitary waves, or solitary-like waves, are generated by a topography when the lower layer is thicker than the upper layer. The generation mechanism is, perhaps, not so evident as in the case just described.

We simulate tidal flows at a model of a sill in the Sulu Sea where it is observed that large amplitude solitary waves are generated (Apel et al. 1985). The dimensions of the sill and layer thicknesses in the model are the same as those in the ocean. The velocity U of the flow is less than the linear long wave speed, which we denote by c_0. Computations are made for several ratios U/c_0. For U/c_0 slightly less than unity we find rather pronounced interaction bwteen the sill and the tidal flow. For U/c_0 as small as 0.4 we also find som interaction, which, however, is very weak. For U/c_0 much larger than unity the flow is supercritical. In this case no waves are generated by the topography.

Examples of waves propagating along the pycnocline with $U/c_0 = 0.7\sin(\omega t)$ are visualized in figures 3–4. Here $\omega = 2\pi/T$, where T denotes the tidal period. The motion started from rest. In the initial phase of the motion a significant depression is formed at the sill, while a corresponding elevation of the pycnocline propagates upstream. Shorter waves, with group velocity smaller that the velocity of the tidal flow, are formed on the depression (figure 3). When the tidal flow slackens and turn direction the wavy depression moves upstream. The leading part of the depression forms a pulse. The pulse has larger speed than the linear long wave speed and overcomes the upstream elevation, after a while. The wave approaches the form and speed of a perfect solitary wave (figure 4).

Several simulations of interfacial flow over topography are performed. We always find that an elevation of the interface propagates upstream while a depression of the interface is formed above and behind the geometry. This is true when the lower layer is thicker than the upper, and when the geometry is in the thicker layer. In some cases, for very broad topography, the upstream elevation and the downstream depression are separated by some distance. In this case the interface makes a transition between the initial level, which is maintained above the topography, and the upstream elevation. This transition always appears with a wavy form. The waves are, however, far from solitary waves. Our computations on this point fit with several observations of internal wave phenomena observed in the ocean. More results and discussion will be presented at the conference.

The Strategic University Programme is funded by the Research Council of Norway.

References

GRUE, J., FRIIS, H. A., PALM, E. AND RUSÅS, P. O. A method for computing unsteady fully nonlinear interfacial waves. *J. Fluid Mech.*, **351**, 1997.

APEL, J. R., HOLBROOK, J. R., LIU, A. K. & TSAI, J. The Sulu Sea internal soliton experiment. *J. Phys. Oceanography.* **15**, 1985.

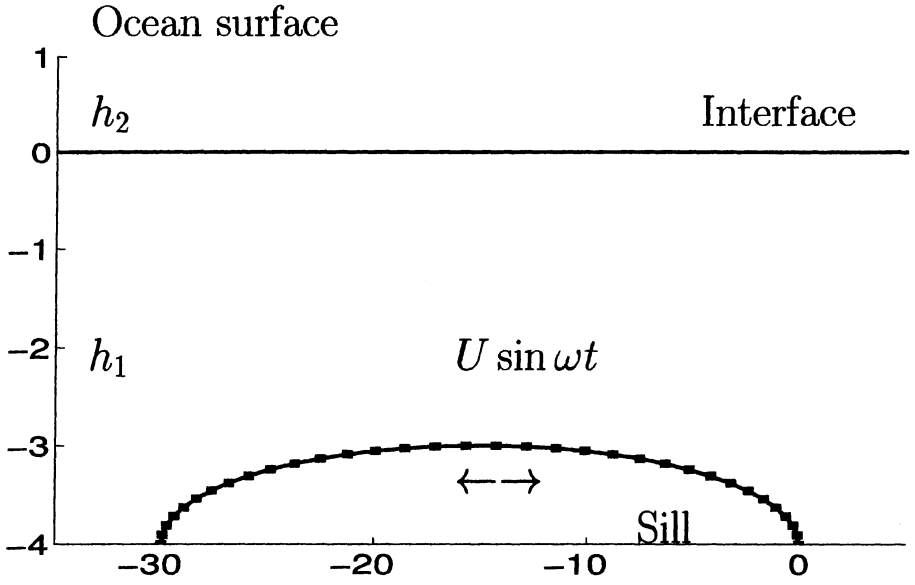

Figure 1: Sketch

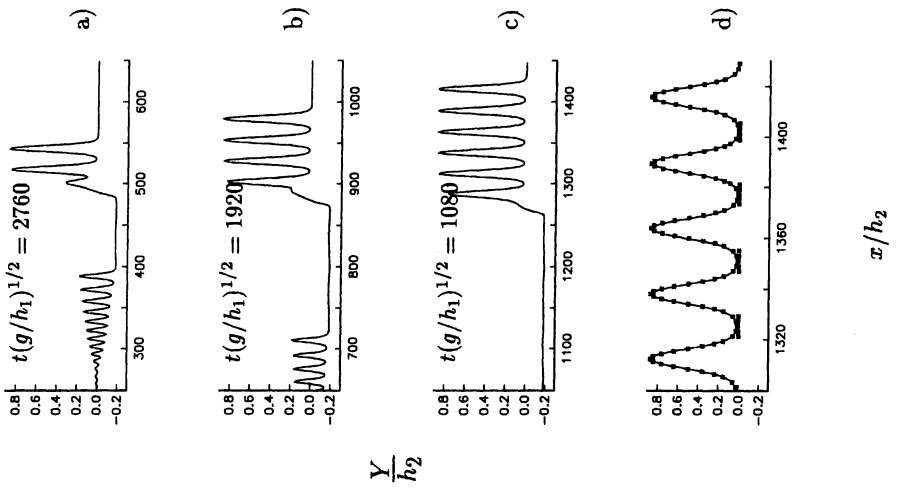

Figure 2: Generation of upstream solitary waves. Moving bottom topography being a half ellipse, horizontal half-axis $10h_1$, vertical half-axis $0.1h_1$. $U/c_0 = 1.1$, $\rho_2/\rho_1 = 0.7873$, $h_2/h_1 = 4$. a) $t(g/h_1)^{1/2} = 1080$. b) $t(g/h_1)^{1/2} = 1920$. c) $t(g/h_1)^{1/2} = 2760$. d) Close up of figure c), black squares mark steady solitary wave solution with $|Y|_{max}/h_1 = 0.869$.

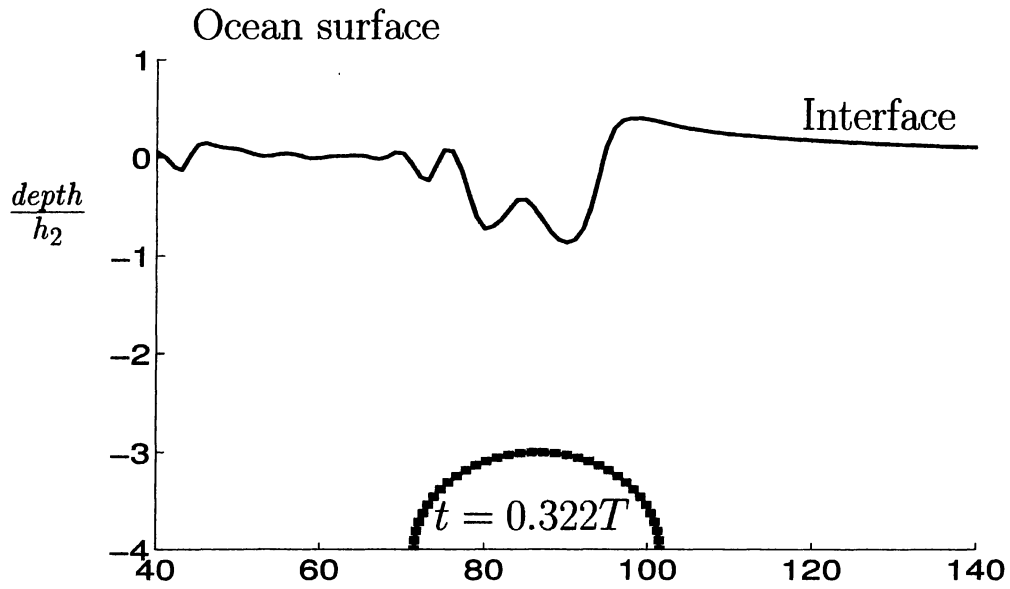

Figure 3: Wavy depression at sill

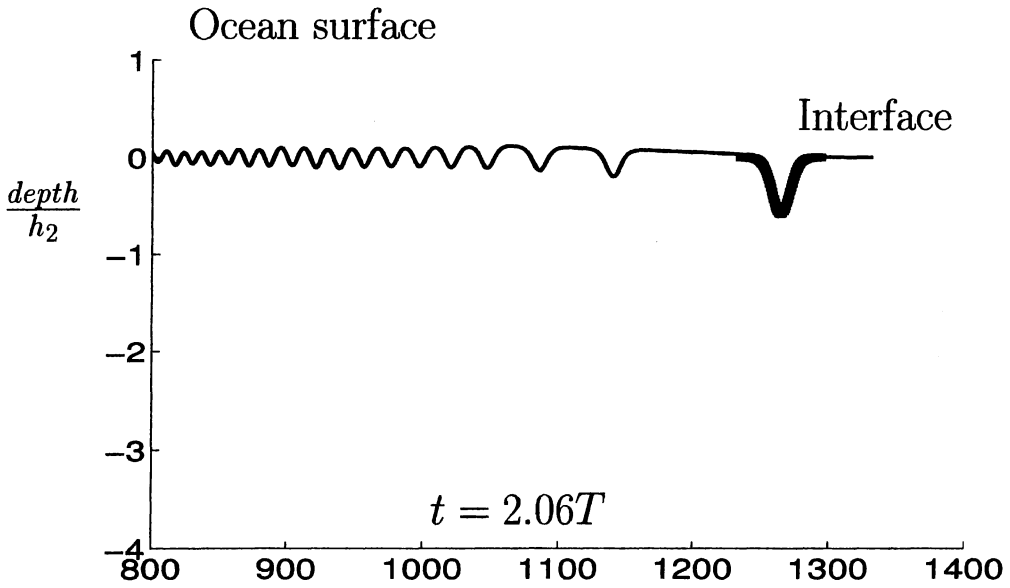

Figure 4: Leading solitary wave

An Agglomerated Multigrid Hybrid Mesh Method for Compressible Flow

K.A. Sørensen*, O. Hassan, K. Morgan and N.P. Weatherill
University of Wales, Swansea

Abstract

A method for solving the compressible Euler and Navier–Stokes equations on unstructured hybrid meshes is described. The solver is accelerated by a FAS multigrid scheme where coarse meshes are created by agglomeration. The method is applicable to a wide variety of problems, as illustrated in a selection of examples.

1 Introduction

The unstructured grid approach is proving to be attractive to engineers who are faced with the requirement of rapidly simulating aerodynamic flows involving complex configurations [1]. Steady inviscid flows about complete aircraft configurations can now be routinely modeled, using fully automatic isotropic tetrahedral mesh generators and explicit time marching schemes with multigrid acceleration [2]. Given this situation, researchers are turning their attention to ways of solving in a routine way more complicated problems involving viscous effects and time dependency. The current approach addresses this problem using an edge–based FV method to discretize the compressible Navier–Stokes equations. For convergence acceleration, the FAS multigrid method is applied with the coarse meshes automatically created by grid agglomeration. A further reduction in the computational expense can often be achieved by employing hybrid meshes and this is exploited in the current work.

2 Numerical Scheme

The unsteady compressible Navier–Stokes equations are discretized using a node–centered, median dual finite volume approach. An edge based representation of the mesh is employed, approximating surface integrals for the

*Sponsored by The Research Council of Norway

control volume associated with node I by

$$\int_{\Gamma_I} \mathbf{f}^j n_j dS \approx \sum_J \frac{1}{2} C_{IJ}^j \left(\mathbf{f}_I^j + \mathbf{f}_J^j \right) + \mathbf{B}_I \tag{1}$$

for a general $\mathbf{f}^j$. Here C_{IJ}^j denotes the coefficients associated with the edge between the node pair I and J. The term $\mathbf{B}_I$ only contributes to nodes I on the boundary of the computational domain. For a simplex triangular/tetrahedral mesh, these procedures produce a discrete equation that is equivalent to a mass–lumped linear finite element Galerkin scheme at interior nodes of the mesh. Stabilisation and discontinuity capturing are achieved by replacing the physical convective flux function over each edge by a consistent numerical flux function of the JST type [2, 3]. For stabilization, the fourth–order diffusion operator is constructed in a form that preserves a linear field [4], while discontinuity capturing is realised by the addition of a pressure–switched second order diffusion. To include turbulence effects, the models of Baldwin and Lomax [5] and Spalart–Allmaras [6] are used. More details of the method can be found in [7].

To reduce the number of edges in the mesh, and thus the computational effort of the solver, unstructured hybrid meshes have been applied for viscous problems. These meshes consist of triangles and quadrilaterals in two dimensions, and tetrahedra, prisms, pyramids and hexahedra in three dimensions. For a two–dimensional mesh, the current approach generates several layers of quadrilaterals around wall boundaries using an advancing layer method and connects this region with a Delaunay generated outer mesh [8], covering the remaining computational domain. A similar approach is used in three dimensions [9].

When time accuracy is required, the time derivative term is discretized using a third order accurate implicit scheme. The resulting equations are then iterated for each physical time step, treating the time derivative term as a source for the steady–state equations. For applications involving moving meshes, the edge coefficients are updated following the approach of [10] to ensure the satisfaction of the geometric conservation law.

To accelerate the convergence of the method, the FAS multigrid scheme of Brandt [11] is applied with local timestepping and explicit 3–stage Runge–Kutta relaxation. The current implementation uses a volume–weighted restriction mapping and injectional prolongation. Coarse mesh generation is automatic and is performed by an agglomeration method [12].

3 Numerical Examples

Results from three test cases are included to demonstrate the current approach. The distribution of the surface pressure coefficient on a symmetric turbulent NACA0012 aerofoil testcase, computed using both hybrid and

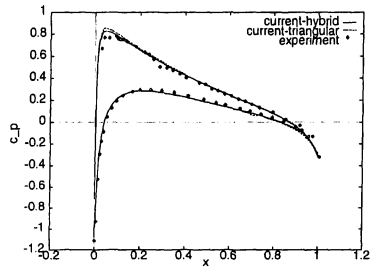

Figure 1: Pressure coefficient comparison between hybrid and triangular meshes with experiment for turbulent aerofoil testcase.

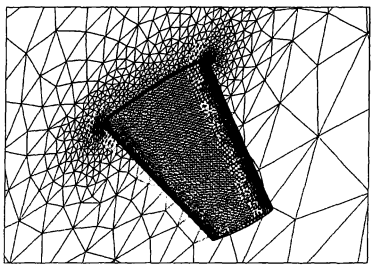

Figure 2: Surface detail of simplex mesh for ONERA M6 testcase. The grid consists of 893007 tetrahedral elements.

simplex meshes, is shown in Figure 1, together with experimental data. The Reynolds number is 2.89×10^6, the Mach number is 0.5 and the angle of attack is $\alpha = 1.77$ degrees. The second test case is laminar flow over an ONERA M6 wing at Reynolds number of one million, Mach number of one–half and $\alpha = 3.0$. Figure 2 shows the surface mesh for the tetrahedral grid. Figure 3 shows the convergence with multigrid acceleration on different hybrid meshes compared with a single grid solver with the same relaxation approach. It can be seen that the hybrid meshes yield a CPU–time reduction of about 70% compared to the convergence on a simplex mesh, and achieve a speedup of about nine compared to the single–grid procedure. Finally, a transient example of inviscid flow around a B60 aircraft configuration, where the wings and engines are oscillating with a prescribed pitch and heave movement, is included. The Mach number is 0.801 and the wings oscillate in a sinusoidal motion with a heave amplitude of 6.5% of the wing semispan and pitch amplitude of five degrees, at the wingtip. A snapshot of the pressure distribution on the surface of the aircraft is shown in Figure 4.

4 Conclusion

A brief outline of an algorithm for the simulation of compressible flows on unstructured hybrid meshes using a multigrid convergence acceleration method has been given. The examples included demonstrate the ability of the method to solve a range of practical aerodynamic flows.

References

[1] D. P. Hills, Numerical Aerodynamics: Past Successes and Future Challenges From an Industrial Point of View, in J. –A. Désidéri et al, editors, *Computational Methods*

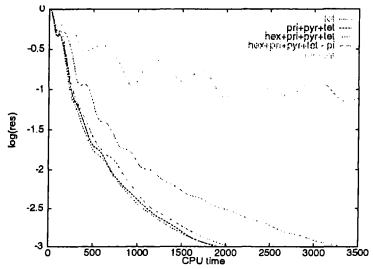

Figure 3: Convergence curves for hybrid meshes of varying complexity, compared with single grid relaxation on the tetrahedral mesh.

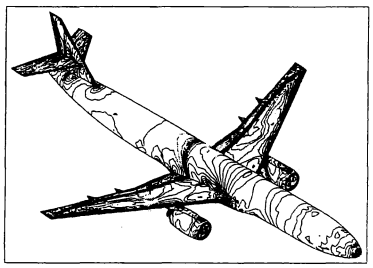

Figure 4: Snapshot of pressure contours on the surface for transient B60 testcase.

in Applied Sciences '96: Invited Lectures and Special Technological Sessions, John Wiley & Son, Chichester, 166–173, 1996.

[2] K. Morgan and J. Peraire, Unstructured Grid Finite Element Methods for Fluid Mechanics, *Reports on Progress in Physics* **61**, 569–638, 1998.

[3] A. Jameson, W. Schmidt and E. Turkel, Numerical Simulation of the Euler Equations by Finite Volume Methods Using Runge–Kutta Time Stepping Schemes, *AIAA Paper 81–1259*, 1981.

[4] P. I. Crumpton, P. Moinier and M. B. Giles, An Unstructured Algorithm for High Reynolds Number Flows on Highly–Stretched Grids, in *Proceedings of the 10th International Conference on Numerical Methods for Laminar and Turbulent Flow*, 1997.

[5] B. S. Baldwin and H. Lomax, Thin Layer Approximation and Algebraic Model for Separated Turbulent Flows, *AIAA Paper 78–257*, 1978.

[6] P. R. Spalart and S. R. Allmaras, A One–Equation Turbulence Model for Aerodynamic Flows, *AIAA Paper 92–0439*, 1992.

[7] K.A. Sørensen, O. Hassan, K. Morgan, N.P. Weatherill, An Agglomerated Unstructured Hybrid Mesh Method for 2D Turbulent Compressible Flows, *ICFD–Journal*, 2001 (in press).

[8] N. P. Weatherill and O. Hassan, Efficient three–dimensional Delaunay Triangulation with Automatic Point Creation and Imposed Boundary Constraints , *International Journal for Numerical Methods in Engineering* **37**, 2005–2039, 1994.

[9] O. Hassan, K.A. Sørensen, K. Morgan and N.P. Weatherill, Unstructured Hybrid Meshes for the Simulation of 3D Viscous Compressible Flow, *Proceedings of the 7th International Conference on Numerical Grid Generation in Computational Fluid Simulations, Whistler, Canada.*

[10] B. Nkonga and H. Guillard, Godunov Type Method on Non–Structured Meshes for Three–Dimensional Moving Boundary Problems, *Comput. Methods Appl. Mech. Engrg.* **113**, 183–204, 1994.

[11] A. Brandt, Multi–level Adaptive Solutions to Boundary Value Problems, *Mathematics of Computation* **21**, 333–390, 1977.

[12] M. H. Lallemand, H. Steve and A. Dervieux, Unstructured Multigridding by Volume Agglomeration: Current Status, *Computers & Fluids* **21**, 397–433, 1992.

Aspects of Algebraic Modelling for Complex Turbulent Flows

B. A. Pettersson Reif
Forsvarets Forskningsinstitutt, N-2027 Kjeller, Norway.

Introduction

Numerical fluid flow predictions have become an integral part of the design cycle in many industries. Single-point closure modelling is the type of models that is used in most applications of computational fluid dynamics (CFD) to engineering flows containing regions of turbulence. It is often remarked that advances in computer speed imply a possibility for more complex Direct Numerical Simulations (DNS) or Large Eddy Simulations (LES) of turbulent fluid flow; the even greater effect on the use of RANS (Reynolds Averaged Navier-Stokes) methods is not so often noted. But it is unquestionably the case that as the use of turbulence models for CFD increases, more sophisticated models will be needed to simulate the range of phenomena that arise.

Full Reynolds stress transport models (RSTMs) represent the most elaborate level of turbulence closures used in practise. This class of closure models exhibits the ability to predict some of the more intricate flow phenomena that arise in engineering flows, most notably some of the effects of imposed body forces associated with e.g. streamline curvature or system rotation. However RSTMs are in general computationally expensive and suffer from numerical stiffness. The result of these practical drawbacks has therefore been that RSTMs only occasionally are used in industrial fluid flow predictions. Standard eddy-viscosity models on the form $\overline{u_i u_j} \propto -\nu_T S_{ij}$ are instead employed and the reason is not so much of a correct physical representation as it is of practical convenience. The turbulent source term in the mean momentum equations can be written as $\partial_j(\nu\partial_j U_i - \overline{u_i u_j}) = \partial_j([\nu + \nu_T]S_{ij})$; this formulation *promotes* numerical stability since the 'turbulent viscosity' $\nu_T \geq 0$.

Recent years, we have seen a resurgence of interest in structural equilibrium analysis of RSTMs (cf. Speziale & Mac Giolla Mhuiris, 1989). As a natural corollary, a revival of explicit algebraic stress constitutive modelling has taken place. The algebraic stress representation circumvents the solution of higly coupled and non-linear partial differential equations contained in full RSTMs; the computational benefit of this approach is immediate. If the RSTM equations are considered to encompass some of the correct physical processes, then a systematic equilibrium approximation to those equations should be imbued with some of those physics. This basic idea is the *physical* motivation behind the systematic approximation of RSTMs that leads to explicit algebraic stress models (EASMs). The *practical* motivation is still the computational benefits of such a formulation. However, there are certain aspects of algebraic stress modelling that are of practical importance and should be elucidated; aspects related precisely to the similarities between physical contents of full RSTMs and EASMs.

The algebraic stress approximation

It is a long standing tradition to calibrate turbulence closure models with data from simple turbulent shear flows, in particular homogeneous shear flows. Homogeneity implies translational invariance of turbulent statistics in space. Structural equilibrium of the Reynolds stress tensor is formally defined by constant values (in time) of the turbulent stress anisotropy tensor $d_t b_{ij} = d_t(\overline{u_i u_j}/k) = 0$ and $d_t(S_{ij}k/\varepsilon) = 0 = d_t(\Omega^A_{ij}k/\varepsilon)$ where $S_{ij} = 1/2(\partial_i U_j + \partial_j U_i)$ and $\Omega^A_{ij} = 1/2(\partial_i U_j - \partial_j U_i) + \epsilon_{ijk}\Omega^F_k$. $\mathbf{S}$ and $\Omega^{\mathbf{A}}$ are the mean rate of strain and absolute mean vorticity tensors, respectively. Ω^F_k denotes the angular velocity of the reference frame about the x_k axis.

Imposing these conditions on the RSTM equations in a *a priori* selected frame of reference results in a set of implicit algebraic relations;

$$\mathbf{b} = \mathcal{F}(\mathbf{b}, \mathbf{S}, \Omega^{\mathbf{A}}, \Omega^{\mathbf{F}}, k, \varepsilon). \tag{1}$$

The set of equations is closed in practise by solving model equations for the turbulent kinetic energy k and its rate of viscous dissipation ε (e.g. standard $k-\varepsilon$). However the numerical solution of these algebraic relations is not necessarily straightforward; the coupling between different components of $\mathbf{b}$ may have an adverse effect on the numerical stability. From a computational point of view, it would certainly be an advantage if an explicit and non-coupled solution for $\mathbf{b}$ could be found. This is in fact possible. The matrix equation (1) can be solved either by Integrity Bases (Pope, 1975) or by Direct Product (Shabany & Durbin, 1998) methods. The result for a 2-D mean flow can syjmbolaiccaly be written as

$$b_{ij} = \frac{k}{\varepsilon}\left(C^*_\mu S_{ij} + \alpha_2\frac{k}{\varepsilon}[S_{ik}\Omega^A_{kj} + S_{jk}\Omega^A_{ki}] - \alpha_3\frac{k}{\varepsilon}[S_{ik}S_{kj} - \frac{1}{3}S_{kl}S_{lk}\delta_{ij}]\right) \tag{2}$$

where $C^*_\mu = \mathcal{F}(\eta_1, \eta_2)$. The linear eddy-viscosity coefficient C^*_μ is expressed in terms of invariants $\eta_1 = S^*_{ij}S^*_{ji}$ and $\eta_2 = \Omega^A_{ij}\Omega^A_{ji}$ of the *normalized* tensors:

$$S^*_{ij} \propto \frac{k}{\varepsilon}S_{ij}, \quad \Omega^{A*}_{ij} \propto \frac{k}{\varepsilon}\left(\Omega^A_{ij} + C_\omega\epsilon_{ijk}\Omega^F_k\right). \tag{3}$$

The solution (2) might, at a first glance, seem of limited value since it corresponds to a 2-D mean flow. However, this *is* in fact the most general equilibrium solution. It was shown by Durbin & Pettersson Reif (1999) that the solution based on the 3-D integrity bases (e.g. Gatski & Speziale, 1993) is not true equilibria. The 3-D solutions do not generally correspond to permissible steady mean flows; they are therefore not structural equilibrium solutions. The practical consequences of this is discussed below.

Bifurcation of structural equilibria

As already alluded to, it is expected that some of the physical processes encompassed by RSTMs are retained in the algebraic representation (2). The

systematic approximation leading to (2) has also introduced the concept of non-linear eddy-viscosity models; the terminology alludes to tensoral non-linearity, i.e. terms like S_{ij}^2. What can now be expected of this constitutive relation in terms of representing 'real' physical processes? The response to an imposed body force, e.g. the Coriolis force associated with an imposed system rotation $\Omega^{\mathbf{F}}$, is a prototype example. But to elucidate this ability we first need to introduce the concept of bifurcation of equilibria.

The origin of the bifurcation of equilibria can be understood by attributing it to an external stabilizing force (e.g. an imposed rotation). If the stabilizing force is weak, then the equilibrium state is fully turbulent – turbulent kinetic energy k grows exponentially in time. This is a state of 'healthy' turbulence. If the stabilizing force becomes stronger a structural equilibrium still exists but k only grows algebraically in time. This is a state of 'sick' turbulence. If the stabilizing force gets even stronger the equilibrium state is 'dying' turbulence – k exhibits an algebraic decay in time. The ability to predict this rotational stabilization of turbulent flows constitutes a major improvment as compared to the original formulation. This phenomenon exerts profound effects on the flow field in many flows of engineering and geophysical relevance.

Durbin & Pettersson Reif (1999) introduced the so-called 'bifurcation criterion' which can be used to assess the response of an algebraic stress model to imposed rotation:

$$lim_{|S^*|\to\infty} b_{ij}S_{ij} = \mathcal{O}(1). \tag{4}$$

This criterion is a simple and powerful guidance to closure model formulations. Models that do not meet this criterion is precluded the ability to predict rotational stabilization. The limit $|S^*| \to \infty$ physically implies a clear-cut separation between the turbulent and mean flow time scales.

Concluding Remarks

As the industrial use of CFD increases more complex flow configurations are considered and analyzed. From a practical point of view there will always be a compromize between computational cost and a physically sound representation of the turbulence. It is unfortunately the case that advanced closure models that encompass some of the intricate flow physics are computationally very demanding and therefore rarely employed.

The systematic approximation of these closures that lead to explicit algebraic stress models constitute a viable compromize between computational cost and an accurate representation of turbulence at an engineering level. It is primarily the ability to predict body force effects that has motivated improved eddy-viscosity formulations. But the value of this exercise goes beyond a new model formulation; it provides insight of the effects of imposed body forces. This can be put to good use in analyzing existing eddy-viscosity type models as well as providing a powerful guidence to new closure model formulations.

The objective of this paper is to summarize some important theoretical observations of models intended for complex turbulent flow computations, i.e algebraic stress models. These observations might be valuable not only for those

formulating closure models, but also for those using CFD as a predictive tool.

• The systematic approximation of RSTMs takes place in *a priori* selected frame of reference (inertial or noninertial). The models are therefore *coordinate dependent* and should be used with caution, cf. (3).

• A non-linear stress-strain relationship *is not* needed to predict rotational stabilization of turbulent flows, this can be easily verified by using (4). It therefore suffice to retain a variable coefficient, linear eddy-viscosity model (cf. Pettersson Reif *et al.*, 1999).

• It can readily be shown (Durbin & Pettersson Reif, 1999) that 3-D EASMs do not meet the criterion (4) and they are therefore precluded the ability to predict rotational stabilization.

• By using (4) it can be demonstrated that virtually *all* existing non-linear eddy-viscosity models[1] lack the ability to predict rotational stabilization (e.g. the models by Shih *et al.* 1995 and Lien & Leschziner 1996).

• It is still not clear whether a non-linear stress-strain relationship improves the predictions of complex flows as compared to the computationally simpler linear eddy-viscosity formulations. The improvments when using (2) apparently is due to the *variable* linear coefficient C_μ^*. If this is the case, it serves as good news for CFD code developers.

References

Durbin, P. A. & Pettersson Reif, B. A. 1999. On algebraic second-moment models, *Flow, Turbulence and Combustion*, **63**, 23 – 37.

Gatski, T. B. & Speziale, C. G. 1993. On axplicit algebraic stress models for complex turbulent flows, *J. Fluid Mech.*, **254**, 59 – 78.

Lien, F. S. & Leschziner, M. A. 1996. Low-Reynolds-number eddy-viscosity modelling based on non-linear stress-strain/vorticity relations, *Engng Turbulence Modelling and Expts.*, **3**, 91 – 101.

Pettersson Reif, B. A., Durbin, P. A. & Ooi, A. 1999. Modeling rotational effects in eddy-viscosity closures, *Int. J. Heat and Fluid Flow*, **20.**, 563 – 573.

Pope, S. B. 1975. A more general effective-viscosity hypothesis, *J. Fluid Mech.*, **72**, 331 – 340.

Shabany, Y. & Durbin, P. A. 1997. Explicit algebraic scalar flux approximation, *AIAA*, **35**, 985 – 989.

Shih, T. S., Zhu & Lumley, J.L. 1995. A new Reynolds stress algebraic equation model, *Comput. Methods Appl. Mech. Engng*, **125**, 287 – 302.

Speziale, C. G. & Mac Giolla Mhuiris, N. 1989. On the prediction of equilibrium states in homogeneous turbulence, *J. Fluid Mech.*, **209**, 591 – 615.

[1] except the exact 2-D solution (2).

Waves around moving bodies — Project "UNDA"

KARSTEN TRULSEN* & BJØRN SPJELKAVIK

SINTEF Applied Mathematics, P.O.Box 124 Blindern, N–0314 Oslo, Norway

*Corresponding and presenting author. E-mail: karsten.trulsen@math.sintef.no.

Within the potential theory for inviscid and irrotational ocean waves, it is necessary to perform fully nonlinear simulations of waves around marine structures in the time domain. In the UNDA project we employ spline-based quasi-spectral expansions in terms of stationary basis potentials $\phi_m(\boldsymbol{x})$, where $\boldsymbol{x} = (x, y, z)$ is the spatial coordinate vector. See [1, 2]. These basis potentials have been constructed to be continuous throughout the fluid and the bodies, satisfying the Laplace equation in water, $\nabla^2\phi_m(\boldsymbol{x}) = 0$, and a higher order tri-harmonic equation inside the bodies, $\nabla^6\phi_m(\boldsymbol{x}) = 0$. This provides sufficient freedom to satisfy appropriate continuity and no-flux boundary conditions at the wet surfaces of the fixed bodies, as well as appropriate boundary conditions at the walls of the channel or at open sides of the computational domain.

Recently, we have generalized this approach to also describe waves around moving marine structures. To this end, special basis potentials, $\phi_j^D(\boldsymbol{x})$, are constructed to account for body movement along the desired degrees of freedom $j = 1, 2, \ldots, 6$. The basis potentials for moving bodies typically describe motion with unit velocity along the appropriate degree of freedom.

All the basis potentials are independent of time. Time dependence is introduced through time coefficients to be multiplied with the basis potentials. Hence the total potential is written as

$$\phi(\boldsymbol{x}, t) = \sum_m c_m(t)\phi_m(\boldsymbol{x}) + \sum_j v_j(t)\phi_j^D(\boldsymbol{x}),$$

where $c_m(t)$ are unknown time coefficients, and $v_j(t)$ are either unknown or prescribed. Time dependence is governed by the free-surface boundary conditions, as well as the specification of incoming waves, and now also by prescribed movement of bodies.

The following example is for a vertical cylinder with prescribed sway motion in a narrow channel. The channel has length 4.3 m, width 0.54 m and depth 0.42 m. The body is a bottom-standing and surface-piercing vertical cylinder with radius 0.12 m located on the centerline of the channel at a distance 1.45 m from the left end of the channel. The cylinder has a prescribed velocity

$$v(t) = a \sin\left(\frac{2\pi t}{T}\right)$$

with amplitude $a = 0.01$ m and period $T = 1$ s, starting from rest at $t = 0$ with a smooth ramp function of length 1 s.

The basis potential for sway motion, $\phi_2^D(\boldsymbol{x})$, is shown in figure 1. The potential is seen from above at the equilibrium water surface, with the implied velocity field indicated with arrows.

A typical surface displacement, here taken at time $t = 3$ s is shown in figure 2 for the left end of the tank.

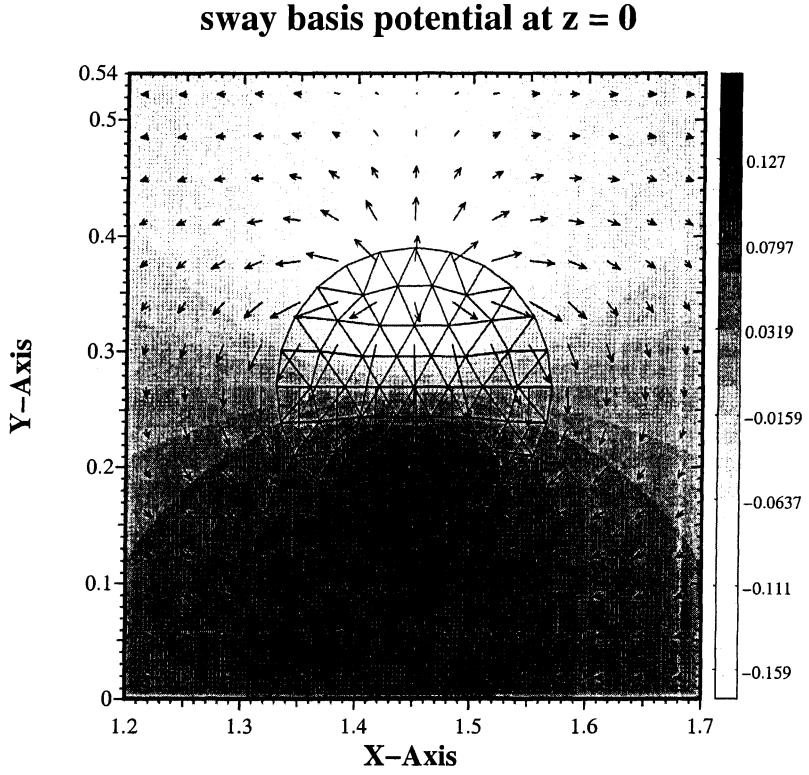

Figure 1: Sway basis potential computed by UNDA for moving vertical cylinder. The finite element grid for the cylinder is superposed.

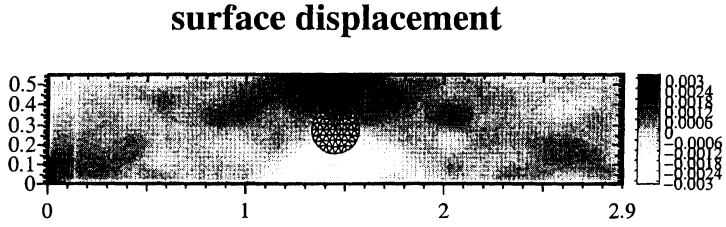

Figure 2: Typical surface displacement around cylinder with prescribed sway motion in a narrow tank.

References

[1] Cai, X. & Mehlum, E. (1996). Two fragments of a method for fully nonlinear simulations of water waves. In B. Gjevik, J. Grue, & J. E. Weber (Eds.), *Waves and Nonlinear Processes in Hydrodynamics* (pp. 37–50): Kluwer.

[2] Mehlum, E. (1998). Fully nonlinear simulation of ocean waves in interaction with offshore structures — project "UNDA". In J. Zhang (Ed.), *Ocean Wave Kinematics, Dynamics and Loads on Structures* (pp. 96–99): ASCE.

Adaptive solid modeling using our program FEM90

Per Kettil, Torbjörn Ekevid and Nils–Erik Wiberg
Department of Structural Mechanics, Chalmers University of Technology
S–41296 Göteborg, Sweden

1.Computational structural design

This paper presents some details of our current work in the field of computational structural design Per Kettil and Nils–Erik Wiberg: Adaptive design and analysis of structures – an integration of tools, Design Optimization, 1, 440–464, (November 1999).. The aim is to rationalize the design of structures by integrated use of computational techniques, e.g. CAD, FEA, optimization and visualization. In this paper we present some details of our finite element program FEM90. We then show an example of adaptive solid modeling and simulation of a major bridge structure.

2.The structure of our finite element program FEM90

We started the development of the program in November 1999. The program already contains many advanced features such as several solution algorithms for static, dynamic and eigenvalue problems, constraint equations and many types of elements. The program is mainly written in Fortran90 but also contains some C–routines. The rapid development is much due to the complex data–types and module facilities of Fortran90 that allow for an object–oriented programming approach that make the program more easy to extend. Since it might be of interest to other program developers, we give a brief presentation of the data–types and functions of the most important modules of FEM90. Figure 1 shows an overview of the FEM90 modules ("classes").

FEM90 is a pure FE–solver. It does not contain any graphics for pre– and post–processing. FEM90 reads data from an input file and generates output files with results. Currently FEM90 supports ABAQUS ABAQUS, Hibbitt, Karlsson & Sorensen, Inc. format for the input file and AVS AVS/Express, Advanced Visual Systems, Inc. or ANSYS ANSYS, SAS IP, Inc. format for the output files. In the examples in this paper we have used IDEAS IDEAS, Structural Dynamics Research Corporation, SDRC for pre–processing (IDEAS supports ABAQUS format) and ANSYS for post–processing.

The top level of FEM90 consists of the PROBLEM and ASSEMBLY modules. The PROBLEM module carries the problem definition (grid, elements, materials etc.) and solution fields (displacement, stress etc.) and performs time stepping and iteration loops. The ASSEMBLY module manages assembly and solution of system of linear equations. We currently plan to make parallel implementations of both multi–frontal equation solving and of the explicit dynamics procedure Torbjörn Ekevid and Nils–Erik Wiberg: Parallel computing of wave problems, Nordic Seminar on Computational Mechanics, NSCM13, Oslo, Norway, 2000..

The GRAPH module assists with setting up graphs to obtain efficient numberings of the variables. The MATRIX module stores and operates with sparse matrixes and the SP_VEC module deals with sparse vectors. The SUPERELEMENT module stores the

super–elements that arise in a multi–frontal solution of equations. The HARWELL module encapsulates the HSL Harwell Subroutine Library (HSL), (release 12), AEA Technology, Harwell Laboratory, Oxfordshire, England, 1995. subroutine package mainly used for solution of systems of equations. SUPERLU is a C–library that contains the SuperLU SuperLU (version 2.0), Univ. of California Berkeley, Xerox Palo Alto Research Center and Lawrence Berkeley National Lab, November 15, 1997 systems of equations solver. The MATHS module contains a few basic mathematics subroutines for sorting etc. Otherwise built in Fortran functions and the BLAS and LAPACK libraries are mainly used for lower–level mathematical operations.

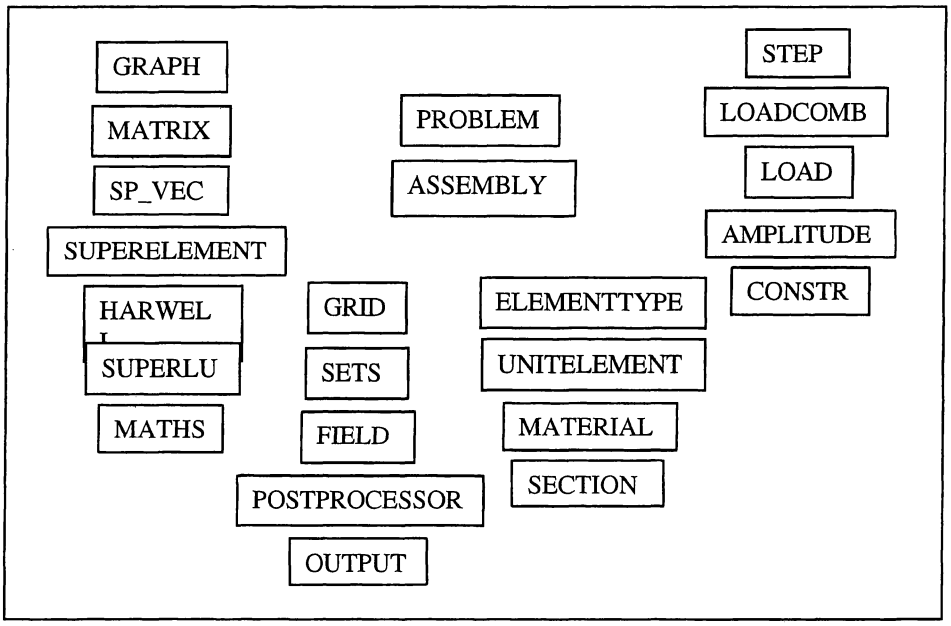

Figure 1. Modules ("classes") contained in our program FEM90.

The GRID module stores and operates on the grid (mesh) definition (node coordinates, element connectivity, element, material and section types, equation numbers, normals, orientations etc.). The SETS module manages sets of element or node numbers. FIELD stores and operates with solution fields, either as "point fields" (e.g. displacements at nodes) or "element fields" (e.g. stress in element integration points). The POSTPROCESSOR projects, extrapolates and interpolates values between element integration points and element nodes. This is useful prior to output for visualization and accuracy assessment. The OUTPUT module stores when and what results should be printed to file, and manage the required post–processing and print operations.

ELEMENTTYPE is a large module. It carries the definition of different element types (e.g. type, number of nodes, number of stress, active degrees of freedom etc.). It also contains routines for calculation of integrals over elements (e.g. element stiffness and mass matrixes, internal and external load vectors, scalar products etc.),

derivatives (strains), interpolation etc. The element library is based on linear, quadratic and qubic isoparametric elements for 1, 2 and 3D solid, shell, beam, membrane and truss, for small or large displacement analysis. The UNITELEMENT module keeps definition of "unit–elements" containing basis functions and integration weights. MATERIAL stores material data and computes stress according to strain increments. The material library currently consists of linear elastic and non–linear elasto–plastic materials and a concrete material model. SECTION keeps the definition of the element cross–section. A 1D or 2D mesh defines the section. The nodes are quadrature points. The user can directly input a section mesh, or the program can automatically generate the mesh from input of key dimensions for standard sections. Sections may be constant or vary along the element and may be defined for sets of elements or nodes.

The STEP module carries data that varies from a time step to another (c.f. the definition of a step in ABAQUS ABAQUS, Hibbitt, Karlsson & Sorensen, Inc.), e.g. the solution type, loads, boundary conditions, constraint equations etc. LOAD stores load and boundary condition data and manages computation of load vectors. Loads that are not dependent on displacements is computed once and stored as sparse vectors. At assembly the current time amplitude scales these loads and then other displacement dependent loads are computed and added. AMPLITUDE compute time–dependent load amplitude factors. The LOADCOMB module performs load combination to find extreme values of results. CONSTR stores, generates and operates with linear and non–linear constraint equations useful for instance for connecting meshes of different type.

3.Adaptive solid modeling and analysis of a major bridge

We show adaptive solid modeling and simulation of a major bridge example using our program FEM90, see Figures 2–5.

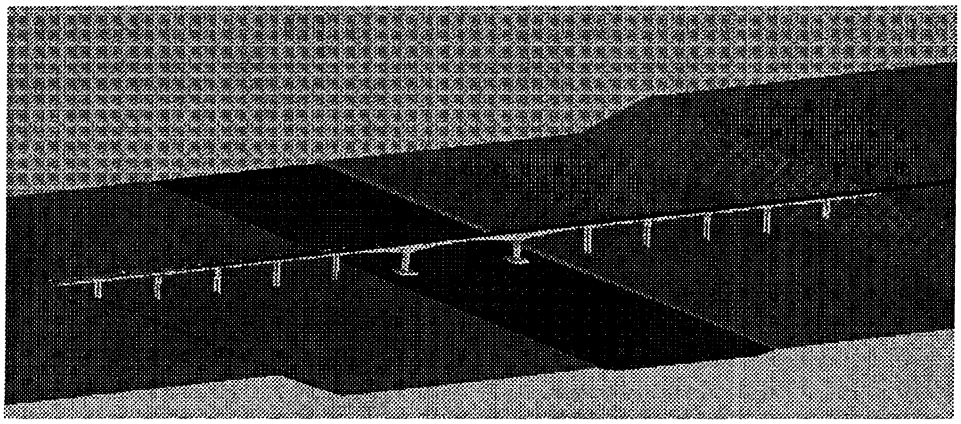

Figure 2. Box bridge geometry model placed in the environment

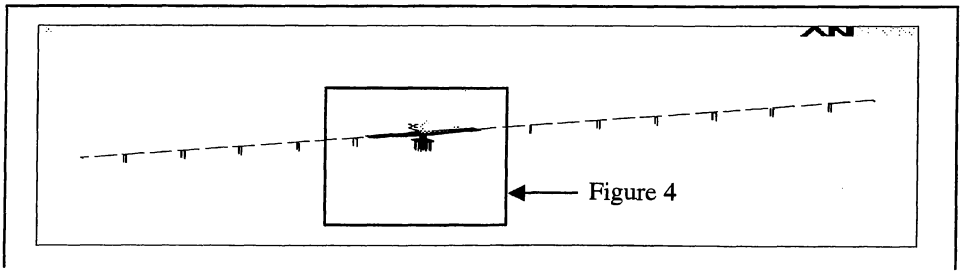

Figure 3. Model adaptation: A solid model of the main bridge T (see also Figure 4) locally refines the global frame model.

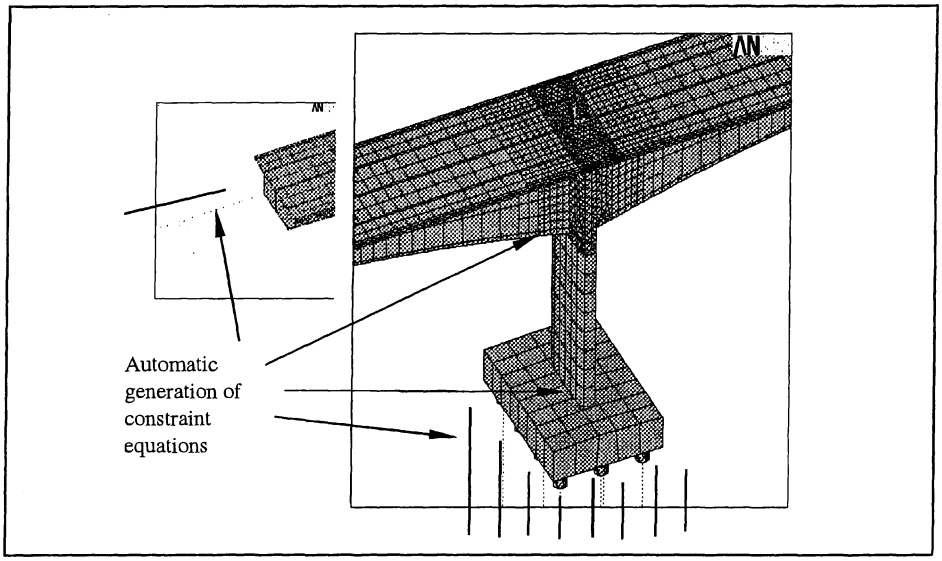

Figure 4. The FEM90 "glue–algorithm" for automatic generation of constraint equations simplifies efficient local model– and mesh adaptation. The technique is useful wherever parts with different element types and element size join up.

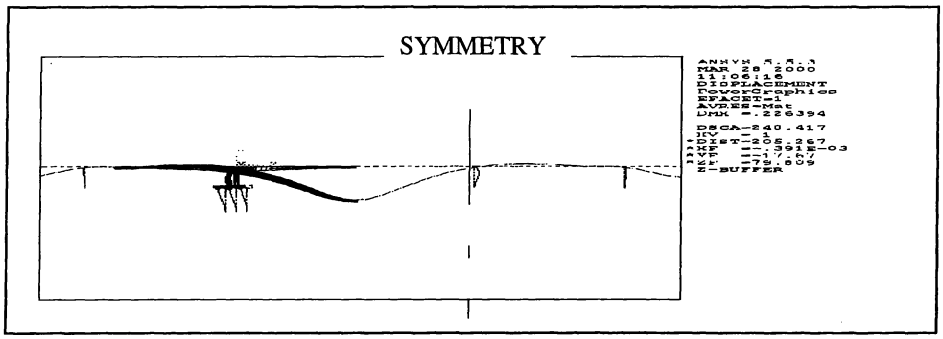

Figure 5. The entire bridge loaded by dead load, exaggerated deformations. The symmetry of the deformed shape indicates both that the beam model captures the global response accurately and that the constraints work as intended.

4.References

[1] Per Kettil and Nils–Erik Wiberg: Adaptive design and analysis of structures – an integration of tools, *Design Optimization, 1, 440–464,* (November 1999).
[2] IDEAS, Structural Dynamics Research Corporation, SDRC
[3] ABAQUS, Hibbitt, Karlsson & Sorensen, Inc.
[4] AVS/Express, Advanced Visual Systems, Inc.
[5] ANSYS, SAS IP, Inc.

[6] Harwell Subroutine Library (HSL), (release 12), AEA Technology, Harwell Laboratory, Oxfordshire, England, 1995.

[7] SuperLU (version 2.0), Univ. of California Berkeley, Xerox Palo Alto Research Center and Lawrence Berkeley National Lab, November 15, 1997

[8] Torbjörn Ekevid and Nils–Erik Wiberg: *Parallel computing of wave problems*, Nordic Seminar on Computational Mechanics, NSCM13, Oslo, Norway, 2000.

Adaptive Methods for Shell Problems with Geometric and Material Nonlinearities

Ivar Tiller* **and Kjell Magne Mathisen**
Department of Structural Engineering
Norwegian University of Science and Technology, Trondheim, Norway
e-mail: ivar.tiller@bygg.ntnu.no

Knut Morten Okstad
Fedem Technology, Trondheim, Norway

ABSTRACT

This paper presents an investigation of automatic adaptive numerical solutions to geometrically non-linear shell–type problems involving history-dependent materials. The paper briefly reviews an adaptive non-linear solution procedure, error estimators for history-dependent materials, an h-adaptive mesh refinement strategy and aspects of the solution transfer between the successive refined meshes. A numerical example are presented to illustrate some practical features of the adaptive solution procedure and the efficiency of the error estimator adopted herein.

1. INTRODUCTION

During the last two decades much research has been devoted to development of error estimators and adaptive finite element (FE) strategies for solving linear problems in structural mechanics. In particular, the development of automatic adaptive FE programs has received much attention as such programs allows the user to obtain solutions to linear problems within some prescribed accuracy, with minimum computational efforts and without user intervention.

When considering non-linear problems, adaptive FE solution strategies become even more appealing, particularly for problems where the optimal mesh changes continuously throughout the analysis since the CPU time consumption when solving for such problems may become prohibitive large. In general, the performance of a non-linear FE solution procedure can be scrutinized from three different perspectives; (1) computational efficiency, (2) solution accuracy, and (3) effectiveness. It turns out that all of these attributes may be improved by moving towards an adaptive environment.

In prior studies, an overview of key aspects which have to be considered in an adaptive non-linear solution procedure has been presented along with the implementation of an h-adaptive mesh refinement technique into a general purpose non-linear FE program for solving geometrically non-linear shell-type problems involving linear elastic materials [1, 2].

2. FORMULATION OF THE ELASTOPLASTIC SHELL PROBLEM

A major problem in the non-linear analysis of shell structures is to find sufficiently reliable and accurate shell elements that are insensitive to both in-plane and out-of-plane mesh distortion. It appears that most of the recent research on shell elements is concentrated around four-noded quadrilaterals based on the Mindlin/Reissner theory which naturally incorporates transverse shear, since these elements appear to be more accurate and more robust compared to their three-noded counterparts. However, for thin shells Mindlin/Reissner elements tend to exhibit severe stiffening, known as locking. It is well known that locking can be avoided with hybrid–mixed formulations in which additional assumptions for strains or stresses are made.

Throughout this work, the stress resultant based geometrically exact shell (GES) model due to Simo et. al. [3, 4, 5] is considered. We have implemented a version of the four-noded bi-linear quadrilateral shell element proposed by Simo et. al. [4, 5], in which the membrane and bending fields are based on a displacement formulation with strains referred to local cartesian co-ordinates. The *assumed natural coordinate strain* concept is adopted for the transverse shear strain part, in order to avoid *shear locking*.

The material formulation adopted in this work is the elastoplastic shell model developed by Simo and Kennedy [6]. Our implementation follows this work exactly apart from one point. In our work we have regarded the transverse shear part to be purely elastic. As a consequence only the membrane and bending parts are included in the yield criterion. As a consequence only the membrane and bending parts are included in the yield criterion.

2.1. *Error estimation and mesh adaption*

In the displacement formulated FE method, the displacements are the primary variables while the stresses and strains are obtained from the displacements through differentiation. This causes the stresses and strains to be discontinuous across the element boundaries. A better approximation of these quantities could be obtained by smoothing of the FE quantities. The SPR-method by Zienkiewicz and Zhu [7] has become the most popular method for such smoothing and is also adopted herein. This method exploits the fact that the derived quantities are of better quality at certain points within each element, the so-called superconvergent points. An even better approximation may be obtained by including boundary conditions and interior equilibrium as constraints on the recovery process. In the current work, however, only the plain SPR-method is used.

The error is approximated by the difference between the quantities obtained by the FE solution and the corresponding recovered quantities. For the stresses this reads

$$e^* = \boldsymbol{\sigma}^* - \boldsymbol{\sigma}^h \tag{1}$$

where $\boldsymbol{\sigma}^h$ denotes the stresses obtained directly from the FE solution and $\boldsymbol{\sigma}^*$ represents the corresponding stresses recovered by means of SPR. Based on (1), several error estimates have been proposed by different authors, see, e.g., Perić e. al. [8]. Herein, we use the following error estimate which also apply to elastic-plastic analyzes:

$$\|e^*\|_{\mathrm{E}}^2 := \int_{\Omega} \left(\boldsymbol{\sigma}^* - \boldsymbol{\sigma}^h\right)^{\mathrm{T}} \left(\dot{\boldsymbol{\epsilon}}^* - \dot{\boldsymbol{\epsilon}}^h\right) \mathrm{d}V \tag{2}$$

Here, $\dot{\boldsymbol{\epsilon}}$ denote the incremental total strains. Based on some mesh optimality criterion, the estimated relative errors η_e are transformed into a set of mesh refinement indicators [9, 10] which are input to the mesh generator actually carrying out the mesh adaption. The unstructured finite octree mesh generator by Shephard and Georges [11] is herein used for mesh generation and adaption. This mesh generator creates first a triangularization of the shell surface. The triangular mesh is then converted into a quadrilateral mesh by joining two and two triangles in a sequence determined by the shape of the resulting quadrilaterals. Mesh refinements (and possibly de-refinements in some areas) are carried out by a complete regeneration of the whole mesh guided by the computed refinement indicators when the estimated relative global error, η, is larger than a prescribed tolerance.

2.2. *Solution transfer between finite element meshes*

An important but crucial step of an adaptive non-linear solution process is the transfer of solution variables (i.e., the state variables and the history-dependent variables) from the old mesh to the new mesh after a mesh refinement. The state variables consists of the nodal displacements whereas the history-dependent variables that need to be transferred are the stresses, $\boldsymbol{\sigma}$, the plastic strains, $\boldsymbol{\epsilon}_{\mathrm{p}}$, and the vector of internal variables (e.g., the hardening parameters), $\boldsymbol{\kappa}$. The variables associated with the history of the material also need to be mapped. These variables are plastic strains which are permanent and accumulative through the analysis and hardening variables if present. These variables are part of the initial condition in the material routine. The plastic strains are vectors and mapped in the same manner as the total stress resultants, while the hardening variables are scalars and may thus be mapped without any transfere between co-ordinate systems.
After the mapping between the old and new finite element models has been carried out the restart with the new finite element model is performed.
The first step after the rezoning should be performed with the mapped plastic strains from the

current increment instead of the plastic strains from the previous increment which are the normal procedure when calculating a new increment. This lead to a near elastic step and the trial stresses are evaluated through the equation

$$\boldsymbol{\sigma}_{n+1}^{trial} = \boldsymbol{C}\left(\boldsymbol{\varepsilon}_{n+1} - \boldsymbol{\varepsilon}_{n+1}^{p}\right) \tag{3}$$

where $\boldsymbol{\varepsilon}_{n+1} = \nabla \mathbf{u}_{n+1}$ are the total strains from the current increment and $\boldsymbol{\varepsilon}_{n+1}^{p}$ are the plastic strains from the same increment. The restart should though be done with care since the incoming variables may not be consistent. Therefore in the first iteration of the first increment after the rezoning a pre-entrance in to the material-routine is performed in order to ensure that the variables entering the material-routine to calculate the new plastic strains, hardening parameter and the consistent material matrix are consistent. In the subsequent iterations the material-routine are entered only once. In addition the plastic strains are set equal to zero if the hardening variable is less or equal to zero from the mapping procedure.

3. NUMERICAL EXAMPLE

The proposed adaptive regime for non-linear geometric as well as non-linear material problems is demonstrated on a highly non-linear problem below. The pinched closed cylinder problem has also been analysed by Simo and Kennedy [6], which is used as reference herein. The results from adaptive analyses using 10% as global error limit and 7% and 8% as local error bounds in the remeshing procedure give results that are in good agreement with the reference solution. Also note the substantial lower computational cost in the adaptive analyses compared to a single mesh analysis using a finite element model consisting 2185 nodes with an error bound equal to 10%. The left hand side in Figure 1 the force-displacement diagram and on right the accumulated CPU-time for the adaptive analyses and the single mesh analysis are shown for the current adaptive analyses. Finally, the adaptive mesh-sequence for the analysis using 10% and 7% as global and local error bound respectively are shown in Figure 2. More results will be presented at the seminar.

4. CONCLUSION

An adaptive regime for analysis of geometric as well as material non-linear shell problems are developed. Herein the regime's ability to analyse a highly non-linear geometric and material shell-type problem is presented. The results obtained does agree with the reference solution and the CPU-time spent on the adaptive analysis is compared to a single-mesh analysis with the same demand of accuracy in the error norm chosen. The CPU-time spent in the adaptive analysis is considerably lower than in the single-mesh analysis.

5. REFERENCES

[1] K. M. Okstad and K. M. Mathisen. Towards automatic adaptive geometrically nonlinear shell analysis. Part I: Implementation of an h–adaptive mesh refinement procedure. *International Journal for Numerical Methods*

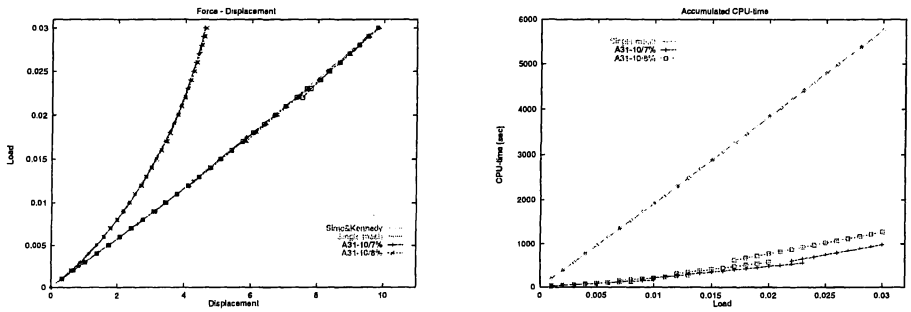

Figure 1: Load-Displacement and Accumulated CPU-time

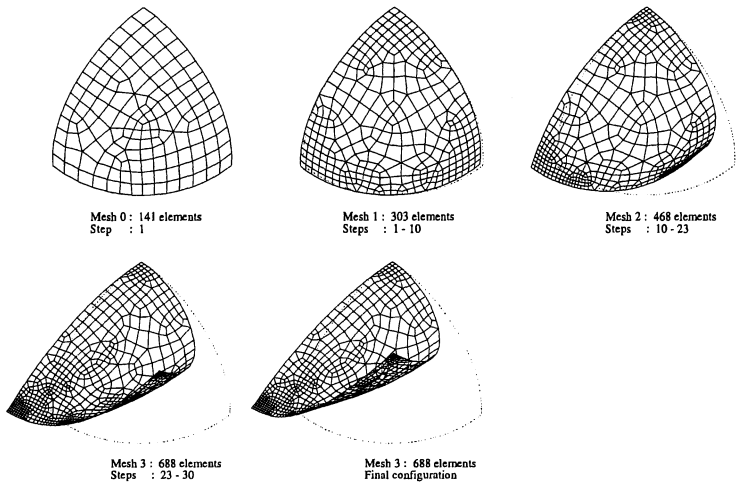

Figure 2: Adaptive Mesh Sequence

in Engineering, 37:2657–2678, 1994.

[2] K. M. Okstad. *Adaptive Methods for Nonlinear Finite Element Analysis of Shell Structures.* Dr. Ing. dissertation, Department of Structural Engineering, The Norwegian Institute of Technology, Trondheim, Norway, 1994.

[3] J. C. Simo and D. D. Fox. On a stress resultant geometrically exact shell model. Part I: Formulation and optimal parametrization. *Computer Methods in Applied Mechanics and Engineering*, 72:267–304, 1989.

[4] J. C. Simo, D. D. Fox, and M. S. Rifai. On a stress resultant geometrically exact shell model. Part II: The linear theory: Computational aspects. *Computer Methods in Applied Mechanics and Engineering*, 73:53–92, 1989.

[5] J. C. Simo, D. D. Fox, and M. S. Rifai. On a stress resultant geometrically exact shell model. Part III: Computational aspects of the nonlinear theory. *Computer Methods in Applied Mechanics and Engineering*, 79:21–70, 1990.

[6] J. C. Simo and J. G. Kennedy. On a stress resultant geometrically exact shell model. Part V. Nonlinear plasticity: formulation and integration algorithms. *Computer Methods in Applied Mechanics and Engineering*, 96:133–171, 1992.

[7] O. C. Zienkiewicz and J. Z. Zhu. The superconvergent patch recovery and *a posteriori* error estimates. Part 1: The recovery technique. *International Journal for Numerical Methods in Engineering*, 33:1331–1364, 1992.

[8] D. Perić, J. Yu, and D. R. J. Owen. On error estimates and adaptivity in elastoplastic solids: Applications to the numerical simulation of strain localization in classical and Cosserat continua. *International Journal for Numerical Methods in Engineering*, 37:1351–1379, 1994.

[9] O. C. Zienkiewicz and J. Z. Zhu. A simple error estimator and adaptive procedures for practical engineering analysis. *International Journal for Numerical Methods in Engineering*, 24:337–357, 1987.

[10] J. Z. Zhu and O. C. Zienkiewicz. Adaptive techniques in the finite element method. *Communications in Applied Numerical Methods*, 4:197–204, 1988.

[11] M. S. Shephard and M. K. Georges. Automatic three–dimensional mesh generation by the finite octree technique. *International Journal for Numerical Methods in Engineering*, 32:709–749, 1991.

A PATCH RECOVERY METHOD IN CONNECTION WITH EQUAL ORDER FEM FOR 2D STOKES FLOW

Martti Perälä*

Laboratory of Structural Mechanics
Helsinki University of Technology, P.O. Box 2100, 02015 HUT, FINLAND

1. Introduction

A patch recovery method in connection with the equal order *uvp*-finite element formulation for a steady, incompressible 2D Stokes flow is introduced. The method uses local polynomial representations containing information from the field equations. The field equations of the 2D Stokes flow are written in such a way that a separate patch recovery methods for the pressure and velocity components can be formed. The method has been implemented to a finite element code, which uses linear and bilinear C^0-continuous interpolations for the velocities and pressure [1]. Numerical comparison of the present, the method of Ref. [2] and the SPR method [3], is finally given.

2. Patch recovery procedure

We express field equations of steady, incompressible 2D Stokes flow as

$$R_p(p) \equiv \nabla^2 p - \rho\left(\frac{\partial b_x}{\partial x} + \frac{\partial b_y}{\partial y}\right) = 0, \tag{1}$$

$$R_u(u) \equiv \eta\nabla^2 u - \frac{\partial \overline{p}}{\partial x} + \rho b_x = 0, \tag{2}$$

$$R_v(v) \equiv \eta\nabla^2 v - \frac{\partial \overline{p}}{\partial y} + \rho b_y = 0, \tag{3}$$

where $p(x,y)$ is pressure, $u(x,y)$ and $v(x,y)$ are velocities, η is viscosity, ρ is density and $b_x(x,y)$ and $b_y(x,y)$ are known volume forces. Equations (2) and (3) are the equations of motion and equation (1) has been obtained by differentiating equations (2) and (3) with respect to x and y, respectively, summing and taking into account the continuity equation

$$\frac{\partial u}{\partial x} + \frac{\partial v}{\partial y} = 0. \tag{4}$$

Equation (1) is separate equation of the Poisson type, which can first be solved for p. If $\overline{p}$ in equations (2) and (3) is the corresponding solution, these equations can also be regarded as two separate equations of the Poisson type for u and v, respectively.

Based on equations (1) - (3) separate patch recovery methods for the pressure p and the velocity components u and v can be established. In the following R_k, $k = p,u,v$ are used to

* Address: Pinkelikatu 6 B 36, 90520 OULU, FINLAND

denote the residuals of the corresponding field equations. We express the pressure $p(x,y)$ locally using a complete polynomial of degree q as

$$\tilde{p}(\lambda,\mu)=\sum_{i=0}^{q}\sum_{j=0}^{i}\lambda^{i-j}\mu^{j}p_{ij}, \tag{5}$$

where p_{ij} are unknown parameters, $\lambda=(x-x_0)/h$, $\mu=(y-y_0)/h$ are dimensionless coordinates, x_0 and y_0 are coordinates of the patch assembly node and h is characteristic length of the patch. We further express the velocities $u(x,y)$ and $v(x,y)$ using similar polynomials of degree q with unknown parameters u_{ij} and v_{ij}. Known volume forces $b_x(x,y)$ and $b_y(x,y)$ are expressed using similar polynomials of degree q-1 with corresponding known coefficients b_{xij} and b_{yij}, respectively.

Substituting polynomial representations of the pressure, velocities and volume forces into the residuals of the field equations (1) - (3) results to

$$\tilde{R}_k(\lambda,\mu)=\sum_{i=0}^{q-2}\sum_{j=0}^{i}\lambda^{i-j}\mu^{j}R_{kij}, \quad k=p,u,v. \tag{6}$$

By demanding that polynomial representations (6) of the residuals of the field equations (1) - (3) should vanish with all values of λ and μ results to three separate set of equations: $R_{pij}=0$, $R_{uij}=0$ and $R_{vij}=0$, $i=0,\cdots,q-2$; $j=0,\cdots,i$. They are three set of the $(q-1)q/2$ linear constraint equations between the $(q+1)(q+2)/2$ unknown parameters p_{ij}, u_{ij} and v_{ij} and exists if $q\geq 2$. With the help of the constraint equations $R_{pij}=0$, the unknown parameters p_{ij} can be expressed in terms of the $2q+1$ remaining ones, which can be considered as independent parameters a_{ip}, $i=1,\cdots,2q+1$. Using now the local polynomial representation (5), the pressure can be written in terms of the independent parameters a_{ip} as

$$\tilde{p}(\lambda,\mu)=\sum_{i=1}^{2q+1}N_i(\lambda,\mu)a_{ip}+p_0(\lambda,\mu). \tag{7}$$

With the help of constrait equations $R_{uij}=0$ and $R_{vij}=0$, a similar local polynomial representations for the velocities in terms of the independent parameters a_{iu}, $i=1,\cdots,2q+1$ and a_{iv}, $i=1,\cdots,2q+1$ can be written as

$$\tilde{u}(\lambda,\mu)=\sum_{i=1}^{2q+1}N_i(\lambda,\mu)a_{iu}+u_0(\lambda,\mu) \tag{8}$$

and

$$\tilde{v}(\lambda,\mu)=\sum_{i=1}^{2q+1}N_i(\lambda,\mu)a_{iv}+v_0(\lambda,\mu). \tag{9}$$

Equations (7) - (9) are the local polynomial representations for the pressure and velocities, which contain "built-in" information from the field equations. The polynomial degrees of

these representations are q. Correspondingly, we get local polynomial representations of order q-1 for the strain rates $d_x \equiv \partial u / \partial x$, $d_y \equiv \partial v / \partial y$ and $d_{xy} \equiv \partial u / \partial y + \partial v / \partial x$ by simply differentiating representations (8) and (9).

The unknown parameters a_{ip}, a_{iu} and a_{iv} are obtained by least squares fitting of the polynomial representations $\tilde{p}(\lambda,\mu)$, $\tilde{u}(\lambda,\mu)$ and $\tilde{v}(\lambda,\mu)$ to the corresponding nodal values $\hat{p}_i$, $\hat{u}_i$ and $\hat{v}_i$ of the original finite element solution at the nodes of the patch. Each least squares fitting procedure is made separately. Note that the least squares pressure fitting must be done at first. After that, the pressure parameters a_{ip} are known and the (known) terms $\partial \bar{p} / \partial x$ and $\partial \bar{p} / \partial y$ in the field equations (2) and (3) can be calculated. The final, C^0-continuous field for the strain rates are calculated using the patchwise representations for them and averaging at the system nodes.

3. Numerical example

Based on the well known analogy between incompressible plane elasticity and Stokes flow, infinite plate with a circular hole under unidirectional tension (Fig. 1) was considered as a test problem with known analytical solution.

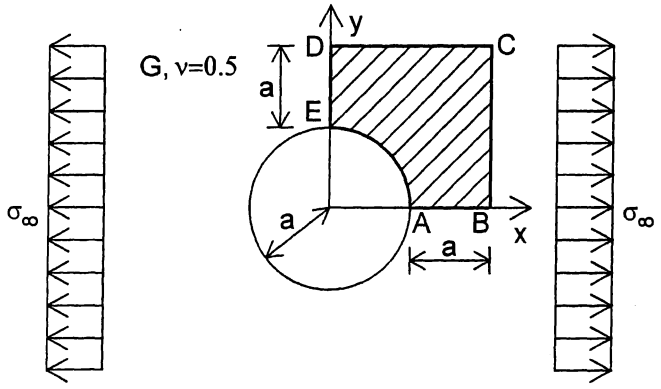

Fig. 1: Infinite plate with circular hole

In connection with the present method (BUI) polynomial degrees $q = 2$ and $q = 3$ were used in connection with linear triangles and bilinear quadrilaterals. In addition to the present patch recovery method the method of Ref. [2] (called here BUIS method, which is based on a stream function formulation of the field equations) and the so called SPR method of Ref. [3] for obtaining smoothed strain rates was also implemented and used. Results of the BUIS method were calculated using polynomial degree $q = 3$ for the stream function. Figs. 2a and 2b show experimental convergence studies of the error in energy (η_E) obtained with linear triangles and bilinear quadrilaterals. Table 1 shows effectivity indices (θ) of the error estimates obtained with the different patch recovery methods in case of the bilinear quadrilaterals.

4. Conclusions

A simple and fast patch recovery method for 2D Stokes flow has been presented. The method

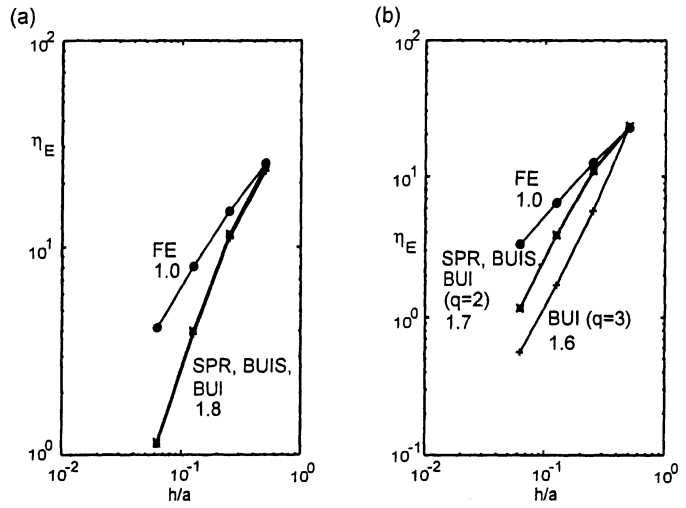

Fig 2: Experimental convergence study of the error in energy (η_E): (a) linear triangles (b) bilinear quadrilaterals

Table 1: Effectivity indices (θ) of the bilinear quadrilaterals

h/a	SPR	BUIS	BUI (2)	BUI (3)
0.5	0.830	0.917	0.874	1.053
0.25	0.894	0.925	0.915	0.861
0.125	0.929	0.935	0.934	0.971
0.0625	0.970	0.969	0.971	1.009

uses local polynomial representations containing information from the field equations for the pressure and velocities. Numerical results obtained show, that the method works well and seems to give results, which are comparable to those of the methods of Refs. [2,3] and in case of the bilinear quadrilaterals with degree $q = 3$ even better. The presented method can be generalized to 3D and to steady, incompressible Navier-Stokes flow.

References

[1] T.J.R. Hughes, L.P. Franca and M. Balestra: '*A new finite element formulation for computational fluid dynamics: V. Circumventing the Babuska-Brezzi condition: A stable Petrov-Galerkin formulation of the Stokes problem accommodating equal-order interpolations*', Comput. Methods Appl. Mech. Engrg. 59 (1986) 85-99.

[2] J. Aalto and R. Hannila: *A patch recovery method for 2D Stokes flow*, Proceedings of the Eleventh Nordic Seminar on Computational Mechanics (NSCM XI), Stockholm, (1998).

[3] O.C. Zienkiewich and J.Z. Zhu: *The superconvergent patch recovery and a posteriori error estimates. Part 1: The recovery technique*, Int. J. Numer. Meth. Engng. 33 (1992), 1331- 1364.

Strategies for goal-oriented a posteriori error measures in nonlinear elasticity

Marcus Rüter[1], Fredrik Larsson[2], Peter Hansbo[2] and Kenneth Runesson[2]

[1]Institute for Structural and Computational Mechanics (IBNM), Universität Hannover, Appelstrasse 9A, D-30167 Hannover, Germany

[2]Department of Solid Mechanics, Chalmers University of Technology, S-41296 Göteborg, Sweden, email keru@solid.chalmers.se

Abstract

In this contribution we consider hyperelasticity as the important representative of a class of nonlinear elliptic problems, and we investigate the characteristics and the performance of a few strategies to compute goal-oriented error measures. The chosen error measure is used as a part of the associated adaptive mesh-refinement procedure in order to meet a predefined stopping criterion (tolerance) in the usual fashion. It is emphasized that the chosen error measure can be, in principle, any given (linear or nonlinear) functional $E(\boldsymbol{u}, \boldsymbol{u}_h)$ of the exact displacement field $\boldsymbol{u}(\boldsymbol{x})$ and its approximate FE-solution $\boldsymbol{u}_h(\boldsymbol{x})$ on a given mesh. Typically we use expressions of the form $E(\boldsymbol{u}, \boldsymbol{u}_h) = Q(\boldsymbol{u}) - Q(\boldsymbol{u}_h)$ or $E(\boldsymbol{u}, \boldsymbol{u}_h) = Q(\boldsymbol{u} - \boldsymbol{u}_h)$ where Q is some (generally non-linear) functional. Hence, $E(\boldsymbol{u}, \boldsymbol{u}_h)$ may be a global or local (i.e. defined in a spatial point) measure. An example of $Q(\boldsymbol{u})$ representing a global measure is the L_2 norm $||\boldsymbol{u}||_{L_2}$, whereas an example of a local measure is the equivalent stress $\sigma_e(\boldsymbol{\epsilon}(\boldsymbol{u}(\boldsymbol{x})))$, where $\boldsymbol{\epsilon}(\boldsymbol{u})$ is the strain operator and $\sigma_e = \sqrt{3/2}|\boldsymbol{\sigma}_{dev}|$.

The basic idea is to use the now well-known and widely used strategy of solving a dual problem that represents the linearized elasticity problem at the point of interest along the solution path in the load-displacement space. Thereby, the pertinent energy metric is defined by the tangent stiffness tensor of the stress-strain relation, and the load is chosen in such a fashion that an exact error representation of $E(\boldsymbol{u}, \boldsymbol{u}_h)$ is obtained (at least formally). The dual solution (or influence function) $\boldsymbol{\varphi}$ is, typically, computed on the same mesh as the "direct" problem in $\boldsymbol{u}_h$, which gives the FE-solution $\boldsymbol{\varphi}_h$. However, as it turns out, by using the Galerkin-orthogonality it is possible to conclude that it is the difference $\boldsymbol{\varphi} - \boldsymbol{\varphi}_h$ that occurs in the error representation formula and must, therefore, be computed in a sufficiently accurate (yet inexpensive) fashion. To this end (at least) two principally different strategies for the further error analysis can be envisioned:

The first strategy is to use the Cauchy-Schwarz inequality on the exact error representation to obtain a guaranteed upper bound in terms of the energy norm of $\boldsymbol{u} - \boldsymbol{u}_h$ times the energy norm of $\boldsymbol{\varphi} - \boldsymbol{\varphi}_h$. Now, it is possible to estimate these norms by solving, in turn, two associated "local Neumann problems" corresponding to solutions in "broken spaces".

These problems are established on each individual element subjected to self-equilibrating loads. In this fashion a "strict" upper bound (which may not be very sharp) of the error can be obtained.

The second strategy aims at computing a good approximation of φ by solving a "local Dirichlet-problem" on each element, whereby a higher polynomial approximation is introduced on the particular element under consideration. The approximate dual solution $\tilde{\varphi}$ thus computed infers that an approximate error representation is obtained. Although a good estimate can be expected no guaranteed lower or upper bound can be obtained.

The two procedures are compared numerically in this presentation for a simple model problem, and their possible merits in terms of accuracy, ease of implementation and reliability are discussed.

Simulation of nonlinear wave interaction for elastic material properties evaluation

Andres Braunbrück and Arvi Ravasoo

Institute of Cybernetics at Tallinn Technical University,
Akadeemia tee 21, 12618 Tallinn, Estonia
E-mail: andres@egoist.ioc.ee

Abstract. Simultaneous propagation, reflection and interaction of two longitudinal sine waves in nonlinear elastic material is considered. Making use of the symbolic software the analytical solution that describes the wave motion is analyzed. The material properties evaluation problem is posed. It clears up that a convenient choice of sine wave frequency enables to characterize the material properties on the basis of wave harmonics amplitude and phase shift measurement data. The algorithm for material properties evaluation is proposed.

Keywords: nonlinearity, wave interaction, material properties characterization

1 Introduction

The topic of this paper may be regarded as a development of the ideas presented in [1]. The simultaneous propagation of longitudinal sine waves in nonlinear homogeneous elastic material described by the five constant nonlinear theory of elasticity [2] is studied in more detail. The nonlinear wave interaction peculiarities in the material are clarified on the basis of the analytical solution. Material characterization problem is posed as follows. Wave process in the specimen is excited in terms of particle velocity and it is recorded in terms of wave induced stress. The plots stress components (harmonics amplitudes and phase shifts) versus material parameters are computed. Analyses of plots enables to propose a method to evaluate linear and nonlinear material parameters.

2 Problem formulation

We consider a specimen (structural element) with two parallel traction free surfaces. Material of the specimen is isotropic and homogeneous and it is described by the five constant nonlinear theory of elasticity [2]. The longitudinal wave process is exited simultaneously on two traction free surfaces. Wave propagation is governed by the equation of motion

$$[1 + k_1 U_{,X}]\, U_{,XX} = c^{-2} U_{,tt}\,, \tag{1}$$

where X denotes Lagrangian coordinate, U the displacement and t the time. Commas in the indices represent partial derivation.

The equation of motion (1) includes two constants: the wave velocity c and the dimensionless parameter k_1. They originate from the five constant nonlinear theory of elasticity:

$$k_1 = 3\left[1 + 2\frac{\nu_1 + \nu_2 + \nu_3}{\lambda + 2\mu}\right], \quad c^2 = \frac{\lambda + 2\mu}{\rho}, \tag{2}$$

where ρ denotes the material density, λ and μ are Lamé constants and ν_1, ν_2 and ν_3 are the third order constants of elasticity.

With the aim to excite simultaneously two sine waves in the specimen Eq. (1) is solved under the following initial and boundary conditions:

$$\begin{aligned} &U(X,0) = U_{,t}(X,0) = 0 \\ &U_{,t}(0,t) = \varepsilon\, a_0 \sin\omega t, \quad U_{,t}(L,t) = \varepsilon\, a_L \sin\omega t\,. \end{aligned} \tag{3}$$

Here a_0 and a_L are constants and ε may be regarded as a small parameter ($\varepsilon \ll 1$).

3 Wave interaction

Analytical solutions to Eq. (1) has been found in [1] making use of the perturbation procedure. The solution has the form of power series with a positive small parameter ε:

$$U(X,t) = \sum_{n=1}^{\infty} \varepsilon^n\, U^{(n)}(X,t), \quad \varepsilon \ll 1. \tag{4}$$

We consider the first three terms of this series. The first term in solution satisfies the boundary conditions (3) whereas the higher order terms are derived under the boundary conditions equal to zero.

The analytical expressions for functions $U^{(i)}(X,t)$ $(i = 1,2,3)$ are too cumbersome to be represented here; they describe longitudinal wave propagation, interaction and reflection in homogeneous nonlinear elastic material (Fig. 1). The obtained solution is valid in the space region $0 \le X \le L$ and in the time interval $0 \le t < 2L/c$. The first term in solution (4) describes linear propagation, interaction and reflection of the wave's first harmonic in the physically linear elastic material. The subsequent terms take the nonlinearity of the problem into account. The second term determines the propagation, interaction and reflection of the second harmonic. The third term determines evolution of the third harmonic and in addition it corrects the first harmonic for nonlinear effects.

The general nonlinear wave interaction pattern is drawn on Fig. 1. The bold line $A\,B\,C$

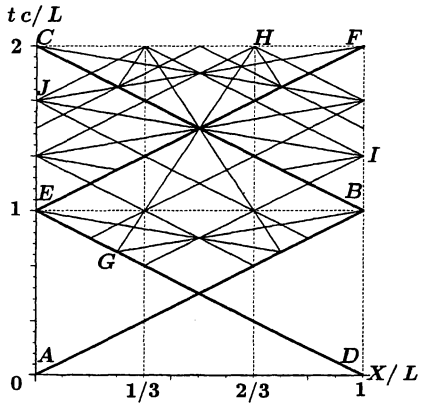

Fig.1. Nonlinear interaction of longitudinal waves.

marks a front of the linear wave generated at the boundary $X = 0$ and the bold line $D\,E\,F$ marks the front of the wave generated at the boundary $X = L$. The other lines on Fig. 1 correspond to the wave fronts that emerge, when considering nonlinear wave interaction. It is interesting to notice that some nonlinear interaction components travel three times slower (line $G\,H$) and some travel three times faster (line $I\,J$) compared with the wave velocity c.

4 Elastic material characterization

The homogeneous nonlinear elastic material is characterized by the density ρ and five elastic constants λ, μ, ν_1, ν_2 and ν_3 (see Eq. (2)). All these parameters can not be determined on the basis of one-dimensional longitudinal wave propagation data. The reason is that in the equation of motion (1) the elastic parameters are grouped as follows:

$$\alpha = \lambda + 2\mu\,, \quad \beta = 2\,[\nu_1 + \nu_2 + \nu_3]\,. \tag{5}$$

The homogeneous elastic material characterization problem consists in the evaluation of three quantities: material density ρ, linear elasticity constant α and nonlinear elasticity constant β.

We propose the following scheme of nondestructive testing (NDT). Wave process in the material is excited in terms of particle velocity and it is recorded in terms of stress. The stress is a function of $U_{,X}(X,t)$ determined from the solution (4).

With a proper choice of radial frequency

$$\omega = \frac{2\,\pi\,c\,n}{L}, \tag{6}$$

where n is an integer, it is possible to analyze the solution $U_{,X}(X,t)$ on the boundaries $X = 0$ and $X = L$ in a form of harmonics:

$$U_{,X}(X,t) = A_0 + A_1\,sin(\omega\tau + \phi_1) + A_2\,sin(2\omega\tau + \phi_2) + A_3\,sin(3\omega\tau + \phi_3)\,. \tag{7}$$

Here A_0 is a nonperiodical term, A_i and ϕ_i $(i = 1, 2, 3)$ are the amplitudes and phase shifts of harmonics and $\tau = L/c$. To utilize Eq. (6) it is necessary to determine the wave velocity c beforehand.

The nonlinear elastic material characterization problem is illustrated by the numerical experiment. Let us assume that we have the preliminary information about the rough values of the material properties ($\rho = 8000\,kg/m^3$, $\alpha = 300\,GPa$ and $\beta = -1500\,GPa$), which we call the basic material properties. These values correspond to the steel CT3 [4]. Initial wave amplitude is characterized by the constants $\varepsilon = 10^{-4}$, $a_0 = -a_L = -c$. We plot the curves wave characteristics versus material properties α and β (Figs. 2 and 3). The amplitudes A_{10} and A_{20} in these figures are computed for the basic material.

Fig. 2 illustrates the sensitivity of the first harmonic relative amplitude to the variation of material properties α and β and Fig. 3 the same phenomenon for the second harmonic amplitude. The real values of constants α and β for the specimen under consideration may be evaluated if the curves in Figs. 2 and 3 are approximated by the second order equations.

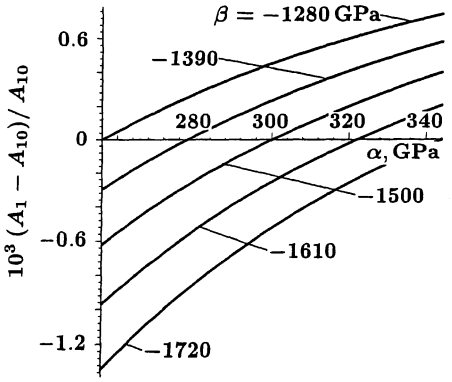

Fig.2. First harmonic relative amplitude versus the elastic properties of material.

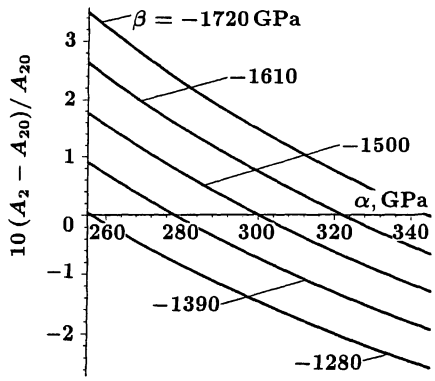

Fig.3. The second harmonic amplitude variation in nonlinear elastic material.

When the recorded amplitude values are known the solution to the set of two second order equations determines the values of α and β. Material density ρ may be evaluated whether by the non-acoustical method or it may be determined from Eqs. (2) and (5) taking the wave velocity c as known.

5 Conclusions

Physically nonlinear homogeneous elastic material characterization on the basis of two nonlinear one-dimensional longitudinal sine wave simultaneous propagation, reflection and interaction data has been studied. A relatively simple method to evaluate the material physical properties has been proposed. The wave characteristics versus the properties of material plots have been computed. The analyses of these plots leads to the conclusion that information extraction from the wave interaction data enables to enhance the efficiency of nondestructive material properties evaluation.

References

1. Braunbrück A. and Ravasoo A. (1999) Symbolic software application for modelling of wave interaction process. In R. Kouhia and M. Mikkola (eds.), Proc. of the Twelfth Nordic Seminar on Computational Mechanics (NSCM-12). Helsinki, HUT, 89-92.

2. Bland D. R. (1969) *Nonlinear Dynamic Elasticity.* Blaisdell Publishing Co, London.

3. Ravasoo A. and Braunbrück A. (1999) Nonlinear interaction of longitudinal waves in elastic material. Proc. Estonian Acad. Sci. Phys. Math., 48, 3/4, 252-264.

4. Bobrenko V. M., Vangeli M. S. and Kutsenko A. N. (1991) *Acoustical Tensometry.* Štiintsa, Kišinev (in Russian).

ON SOLITONIC STRUCTURES IN MICROSTRUCTURED MATERIALS

ANDRUS SALUPERE AND OLARI ILISON

Institute of Cybernetics at Tallinn Technical University
Department of Mechanics, Tallinn Technical University
Akadeemia tee 21, 12618, Tallinn, Estonia

ABSTRACT

Numerical analysis of wave propagation in microstructured media is presented. KdV type evolution equation with a quartic nonlinearity, and both the third- and the fifth-order dispersion is used as a model equation. Periodic boundary conditions and harmonic initial condition are applied. Solution type is determined and analysed for the normal dispersion case, i.e., for the case if the third- and the fifth-order dispersion parameters have different signs.

1. INTRODUCTION

Wave propagation in microstructured media is studied. Higher order dispersion as well as higher order nonlinearity characterise such materials [1, 2]. A Korteweg-de Vries type nonlinear evolution equation

$$u_t + [P(u)]_x + du_{3x} + bu_{5x} = 0 \tag{1}$$

is used as model equation [3]. Here d and b are the third- and the fifth-order dispersion parameter respectively. Nonlinear effects are described the fourth-order elastic potential

$$P(u) = (-\frac{u^2}{2} + \frac{u^4}{4}). \tag{2}$$

Logarithmic dispersion parameters $d_l = -\log d$ and $b_l = -\log(-b)$ are used below instead of d and b. Equation (1)–(2) is integrated numerically making use the pseudospectral method, based on the fast Fourier transform and the Runge-Kutta-Fehlberg (RKF) integrator in time [4, 5]. Periodic boundary conditions

$$u(x,t) = u(x + 2n\pi, t), \quad n = \pm 1, \pm 2, ... \tag{3}$$

and harmonic initial condition

$$u(x,0) = \sin x, \quad 0 \le x \le 2\pi . \tag{4}$$

are used.

The case with $d > 0$ and $b > 0$ is analysed in [3, 6]. In this case the dispersion can be normal as well as anomal [6] and complicated solitonic structures (train of solitons, train of negative solitons, multiple solitons) or chaotic solution can emerge depending on the values of the third- and the fifth-order dispersion parameters [3].

In the present paper the dispersion parameter d is still positive, but b is considered to be negative, which results pure normal dispersion. Our main goal is to define the essence of the numerical solution of the stated problem — to define the solution type and to determine qualitative and quantitative changes of the solution against logarithmic dispersion parameters d_l and b_l.

2. NUMERICAL RESULTS AND DISCUSSION

Numerical integration is carried out in the range $d_l = \{0.8, 1.2, 1.6, 2.0, 2.4\}$ and $b_l = \{0.4, 1.2, 2.0, 2.8, 3.6, 4.0, 4.4, 4.8\}$. The value $\delta = 10^{-10}$ is used for the accuracy parameter which controls the time-step size of the RKF integration algorithm. Space-step $\Delta x = 2\pi/n$ (n = 64).

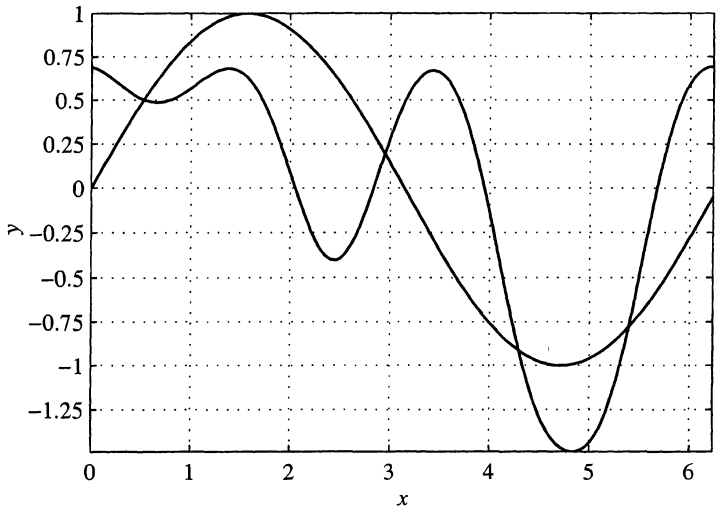

Figure 1. Initial sine wave and train of three negative solitons ($d_l = 2.0$ and $b_l = 2.8$).

For $d > 0$ and $b > 0$, as was mentioned above, four different solution types can appear from the harmonic initial excitation. In the present case only one type — train of negative solitons — is detected. In Figure 1 the initial sine wave and wave-profile at t = 5.7 are presented for $d_l = 2.0$ and $b_l = 2.8$. Emerged solitary waves can be called solitons because their behaviour corresponds to the soliton definition[1]. One can see that the zero level of the soliton train $u_0 < 1$ and $u_{min} < -1$, i.e., the wave-profile is "shifted down" and "stretched in the negative direction" with respect to the initial sine wave. Therefore they are called negative solitons.

As a rule, the evolution of the solution is found to be periodic in time. Periodic behaviour can be detected making use time dependencies of wave-profile minima or spectral amplitudes. The shortest period is detected for the strongest dispersion in the considered domain ($d_l = 0.8$

[1] Soliton is a solitary wave, which propagates with constant speed and constant amplitude. During interaction with other soliton the amplitude of higher soliton is decreasing and both trajectories are phase shifted. After interaction solitons restore their speed and amplitude.

and $b_l = 0.4$). If d_l (or b_l) has a fixed value in the domain $d_l \leq 1.6$ (or $b_l \leq 2.0$) and b_l (or d_l) increases, then the length of the period has a limit value. However, if both logarithmic dispersion parameters have higher values (the weak dispersion case) the solution lost the periodic behaviour.

In Table 1 minimum and maximum values of u are presented against d_l and b_l. For periodic cases, $u_{\min}$ and $u_{\max}$ are found over $0 < t < \tau$, where τ is the length of the period. For non-periodic cases maximum and minimum values are found over the whole integration interval. It is clear that $-1 \leq u \leq 1$ at $t = 0$. If both logarithmic dispersion parameters have relatively small values, then the maximum value of u deviates slightly from the initial value. At same time, absolute value $|u_{\min}|$ and the value $u_{\max}$ differ significantly. For the weaker dispersion, i.e., for $d_l = \{2.0, 2.4\}$ and $b_l = \{2.8, 3.6, 4.0, 4.4, 4.8\}$ $u_{\max}$ deviates significantly from the initial value. Furthermore, the greater are d_l and b_l the close are $|u_{\min}|$ and $u_{\max}$. Therefore in this case the wave-profile is stretched in the positive direction as well as in the negative.

In Table 2 the number of emerging solitons is given against logarithmic dispersion parameters d_l and b_l. Actually, figures in Table 2 represent the number of wave-profile minima. Some of such minima (small amplitude solitons) appear for very short time interval only. The time moment when they emerge first time may be greater than τ, i.e., such small solitons may be undetectable during the first period $[0,\tau]$. Furthermore, some solitons that take part in the interaction process have so small amplitude, that they can not be detected as a local minima. Such small amplitude solitons are called as virtual solitons [7]. Their existence is reflected by distinctive changes in amplitudes (amplitude is decreasing) and trajectories (trajectories are phase shifted) of higher amplitude solitons. To obtain the actual number of solitons, one has to add to the number of "visible" solitons (given in the Table 2) the number of virtual solitons.

Table. 1. Wave-profile maxima and minima against dispersion parameters b_l and d_l.

b_l \ d_l	0.8	1.2	1.6	2.0	2.4
0.4	1.0005 −1.0380	1.0006 -1.0395	1.0004 -1.0401	0.9998 -1.0401	0.9997 -1.0403
1.2	1.0007 −1.1566	1.0027 -1.1878	1.0031 -1.2031	0.9998 -1.2088	1.0027 -1.2153
2.0	1.0051 −1.2911	1.0053 -1.3955	1.0180 -1.4413	1.0210 -1.4602	1.0312 -1.4698
2.8	1.0108 −1.3385	1.0419 -1.4856	1.1761 -1.5548	1.2114 -1.5733	1.3044 -1.6153
3.6	1.0015 −1.3349	1.1074 -1.5068	1.1435 -1.5187	1.1695 -1.5384	1.4647 -1.5994
4.0	1.0023 −1.3349	1.1183 -1.4845	1.0951 -1.5152	1.3040 -1.5551	1.4032 -1.6062
4.4	1.0033 −1.3322	1.1430 -1.4625	1.0762 -1.5155	1.8129 -1.5549	1.5223 -1.5827
4.8	1.0037 −1.3324	1.1418 -1.4656	1.0953 -1.5101	1.6314 -1.5556	1.4687 -1.4828

Table. 2. Number of solitons against dispersion parameters b_l and d_l.

b_l \ d_l	0.8	1.2	1.6	2.0	2.4
0.4	1	1	1	1	1
1.2	1	1	1	1	1
2.0	2	2	2	2	2
2.8	2	2	3	3	3
3.6	2	2	3	3	3
4.0	2	3	3	4	5
4.4	2	3	3	4	5
4.8	2	3	3	5	6

Here we are not going to present corresponding analysis, but only state that at least one virtual soliton can be detected for any $d_l - b_l$ pair.

3. CONCLUSIONS

1. Numerical solution of problem (1)–(4) is analysed for dispersion parameters $d > 0$ and $b < 0$, i.e., for the normal dispersion case. The solution type is train of negative solitons for each value of dispersion parameters in the considered domain.
2. The number of solitons is increasing if dispersion parameters are decreasing, i.e., the weaker is the dispersion the more solitons can be detected in the train.
3. In the case of stronger dispersion (either d_l or b_l have smaller values) the solution is periodic in time. The stronger the dispersion the shorter the period. In the case of weak dispersion (higher values of d_l and b_l) periodic behaviour can not be detected.

ACKNOWLEDGEMENTS

The financial support from the Estonian Science Foundation (grants 2631/1997–99 and 4068/2000) is greatly appreciated. Authors are indebted to Prof. J. Engelbrecht and Prof. G.A. Maugin for stimulating discussions.

REFERENCES

[1] G.A. Maugin. *Material Inhomogeneities in Elasticity.* Chapman & Hall, London et al., 1993.

[2] G.A. Maugin. *On some generalizations of Boussinesq and KdV systems.* Proc. Estonian Acad. Sci. Phys. Math., 199), **44**, 1, 40-55.

[3] A. Salupere, G.A. Maugin, J. Engelbrecht: *Solitons in systems with a quartic potential and higher-order dispersion.* Proc. Estonian Acad. Sci. Phys. Math., 1997, **46**, 1/2, 118–127.

[4] B. Fornberg, G.B. Whitham. A numerical and theoretical study of certain nonlinear wave phenomena. *Phil. Trans. Roy. Soc.*, 1978, **A289**, 373–404.

[5] A. Salupere. On the application of pseudospectral methods for solving nonlinear evolution equations, and discrete spectral analysis. In *Proc. of 10th Nordic Seminar on Computational Mechanics*, Tallinn, 1997, 76-83

[6] A. Salupere, J. Engelbrecht, G. A. Maugin. Solitonic structures in KdV-based higher-order systems. *Wave Motion* (accepted).

[7] A. Salupere, G.A. Maugin, J. Engelbrecht, J. Kalda. On the KdV soliton formation and discrete spectral analysis. *Wave Motion*, 1996, **23**, 49–66.

Computational Analysis of Composite Joints

Alfred Andersen, Harald Osnes and Jostein Hellesland

Mechanics Division, Dept. of Mathematics,
University of Oslo, P.O. Box 1053 Blindern,
N-0316 Oslo, Norway

September 28, 2000

Introduction

Adhesively bonded joints are extensively used in fibre composite structures. Such joints have an advantage over traditional mechanically fastened joints, including bolted joints, in that they avoid the use of drilled holes, which results in broken fibres and stress concentrations. There are also benefits to be achieved from using adhesives instead of welding. As a part of an ongoing project involving adhesively bonded joints, a comprehensive study of geometric nonlinear effects in the analysis of such joints has been carried out. These examinations reveal some of the physical properties connected to bonded composite joints, e.g. the flexibility offered by laminates, and the possibilities that arise when the finite element method is applied in the design process for such joints and materials. The main focus in this paper will be on the numerical analysis methods used, and general features of composite joints.

Joint geometries and analysis

We assume that the joints are wide compared to their thickness and the length of the overlap region. The adhesive is uniformly distributed in the overlap. Furthermore, each laminated plate consists of eight plies with fibre directions 0 and 90 degrees. Thus, out-of-plane bending is avoided, and the joint can be investigated as a 2-D plane strain problem. The well-known software package *ANSYS* [1] is applied in the analysis. Instead of using some of *ANSYS*' own composite elements we decided to use 4 noded bilinear elements and implement the material matrices manually. Additionally, the relatively complicated expressions defining relations between stresses and strains (including modifications related to the geometric non-linear model from Zienkiewicz and Taylor [5]) for laminated composites are

derived and implemented in a general elasticity module using the commercial C++ class library *Diffpack* [2]. This combination of the use of a relatively robust method in *ANSYS* with a self-implemented module in *Diffpack*, in which all programming details are known, has been very fruitful and has provided valuable insight into important modeling aspects (for example, it is observed that certain 2-D anisotropic problems have to be treated with extreme care if *ANSYS* is used). The agreement between the numerical results obtained by *ANSYS* and *Diffpack* is excellent for the problems in the present investigation although the finite element meshes are not identical. The numerical, 2-D domain is sketched in figure 1, which also defines the adopted boundary conditions. The laminated plates consist of eight plies

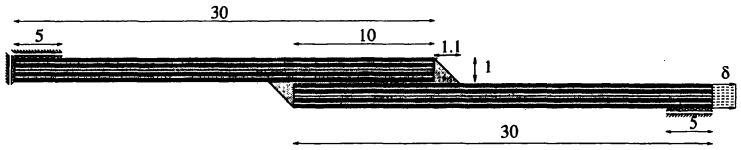

Figure 1: The 2-D domain for the numerical simulations. (Not to scale).

with thickness 0.125 mm. Furthermore, the thickness of the adhesive layer is 0.1 mm. Notice that the horizontal and vertical length scales in figure 1 are different. The mesh consists of mainly four-noded bilinear elements. In

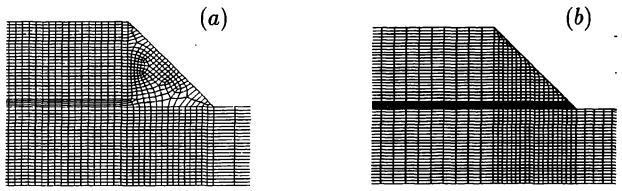

Figure 2: *The ANSYS* (a) and *Diffpack* (b) grids around the fillet tip.

the *ANSYS* models the PLANE13 elements are used with standard shape functions and displacement degrees of freedom. Consequently the elements have the same properties as those used in the *Diffpack* models. There are three elements through the thickness of each ply and four to eight through the adhesive layer. This is enough to achieve a decent picture of the stress distributions that appears in these joints. In addition to the bilinear elements there are some three-noded triangular elements (CST) in the spew fillet. The total number of elements is approximately 10000.

The linear material properties are picked from Kairouz and Matthews [3], where the adherents are made of $XAS/914C$ carbon fibre/epoxy resin and the adhesive used is Ciba-Geigy Redux $308A$. These properties are implemented in *ANSYS* and *Diffpack* as either compliance or stiffness matrices.

Investigation

Firstly, we investigate the behaviour of the single lap joint with the stacking sequence $[0/90]_{2s}$ lay-up in the adherents. The examination reveals that the 0-layers adjacent to the bond by far carry the largest amount of stress and that the maximum value of the equivalent stress is located near the fillet tips. A stress distribution like this, indicates a possibility for cracking just in the bond area. In several applications it is desirable to avoid maximum values for the stress components next to the adhesive layer. When working with composite materials this may be achieved by changing the lay up of the plies. For examle, by using laminates with the stacking sequence $[90/0]_{2s}$ the stress in the layers adjacent to the bond is reduced considerably. As can be seen from figure 3, the maximum value of the equivalent stress is still in the upper 0-layer, but the value is slightly less than the corresponding maximum obtained from the $[0/90]_{2s}$ laminate . However, the transverse displacements are lager when using the $[90/0]_{2s}$ laminates. Although the

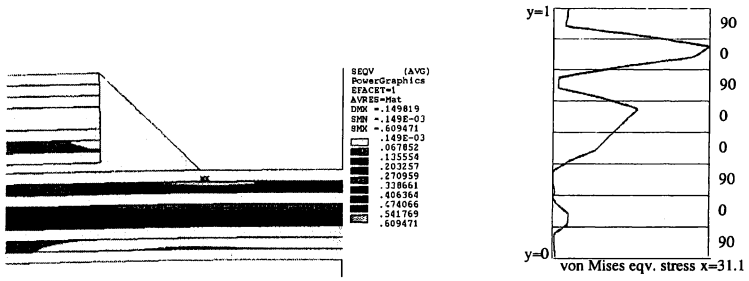

Figure 3: Distribution of von Mises equivalent stress near the fillet tip and stress distribution over lower plate at x=31.1 for $\delta = 0.1$ and $[90/0]_{2s}$ stacking sequence. *ANSYS*

above results are well-known from advanced theory of composite materials, they clearly illustrate some of the flexibility offered by laminates. Additionally the fact that numerical finite element analysis is well suited in the design and optimization process of such materials is shown.

In the latter part of the paper we will refer some of the main results regarding the ongoing project on geometric nonlinear effects of single lap composite joints. Eventhough the average longitudinal strains are small, typically less than 0.6% considerable nonlinear behaviour is observed for this kind of joints. From figure 4 it is seen that especially the transverse displavement is strongly influenced by geometric nonlinear effects. However, also most of the stress components deviate significantly from linear behaviour. Trough careful investigations it appears that the non-symmetric geometry of single lap joints is an important reason for the gemetric nonlinear effects. Nevertheless, also the distribution of materials within the joint

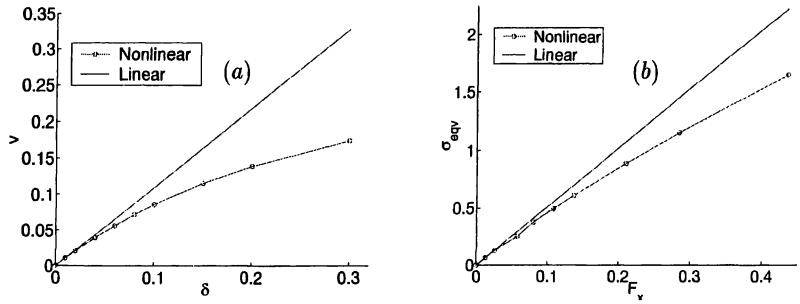

Figure 4: Comparison of geometric nonlinear (o) and linear (solid line) results for the $[0/90]_{2s}$ laminate. Figure (a): Vertical displacement at the fillet tip as a function of joint end displacement. Figure (b): von Mises equivalent stress at the fillet tip as a function of external load.

plays a crucial role.

Summary

The finite element method is used to study important physical properties of composite joints. Furthermore these examinations have revealed that geometric nonlinear effects are of great importance and should therefore always be taken into account when dealing with adhesively bonded single lap joints.

Acknowledgement

The project is supported by the University of Oslo.

References

[1] *ANSYS* World Wide Web home page:
http://www.ansys.com.

[2] *Diffpack* World Wide Web home page:
http://www.nobjects.com/prodserv/diffpack.

[3] Kairouz, K. C., & Matthews, F. L., Strength and failure modes of bonded single lap joints between cross-ply adherends. *Composites*, 24 (6), 1993, pp. 475-484.

[4] Hildebrand, M., Non-linear analysis and optimization of adhesively bonded single lap joints between fibre-reinforced plastics and metals. *Int. J. Adhesion and Adhesives*, 14 (4), 1994, pp. 261-267.

[5] Zienkiewicz, O. C., & Taylor, R. L., *The Finite Element Method, Fourth Edition.* McGraw-Hill Book Company, London, 1989.

Numerical analysis of progressive delamination in DCB composite specimens.

M.Valdats V.Tamuþs
Institute of Polymer mechanics, Rîga, Aizkraukles 32, Latvia

Abstract

For many structural materials the resistance of crack propagation G depends on the length of crack increment Δa. This phenomenon which is known as R curve effect is a result of bridging, when faces of propagated crack beyond the tip are still joined by crossover tights. Bridging phenomenon is highly expressed in the delamination process of laminate composites. The R curve of composite delamination experimentally is determined on DCB (double cantilever beam) specimen and it is known that the result depends on the geometry of the specimen tested [1]. Therefore it is necessary to analyze crack delamination and bridging in DCB composite specimen to create the methodology of R curve prediction for any composite beam thickness. In [1] the DCB specimens with different geometry loaded by pure bending moments were investigated, In [2] the scheme of measurements and numerical model was described for R curves with bridging obtained on traditional DCB specimens loaded by wedge forces. The numerical analysis in [2] was carried out by using a non-linear finite element method with interface elements which are embedded along potential delamination line. The alternative numerical procedure based on the solving of classical beam deflection equations with nonlinear bridging forces is proposed and described in the present paper.

Experimental results

The scheme of loading and measurements is shown on Fig.1. During the experiment the value of applied wedge load $P(a)$ and displacement $d(a)$ were measured. For one specimen the displacement at the tip of precrack a_0 $\delta(a)$ was measured too. All parameters were registered as values of crack extension Δa. More detailed the experiment is described in [2]. On fig. 3 the experimental R curves of $G(a)$ are shown which are calculated by formula (1)

$$G = \frac{1}{b}\frac{\partial \Pi}{\partial a} = \frac{P^2(a)}{2b}\frac{\partial C(a)}{\partial a}, \qquad (1)$$

where $C = \frac{d}{2P}$ is the compliance of half of specimen.

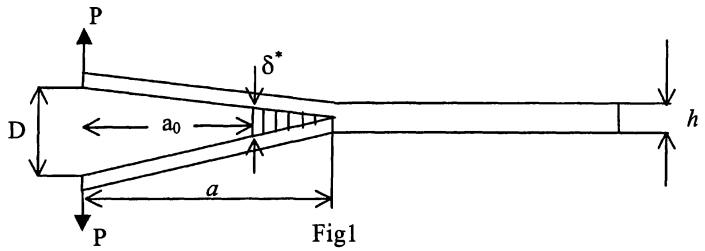

Fig1

These curves depend on the geometry of specimen as it was noted above. The task consists in finding the unknown bridging law function $f(w)$ which acts on crack faces in segment $[a_0 a]$ and in elaborating the numerical procedure to find $P(d)$ and $G(a)$ for any thickness of sample.

The deflection of beam in fig. 1 is governed by equation

$$\frac{d^4 w}{dx^4} + \frac{f(w)}{EJ} = 0 \tag{2}$$

with five boundary conditions. Two of them are geometrical

$$w(a) = w'(a) = 0 \tag{3}$$

the third

$$w'(a)^2 = \frac{G_{1c} b}{EJ} \tag{4}$$

reflects the condition that the crack propagates when energy release rate at the crack tip reaches the value G_{1c}. The fourth and fifth condition reflects the value of applied force P:

$$w^{II}_{x=a_0} = \frac{P a_0}{EJ} \qquad w^{III}_{x=a_0} = \frac{P}{EJ} \tag{5,6}$$

So the 4-th degree equation has 5 boundary conditions (2-6) but it also includes two parameters a and P. So the solution will depend on one free parameter e.g. a, and result will be functions $P=P(a)$ and $W=W(a,x)$. The displacement at the point where load P is applied also depends on a

$$D = W(a_0) - W'(a_0) * a_0 + \frac{P a_0^3}{3EJ} \tag{7}$$

From this we can find both our functions of interest $P=P(D)$ and $G=G(a)$. What we have to do is to solve the differential equation.

For linear bridging law analytic solution has been found in [4], but it is evident, that it is not possible to solve this equation analytically for arbitrary bridging law $f=f(W)$. So, as we are considering general case, we have to solve it numerically. But with these boundary conditions a straightforward calculation is not possible. At first boundary conditions are reduced to initial conditions at the crack tip, and afterwards the calculation is done with ordinary Newton method.

Almost all initial conditions at the crack tip are given: $W(a)=W(a)=0$, $W(a)= \sqrt{G_{1c} b / EJ}$, only $W(a)$ is missing. So instead of choosing a as a free parameter, we use $W(a)=W3$ as a parameter. Now using Newton method we can calculate functions $a=a(W3)$, $P=P(W3)$, $W=W(W3,x)$ in as many points as we want.

From data obtained using formulas (1) and (7) we get functions $G=G(a)$ and $P=P(D)$

.

Results

The R-curves G=G(a) for linear and nonlinear bridging laws Fig[2] are shown in Fig[3]. It seems that nonlinear R-curve fits experimental data better than linear, however one could wish still better. Curves P=P(d) fits experimental data better, but it would require too much space to show them, too.

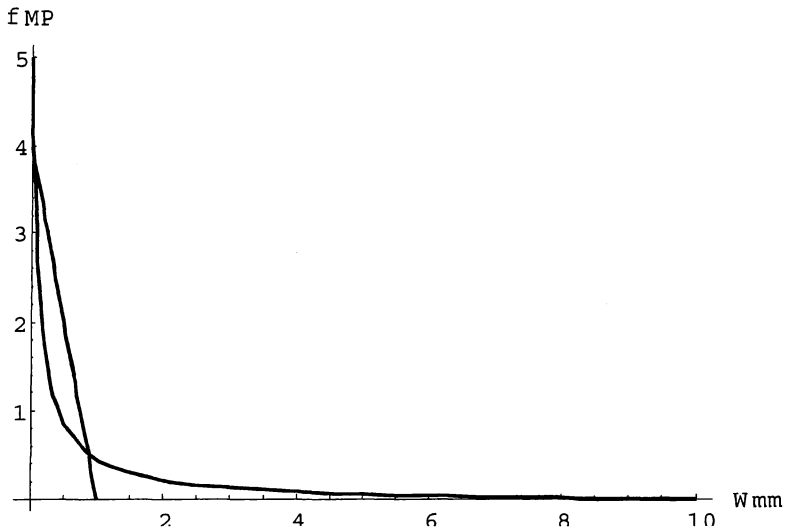

Fig2

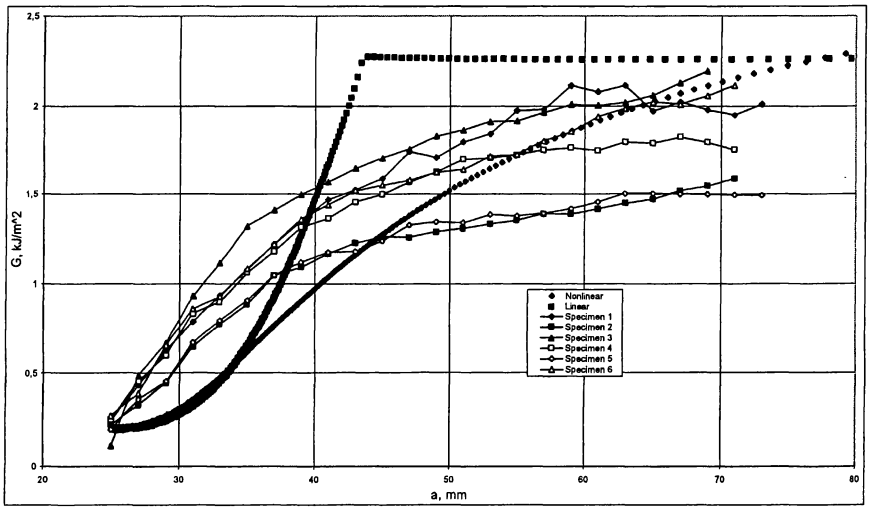

Fig3

Conclusion

It follows from experimental data, that the bridging law is quite unlinear. Numerical modeling shows, that R curve for unlinear bridging law fits experimental data better.

References

1. Sorensen B.F., Jacobsen T.K. (1998) Large-scale bridging in composites: R-curves and bridging laws. *Composites Part A*, **29A**, 1443-1451.
2. V.Tamuļs and S.Tarasovs (2000) Progressive delamination and fiber bridging modeling in double cantilever beam composite specimens. Submitted to *Engineering fracture mechanics*
3. J.W.Williams (1988) On calculation of energy release rates for cracked laminates Inf. J. Fracture 36. 109-119.
4. Daridon L., Cochelin B. and Potier Ferry M. (1997) Delamination and Fiber Bridging Modeling in Composite Samples. *Journal of Composite Materials*, **31**, 9, 874-888.

(13th Nordic Seminar on Computational Mechanics, October 20-21, 2000 Oslo, Norway.)

Fast fully nonlinear simulations of water waves

DIDIER CLAMOND & JOHN GRUE
DEPARTMENT OF MATHEMATICS, UNIVERSITY OF OSLO, NORWAY.
didier@math.uio.no, johng@math.uio.no

Introduction

Computationally fast fully, highly or weakly nonlinear methods exist. These methods have several drawbacks including limitation of 2D-flows (Fornberg 1980) or limited accuracy for approximated methods (Dommermuth & Yue 1987, West *et al.* 1987, Yasuda & Mori 1994, Trulsen & Dysthe 1996). We here derive a novel rapid method for fully nonlinear non-overturning water waves. The method has been derived in two and three dimensions, but it is here outlined in two dimensions only.

A fast Laplace equation solver is obtained by means of integral equations. One part of the solution is obtained by Fast Fourier Transform of the potential at the free surface and products between this potential, or its horizontal derivatives, and the wave elevation. The other part is highly nonlinear and consists of integrals that may be evaluated in a rapid way since the integrands are quickly decaying in space. Computations for one-dimensional wave propagation show that integration over a distance of one characteristic wavelength is sufficient for these integrals, even for highly nonlinear waves. The resulting implicit equation for the unknown function forms a basis for an iterative scheme with rapid convergence. The number of operations required is asymptotically $\mathcal{O}(N \log N)$, where N is the number of computational nodes. One iteration of the scheme is found to be sufficient for practical purposes. We shall term this approximation to be the explicit approximation of the method. However, any accuracy is achieved by a continued iteration of the equations.

The fast Laplace equation solver allows for simulations in long tanks. To simulate long time evolution, the explicit temporal scheme involves higher derivatives and is stable for arbitrary small scale perturbations. The scheme is therefore robust. It is based on Padé approximations, instead of Taylor expansions.

Laplace's equation solver

The Laplace equation solver is the heart of our method, and is hence detailed here. For simplicity, all derivations are demonstrated for water of infinite depth. The method may, however, easily be extended to a fluid layer bounded by a bottom, where the latter may be varying.

The fundamental equations can be formulated involving quantities at the surface only. The flow conservation gives a temporal evolution of the free surface η, while the Bernoulli equation gives a temporal evolution of the velocity potential at the surface $\widetilde{\phi}$. To close the system, an equation giving the stream function at the surface $\widetilde{\psi}$ is needed. It can be obtained using the Cauchy integral formula, splitted into real and imaginary parts, i.e.

$$\widetilde{\phi} = \frac{1}{\pi} \fint_{-\infty}^{\infty} \frac{D\,(\widetilde{\phi}' - \eta_x' \widetilde{\psi}') - \widetilde{\psi}' - \eta_x' \widetilde{\phi}'}{1 + D^2} \frac{\mathrm{d}x'}{x' - x}, \tag{1}$$

$$\widetilde{\psi} = \frac{1}{\pi} \fint_{-\infty}^{\infty} \frac{\widetilde{\phi}' - \eta_x' \widetilde{\psi}' + D\,(\widetilde{\psi}' + \eta_x' \widetilde{\phi}')}{1 + D^2} \frac{\mathrm{d}x'}{x' - x}, \tag{2}$$

where $\widetilde{\phi} = \widetilde{\phi}(x,t)$, $\widetilde{\phi}' = \widetilde{\phi}(x',t)$, etc. In (1)–(2) the function $D = (\eta' - \eta)/(x' - x)$ is introduced, where D decays according to $|x' - x|^{-1}$ for $|x' - x| \to \infty$ and $D \to \eta_x$ for $x' \to x$. To obtain $\widetilde{\psi}$, given η and $\widetilde{\phi}$, it is common to use the equation (2) which is typically solved iteratively with $\mathcal{O}(N^2)$ operations.

This is a very slow alternative non-usable for realistic computations. It is much more efficient to obtain $\tilde{\psi}$ from the conjugate equation (1).

Splitting (1) into singular and regular integrals, applying one integration by parts and one Hilbert transform (denoted $\mathcal{H}$), the relation (1) gives

$$\tilde{\psi} = \mathcal{H}\left\{\tilde{\phi}\right\} + \eta\tilde{\phi}_x + \mathcal{H}\left\{\eta\,\mathcal{H}\left\{\tilde{\phi}_x\right\}\right\} - \mathcal{H}\left\{\frac{1}{\pi}\int_{-\infty}^{\infty}[\arctan(D) - D]\,\tilde{\phi}'_x\,\mathrm{d}x' + \frac{1}{\pi}\int_{-\infty}^{\infty}\frac{D\,(D-\eta'_x)\,\tilde{\psi}'}{1+D^2}\,\frac{\mathrm{d}x'}{x'-x}\right\}, \tag{3}$$

which is another equation for $\tilde{\psi}$. In (3), the singular integrals are convolutions and can thus be computed quickly, with computational burden $\mathcal{O}(N \log N)$. The remaining regular integrals have kernels that decrease rapidly, as $|x'-x|^{-3}$ and $|x'-x|^{-2}$, respectively. Therefore, integrations over $(-\infty, +\infty)$ can be approximated by integrations over a limited interval $(x-\lambda, x+\lambda)$, λ being chosen in accordance with the precision needed, and depending on the wave characteristics (and not on the length of the computational domain). Moreover, the contribution on the right hand side of (3) involving $\tilde{\psi}$, is cubic in nonlinearity, while in equation (2) the corresponding term is quadratic. For nonbreaking waves, where cubic terms are smaller than quadratic ones, iterations with (3) converge faster than iterations with (2). An iterative scheme is initialized by the explicit quadratic approximation

$$\tilde{\psi}_1 = \mathcal{H}\left\{\tilde{\phi}\right\} + \eta\tilde{\phi}_x + \mathcal{H}\left\{\eta\,\mathcal{H}\left\{\tilde{\phi}_x\right\}\right\}. \tag{4}$$

Applying one analytical iteration, neglecting integrals being of quartic nonlinearity, we get another approximation

$$\tilde{\psi}_{2,\lambda} = \tilde{\psi}_1 - \mathcal{H}\left\{\frac{1}{\pi}\int_{x-\lambda}^{x+\lambda}\frac{D\,(D-\eta'_x)\,\tilde{\psi}'_1}{1+D^2}\,\frac{\mathrm{d}x'}{x'-x}\right\}. \tag{5}$$

The latter is explicit and does not involve transcendental functions.

Numerical comparisons

The approximation (5) is very accurate, even for steep waves. Comparison with a steady steep wave (fig. 1), shows that $\tilde{\psi}$ is computed from (5) (with $\lambda = \pi/k$) with an error smaller than 1%.

We also applied the approximation $\tilde{\psi}_{2,\lambda}$ in unsteady wave simulations. In this test, waves are generated from rest with a pneumatic wavemaker, and simulations using (2) and (5) are compared. The results show that the two methods are almost identical (fig. 2). (5) gave the results about fifteen times faster than by using equation (2), for a computational domain of about thirty characteristic wavelengths. If a longer tank is used the gain increases.

The unsteady simulation shows huge acceleration in the leading part of the wave train (fig. 3). It appears that this large acceleration is considerably decreased if smoothing or a low order approximation is employed. Our scheme seems promising, to be able to investigate complicated steep wave fields.

References

DOMMERMUTH, D. & YUE, D. K. P. 1987. A high-order spectral method for the study of nonlinear gravity waves. *J. Fluid Mech.* **184**, 267–288.

FORNBERG, B. 1980. A numerical method for conformal mapping. *SIAM J. Sci. Stat. Comp.* **1**, 386–400.

TRULSEN, K. & DYSTHE, K. B. 1996. Freak Waves – A Three-Dimensional Wave Simulation. *Proc. 21st Symp. on Naval Hydrodynamics* Trondheim, 550-558.

WEST, B. J., BRUECKNER, K. A., JANDA, R. S., MILDER, D. M. & MILTON, R. L. 1987. A new numerical method for surface hydrodynamics. *J. Geophys. Res.* **92**, 11, 11803–11824.

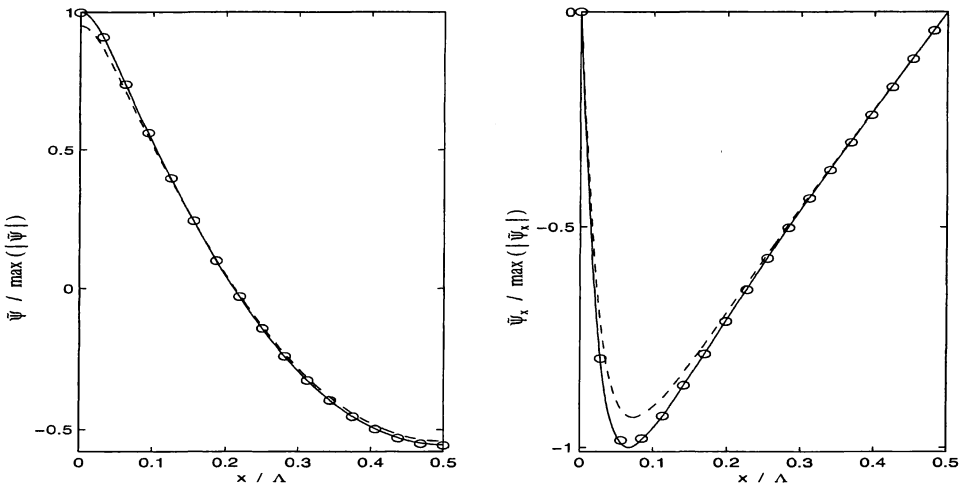

Figure 1: *Comparison of approximations for* $ak = 0.41$.

— exact, - - $\widetilde{\psi}_1$ (eq. 4), o $\widetilde{\psi}_{2,\lambda}$ (eq. 5 with $\lambda = \pi/k$).

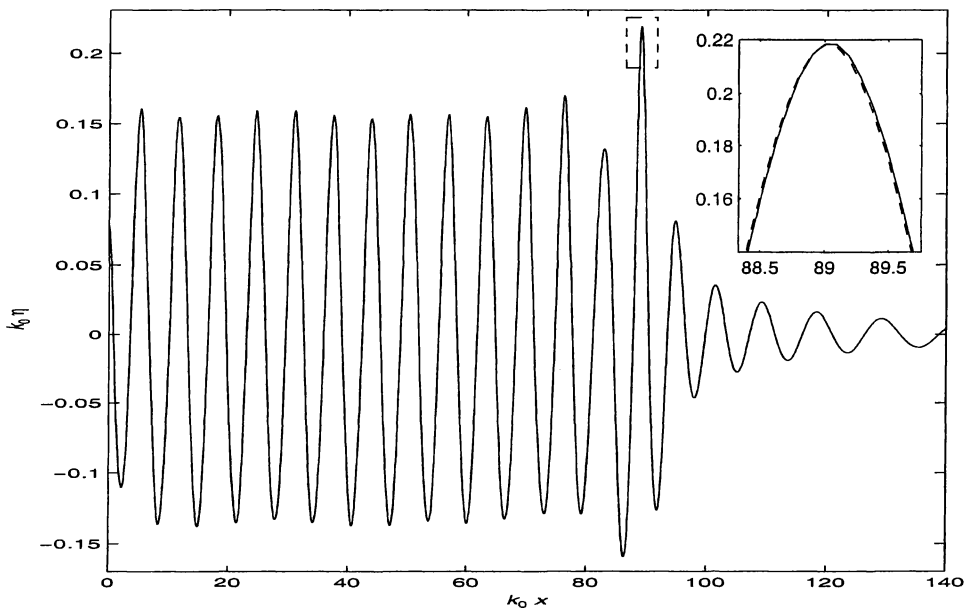

Figure 2: *The transient leading part of a wave train.*

— exact, - - $\widetilde{\psi}_{2,\lambda}$ (eq. 5 with $\lambda = \pi/k_0$, $k_0 \Delta x = 0.095$).

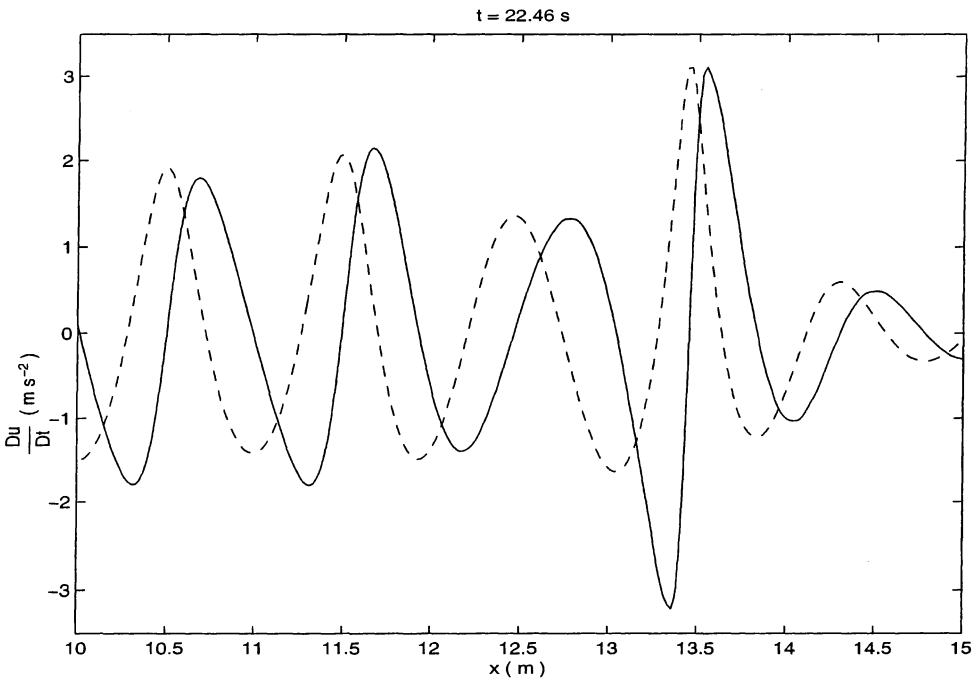

Figure 3: *Horizontal acceleration at the surface.*

(—) acceleration, (- -) surface elevation, depth=60 cm.

A CFD PREDICTION PROCEDURE FOR INTERFERENCE AND COLLISION OF MULTIPLE RISERS

Joar Dalheim
Det Norske Veritas, Høvik

ABSTRACT

This paper presents a numerical procedure to solve the coupled motion of multiple risers and a viscous incompressible fluid. The former is solved by a multi-modal response model and the latter is solved by a sectional solution (strip theory) method. In every fluid section the 2D vorticity equation is solved by a Vortex-in-Cell method and the different fluid sections are coupled through the boundary conditions from the motion of the riser. The procedure is used to solve the vortex-induced vibration (VIV) response of two flexible risers in a fluid flow. The hydrodynamic interaction effects are investigated together with the onset conditions for riser collision. The numerical results are visualized to obtain better understanding of the computed results and the phenomenon. The presented procedure may be used as a tool for determining optimal distance between marine risers in offshore production systems.

INTRODUCTION

As the oil industry has been moving into deeper and deeper waters, the structures have become more and more slender and hence prone to vortex induced vibrations and large displacements. When one or more risers are exposed to a sheared current there will almost always be induced some kind of vortex-induced vibration. In order to be able to predict the fatigue damage caused by these transverse vibrations it is crucial to know which modes that will dominate the response of the risers and at what amplitudes they are responding. In addition, if more than one riser is analyzed, it is important to be able to predict the coupled response of the riser system. Numerical tools with this feature included will therefore be of great support for riser system design in the oil industry. An example of where the interaction problems are important is the riser array in a Spar buoy. Because of the relative small hull of the Spar, the riser spacing is limited and the question of riser interaction and collision becomes crucial. In order to help the engineer to understand the coupled motion of long and flexible cylinders in fluid flow, a computer program with the capability of visualizing these motions is developed. A multi modal analysis is used to predict the cylinder motion, and the fluid domain is solved by the vortex in cell method. General physical equations are utilized in order to make an effort of making the computer program general and being able to solve a number of different classes of VIV problems (such as collision of multiple risers, steel catenary risers, deepwater risers, surface waves, etc.).

NUMERICAL RESULTS

The numerical procedure is validated by performing interaction and collision tests of two flexible risers aligned in the inline direction and with variable distance between them. The validation is to be regarded as qualitative since there has been no comparison with experimental data. The reason for not doing this is purely because there were found no data without proprietary restrictions. However, the capability of predicting riser interference and collision by the present tool is demonstrated through these experiments. The risers properties used in the study is stated in **Table 1** below.

Property	Upstream	Downstream
Outer Diameter	1.0 m	1.0 m
Length	75 m	75 m
Total mass	32000 kg	32000 kg
Natural frequency no. 1	1.5 rad/s	1.5 rad/s
Natural frequency no. 2	3.0 rad/s	3.0 rad/s
Natural frequency no. 3	4.5 rad/s	4.5 rad/s
Natural frequency no. 4	6.0 rad/s	6.0 rad/s
Natural frequency no. 5	7.5 rad/s	7.5 rad/s

Table 1 – Properties of analyzed risers

The inflowing current profile is modeled to be spanwise constant and with an absolute velocity of U = 1.22 m/s. The two risers were aligned with the direction of the flow, i.e. the downstream riser was modeled to be in the middle of the wake of the upstream riser. The spacing between the riser fixation points was decreased until collision occurred. When collision occurred the relative speed of the risers at the elevation of impact was determined. Both the absolute value and the direction of the relative impact velocity was obtained. In all cases of collision the relative impact velocity had a component in both the inline and the transverse direction. The relative collision velocities were found to be dominated by the VIV motion, which allows for relatively straight forward assessment of the upper limit for relative collision speed and corresponding energy involved. The (**Fig. 1 – Fig. 6**) below shows the main results of the numerical investigation. When the risers were spaced 4 diameters apart the first mode was the dominating mode for both risers. The transverse vibration was very similar for both risers and was also occurring at the same frequencies. When reducing the distance to 3 diameters it appeared that the transverse response energy was shifted to a multi-modal type with clear contributions from the second mode. The frequency of the transverse vibration was still correlated. It was also clear that the mean inline displacement for the upstream riser was increasing more than for the downstream riser. The two risers collided when the initial downstream spacing was 2.8125 diameters and the relative collision impact speed was U_{imp}= 2.6 m/s. Assuming a sinusoidal motion of the VIV vibration, the amplitude of the bilateral velocity should be in the order of ωA, where ω is the vibrating frequency in rad/s and A is the amplitude. This assumption will give a maximum velocity of each riser in the order of 1.5 m/s, and the maximum relative velocity equal to twice that velocity (3 m/s).

The presented program has been subject to a substantial validation process and additional validation work is referred to in Dalheim[5].

ACKNOWLEDGMENTS

The development of the present tool is based on internal funding and resources from Det Norske Veritas.

REFERENCES

1. Baldwin, B.S. and Lomax, H.: "Thin Layer Approximation and Algebraic Model for Separated Turbulent flows", AIAA 16th Aerospace Sciences Meeting, 1978.
2. Skomedal, N.G. and Vada, T.: "The vortex-in-cell method. Capability of numerical simulation of the flow past one circular cylinder in laminar and turbulent flow", AS Veritas Research Report No. 85-2043, 1985.
3. Blevins, R.D.: "Flow-Induced Vibration", *VanNostrand Reinold*, New York, Second Edition,1990.
4. Dalheim, J.: "VISFLO 3: Modal Analysis", Det Norske Veritas Report No. 97-2052, 1997.
5. Dalheim, J.: "Numerical Prediction of VIV on Deepwater Risers Subjected to Shear Current and Waves", OTC paper No 10933, Offshore Technology Conference, Houston 1999.

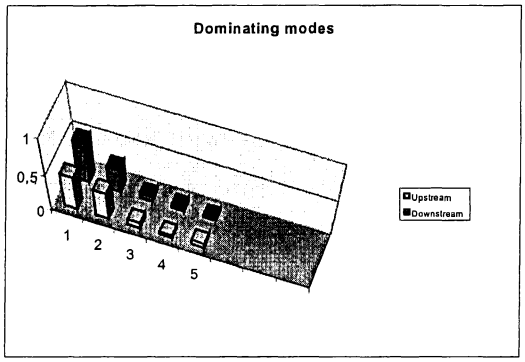

Fig. 1 – Modal energy – distance 3D

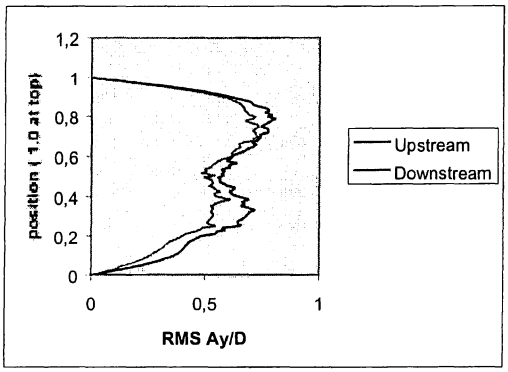

Fig. 2 – Transverse VIV – distance 3D

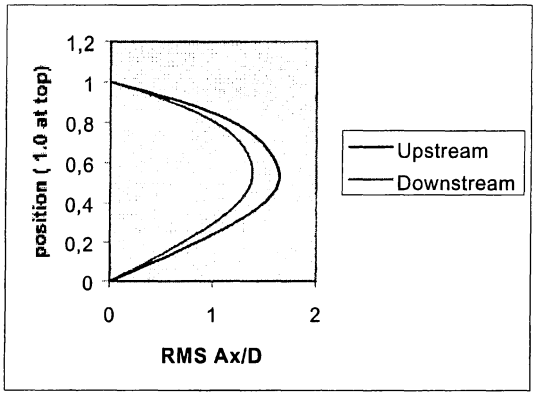

Fig. 3 – Mean inline displacement – distance 3D

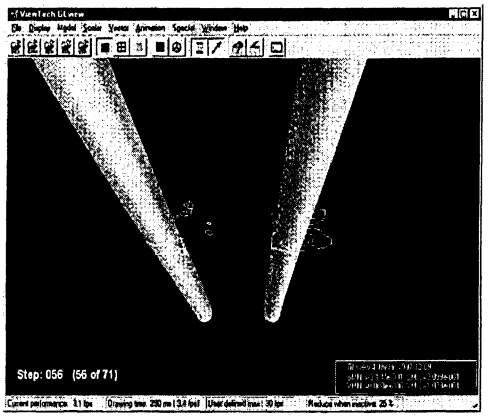

Fig. 4. – Vortex shedding on two cylinders

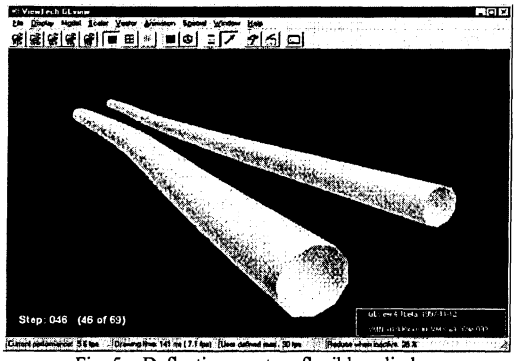

Fig. 5 – Deflections on two flexible cylinders

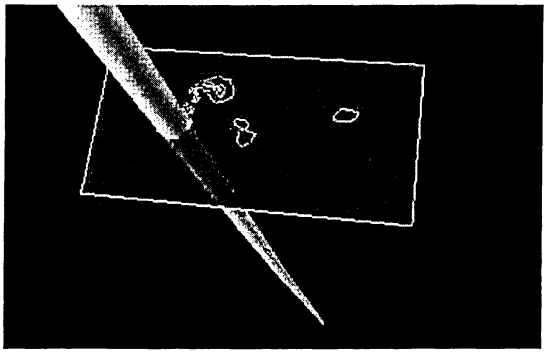

Fig. 6 – Vortex shedding pattern

An effective iterative approach to a fully implicit mixed finite element formulation for the Navier-Stokes equations

Kent-Andre Mardal Hans Petter Langtangen

Department of Informatics
University of Oslo

Abstract

In this paper we consider a fully implicit method for Navier-Stokes equations for incompressible viscous flow. We use mixed finite elements and utilize block preconditioning to construct an efficient solution algorithm for the resulting non-symmetric, indefinite linear system. The present work is inspired by a block preconditioning strategy for the Stokes problem which leads to an optimal solution algorithm with a suitable Krylov solver. Numerical experiments are presented for different Reynolds numbers for the lid driven cavity problem.

1 Motivation

In this paper we consider a fully implicit scheme for the incompressible Navier-Stokes equations. The scheme leads to systems of nonlinear algebraic equations, and to solve the system we use either the Newton-Raphson or the Piccard iteration method. These nonlinear methods require the assembling and solution of a sequence of linear systems. Traditionally, direct methods like banded Gaussian elimination have been used to solve the linear systems arising from fully implicit methods for the Navier-Stokes equations. Then the solution of the linear system is much more storage and CPU-time consuming than the finite element assembly of the same system. To speed up the code, one should apply iterative methods, and in this paper we address preconditioned Krylov (or Conjugate Gradient-like) methods. The efficiency of Krylov methods depends heavily on the quality of the preconditioner. In [2] it was shown that a block structured preconditioner gave optimal convergence for the Stokes problem. The main point is that by making a block preconditioner one keep the system indefinite, with a bounded spectrum

away from zero, hence avoiding breakdown of the Krylov solver. We extend this method to the fully implicit Navier-Stokes equations.

Part of the motivation of the current study is to design and apply generic software tools for such complicated tasks as CFD. The implementation relies heavily on object-oriented design and is built using Diffpack, a C++ library (see [1]). Diffpack comes with an object-oriented plug-and-play interface to various finite elements, linear solvers, preconditioners, convergence criteria, etc and is therefore suitable for numerical experiments involving these parameters.

2 Scheme

The Navier-Stokes equations reads

$$\varrho(\frac{\partial \mathbf{v}}{\partial t} + \mathbf{v}\cdot\nabla\mathbf{v}) = -\nabla p + \mu\Delta\mathbf{v} + \varrho b \quad in\ \Omega \tag{1}$$

$$\nabla\cdot\mathbf{v} = 0 \quad in\ \Omega, \tag{2}$$

$$\mathbf{v} = \mathbf{g} \quad on\ d\Omega. \tag{3}$$

We discretize the problem using finite differences in time and mixed finite element in space. The time discretization is based on the so-called "θ-rule". The discretization of the problem, using Einstein's summation convention, becomes

$$\alpha\varrho\frac{\hat{\mathbf{v}}_r^l - \hat{\mathbf{v}}_r^{l-1}}{\Delta t} + \theta\varrho\hat{\mathbf{v}}_s^l\hat{\mathbf{v}}_{r,s}^l + (1-\theta)\varrho\hat{\mathbf{v}}_s^{l-1}\hat{\mathbf{v}}_{r,s}^{l-1} = \tag{4}$$

$$-\theta\hat{p}_{,r}^l - (1-\theta)\hat{p}_{,r}^{l-1} + \theta\hat{\mathbf{v}}_{r,ss}^l + (1-\theta)\hat{\mathbf{v}}_{r,ss}^{l-1} \tag{5}$$

$$+\rho\theta b_r^l + \rho(1-\theta)b_r^{l-1}, \tag{6}$$

$$\hat{\mathbf{v}}_{r,r}^l = 0, \tag{7}$$

where $\hat{\mathbf{v}}_r^l(x_1,\ldots,x_d,t) = \sum_{j=1}^n v_j^{r,l}N_j(x_1,\ldots,x_d)$ and $\hat{p}^l(x_1,\ldots,x_d,t) = \sum_{j=1}^m p_j^l L_j(x_1,\ldots,x_d)$. The implicit time stepping forces us to use mixed elements (N_i and L_j) that satisfy the Babuska-Brezzi condition. Several elements are known to satisfy this condition e.g. the Crouiex-Raviart element combined with piecewise constant pressure elements, the MINI element for the velocity combined with linear elements and biquadratic velocity and linear pressure elements for certain grids.

In order to construct efficient preconditioners for a Krylov solver we keep the nonlinear equations block-structured. That is, the degrees of freedom of

the system are numbered in the following way in three dimensions:

$$\mathbf{u} = [v_1^1, \ldots, v_n^1, v_1^2, \ldots, v_n^2, v_1^3, \ldots v_n^3, p_1, \ldots, p_m].$$

where n is the number of degrees of freedom associated with one of the scalar fields related to the velocity approximation and m is number of degrees of freedom related to the pressure.

The structure of the scheme is as follows:

$$F(\hat{\mathbf{v}}^l, \hat{p}^l) = \begin{bmatrix} A(\mathbf{v}^l) & B^T \\ B & 0 \end{bmatrix} \begin{bmatrix} \hat{\mathbf{v}}^l \\ \hat{p}^l \end{bmatrix} - \begin{bmatrix} \mathbf{f} \\ g \end{bmatrix} = 0. \tag{8}$$

3 Efficient solvers

What is the problem when solving the system (8) with a Krylov solver ? The system is a discretization of an unbounded operator resulting in the fact that the condition number increase at least as $O(h^{-2})$, where h is a characteristic grid size. A coarse estimate on the efficiency of a Krylov solver can be given in terms of the condition number, hence we want to replace the system with an equivalent system that is better conditioned.

$$Ax = b \rightarrow BAx = Bb \tag{9}$$

The problem is to find a suitable B. The equations (8) has a structure that we may take advantage of by constructing a block preconditioner $B = diag(M, N)$ as proposed in [2]. The preconditioned system then becomes:

$$\begin{bmatrix} M(\mathbf{v}^l) & 0 \\ 0 & N \end{bmatrix} \begin{bmatrix} A(\mathbf{v}^l) & B^T \\ B & 0 \end{bmatrix} \begin{bmatrix} \hat{\mathbf{v}}^l \\ \hat{p}^l \end{bmatrix} - \begin{bmatrix} M(\mathbf{v}^l) & 0 \\ 0 & N \end{bmatrix} \begin{bmatrix} \mathbf{f} \\ g \end{bmatrix} = 0, \tag{10}$$

The condition number of this system can be expressed by the spectrum of MA and $NBMB^T$. We choose $N = L^{-1}$, where L is the mass matrix related to $\hat{p}$. M is chosen as a preconditioner for the discrete Laplace operator, where we use both multigrid and RILU-factorization. This preconditioner is actually an optimal preconditioner for the Stokes problem (see [2]). How will this preconditioner behave in the fully nonlinear and non-symmetric problem? Nobody knows, but the truth is out there, and numerical experiments with the suggested scheme will recover some of the answer.

References

[1] H. P. Langtangen. *Computational Partial Differential Equations - Numerical Methods and Diffpack Programming.* Springer-Verlag, 1999.

[2] T. Rusten and R. Winther. A preconditioned iterative method for saddlepoint problems. *SIAM J. Matrix Anal.*, 1992.

Modelling of wave run-up

D.J.Wood, A.Jensen and G.Pedersen

September 15, 2000

1 Introduction

Large destructive waves on the sea (tsunamis) can be caused by slides, earthquakes or volcanoes. These tsunamis are the number 5 killer among natural hazards in the world. In Norway these waves are created by rock slides and have caused 170 deaths in Norway this century. Hence, the prediction of the evolution of these waves is important. Characteristics of wave run-up which are particular challenges when trying to model, are a moving shore-line, features of breaking, large velocities and large accelerations. These features make it difficult to model mathematically, and also to make measurements.

At the University of Oslo we are carrying out experiments of a wave running up a beach, and we can measure the velocity and, to some extent, acceleration within the wave using PIV (Particle Image Velocimetry). In addition we use wave gauges and images to measure the motion of the free-surface. These waves are generated in the laboratory using a wave paddle (piston). A definition sketch of the wave tank is shown in figure 1.

We simulate these waves using an industrial Navier Stokes solver (FLUENT)as a 'numerical wave tank' to create the same waves as we have in the laboratory. In addition we use a less general, but simpler and much faster to run, Lagrangian Boussinesq model for long waves. Our intention is to use these models together with the experimental data to gain physical insight into run-up. In addition we will examine the ability of the two models to predict features such as velocity distribution, and make some conclusions about the applicability of the models.

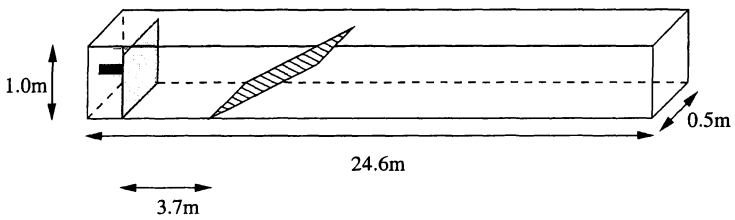

Figure 1: The wave tank. The grey region is the wave paddle, and the striped region the beach.

2 Modelling

In the Navier Stokes model we use a moving-mesh to create a piston with the same motion as the laboratory piston, and use VOF (volume of fluid) method to model the free-surface of the wave as it travels first in deep water and then up the beach. The Navier Stokes model can be used to predict among other things the velocity distribution in the wave and the free-surface motion. Moreover, in principle, the VOF algorithm allows the computation of breaking waves and the trapping of bubbles. The Boussinesq model also takes the input of the laboratory piston motion and should be able to make similar predictions to that of the Navier Stokes model, but it is only expected to give good agreement when the waves are long.

We will show detailed comparisons of both the described models with the velocity fields and surface profiles from the experiments. We will show that the Navier Stokes model appears to capture the essential properties of run-up of steep waves, including a high speed jet shooting up the beach. See figure 2. The Navier Stokes model gives good agreement of velocity distribution and surface profile for both steep and long waves. The Boussinesq model also gives good agreement for the long waves, and fairly good aggreement even for rather steep waves. An example of such velocity comparisons between the experiments, Boussinesq and Navier Stokes models for a long wave are shown in figure 3. In figure 3 we also include a diagram to show the free surface profile of the wave at the time the PIV measurements were taken, and an indication of where the velocities we compare are taken from.

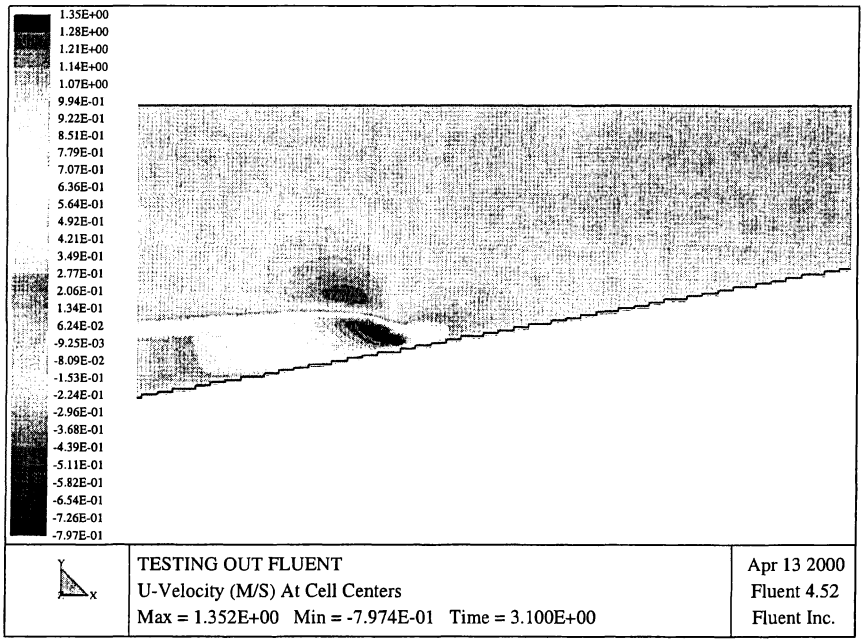

Figure 2: Horizontal velocity contours in both the fluid and air. We can clearly observei the steep wave front that is about to form an onshore jet.

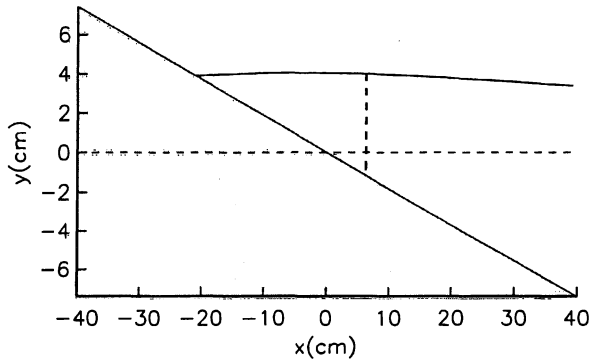

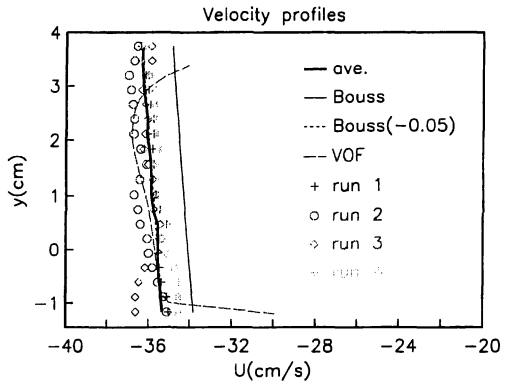

Figure 3: Upper panel: The surface at $t = 4.55$ sec, as computed by the Boussinesq model. The origin is in the equilibrium shoreline and the vertical dashes indicate the cross section for velocity comparisons.
Lower panel: Comparison of the horizontal velocity component in cross section. Averaged PIV measurements (ave.) are compared to results from the Boussinesq (Bouss) and Navier Stokes (VOF) models. The Boussinesq results delayed by 0.05 sec are also displayed. Velocities from the separate experiments (symbols) are included to demonstrate the degree of repeatability.

Manifold Method in Hydraulic Fracturing Analysis

Bård Bostrøm and Ming Lu
SINTEF Civil and Environmental Engineering, Norway

Introduction

CMC is a long –term research programme on computational mechanics issues in civil engineering, especially related to *integrated analysis* [1]. That is, analysis where two or more interacting effects or phenomena are analysed either staggered or simultaneously. CMC contains five main projects where frequently encountered problems in civil engineering will be treated by an integrated approach. One of the projects focuses on the analysis of hydraulic fracturing. In such an analysis there are two interacting effects. Firstly, the pore fluid flow and pressure interact with the dynamic behaviour of the rock matrix. Secondly, there is an interaction at the domain interface between the fluid saturated rock and the fluid in the crack. Fluid will flow from one domain to the other through the moving boundary between the two domains. Within each domain, the field equations must be solved with the location of the internal boundary being determined simultaneously.

In the CMC-programme one of the main objectives is to apply state-of–the-art software to solve interdisciplinary and integrated civil engineering problems. Having performed a comprehensive review of existing software [2], it is decided that the analysis of hydraulic fracturing in this project will be accomplished with the Numerical Manifold Method (MM) developed by Shi [3].

Manifold Method

Numerical Manifold Method is a newly invented numerical method based on sound theoretical basis. It is an improvement and further development to its predecessor, Discontinuous Displacement Analysis (DDA) [4]. A MM model consists of two meshes – the physical mesh and the mathematical mesh. The physical mesh simply outlines the physical boundaries of the object, such as the discontinuities and material interfaces. The mathematical mesh is an assembly of 'covers' that can be overlapped and chosen freely by the user. The general features of MM may include:

- Both Finite Element Method and DDA are special cases of MM
- Large displacement and large deformation
- Both dynamic and static problems can be readily handled in the same way
- The burden of generating complex model geometry is considerably reduced
- The improved block kinematics based on the entrance theory ensures proper simulations of discontinuities
- The simplex integration gives analytical solution

The method may provide better solutions for the problems involving complex geometry, stress concentration, fracture propagation, multi-phase bodies and multi-

body systems. The potential applications include reservoir compaction, hydraulic fracturing, tunnels in jointed rock mass, slope stability, structures under earthquake loading, seepage of dam foundation and coupled thermo-mechanical study of nuclear waste disposal in rock caverns.

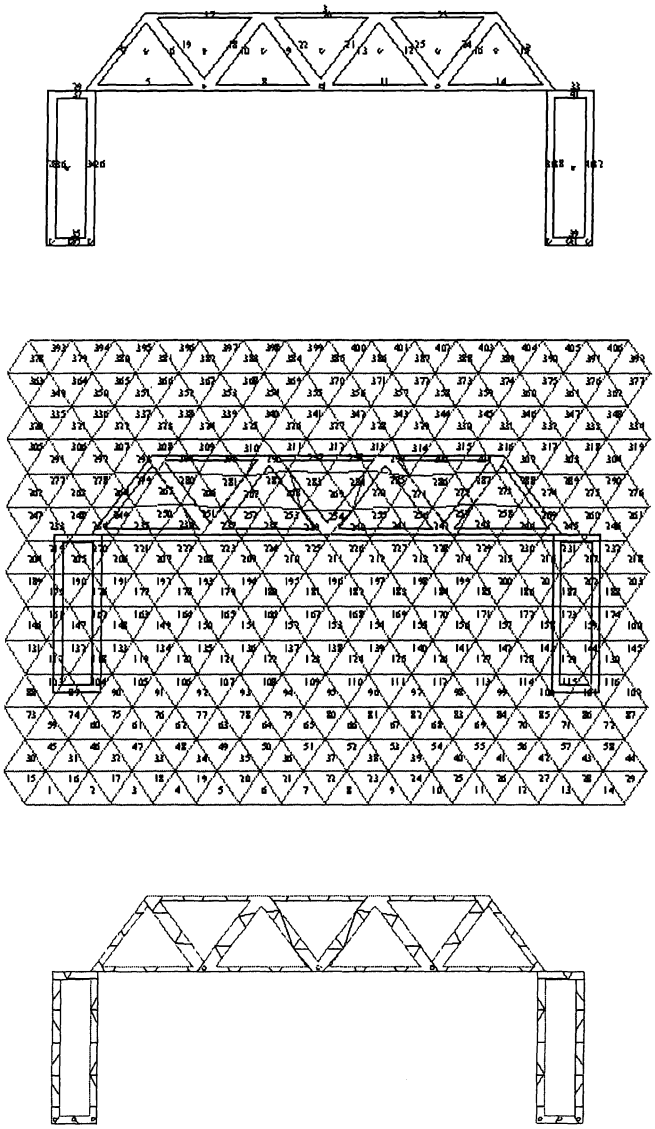

Figure 1. Spatial discretization.

An example is presented here showing some of the abilities of the manifold method. A dynamic simulation of a simply supported beam is carried out. Figure 1 shows the steps in the spatial discretization process. The top figure presents the physical mesh consisting of three continuous "blocks". Triangular elements form the mathematical mesh as shown in the middle figure. Finally, the bottom picture shows the resulting manifold mesh.

The failure of the structure is shown in Figure 2. Large deformation of the joints, blocks and the continuous materials are seen.

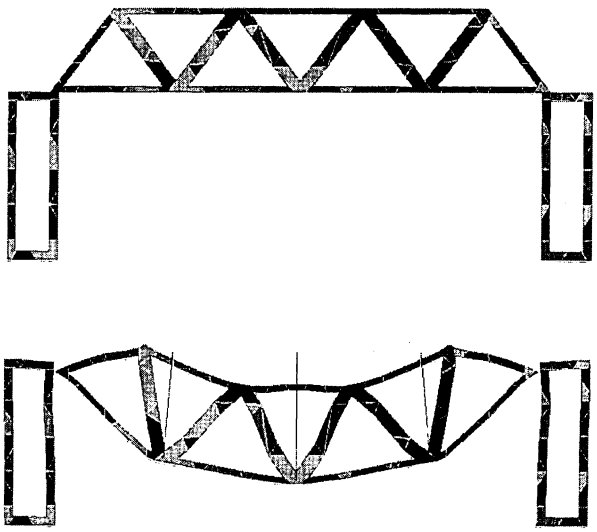

Figure 2. Failure of structure.

Hydraulic Fracturing

The 2D manifold code by Shi handles multi-body interaction of elastic blocks. The code to be developed will include

- Fluid flow between and inside rock blocks
- Discrete crack propagation (mixed mode)
- Fluid flow in propagating crack

Biot's poro-elastic equations governs the deformation and consolidation of the porous rock, while the Navier Stoke equations will be used to model the viscous fracture flow. For the Navier Stokes model, the basic DOFs are pressure and velocities p, v_x, v_y; while for the poro-elastic model they are pressure and displacements p, u, v.

Linear elastic behaviour of the rock matrix will be combined with linear elastic fracture mechanics. High order displacement functions will be adopted ensuring accurate evaluation of stress singularity at the crack tip leading to correct prediction of onset of crack propagation. A special numerical technique of splitting the element, in which the crack tip lies, facilities precise locating of the crack tip in the course of crack propagation.

For the first stage, visualisation of the results will be done by the simple post-processing built-in in the original manifold code. The output from this analysis will be distribution of fracture width and height, and fluid pressure in the fracture. Stresses and deformations are of interest for the intact rock mass.

We also firmly believe that the manifold code has a potential in prediction of sand production as the process of detachment of blocks of arbitrary size and pattern (depends on the discretization) may be modelled.

References

[1] Høiseth, H., Lu, M. and Svanø, G., 1998, Computational mechanics in civil engineering (CMC). Proceedings of NSCM-11.

[2] Lu, M. and Bostrøm, B. 1999. CMC - Computational mechanics in civil engineering -Investigation of capacity of existing computer programs for simulating crack propagation. SINTEF report STF22 A99105. http://www.sintef.no/units/civil/projects/cmc/index.htm.

[3] Shi, G. H. 1996. Manifold method. Proceedings of the first international forum on discontinuous deformation analysis (DDA) and simulation of discontinuous media. pp. 52-204.

[4] Shi, G. H. 1993. Block system modelling by discontinuous deformation analysis (Topics in Engineering). Southampton UK and Boston USA.

Numerical Scheme of a Coupled FE-IC Technique for Simulating Sharp fluid Interface in Porous Medium

N. H. Sharif, N-E Wiberg,
Department of Structural Mechanics, Chalmers University of Technology
Sven Hultins gata 8, S-412 96 Gothenburg, Sweden
e-mail: nahidh@sm.chalmers.se

Keywords: ***level set method, free surface, finite element method, porous medium***

Abstract:
We present a numerical procedure for solving a coupled system of FE-equations. A modified version of the level set equation utilizing a technique from the method of vanishing viscosity is developed and solved together with the Navier-Stokes equation for flow in porous medium. The discretized-coupled system is solved over a fixed mesh domain. The Streamline/Upwind technique is used to stabilize the solved-coupled system of FE-equation on a triangulated flow domain. Examples on the application of the technique for evolving sharp interface under a steady-state seepage flow in earth fill dam are demonstrated.

Introduction:
Recently, the Interface Capturing Technique (ICT) has been developed and used in many areas where motions of interfaces are studied [1,8]. The main idea in using this technique in capturing sharp interfaces is to avoid the sequences of remeshing the flow domain and to use the one-phase PDE equation to model two-phase flow [4,5]. These reductions in the number of the needed computation effort provide the technique with simple tools to relate an unbounded number of phase dependent variables to the interface motion and its position. The ICT is constructed on the base of adding one extra variable and one extra PDE of the hamiltonian-Jacobi type to the governing flow equation [8]. The PDE equation is simply derived from the definition of the location of the interface. The location of the interface is defined by the zero level set. Problems with sharp interface usually involve discontinuous initial profile at the interface or in the vicinity of the interface. The discontinuity characteristic gives arise to numerical instability and reduce the accuracy of the solution for the final location of the interface. If the dependent phase variables are extremely different, the coefficients of the produced element matrix exhibit large jumps, which conserves strong discontinuous characteristics on the interface. However, a lot of works has been done towards simulating one phase flow with an external interface (Free surface). This classical technique based on the fact that the significant difference between the phase dependent variables make use to neglect the effect of the weaker represented phase e.g. air- water system. But it still to find the unknown location of the external free surface. Hence a modification of the mesh during each iteration and time steps is required. We refer to [2,10] for the application of moving mesh technique.

The main issue in this study is to develop a technique that can handle moving boundary problems with less computation efforts and to produce accurate sharp interface on a fixed mesh domain. Recently we have simulated 2D and 3D steady

seepage flow problems in Rock-fill dams by utilizing the ICT [6,7]. The Interface Capturing technique (ICT) has shown powerful tools to model unbounded number of phases. Furthermore, free boundary problems can simply extend from one-dimensional to two- and three-dimensional flow problems that accompanied with complicated geometry. However, using technique derived from the level set method stipulate a very special numerical scheme and solution algorithm. Hence, we have addressed in our recently work a special iterative solver to avoid any numerical instability. The main idea is to normalize the solution of the front by using an artificial time step then to solve the blocked system in a staggered way. Fortunately, the algorithm produced a stable and accurate solution, at the same time it is required definitely large number of iterations and time steps.

In this article we have investigated a new solution spectrum. A numerical scheme for a coupled system of the Navier-Stokes equations and the advection equation is formulated. The scheme implies the regularization of the advection equation:

$$\phi_t + \boldsymbol{u} \cdot \nabla \phi = 0. \qquad \text{in } \Re^n \times t \in (0, T) \qquad (1)$$

Our approach was to consider the approximation of the Hamilton-Jacobi PDE for ε>0:

$$\phi_t^{\varepsilon} + \boldsymbol{u} \cdot \nabla \phi - \varepsilon \Delta \phi^{\varepsilon} = 0. \qquad \text{in } \Re^n \times t \in (0, T) \qquad (2)$$

The idea is that Eq. (1) involves a fully nonlinear first – order PDE, while (2) is an initial – value problem for a quasilinear parabolic PDE, which turns out to have a smooth solution. The term $\varepsilon\Delta$ in Eq. (2) is regularizing the Hamilton-Jacobi type PDE of the advection equation. Then it is proved and supposed that, where $\varepsilon \to 0$ the solution of the level set function ϕ^{ε} of Eq. (2) will converge to some sort of solution of Eq. (1). This technique is the method of vanishing viscosity. We refer furthermore to [3] for more details on the existence and the uniqueness and the motivation for the definition of the viscosity solution. The algorithm adopted here is to solve Eq. (2) for steady state together with the time independent Navier-Stokes equation and the compressibility constraint. The SUPG-type weighting function permits the usage of the same interpolation function over all the unknowns and provides reasonable accuracy to the solution [9]. The coupled FE system becomes:

$$\begin{pmatrix} 2\mathbf{K}_{ii}+\mathbf{K}_{jj}+\mathbf{B}_i(u_i)+\mathbf{K}_{ij}+\mathbf{A}_i(u_i) & -\mathbf{C}_i & \mathbf{0} \\ -\mathbf{C}_i^T+\mathbf{L}_i & \mathbf{W}_i & \mathbf{0} \\ \mathbf{0} & \mathbf{0} & \mathbf{D}_i(u_i)+\sum\mathbf{Y}_i \end{pmatrix} \begin{pmatrix} \tilde{\mathbf{u}}_i \\ \tilde{\mathbf{p}} \\ \tilde{\boldsymbol{\Phi}} \end{pmatrix} = \begin{pmatrix} \mathbf{F}_i \\ \mathbf{0} \\ \mathbf{0} \end{pmatrix} \qquad (3)$$

The system is unsymmetrical and strongly nonlinear and it has to be solved iteratively by a coupled solver. We notice that the regularization is changed adaptively through the iterative solution. Hence, the term $\varepsilon\Delta$ is turned to be very small in effect when the solution is converged.

2D Test problem: The numerical example use to test the performance of the FE-solution is shown in Fig. 1. The dimension of the dam and the hydrostatic water levels applied at upstream and downstream boundaries are specified in meter. The flow

domain is homogenous with isotropic characteristics. No heterogeneous feature is

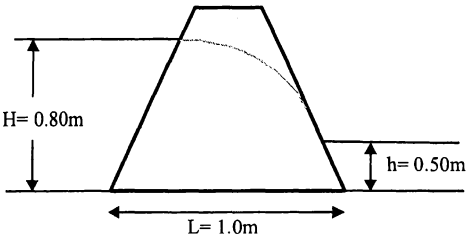

assumed.

Fig. 1. free surface flow problem in earth-fill dam with sloping sides

The solution procedure is shown in the flow chart of Fig. 2

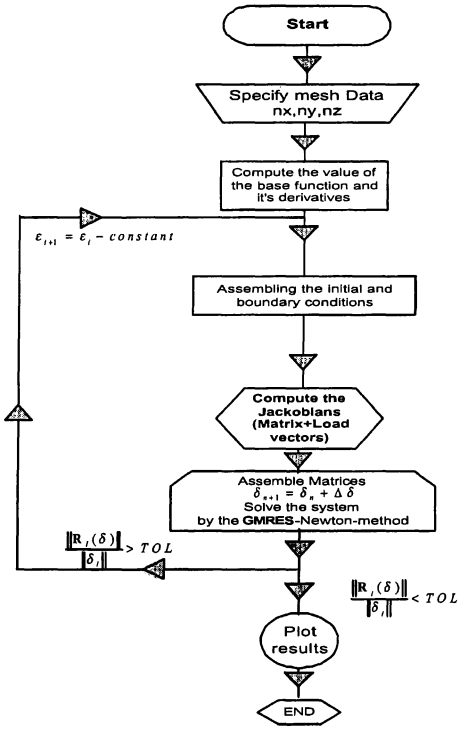

Fig. 2. Flow chart of the solution algorithm

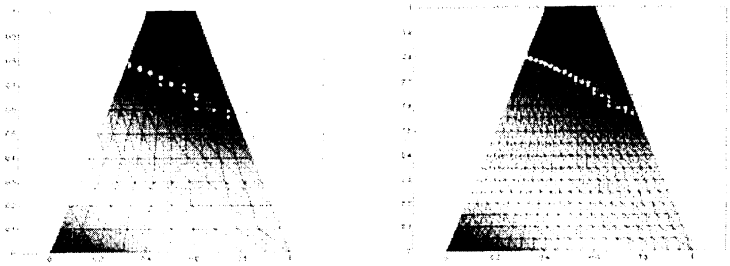

Fig. 3. FE-IC solutions for the pressure distribution, the velocity field, the interface with the zero level set

References:

[1] J. A. Sethian, Level Set Methods, Evolving Interface in Geometry, Fluid Mechanics, Computer Vision, and Material Science, Cambridge University Press (1996).

[2] KY Chung, N. Kikuchi, "Adaptive methods to solve free boundary problems of flow through porous media, *Int. Jour. Num. Analyt. Meth. Geomech.* Vol. 11, 17-31, (1987)".

[3] L. C. Evans, "Partial Differential Equations", American Mathematical Socity, Vol. 19, (1998).

[4] M. Sussman, P. Smareka and S. Osher, "A Level Set Approach for Computing Incompressible Two-Phase Flows", *J. Comp. Phys.,* 114, 146-168, (1994).

[5] M. Sussman, E. Fatemi, P. Smareka and S. Osher, "A Improved Level Set Method for Incompressible Two-Phase Flows", *J. Computers and Fluids*, 212-223 (1996).

[6] N. H. Sharif, N.-E. Wiberg, "Free-Surface Flow Predictions by an Interface Capturing FE-Technique" to appear in the International Journal for Computational Civil and Structural Engineering (IJCCSE).

[7] N. H. Sharif, N.-E. Wiberg, "Free Surface Flow through Rock-Fill Dams Analyzed by FEM with Level Set Approach" to appear in Journal of Computer Modeling and Simulation in Engineering (C.M.S.E).

[8] T. J. Barth and J. A. Sethian, "Numerical Schemes for the Hamilton-Jacobi and Level Set Equations on Triangulated Domains", *J. Comp. Phys.,* 145, 1-40, (1998)

[9] T. Tezduyar, S. Aliabadi, M. Behr, "Enhanced-Discretization Interface-Capturing Technique (EDICT) for Computation of Unsteady Flows with Interfaces", *Comp. Methods Appl. Mech. Eng.*, 155, pp. 235-248, (1998).

[10] Y. H. Tomas, "Numerical Solution to Free Boundary Problems", in *Acta Numerica* 1995, Cambridge University Press, pp. 335-415 (1995).

Modeling large strain thermo-mechanical behavior of semi-crystalline polymers

Bo Häggblad [a,b] and Göran Paulsson [a,b]
[a]Dept. of Solid Mechanics, Royal Institute of Technology, S-100 44 Stockholm, Sweden
[b]ABB Corporate Research, S-721 78 Västerås, Sweden

1. Introduction

We formulate and verify a thermodynamically admissible constitutive model for a class of common semi-crystalline polymers, such as cross-linked polyethylene. The basic constituent in many semi-crystalline polymers can be considered as a two-phase composite inclusion, consisting of a crystalline lamella ("crystallites") and an associated amorphous layer. Recently, several researchers have published results on constitutive modeling of the elastic/viscous/plastic behavior of rubberlike materials with fillers. It is our finding that many of these theories are applicable to semi-crystalline polymers, where the crystallites in some respects are acting like fillers in the amorphous phase. Our approach in this work is based on the thoughts expressed in the papers by Lion[1,2,3,6], Govindjee & Reese[4,5]and Miehe & Keck[7], but we enlarge the theoretical framework to cope with physical aging which might be important for certain semi-crystalline polymers.

2. Mechanical properties and their micro-mechanical origin

In order to capture the material properties several quasi-static and dynamic experiments have been done. These include creep, relaxation and quasi-static or dynamic cycling experiments. We give a short review of experimental findings and discuss their possible explanations based on the physics of molecular networks. In the procedure for identification of the material parameters we exploit the characteristic branch structure of our assumed constitutive model and perform separate determination of the parameters for each constitutive branch.

3. Modeling of constitutive properties

Locally (e.g. in a quadrature point), several constitutive branches are supposed to act in parallel, modeling an equilibrium *ground-stress* response together with rate-dependent and rate-independent inelastic *overstress* responses. In principle a saturating damage of virgin states would be expected to act isotropically on all branches. However, experimental results indicate that this kind of damage is negligible in the strain range of interest for our class of material. Thus, we identify the following fundamentally different effects originating from different parts of the free energy:

- a dominating, large-strain elastic back-ground (equilibrium) response (Ψ_{EQ})
- a finite viscoelastic (non-equilibrium) over-stress (Ψ_v^k) governing the rate dependent creep and relaxation phenomena with viscoelastic properties that are affected by physical aging
- a small elastoplastic over-stress (Ψ_p) governing the rate-independent hysteresis phenomena of the relaxed equilibrium states
- a thermal expansion and temperature dependence of material parameters

Introducing multiplicative splittings of the deformation gradients ($\mathbf{F}_\mathrm{M}$ =mechanical stress producing part, $\mathbf{F}_\theta$ =thermal part, N = number of viscous branches, see Fig. 1)

$$\begin{aligned}
&\mathbf{F} = \mathbf{F}_\mathrm{M}\mathbf{F}_\theta \\
&\mathbf{F}_\mathrm{M} = \mathbf{F}_{ev}^k\mathbf{F}_v^k \\
&(k = 1,\ldots,N) \\
&\mathbf{F}_\mathrm{M} = \mathbf{F}_{ep}\mathbf{F}_p
\end{aligned} \tag{1}$$

the free energy can be written

$$\begin{aligned}
\Psi &= \Psi\left(\Theta, \mathbf{C}_\mathrm{M}, \mathbf{F}_v^k, \mathbf{F}_p\right) = \Psi_{EQ}\left(\Theta, \mathbf{C}_\mathrm{M}\right) + \sum_{k=1}^{N}\Psi_v^k\left(\Theta, \mathbf{C}_{ev}^k\right) + \Psi_p\left(\Theta, \mathbf{C}_{ep}\right) + \varsigma(\Theta) \\
&= \Psi_{EQ}\left(\Theta, \mathbf{C}_\mathrm{M}\right) + \sum_{k=1}^{N}\Psi_v^k\left(\Theta, \mathbf{F}_v^{k\,-\mathrm{T}}\mathbf{C}_\mathrm{M}\mathbf{F}_v^{k\,-1}\right) + \Psi_p\left(\Theta, \mathbf{F}_p^{-\mathrm{T}}\mathbf{C}_\mathrm{M}\mathbf{F}_p^{-1}\right) + \varsigma(\Theta)
\end{aligned} \tag{2}$$

where $\mathbf{C}_\mathrm{M}$, $\mathbf{C}_{ev}^k$ and $\mathbf{C}_{ep}$ are right Cauchy-Green deformation tensors.

The chosen internal (non-equilibrium) variables are measures of different kinds of internal inelastic deformations (not stresses !), modeling nonlinear viscous ($\mathbf{F}_v^k$) and plastic ($\mathbf{F}_p$) effects.

As the general tool in the formulation of the constitutive laws we use the local form of Clausius-Duhem inequality (the second law of thermodynamics) together with the argumentation of Coleman and Gurtin [8] so that the dissipation will be non-negative for arbitrary deformation processes. This has also resulted in a uniform formalism for the treatment of different phenomena and their numerical implementations.

The total Kirchhoff stress is the sum of the Kirchhoff stresses $\boldsymbol{\tau}_{EQ}, \boldsymbol{\tau}_{ev}^k$ and $\boldsymbol{\tau}_{ep}$ for the ground- and over-stress responses, respectively. If these are expressed in the local principal axis systems of each branch (isotropy assumed) we obtain:

$$\begin{aligned}
\boldsymbol{\tau}_{EQ} &= 2\frac{\partial \Psi_{EQ}}{\partial \mathbf{b}_{\mathrm{M}}}\mathbf{b}_{\mathrm{M}} = \sum_{r=1}^{3}\tau_r^{EQ}\mathbf{n}_r^{EQ}\otimes\mathbf{n}_r^{EQ} = \sum_{r=1}^{3}\frac{\partial \Psi_{EQ}}{\partial \lambda_r^{EQ}}\lambda_r^{EQ}\mathbf{n}_r^{EQ}\otimes\mathbf{n}_r^{EQ} \\
\boldsymbol{\tau}_{ev}^k &= 2\frac{\partial \Psi_v^k}{\partial \mathbf{b}_{ev}^k}\mathbf{b}_{ev}^k = \sum_{r=1}^{3}\tau_r^{ev,k}\mathbf{n}_r^{ev,k}\otimes\mathbf{n}_r^{ev,k} = \sum_{r=1}^{3}\frac{\partial \Psi_v^k}{\partial \lambda_r^{ev,k}}\lambda_r^{ev,k}\mathbf{n}_r^{ev,k}\otimes\mathbf{n}_r^{ev,k} \\
\boldsymbol{\tau}_{ep} &= 2\frac{\partial \Psi_p}{\partial \mathbf{b}_{ep}}\mathbf{b}_{ep} = \sum_{r=1}^{3}\tau_r^{ep}\mathbf{n}_r^{ep}\otimes\mathbf{n}_r^{ep} = \sum_{r=1}^{3}\frac{\partial \Psi_p}{\partial \lambda_r^{ep}}\lambda_r^{ep}\mathbf{n}_r^{ep}\otimes\mathbf{n}_r^{ep}
\end{aligned} \tag{3}$$

where $\mathbf{b}_{\mathrm{M}}, \mathbf{b}_{ev}^k$ and $\mathbf{b}_{ep}$ are left Cauchy-Green deformation tensors.

In our implementation the hyperelastic energy functions Ψ_{EQ}, Ψ_v^k and Ψ_p are of Ogden-type with separable volumetric and isochoric parts.

The evolution laws for the inelastic response quantities are obtained as

$$\begin{aligned}
-\frac{1}{2}\mathbf{F}\frac{d}{dt}\left(\left[\mathbf{C}_v^k\right]^{-1}\right)\mathbf{F}^T\left[\mathbf{b}_{ev}^k\right]^{-1} &= -\frac{1}{2}\mathsf{L}_v\left(\mathbf{b}_{ev}^k\right)\left[\mathbf{b}_{ev}^k\right]^{-1} = \left[\mathbb{V}_v^k\right]^{-1} : \boldsymbol{\tau}_{ev}^k \\
-\frac{1}{2}\mathbf{F}\frac{d}{dt}\left(\left[\mathbf{C}_p\right]^{-1}\right)\mathbf{F}^T\left[\mathbf{b}_{ep}\right]^{-1} &= -\frac{1}{2}\mathsf{L}_v\left(\mathbf{b}_{ep}\right)\left[\mathbf{b}_{ep}\right]^{-1} = \left[\mathbb{V}_p\right]^{-1} : \boldsymbol{\tau}_{ep}
\end{aligned} \tag{4}$$

Here $\mathsf{L}_v(\ )$ denotes a Lie derivative and $\left[\mathbb{V}_v^k\right]^{-1}$ and $\left[\mathbb{V}_p\right]^{-1}$ are chosen to be positive definite rank-four constitutive tensors, in general dependent on the deformation. Both large deformations and large deviations from thermodynamic equilibrium are accounted for in the relations (4). Assuming that the volumetric behavior is totally elastic we can write down linear, isotropic versions of these constitutive tensors as

$$\begin{aligned}
\left[\mathbb{V}_v^k\right]^{-1} &= \frac{1}{2\eta_v^k}\left[\mathbf{I}-\frac{1}{3}\mathbf{1}\otimes\mathbf{1}\right] \\
\left[\mathbb{V}_p\right]^{-1} &= \frac{1}{2\eta_p}\left[\mathbf{I}-\frac{1}{3}\mathbf{1}\otimes\mathbf{1}\right]
\end{aligned} \tag{5}$$

The viscosities η_v^k are likely to depend on the total deformation $\mathbf{b}_{\mathrm{M}}$, the inelastic deformation $\mathbf{b}_v^k$ in each branch, the temperature Θ and the physical age of the material t_{age} (i.e the time from the cooling at the end of the manufacturing process):

$$\eta_v^k = \eta_v^k\left(\mathbf{b}_{\mathrm{M}}, \mathbf{b}_v^k, \Theta, t_{age}\right) \tag{6}$$

The free volume of the material can be used as a measure of intermolecular space or fluidity which influences the viscosity, see e.g. [10]. This can be taken into consideration in (6) by introducing a constitutive model for the changes in the free volume in terms of changes of e.g. the volumetric part of the total deformation (det($\mathbf{b}_{\mathrm{M}}$)).

For the plastic parameter η_p we have

$$\eta_p = \eta_p(\mathbf{b}_M, \dot{z}) = \eta_p^0(\mathbf{b}_M)/\dot{z} \tag{7}$$

with the rate of the generalized arc-length z given by e.g.

$$\dot{z} = \sqrt{\frac{2}{3}}\left|\frac{1}{2} ln[\dot{\mathbf{C}}_M]\right| \tag{8}$$

in terms of the total deformation.
Although $(4)_2$ is formally posed as a time history evolution problem (like $(4)_1$), the evolution of the plastic deformation $\mathbf{C}_p$ is rate-independent without a yield surface according to a Valanis-type, endochronic theory [9].

4. Algorithmic implementation

In the FE-implementation we try to fully exploit the branch structure of our constitutive model. In an efficient time integration scheme, where full Newton iterations are used for finding the FE-solution at each incremental step, consistent (algorithmic) element stiffness matrices and internal element forces must be computed in each global iteration loop. Hence, in each quadrature point of a typical element the nonlinear inelastic evolution system (4) need to be solved to obtain element strains and stresses in each branch. To do this, we first perform separate spectral decompositions for the constitutive branches based on initial elastic trial states (Fig. 2). Then the evolution equations are solved on principal axis form in a local loop with an elastic predictor step followed by an exponential map with full Newton iterative corrector steps, analogous to plasticity algorithms that are incrementally objective. Also the consistent element stiffness matrix is built up by adding contributions from different branches that are computed by using the spectral decompositions of corresponding initial elastic trial states, see Fig. 2. Detailed expressions that show the structure of the stiffness contributions will be presented.

5. Illustrations

Comparisons between computed and measured results will be presented.

6. References

[1] A. Lion, A constitutive model for carbon black filled rubber :experimental investigations and mathematical representation, Continuum Mech. Thermodyn. 6 (1996) 153-168

[2] A. Lion, A physically based method to represent the thermo-mechanical behavior of elastomers, Acta Mechanica 123 (1997) 1-25

[3] A. Lion, On the large deformation behavior of reinforced rubber at different temperatures, J.Mech.Phys:Solids, Vol. 45, No 11/12 (1997) 1805-1834

[4] S. Govindjee and S. Reese, A presentation and comparison of two large deformation viscoelastic models, J. Eng. Materials and Technology Vol. 119 (1997) 251-255

[5] S.Reese and S. Govindjee, A theory of finite viscoelasticity and numerical aspects, Int.J.Solids Structures, Vol. 35, Nos 26-27 (1998) 3455-3482

[6] A.Lion, Thixotropic behavior of rubber under dynamic loading histories: experiments and theory, J.Mech.Phys.Solids, Vol. 46 No. 5 (1998) 895-930

[7] C. Miehe and J. Keck, Superimposed finite elastic-viscoelastic-plastoelastic stress response with damage in filled rubbery polymers. experiments, modeling and algorithmic implementation , J. Mech. Phys. Solids, 48 (2000) 323-365

[8] B.D. Coleman and M.E. Gurtin, Thermodynamics with internal state variables, J. Chemistry and Physics 47 (1967) 597-613

[9] K.C. Valanis, A theory viscoplasticity without a yield surface, Arch. Mech. 23 4 (1971) 517-533

[10] U.L Giancarlo and W.G. Knauss, Free volume theory and nonlinear thermoviscoelasticity, Polym. Eng. Sci. 32 (1992) 542-557

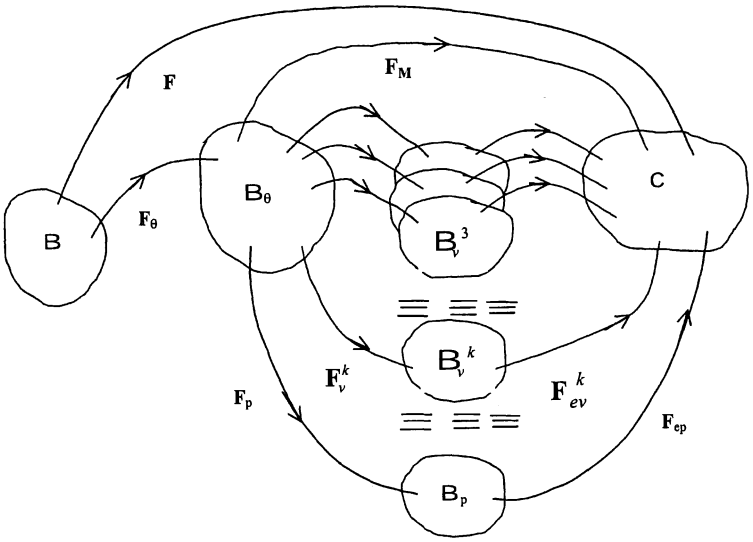

Figure 1 Superposition of branches with multiple intermediate configurations

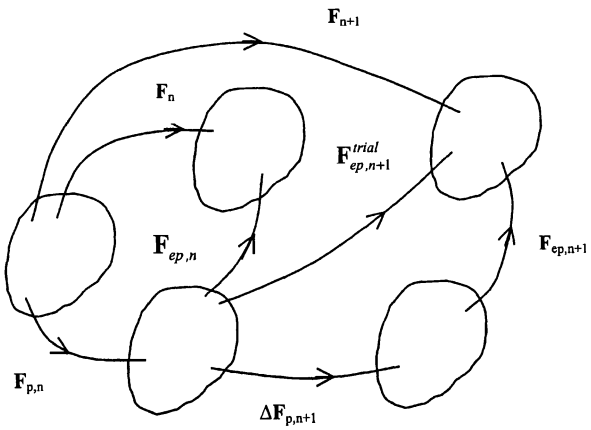

Figure 2. Trial elastic deformation at increments n and n+1

State Space Representation of Bridge Deck Aeroelasticity

J.R. Høgsberg, J. Krabbenhøft and S. Krenk

Department of Structural Engineering and Materials
Technical University of Denmark, DK-2800 Lyngby, Denmark

Abstract. A state space representation of the aeroelastic properties of bridge decks is described. In the state space representation the aeroelastic forces appear as instantaneous added stifffness, damping and mass, plus delayed effects represented by terms with exponential memory. Good accuracy is obtained by 2-3 memory terms, permitting a compact representation in frequency as well as in the time domain.

1. Introduction

A Bridge deck is described through a vertical displacement and a rotation. The corresponding aerodynamic forces are traditionally represented using flutter derivatives, originally introduced by Scanlan & Tomko (1971),

$$\begin{aligned} \frac{F_L}{\frac{1}{2}\rho U^2 B} &= K H_1^* \frac{\dot{x}}{U} + K H_2^* \frac{B\dot{\theta}}{U} + K^2 H_3^* \theta + K^2 H_4^* \frac{x}{B} \\ \frac{F_M}{\frac{1}{2}\rho U^2 B^2} &= K A_1^* \frac{\dot{x}}{U} + K A_2^* \frac{B\dot{\theta}}{U} + K^2 A_3^* \theta + K^2 A_4^* \frac{x}{B} \end{aligned} \tag{1}$$

with the non-dimensional angular frequency $K = \omega B/U$. In the following the aerodynamic forces appear as instantaneous added stiffness, damping and mass, and a memory term,

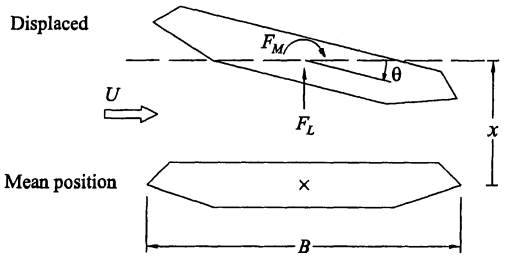

Figure 1. Bridge deck with lift F_L and moment F_M.

which in the time domain is introduced as 2-3 decaying exponentials. This representation leads to a compact matrix formulation which is compared with the analytical results of an airfoil.

2. Systems with delayed effects

The equation of motion for a bridge deck is in the time domain introduced as

$$\mathbf{M}\ddot{\mathbf{u}} + \mathbf{C}\dot{\mathbf{u}} + \mathbf{K}\mathbf{u} = \int_{0-}^{\infty} \mathbf{h}(\tau)\mathbf{u}(t-\tau)\,d\tau + \mathbf{f}_{ext}(t) \tag{2}$$

where $\mathbf{f}_{ext}(t)$ is an arbitrary external force, and the kernel of the convolution integral in general contains the following terms

$$\mathbf{h}(\tau) = -\mathbf{M}_a\ddot{\delta}(\tau) - \mathbf{C}_a\dot{\delta}(\tau) - \mathbf{K}_a\delta(\tau) + \mathbf{h}_m(\tau) \tag{3}$$

Thus, the forces acting on the bridge deck appear as instantaneous aerodynamic mass, damping and stiffness, and the memory of the system, $\mathbf{h}_m(\tau)$. Substituting $\mathbf{h}(\tau)$ into the right hand side of (2) yields

$$(\mathbf{M}-\mathbf{M}_a)\ddot{\mathbf{u}} + (\mathbf{C}-\mathbf{C}_a)\dot{\mathbf{u}} + (\mathbf{K}-\mathbf{K}_a)\mathbf{u} = \int_{0}^{\infty} \mathbf{h}_m\mathbf{u}(t-\tau)d\tau \tag{4}$$

where the instantaneous effects are moved to the left hand side of the equation of motion. These effects are constant in time leaving only the integral on the right hand side of (4) describing the memory of the system. A frequency representation of the aerodynamic forces is given as

$$\mathbf{F} = \mathbf{H}(\omega)\,\mathbf{U} \tag{5}$$

with the complex frequency dependent force matrix

$$\mathbf{H}(\omega) = \int_{0-}^{\infty} \mathbf{h}(\tau)\exp(-i\omega\tau)\,d\tau \tag{6}$$

being the Fourier transform of $\mathbf{h}(\tau)$.

$$\mathbf{H}(\omega) = [\omega^2\mathbf{M}_a - \mathbf{K}_a] - i\omega\mathbf{C}_a + \mathbf{H}_m(\omega) \tag{7}$$

The flutter derivatives are expressed directly through the elements in $\mathbf{H}$ revealing that only 4 flutter derivatives are fully independent.

3. State space representation of delayed forces

The memory part $\mathbf{h}_m(t)$ is represented by the force components

$$\mathbf{f}(t) = \textstyle\sum_j \mathbf{f}_j(t) \quad , \quad \mathbf{f}_j(t) = \int_0^\infty \mathbf{h}_j(\tau)\,\mathbf{u}(t-\tau)\,d\tau \tag{8}$$

with the exponential memories

$$\mathbf{h}_j(\tau) = \mathbf{a}_j\exp(-\gamma_j\tau) \quad , \quad \mathbf{H}_j(\omega) = \frac{1}{\gamma_j + i\omega}\mathbf{a}_j \tag{9}$$

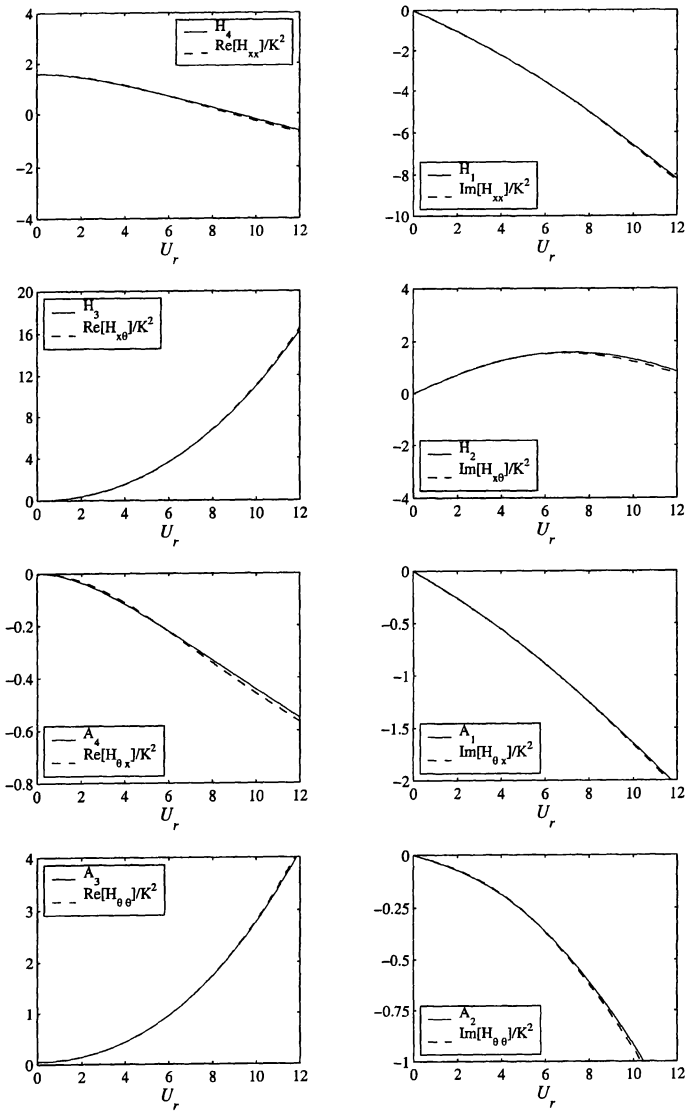

FIGURE 2. Aerodynamic derivatives of an airfoil

Differentiation of (8) with respect to τ and integration by parts introduces an alternative formulation by differential equations in the time domain

$$\dot{\mathbf{f}}_j(t) + \gamma_j \mathbf{f}_j(t) = \mathbf{a}_j \mathbf{u}(t) \quad , \quad j = 1, \cdots \tag{10}$$

The state space formulation in terms of the *augmented state space vector*

$$\mathbf{z}(t) = [\mathbf{u}(t), \dot{\mathbf{u}}(t), \mathbf{f}_1(t), \cdots, \mathbf{f}_n(t)]^T \tag{11}$$

leads to a compact representation of the equation of motion (4).

4. The airfoil as example

The expected accuracy of the state space representation can be estimated by considering the case of an airfoil, for which the analytical solution was obtained by Theodorsen (1935),

$$\begin{bmatrix} F_L^* \\ F_M^* \end{bmatrix} = \tfrac{1}{2}\pi \left\{ \begin{bmatrix} K^2 & iK \\ 0 & \frac{1}{32}K^2 - i\frac{1}{4}K \end{bmatrix} + \Big(F + iG\Big) \begin{bmatrix} -i4K & 4 + iK \\ -iK & 1 + i\frac{1}{4}K \end{bmatrix} \right\} \begin{bmatrix} x* \\ \theta* \end{bmatrix} \tag{12}$$

with the Theodorsen function $F(\frac{1}{2}K) + iG(\frac{1}{2}K)$ and

$$F = \frac{J_1(J_1 + Y_0) + Y_1(Y_1 - J_0)}{(J_1 + Y_0)^2 + (Y_1 - J_0)^2} \quad , \quad G = \frac{J_1 J_0 + Y_1 Y_0}{(J_1 + Y_0)^2 + (Y_1 - J_0)^2} \tag{13}$$

For an airfoil the components of the frequency dependent force matrix, $\mathbf{H}(K)$, are compared with the exact expressions in Fig. 2. The memory part is represented with 2 lag states with coefficients determined by Eversman & Tewari (1991).

5. Conclusions

State space formulation of the aerodynamic derivatives of bridge decks leads to a simple and compact representation of the delayed effects due to the wind field. It secures causality and has the following computational advantages: reduces flutter analysis to a linear eigenvalue problem, permits time integration by simple one-step algorithms, and is compatible with computational bridge models.

Acknowledgment. This project has been supported by the Danish Technical Research Council.

6. References

Eversman, W. and Tewari, A., Modified exponential series for the Theodorsen function, *Journal of Aircraft*, Vol. 28, pp. 553-557, 1991.

Scanlan, R.H. and Tomko, J.J., Airfoil and Bridge Deck Flutter Derivatives, *Journal of the Engineering Mechanics Division*, Vol. 6, pp. 1717-1737, 1971.

Theordorsen, T., General theory of aerodynamic instability and the mechanism of flutter, NACA Report 496, 1935.

A parallel Rayleigh-Ritz Finite Element Method for Unit Cell Problems.

O. Kristensson†
N. J. Sørensen†
B. S. Andersen††
†Division of Mechanics, Lund University, Sweden
††UNI-C, Danish Computing Centre for Research and Education,
The Technical University of Denmark, Lyngby, Denmark

Summary
A general parallel FE-approach for finite strain elasto-plasticity based on a structural decomposition algorithm with a direct solution strategy for the interface equation system is discussed. The performance of the developed program is demonstrated for plane strain cases. The results show that a very good speed-up is obtained for large scale problems where memory as well as CPU-time is demanding. An implementation of unit cell boundary conditions is suggested and it demonstrates the flexibility of the current strategy.

Finite Element Rayleigh-Ritz Method
The incremental form of the principle of virtual work can be discretized, using the finite element formulation, to the well known form

$$\boldsymbol{A}\boldsymbol{d} = \boldsymbol{b} + \boldsymbol{e} \tag{1}$$

Multiplication with a virtual displacement rate $\delta\boldsymbol{d}$ gives

$$\delta\boldsymbol{d}^T\boldsymbol{A}\boldsymbol{d} = \delta\boldsymbol{d}^T\boldsymbol{b} + \delta\boldsymbol{d}^T\boldsymbol{e} \tag{2}$$

where $\boldsymbol{d}$ is the displacement vector, $\boldsymbol{A}$ is the incremental stiffness matrix, $\boldsymbol{b}$ is the external force vector, $\boldsymbol{e}$ is the equilibrium force vector and δ denotes virtual entities. Since the formulation is incrementally linear a Rayleigh-Ritz method can be used.

The Rayleigh-Ritz method approximates the unknown field, $\boldsymbol{d}$, by a sum consisting of terms of an amplitude parameter multiplied with a corresponding trial function. When using Rayleigh-Ritz in conjunction with the finite element method a number of nodes, here denoted R-nodes, are selected and their displacement rates serves as amplitude parameters δ_i. For each of the amplitude parameters prescribed to equal unity one at a time while the rest are prescribed zero the solution of the FE equation system, the displacement rate vector $\boldsymbol{v}_i$, is taken to be the trial function corresponding to the non-zero amplitude parameter [3]. When calculating the trial functions the equation system is solved several times with different right hand sides. This makes use of a direct method suitable when implementing this step. Inserting the approximated displacement rate field,

$$\boldsymbol{d} = \sum_{i=1}^{NRD} \boldsymbol{v}_i\delta_i \tag{3}$$

where NRD denotes the R-nodes number of degrees of freedom, in (2) leads to a mixed FE Rayleigh-Ritz formulation with the R-node displacement rates as the only unknowns

$$\textstyle\sum_{j=1}^{NRD} \boldsymbol{v}_i{}^T\boldsymbol{A}\boldsymbol{v}_j\delta_j = \boldsymbol{v}_i{}^T\boldsymbol{b} + \boldsymbol{v}_i{}^T\boldsymbol{e} \quad i = 1, 2, \ldots, NRD \tag{4}$$

It must be understood that the reduced problem can be viewed as a "super-element" equation with surface dofs only.

Parallelisation Strategy and parallel Performance
The parallelization strategy in this work is to decompose the total structure of the problem into p non-overlapping substructures, Figure 1. The points belonging to more than one substructure define

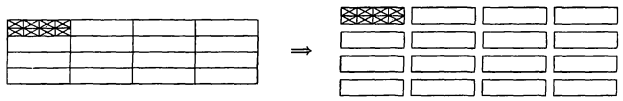

Figure 1: Planar block decomposed into p=16 substructures.

the interface. If the unknown displacement rates at the interface are determined p decoupled boundary value problems are obtained. With the interface nodes choosen as R-nodes, using the FE Rayleigh-Ritz method at substructure level, an interface equation system is obtained when mapping the local equations to the global level. The local interface equations does in fact not need to be mapped to the global level with use of a conectivity table and a parallel solver. The solution of the interface equations, the interface displacements, mapped to the substructure equations gives the p problems which can be solved in parallel. This method were used in [2].

The parallel speed-up, that means, the computer time (wall clock time) required for solution on one processor divided by the time for p-processors, $S(p) = T(1)/T(p)$, is studied for different cases. The test problem used is a planar block loaded in tension modelled by a regular FE-mesh consisting of $N_x \times N_y$ quadrilaterals ("cross-triangles") each consisting of 4 plane strain triangles, Figure 1. Three cases with different values of $\alpha = N_x/N_y$, where $\alpha = 1, 2, 4$, are considered (the number of equations are approximately constant). For $\alpha = 1$ the substructuring data is shown in Table 1 and the timings are shown in Table 2. The computing speedup is shown in Figure 2.

The headlines in the timing table have following meaning. *Init.*: Broadcasting of the initial state structural data to the processors and checking for sufficient memory allocation. *Update, create s.e.s*: Updating of the stresses, calculation of the stiffness, incremental load and out of balance force, assemblage of the substructure equation system, factorization and imposition of boundary and interface conditions. *Create i.e.s*: Calculation of the interface load and interface stiffness. *Communicate*: Broadcasting of the interface system and gathering of the interface displacement rates. *Solve i.e.s*: Solving of the interface equation system. *Solve s.e.s*: Solving of the substructure equation system. *Total*: The total time of the simulation. Figure 2 shows the speed-up relative the two processor case. The solid line

No. of processors	1	2	4	8	16	32
Elements per proc.	36864	18432	9216	4608	2304	1152
Dof per proc.	37250	18722	9410	4754	2402	1226
Bandwidth per proc.	194	97	97	49	49	25
Interface dof per proc.	0	97	97	73/121	49/73/96	37/49/61/72
Interface dof in total	0	97	193	385	573	949

Table 1: Substructuring data, $\alpha = 1$.

represents the theoretically expected linear speedup. The curves show a superlinear speedup, probably due to better memory utilization.

Unit Cell Application
The application in this work is a unit cell formulation with general periodicity conditions. This type of unit cell is often applied in micromecanical material analysis to study overall behavior given a micro-structural description. A four sided cell has been choosen in this work, see Figure 3. The boundary

No. of processors	Init.	Update, create s.e.s	Create i.e.s	Comm-unicate	Solve i.e.s	Solve s.e.s	Total
2	4.06	122.43	584.29	3.55	0.53	1.81	716.52
4	3.47	61.64	294.13	4.51	1.48	0.95	365.77
8	3.34	17.91	94.12	9.30	4.33	0.24	128.29
16	2.82	9.60	38.26	13.44	6.45	0.20	69.67
32	4.24	5.24	9.09	24.24	13.63	0.04	54.99

Table 2: Timings, $\alpha = 1$.

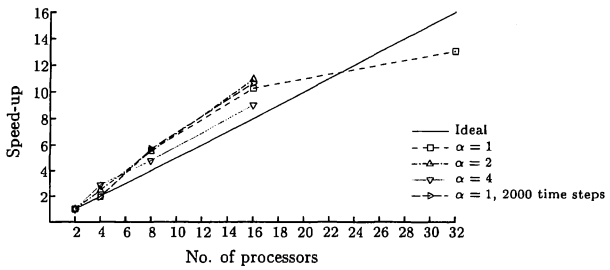

Figure 2: Speed-up for all quadrilateral ratios. (IBM SP, MPI)

condition relations for this cell are defined by the kinematical restriction, opposite sides can be expressed as a translation of the other, and the kinetic restriction, law of action-reaction [1]. The corresponding points on opposite sides are denoted a_i and b_i and the points defining the translation are denoted α_i, see Figure 3. The incremental boundary conditions are of the form,

$$\begin{aligned} \dot{\boldsymbol{u}}^{b_i} &= \dot{\boldsymbol{u}}^{a_i} + \dot{\boldsymbol{u}}^{\alpha_i} \\ \dot{\boldsymbol{T}}^{b_i} &= -\dot{\boldsymbol{T}}^{a_i} \end{aligned} \qquad i = 1, 2 \tag{5}$$

where $\dot{(\,)}$ denotes the material time derivative, $\boldsymbol{u}^\beta$ is the displacement at the point β, $\boldsymbol{T}^\beta$ is the traction at the point β and β follows the point definitions in Figure 2a.

To obtain a suitable form where to incorporate the cell relations the equations are reduced to the level where the boundary displacement rates are the only unknown variables. This reduction is performed in two steps using the FE Rayleigh-Ritz method. In the first reduction step, performed in parallel as decribed above, the interface and boundary nodes are choosen as R-nodes. The second reduction step is performed in serial. Here an assembly is necessary to encapture all couplings. However the size of this system is moderate, when the boundary nodes are R-nodes. The equations are then reduced by use of (5). The resulting equation system has as many equations as number of nodes at the boundary. Since this in many cases will be a small system compared with the global system the equation system is solved with a serial method. In this implementation the simulation is controlled by prescription of the displacement rates at the corner nodes, Figure 3a.

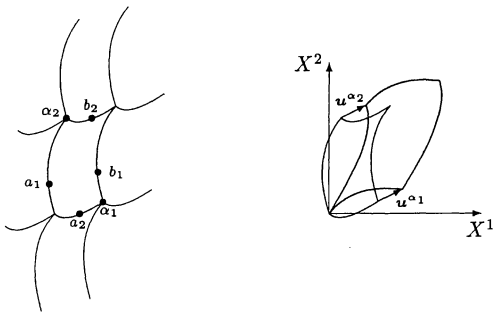

Figure 3: The four side cell a) point definitions b) before and after deformation with the corner node displacements, u^{α_1} and u^{α_2}, indicated.

References

[1] Havner K. S. (1971)
A Discrete Model for the Prediction of Subsequent Yield Surfaces in Polycrystalline Plasticity
Int. J. Solids Struct 7, 719-730

[2] Sørensen N. J., Andersen B. S. (1996)
A parallel finite element method for the analysis of crystalline solids
Comput. Methods Appl. Mech. Engrg. 132, 345-357

[3] Tvergaard V. (1976)
Buckling of elastic-plastic oval cylindrical shells under axial compression
Int. J. Solids Struct 12, 683-691

Stress-Resultant Plasticity on the Morley Element Using a Modified Ilyushin Yield Surface

A. K. Mohammed* J. Amdahl* B. Skallerud †
The Norwegian University of Science and Technology, NTNU, N-7491 Trondheim, Norway.

Abstract

A simplified stress-resultants plasticity is implemented with the geometrically nonlinear constant stress triangle of Morley. The Ilyushin yield surface is rendered a hyperellipse to avoid corner discontinuities. Explicit plasticity equations involving a solution of a single scalar equation for the plasticity multiplier are derived. Numerical examples are also presented.

1 Introduction

Perhaps one of the simple and efficient shell finite elements is the constant stress-resultant shell element commonly referred to as Morley triangle. In the present work, the geometrically non-linear constant stress triangle of Morley (1991) is implemented and extended to include material non-linearity. The element was derived in a Total Lagrangian approach from Hu-Washizu functional under Kirchhoff theory. It is valid for moderate rotations and passes the nonlinear von Kàrmàn patch test. The elastic element has been studied by Providas (1990) showing good a performance within its range.

In the plasticity formulation, stress resultants plasticity is employed. A modification is introduced in the Ilyushin yield surface such that it is rendered a hyperellipse to avoid corner discontinuities. Explicit expression for the modified yield surface is derived from handy matrix algebras, and the resulting equations provide faster computations.

The aim of this work is to present an assessment of the proposed simple plasticity model using the above mentioned simple element. In another work (see e.g. Mohammed *et al.* (2000)a), the present plasticity formulation has been implemented with other elements in the Morley family of triangles that accommodates arbitrary large rotations. The details of the plasticity formulation are referred to Mohammed *et al.* (2000) while for element formulation the reference is made to Morley (1991).

2 Element Description

The element has six nodes and twelve degrees of freedom. Namely, the three displacements at each of the corner nodes, and one rotation at each of the mid–side nodes. The local element system is defined in the rectilinear (nonorthogonal) coordinate system. In the plasticity formulation, however, the local system is referred to the Cartesian coordinates.

At the local level, the curvature tensor κ replaces the rotations so that the resulting expressions are simplified, and the local displacement (connector) vector is defined as,

$$\boldsymbol{a}^T = \begin{pmatrix} \boldsymbol{u}^T & \boldsymbol{w}^T & \boldsymbol{\kappa}^T \end{pmatrix} \tag{1}$$

where $\boldsymbol{u}$ and $\boldsymbol{w}$ are the in–plane and out–of–plane displacement vectors, respectively. By selecting quadratic functions of the triangular coordinates for both in–plane and out–of–plane displacements

*Department of Marine Structures, NTNU.
†Department of Applied Mechanics, NTNU.

(u_i, v_i, w_i), and proceeding as in Providas (1990) and Morley (1991), the symmetric membrane strain tensor can be written as,

$$\boldsymbol{\epsilon} = \boldsymbol{B}_u \boldsymbol{u} + \frac{1}{2}\boldsymbol{B}_w \boldsymbol{w} + \frac{1}{2}\boldsymbol{B}_k \boldsymbol{\kappa} \tag{2}$$

in which $\boldsymbol{B}_u$, $\boldsymbol{B}_w$, and $\boldsymbol{B}_k$, are the strain–displacement matrices.

The constitutive laws are formulated in terms of membrane forces $\boldsymbol{N}$ and bending moments $\boldsymbol{M}$ conjugate with the strains $\boldsymbol{\epsilon}$ and curvatures $\boldsymbol{\kappa}$ of the mid–surface, respectively, such that

$$\begin{Bmatrix} \delta \boldsymbol{N} \\ \delta \boldsymbol{M} \end{Bmatrix} = \begin{bmatrix} \boldsymbol{C} & \boldsymbol{X} \\ \boldsymbol{X}^T & \boldsymbol{D} \end{bmatrix} \begin{Bmatrix} \delta \boldsymbol{\epsilon} \\ \delta \boldsymbol{\kappa} \end{Bmatrix} \quad \Longleftrightarrow \quad \delta \boldsymbol{s} = \boldsymbol{C}_t \delta \boldsymbol{e} \tag{3}$$

where $\boldsymbol{C}_t$ is the standard elasto–plastic tangent modulus.

Then, the principle of virtual work provides the internal force vector $\boldsymbol{F}_{int}$ and the symmetric tangent stiffness matrix $\boldsymbol{K}_t$ as,

$$\delta W^i = A \delta \boldsymbol{e}^T \boldsymbol{s} = \delta \boldsymbol{a}^T \boldsymbol{F}_{int} \tag{4}$$

$$\delta^2 W^i = A(\delta \boldsymbol{a}^T \delta \boldsymbol{s} + \delta^2 \boldsymbol{e}^T \boldsymbol{s}) = \delta \boldsymbol{a}^T \boldsymbol{K}_t \delta \boldsymbol{a} \tag{5}$$

3 Plasticity Formulation

A simplified plasticity formulation that is presented here involves a solution of a single scalar equation for plasticty multiplier. Use of a single scalar equation was initially proposed by Ibrahimbegoviç and Frey (1992), and it based on the work by Matthies (1989). The starting point is Ilyushin yield surface in its generalized quadratic form,

$$f(\boldsymbol{s}, \boldsymbol{e}^p, \varepsilon^p) = \boldsymbol{s}^T \boldsymbol{A} \boldsymbol{s} - \left(1 + \frac{H\varepsilon^p}{\sigma_Y}\right)^2 = 0 \tag{6}$$

where σ_Y is the uni–axial yield stress, H is the hardening modulus, ε^p is an internal scalar variable controlling hardening, and $\boldsymbol{A}$ is a matrix of constant coefficients given by,

$$\boldsymbol{A} = \begin{bmatrix} \frac{1}{n_o^2}\boldsymbol{P} & \frac{\mu}{2\sqrt{3}m_o n_o}\boldsymbol{P} \\ \frac{\mu}{2\sqrt{3}m_o n_o}\boldsymbol{P} & \frac{1}{m_o^2}\boldsymbol{P} \end{bmatrix} \qquad \boldsymbol{P} = \frac{1}{2}\begin{bmatrix} 2 & -1 & 0 \\ -1 & 2 & 0 \\ 0 & 0 & 6 \end{bmatrix} \tag{7}$$

in which $\mu = \pm 1$. The surface described by (6) has corner discontinuities as a result of μ. Here, it is rendered a hyperellipse by setting μ equal to zero. This modification has an advantage that instead of two active yield surfaces, there is only one yield surface for stress update. This modified form was initially proposed by Skallerud and Haugen (1999), and it has been applied with success since then (see e.g. Mohammed *et al.* (2000) and Mohammed *et al.* (2000)). With the present modification, the resulting formulation becomes non–conservative with an error ranging between 0—12 percent. Considering uncertainty involved in other input parameters (e.g. boundary conditions, external loads, geometry, and material properties) and the fact that there is already an introduced approximation in the Ilyushin surface, it can be acceptable to employ this modified surface.

Assuming a work hardening as a generalization of the plastic strain we can write,

$$\boldsymbol{s}^T \dot{\boldsymbol{e}}^p = \sigma \dot{\varepsilon}^p \qquad \sigma = \sqrt{\boldsymbol{s}^T \boldsymbol{A} \boldsymbol{s}} \tag{8}$$

The rate equation for the associated plastic flow model is given as,

$$\dot{\boldsymbol{e}}^p = \dot{\lambda}\frac{\partial f}{\partial \boldsymbol{s}} = \dot{\lambda} 2 \boldsymbol{A} \boldsymbol{s} \tag{9}$$

where $\dot{\boldsymbol{e}}^p$ is the generalized plastic strain rate, and the non–negative scalar $\dot{\lambda}$ is a measure of plastic flow.

In advancing the solution incrementally, the starting point is from the previous converged solution at state n to compute the solution at the current state $n+1$. Initially, the whole increment is assumed elastic, and the trial elastic stress is calculated as,

$$\boldsymbol{s}_{n+1}^{trial} = \boldsymbol{C}_e \left(\boldsymbol{e}_{n+1} - \boldsymbol{e}_n^p\right) \tag{10}$$

where $\boldsymbol{C}_e$ is the elastic material modulus. Within the framework of return mapping algorithm, the yield condition is checked using this trial stress and the plastic quantities from the previous step n. If the yield surface is exceeded, plastic flow has occurred within the current increment. Accordingly, the correct stress resultant tensor must be obtained from,

$$\boldsymbol{s}_{n+1} = \boldsymbol{C}_e \left(\boldsymbol{e}_{n+1} - \boldsymbol{e}_{n+1}^p\right) = \boldsymbol{s}_{n+1}^{trial} - \boldsymbol{C}_e \left(\boldsymbol{e}_{n+1}^p - \boldsymbol{e}_n^p\right) \tag{11}$$

The current plastic strain increment can be obtained by integrating (9) using the backward Euler method as,

$$\boldsymbol{e}_{n+1}^p - \boldsymbol{e}_n^p = (\lambda_{n+1} - \lambda_n)\, 2\boldsymbol{A}\boldsymbol{s}_{n+1} = \lambda 2\boldsymbol{A}\boldsymbol{s}_{n+1} \tag{12}$$

where λ is the so-called consistency parameter or the plasticity multiplier. Substitution of (12) into (11) gives,

$$\boldsymbol{s}_{n+1} = \left[\boldsymbol{I} + 2\lambda \boldsymbol{C}_e \boldsymbol{A}\right]^{-1} \boldsymbol{s}_{n+1}^{trial} \tag{13}$$

and λ remains the sole unknown. At this point, it is convenient to express the inverse matrix in (13) in terms of matrices of eigenvalues $\boldsymbol{\Lambda}$ and eigenvectors $\boldsymbol{Q}$ of matrix $\boldsymbol{C}_e\boldsymbol{A}$. The resulting expression becomes,

$$\boldsymbol{s}_{n+1} = \left(\boldsymbol{Q}\left[\boldsymbol{I} + 2\lambda\boldsymbol{\Lambda}\right]^{-1} \boldsymbol{Q}^{-1}\right) \boldsymbol{s}_{n+1}^{trial} = \boldsymbol{V}\boldsymbol{s}_{n+1}^{trial} \tag{14}$$

With (13) and backward Euler integration of (8) and (9), the updated plastic strains and hardening parameter become,

$$\boldsymbol{e}_{n+1}^p = \boldsymbol{e}_n^p + 2\lambda \boldsymbol{A}\boldsymbol{s}_{n+1} \tag{15}$$

$$\varepsilon_{n+1}^p = \varepsilon_n^p + 2\lambda\sigma_{n+1} \tag{16}$$

Substituting Equations (14) and (16) into (6) with $\mu = 0$, leads to the modified yield surface as a non–linear function of a single scalar variable λ,

$$f(\lambda) = \sigma_{trial}^2 - \left(1 + \frac{H}{\sigma_Y}\left[\varepsilon_n^p + 2\lambda\sigma_{trial}\right]\right)^2 = 0 \tag{17}$$

where the explicit form of σ_{trial} is given in Mohammed *et al.* (2000). The subscript $n+1$ has been omitted for clarity. Newton–Raphson iteration procedure is employed to determine the consistency parameter λ from the non–linear equation (17) so that $\lambda^{k+1} = \lambda^k - f/f_{,\lambda}$, where $\lambda^\circ = 0$, and

$$f_{,\lambda} = \partial\sigma_{trial}^2 - \frac{2H}{\sigma_Y}\left(1 + \frac{H}{\sigma_Y}\left[\varepsilon_n^p + 2\lambda\sigma_{trial}\right]\right)\left(2\sigma_{trial} + \frac{\partial\sigma_{trial}^2}{\sigma_{trial}}\lambda\right) \tag{18}$$

4 Numerical Examples

To demonstrate the performance of the presented model, two examples are presented in Figure 1. The first one is the buckling collapse of short/wide plate under increased displacements. For this example, the results are compared with those by Javaherian and Dowling (1985), and Bergan *et al.* (1990). In the second example, a shell structure commonly known as Scordelis-Lo roof is analyzed. Here, the comparison is made to Peric and Owen (1991), Crisfield and Peng (1992), Roehl and Ramm (1996), and Brank *et al.* (1997).

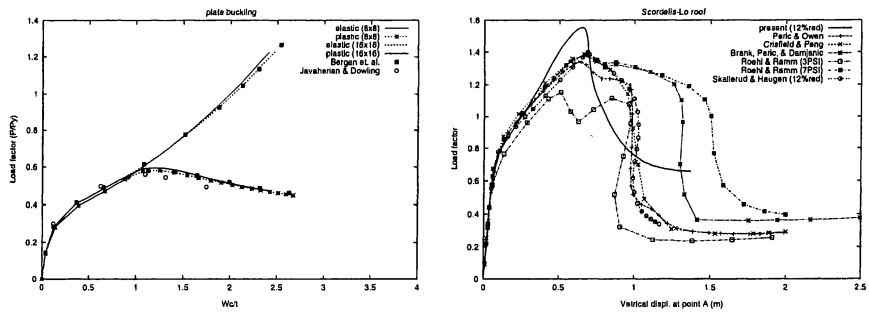

(a) Plate Buckling

(b) Scordelis-Lo roof

Figure 1 Demonstrative Examples.

References

BERGAN, P., M. NYGARD, AND R. BJAERUM (1990). Free formulation elements with drilling freedoms for stability analysis of shells. In W. KRATZIG AND E. ONATE (Eds.), *Computational Mechanics of Nonlinear Response of Shells*, Berlin, pp. 164–182. Springer-Verlag.

BRANK, B., D. PERIC, AND F. B. DAMJANIC (1997). On large deformations of thin elasto-plastic shells: Implementation of a finite rotation model for quadrilateral shell element. *Int. J. Numer. Meth. Engng. 40*, 689–726.

CRISFIELD, M. A. AND X. PENG (1992). Efficient non-linear shell formulation with large-rotations and plasticity. In *COMPLAS-3*, Barcelona, pp. 1979–1997.

IBRAHIMBEGOVIÇ, A. AND F. FREY (1992). Stress resultants elasto-plastic analysis of plates and shallow shells. In *COMPLAS-3*, Barcelona, pp. 2047–2059.

JAVAHERIAN, H. AND P. DOWLING (1985). Large deflection elasto-plastic analysis of thin shells. *Engng. Structures 7*, 154–163.

MATTHIES, H. G. (1989). A decomposition method for integration of elastic-plastic rate problem. *Int. J. Numer. Meth. Engng. 28*, 1–11.

MOHAMMED, A., J. AMDAHL, AND B. SKALLERUD (2000). Collapse analysis of thin shell structures using a displacement–based constant stress–resultants curved element. Technical Report MK/R 146, Marine Structures Dept., Norwegian Univerisity of Science and Technology, NTNU, Norway.

MOHAMMED, A., B. SKALLERUD, AND J. AMDAHL (2000). Simplified stress resultants plasticity on a geometrically non-linear constant moment shell element. Technical Report MK/R 144, Marine Structures Dept., Norwegian Univerisity of Science and Technology, NTNU, Norway.

MORLEY, L. S. D. (1991). Geometrically non-linear constant moment triangle which passes the von Kàrmàn patch test. *Int. J. Numer. Meth. Engng 31*, 241–263.

PERIC, D. AND D. R. J. OWEN (1991). The morley shell finite element for large deformations problems: Simplicity versus sophistication. In *Proc. 4th Int. Conf. on Nonlin. Engrg. Comput. (NEC-91)*, pp. 121–142.

PROVIDAS, E. D. (1990). *On the geometrically nonlinear constant moment triangle (with a note on drilling rotations)*. Ph. D. thesis, Department of Mathematics and statistics, Brunel Univerisity, UK.

ROEHL, D. AND E. RAMM (1996). Large elasto-plastic finite element analysis of solids and shells with the enhanced assumed strain concept. *Int. J. Solids Structures 33*(20-22), 3215–3237.

SKALLERUD, B. AND B. HAUGEN (1999). Collapse of thin shell structures – stress resultant plasticity modelling within a co-rotated ANDES finite element formulation. *Int. J. Numer. Meth. Engng 46*, 1961–1986.

Lower-bound limit analysis of plate structures using nonlinear programming

Kristian Krabbenhøft and Lars Damkilde
Department of Structural Engineering and Materials
Technical University of Denmark, DK-2800, Kgs. Lyngby

Introduction

Limit state analysis of perfectly plastic plates has been used in design for decades. Two basic methods can be applied, either the upper-bound method or the lower-bound method. With the upper-bound method a geometrically possible collapse field for which the load carrying capacity is at a minimum is sought, whereas with the lower-bound method one seeks a statically admissible stress field which maximizes the load carrying capacity.
For hand calculations the upper-bound method is usually superior to the lower-bound method. However, as an automated procedure the latter is more easily generalized. This is achieved by the well-known finite element concept of dividing the structure into a number of elements which each have to fulfill certain equilibrium conditions. Additionally, the stresses must comply with the yield conditions. These two sets of conditions leads to a mathematical programming problem on the form

$$\begin{array}{ll} \text{maximize} & \lambda \\ \text{subject to} & \boldsymbol{H}\boldsymbol{\beta} = \lambda \boldsymbol{R} \\ & f_i(\boldsymbol{\beta}, \boldsymbol{C}_d) \leq 0, \quad i = 1, 2, \ldots, n \end{array} \tag{1}$$

Here the equation system $\boldsymbol{H}\boldsymbol{\beta} = \lambda \boldsymbol{R}$ expresses equilibrium between the stresses $\boldsymbol{\beta}$ and the external load $\lambda \boldsymbol{R}$. The yield conditions are formulated through a number of inequalities $f_i(\boldsymbol{\beta}, \boldsymbol{C}_d) \leq 0$, with $\boldsymbol{C}_d$ being the material strengths. These inequalities will for all but the simplest structures be of a nonlinear nature.
As shown in [1] a reduction of the number of stress variables is possible. By dividing the stress variables into two groups $\boldsymbol{\beta}_0$ and $\boldsymbol{\beta}_1$ such the the equilibrium equations can be written as

$$\boldsymbol{H}_0\boldsymbol{\beta}_0 + \boldsymbol{H}_1\boldsymbol{\beta}_1 = \lambda \boldsymbol{R} \tag{2}$$

the $\boldsymbol{\beta}_0$-variables can be expressed by $\boldsymbol{\beta}_1$ and $\lambda \boldsymbol{R}$. By substitution into the yield condition inequalities a substantial reduction of the system can be achieved.

Following [2] the primal minimization problem associated to the dual problem (1) can be interpreted as the upper-bound load optimization problem. Whereas the variables of (1) are the stresses and the collapse load multiplier, the variables of the primal problem can be interpreted as the displacements and plastic strains. This makes it possible to extract the collapse field from the lower-bound load optimization problem via the shadow or marginal prices which are obtained with no significant extra cost as a byproduct of the iterations.

Solution strategy

The nonlinear programming problem (1) can be solved in a number of ways. The most common approach is to linearize the yield conditions by a sufficient number of hyper-planes. The resulting linear problem can then be solved very efficiently by standard linear programming algorithms such as e.g the simplex method and various interior point methods. This has been done in [1] for a variety of structures and yield conditions.
Another possibility is to linearize the yield criteria as the iterations proceed. With the interior point methods this can be done in a relatively straight-forward manner, and for the lower-bound load optimization problem the so-called dual affine-scaling method is particularly well suited, see [3]. The dual affine-scaling algorithm solves the linear optimization problem

$$\begin{array}{ll} \text{Maximize} & \boldsymbol{b}^T\boldsymbol{y} \\ \text{Subject to} & \boldsymbol{A}^T\boldsymbol{y} + \boldsymbol{s} = \boldsymbol{c} \\ & \boldsymbol{s} \geq \boldsymbol{0} \end{array} \tag{3}$$

This problem corresponds to (1) if the stress variable reduction is performed and slack variables $\boldsymbol{s}$ are added to convert the inequalities into equalities. The slack variables express the relative distance to the boundary.
In contrast to the simplex method where the iteration steps follow the boundary of the feasible region, the points generated by the dual affine-scaling algorithm lie within the interior of the feasible solution space. Each iteration consists of moving in the direction which maximizes the object function the most. For the problem (3) this direction is given by

$$\Delta\boldsymbol{y}^{\boldsymbol{k+1}} = (\boldsymbol{A}\boldsymbol{S}^{-2}\boldsymbol{A}^T)^{-1}\boldsymbol{b} \tag{4}$$

where $\boldsymbol{S} = \text{diag}(\boldsymbol{s}^k)$. As seen the current values of the $\boldsymbol{s}$-variables are taken into consideration when computing the direction. This constitutes a scaling such that the location of the current point in relation to the distance to the boundary is taken into consideration. Details about this scaling can be found in e.g. [4].

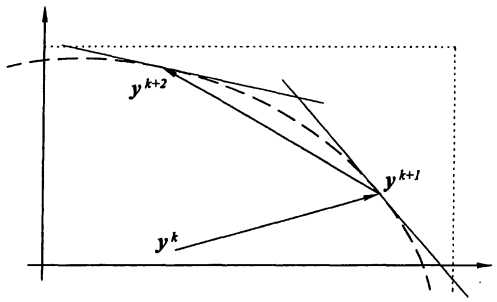

Figure 1: Solution algorithm

The dual affine-scaling algorithm can now be extended to deal with nonlinear problems by linearzing the nonlinear constraints as the iterations proceed. For the computation of the direction (4) a set of initial linear constraints are necessary. These are chosen as circumscribing the nonlinear yield criteria. A direction is then computed and an increment taken in this direction. If the magnitude of the increment is limited by the nonlinear restrictions, an extra linear restriction, corresponding to the tangent plane of the limiting nonlinear constraint, is

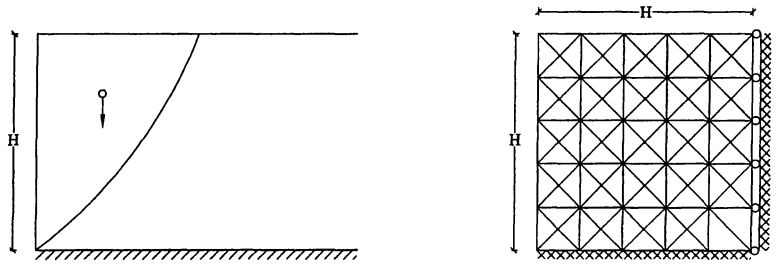

(a) (b)

Figure 2: Critical height problem (a) and element model (b)

added and a new direction computed. Thus, the algorithm consists of computing an increment on the basis of a linear set of restrictions, followed by the inclusion of an additional linear restriction. This is illustrated in figure 1.

Example

The following example is taken from [5] where the critical height of a vertical cut as shown in figure 2(a) was determined.
The upper-bound method was used with a log-spiral defining the plane of failure.
The analytical expression for the critical height H_{cr} is given as

$$H_{cr} = \frac{3.83c}{\gamma} \tan(\tfrac{1}{4}\pi + \tfrac{1}{2}\phi) \tag{5}$$

where c is the cohesion, γ is the unit weight of the soil, and ϕ is the angle of friction following the Coulomb yield criterion

$$|\tau| = c - \sigma \tan\phi \tag{6}$$

Using this yield criterion the value of γ which causes collapse can be determined and the critical height then found by using (5). This has been done by means of a triangular element previously used in [6] for analysis of reinforced concrete structures. The variation of the stresses within the element is linear and the equilibrium equations formulated as to ensure exact equilibrium, i.e. the results are true lower-bound solutions. The problem is solved by linearizing the yield criteria on the safe side by 8 and 16 hyper-planes respectively, and by using the full nonlinear representation.
With the mesh shown in figure 2(b) the critical height has been computed for different values of the angle of friction. The results are shown in figure 3(a). In the light of the modest number of elements the results are very satisfactory. The best agreement with the upper-bound solution is obtained for values of ϕ in the range of $5° - 20°$, while the difference is slightly greater for values outside this range. This must be ascribed to the orientation of the mesh in relation to the exact plane of failure.
The influence on the critical height from using a full nonlinear representation of the yield criteria varies with the angle of friction. With 8 hyper-planes the relative difference is between 4 and 11%, while the results in the case of 16 hyper-planes are less sensitive with a deviation of approximately 1.5%.

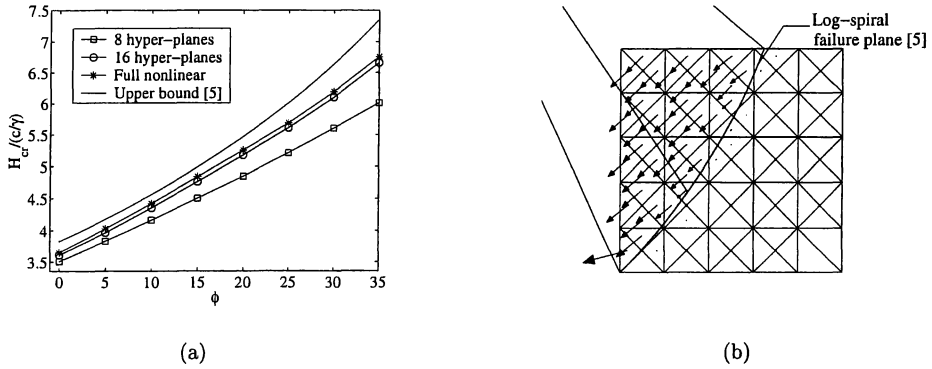

(a) (b)

Figure 3: Upper- and lower-bound solutions (a) and lower-bound displacements (b)

The computational effort in solving the linear 8 hyper-plane problem is comparable to effort in solving the nonlinear problem, while the use of 16 hyper-planes doubles the computational time required.
An indication of the collapse field can be obtained by considering the primal problem displacements associated with the center of the elements. This is shown in figure 3(b) for $\phi = 20°$ where also the log-spiral from [5] has been constructed. As seen, the agreement between the two solutions is good. Although the displacements in some areas do not match the upper-bound solution completely, the general shape of the failure mechanism is well determined.

Conclusion

The lower-bound load optimization problem has been solved using an algorithm which takes into account the nonlinearity of the yield conditions. The extension of the method to different yield conditions and elements than the ones used here is straight-forward.

References

[1] L. Damkilde and S. Krenk. LimitS - a system for limit state analysis and optimal material layout. *Computers & Structures*, 64(1–4):709–718, 1997.

[2] S. Krenk, L. Damkilde, and O. Høyer. Limit analysis and optimal design of plates with equilibrium elements. *Journal of Engineering Mechanics*, 120(6):1237–1254, 1994.

[3] K. Krabbenhøft. *Limit Analysis of Plate Structures.* M.Sc. thesis, Department of Structural Enineering and Materials, Technical University of Denmark, 2000.

[4] C. C. Gonzaga. Path-following methods for linear programming. *SIAM Review*, 34(2):167–224, 1992.

[5] W. F. Chen and X. L. Liu. *Limit Analysis in Soil Mechanics.* Elsevier Science Publishers B.V., Amsterdam, 1990.

[6] P. N. Poulsen and L. Damkilde. Limit analysis of reinforced concrete plates subjected to in-plane forces. *International Journal of Solids and Structures*, to appear october 2000.

A *Mathematica* application in metal plasticity

Mika Reivinen, Jouni Freund

Helsinki University of Technology
Laboratory of Theoretical and Applied Mechanics
P.O.Box 1100, FIN-02015 HUT
e-mail: Mika.Reivinen@hut.fi
web page: http://www.hut.fi/HUT/Dynamics/

INTRODUCTION

The use of the *Mathematica* programming language in the problems of elasto-plasticity is considered. One goal of the study has been to provide a test environment for small scale problems arising in metal forming plasticity. Another goal has been to form a systematic practice for the determination of material parameters. The principal idea for the determination is to minimize the least-squares deviation between computed and measured variables with respect to the constitutive parameters. Both the finite element and the optimization modules are programmed using *Mathematica 3.0* programming language[1,2].

INCREMENTAL PLANE STRESS ELASTO-PLASTICITY

Although specific incremental algorithms for plane stress plasticity exist[3,4], we use a more general incremental approach presented in[5,6]. This is motivated by educational aspects of the code. We consider the Lagrangian form of the problem and assume that the displacements are small. Then there is no need to make difference between the Cauchy and Piola-Kirchhoff stresses and the corresponding 'small displacement' and Green-Lagrange strain measures. Yield function defined in the stress space is

$$f = F - \kappa\left(e^p\right) \le 0\,, \tag{1}$$

where F is the effective stress, and the hardening parameter κ (depending on the equivalent plastic strain e^p) determines the size of elastic domain. In the plastic flow, the increment of the plastic strain is given by the Prandtl-Reuss flow rule.

$$\Delta\boldsymbol{\varepsilon}^p = \Delta\lambda \frac{\partial f}{\partial \boldsymbol{\sigma}} = \Delta\lambda \boldsymbol{a}\,, \tag{2}$$

where $\Delta\lambda$ is the plastic strain multiplier, and $\boldsymbol{a}$ the plastic flow vector. The stress changes are related to the strain changes by

$$\Delta\boldsymbol{\sigma} = \mathbf{C}\left(\Delta\boldsymbol{\varepsilon} - \Delta\boldsymbol{\varepsilon}^p\right) = \mathbf{C}\left(\Delta\boldsymbol{\varepsilon} - \Delta\lambda\boldsymbol{a}\right). \tag{3}$$

Above, $\Delta\boldsymbol{\varepsilon}$ is the increment of total strain vector, which consists of elastic and plastic parts $\Delta\boldsymbol{\varepsilon} = \Delta\boldsymbol{\varepsilon}^e + \Delta\boldsymbol{\varepsilon}^p$, and $\mathbf{C}$ is the 3×3 tangent modulus matrix. For plastic flow, the stresses must remain on the yield surface and hence we get the consistency condition

$$\Delta f = \left(\frac{\partial f}{\partial \boldsymbol{\sigma}}\right)^T \Delta\boldsymbol{\sigma} + \frac{\partial f}{\partial \kappa}\frac{\partial \kappa}{\partial e^p}\Delta e^p = \boldsymbol{a}^T\Delta\boldsymbol{\sigma} - k\Delta e^p = 0, \tag{4}$$

where $k = \partial\kappa / \partial e^p$ is the plastic strain hardening modulus.

The variational formulation reads: find the increment of the displacement field $\Delta\boldsymbol{u}$ so that

$$\int_V (\delta\frac{\partial\Delta\boldsymbol{u}}{\partial\boldsymbol{x}} : \Delta\boldsymbol{\sigma})dV = \int_V (-\delta\frac{\partial\Delta\boldsymbol{u}}{\partial\boldsymbol{x}} : \boldsymbol{\sigma} + \delta\boldsymbol{u}\cdot\boldsymbol{f})dV + \int_A (\delta\Delta\boldsymbol{u}\cdot\boldsymbol{t})dA \quad \forall\delta(\Delta\boldsymbol{u}). \tag{5}$$

The right hand side of the equation represents the out-of balance forces. After substituting expression (3) and the strain increment definition

$$\Delta\boldsymbol{\varepsilon} = \frac{1}{2}[\frac{\partial\Delta\boldsymbol{u}}{\partial\boldsymbol{x}} + (\frac{\partial\Delta\boldsymbol{u}}{\partial\boldsymbol{x}})^T] \tag{6}$$

one may solve $\Delta\boldsymbol{u}$, calculate the increment of the strain $\Delta\boldsymbol{\varepsilon}$ and stress $\Delta\boldsymbol{\sigma}$. Although the solution thus obtained satisfies the equilibrium, the stress may not be located inside the yield surface and therefore a correction stage is needed. We start from the elastic predictor $\Delta\boldsymbol{\sigma}^e = \mathbf{C}\Delta\boldsymbol{\varepsilon}^e$ and apply Newton's method to return the stress on the yield surface. The return mapping is based on the stress and yield surface expressions

$$\begin{aligned} &\boldsymbol{r} \equiv \boldsymbol{\sigma} - \mathbf{C}\left(\boldsymbol{\varepsilon}^e - \Delta\lambda\boldsymbol{a}\right) = 0, \\ &f = 0 \end{aligned} \tag{7}$$

which are considered as nonlinear functions of stress $\boldsymbol{\sigma}$ and the plastic multiplier $\Delta\lambda$. The change of plastic multiplier can be determined from the Taylor expansions of expressions (7). Also, consistent tangent modulus matrix follows when $\Delta\lambda$ is eliminated from the stress and consistency equations.

DETERMINATION OF OPTIMAL MATERIAL PARAMETERS

In this study, an attempt to form a systematic way for the determination of optimal material parameters is made. The principal idea for this is to minimize the least-squares deviation between the computed and measured variables with respect to the constitutive parameters. The least-squares expression may contain any observable quantities such as forces, strains, or geometrical shape. The observable and the corresponding calculated variables are collected into the vectors $\boldsymbol{v}^o$ and $\boldsymbol{v}^c$, respectively. The constitutive parameters are collected into the vector $\boldsymbol{m}$. All the calculated variables are functions of material parameters, i.e.,

$$\boldsymbol{v}^c = \boldsymbol{v}^c(\boldsymbol{m}). \tag{8}$$

We can determine the sensitivities

$$\mathbf{S} = \frac{\partial \boldsymbol{v}^c}{\partial \boldsymbol{m}} \approx \frac{\Delta \boldsymbol{v}^c}{\Delta \boldsymbol{m}} \tag{9}$$

by solving the problem first with the current values of the design parameters and then giving a small increment to each parameter at a time. The new values of the calculated parameters can then be approximated as

$$\boldsymbol{v}^{cn} = \boldsymbol{v}^c + \mathbf{S}\Delta\boldsymbol{m}. \tag{10}$$

To get the increments of the constitutive parameters $\Delta\boldsymbol{m}$, we form a least-squares expression

$$p(\Delta\boldsymbol{m}) = \frac{1}{2}\left(\boldsymbol{v}^{cn} - \boldsymbol{v}^o\right)^2 \tag{11}$$

using the new values (10) for the variables and minimize the expression with respect to the increments. The new material parameters to be used at the next stage are then

$$\boldsymbol{m}^n = \boldsymbol{m} + \Delta\boldsymbol{m}. \tag{12}$$

NUMERICAL EXAMPLE

As our numerical example, appropriate anisotropy parameter is searched using numerical simulation of a rectangular strip in tension. Length of the specimen is $2l$ and width $2b$. In general, material anisotropy of the sheet follows as a consequence of the rolling process. A natural set of material axes related to the rolling process are the rolling direction (x-axis in our example, say), the transverse direction (y-axis), and the normal of the sheet plane (thickness direction). In the present example, we use Hill's quadratic yield function in the form

$$f = \sqrt{\sigma_1^2 + \sigma_2^2 - \frac{2r}{1+r}\sigma_1\sigma_2} - \kappa\left(e^p\right) = 0. \tag{13}$$

Above, r is the plastic anisotropy parameter which expresses the ratio of transverse to through-thickness plastic strain increments, and σ_1, σ_2 are the principal stresses. The principal directions of these are assumed to coincide with the principal axes of anisotropy of the material. Setting the anisotropy parameter r = 1 in (13) gives the widely used von Mises yield condition. In this example we use the linear hardening material model $\kappa(e^p) = \sigma_0 + ke^p$, where σ_0 is the initial yield strength.

Our task is now to optimize the anisotropy parameter r so that the calculated stress-strain relation is as close as possible to the observed stress-strain curve. Here, we use a simple

example[7]. The observed stress-strain relation in the plastic region is $\sigma_1 = 500\varepsilon_1^{0.25}$ [MPa]. Young's modulus is $E = 52.5$ GPa, Poisson's ratio $\nu = 0.30$, initial yield strength $\sigma_0 = 0.0021E$, and plastic hardening modulus $k = 0.050E$. For the linear hardening material model, we consider the range $\varepsilon_0 \le \varepsilon_1 \le 10\varepsilon_0$ ($\varepsilon_0 = 0.002$ is the yield strain) for the strain in the x-direction. We start the optimization process from the value $r = 1$. The problem is solved using prescribed horizontal increments of displacement of $0.0005\ l$ in the plastic region on the right boundary at $x = l$. The function to be optimized is formed using discrete values of the simulated and observed stress-strain relation

$$p = \frac{1}{2}\sum_{k=1}^{n\varepsilon}\left(\sigma^{cn}(\varepsilon_k) - \sigma^{o}(\varepsilon_k)\right)^2 \tag{14}$$

where $n\varepsilon$ is the number of stress-strain points in the range under consideration. The optimization process proceeds as follows: $p(r=1) = 3059$, $p(r=1.27) = 2220$, $p(r=1.26) = 2219$, $p(r=1.26) = 2219$, and the value $r = 1.26$ can be considered as the final one.

CONCLUDING REMARKS

The *Mathematica* programming language has been utilized in elasto-plastic analysis and in systematic derivation of material parameters. It was found that a relatively small amount of programming effort is needed to analyze complicated physical phenomena of metal plasticity. Also, integrated graphics makes it possible to visualize the state of computation, e.g., the status of plastic internal variables, stress and strain fields, at every stage. As the ideas of computational inelasticity appear clearly, the code serves well for educational purposes. However, the simulation of the material undergoing large plastic deformation is a time consuming task, and we emphasize that the approach fits best in small scale problems. The present study is still on its early stage. Attractive future applications in the field of metal forming analysis may be, for example, studies on more complicated strain and stress measures, contact and friction models, and meshless methods.

REFERENCES

[1] S. Wolfram, *The Mathematica book*, Wolfram Media/Cambridge University Press, 3rd ed., (1996).

[2] H. Ruskeepää, *Mathematica Navigator*, Academic Press, (1999).

[3] Simo, J.C. and R.L. Taylor, *A return mapping algorithm for plane stress elastoplasticity*, Int. J. Numer. Math. Engrg. 22 (1986) 649-670.

[4] J.C. Simo, T.J.R Hughes, *Computational inelasticity*, Springer-Verlag, Berlin, (1998).

[5] M.A. Crisfield, *Non-linear Finite Element Analysis of Solids and Structures*, Volume 1: Essentials, Wiley, (1991).

[6] M.A. Crisfield, *Non-linear Finite Element Analysis of Solids and Structures*, Volume 2: Advanced Topics, Wiley, (1997).

[7] Wagoner R.H., Chenot J-L., *Fundamentals of metal forming*, Wiley, (1997).

Numerical simulation of temperature and strain development in the Maridal culvert

DANIELA BOSNJAK and TERJE KANSTAD
Norwegian University of Science and Technology
N-7491 Trondheim, Norway.

Introduction

This paper presents measured and calculated temperature and stress distribution in a real concrete structure, the Maridalen culvert in Oslo. The culvert is a part of the Ring road around Oslo. The total length of approximately 340 m has been cast in sections of 15 m length. Foundations, walls and slabs in three sections were instrumented [1] and temperature and strains were recorded in the hardening period. The structures are modelled and analysed by the general finite element program DIANA. In this paper one wall with thickness 0.65 m and height 5.8 m is considered. The wall is cast on a previously cast foundation (2.8 x 1.0 m). Temperature, stress and strain development during the first seven days of the wall are calculated and presented here. Different ways of modelling the structure and and the restraint conditions, and their impact on stresses are investigated using 3D models. The main objective is to verify material models and calculation methods against the measurements. The work is a part of a nearly finished doctoral thesis [2], and is supported by a financial contribution from the Brite-Euram Project IPACS.

Finite element analysis

The influence of the mechanical responses on the temperature development in hardening concrete is negligible, and the thermal and mechanical problem may therefore be separated. The thermal problem is solved first, and results are used as input for the subsequent stress calculation.

Both the temperature and the stress analysis are performed by the general purpose finite element program system DIANA [3] with some new implementations described in [2]. DIANA allows use of the same element model in both temperature and stress analysis. To avoid spatial oscillation of stresses, element in stress analysis have an order higher interpolation polynomial than element in temperature analysis. Solid elements describing linear variation of temperature and quadratic variation of stresses are used in this case. The exchange of temperature with surroundings is modelled by the conduction coefficient of boundary elements. Quadrilateral elements were used at the faces of three-dimensional model.

Two element models are used in numerical simulation: a full 3D model and a simplified model which is a "slice" of the wall with unit thickness. The basic assumption for the simplified model is that the wall can be treated like an infinitely long structure with constant temperatures and stresses in the longitudinal direction. In this case the plane bending principle for deformations holds. To find out to what extent the simplification about plane cross-sections influences stress and strain results in the structure, analysis with full 3D model is also performed. Phased analysis is used to simulate effect of casting history. The wall is modelled in two phases cast with four hours' time difference. The finite element calculation is carried out in 81 steps, starting with step of 1 h up to steps of 4 h in the end.

Material models

A comprehensive laboratory test program to identify model parameters for the actual concrete has been performed at NTNU [4]. To obtain reliable analysis results, both thermal and mechanical properties have been determined in a comprehensive laboratory test programme:

- semi-adiabatic test to estimate hydration heat development
- testing of compressive strength, tensile strength, and E-modulus
- isothermal creep test
- shrinkage rig and stress-rig tests

In the shrinkage and stress-rig tests the concrete has been exposed to identical realistic temperature histories. In the shrinkage rig the total free deformation – ie the sum of thermal dilation and autogenous shrinkage- was measured on unrestrained specimen. Assuming constant value for the thermal dilation coefficient, the autogenous deformation is determined by subtracting the thermal dilation from the total deformation. For further identification of model parameters, the stress generation in was examined under well defined restrained conditions in the stress rig. On this basis, the creep model has been modified, and transitional thermal creep has been taken into account.

Results from the Temperature calculation

Since the goal of this work is to compare calculated and measured temperature and stress histories, the actual conditions on site are used for temperature calculations (air temperature, fresh concrete temperature, temperature of the previously cast slab, type of formwork and time of striking, etc.). Calculated temperatures in the simplified model and in the middle of the 3D model completely overlap. Fig(1) shows measured and calculated temperature in two points in the middle of the wall.

Results from the Stress calculation

Two analyses with different assumptions of subgrade restraint conditions have been performed with the simplified model representative for an infinitely long structure: fixed, or alternatively free rotation of the cross section of the wall.

The simplifications represent two extreme cases of the boundary conditions of the real structure, and are also the basic cases used in the most commonly used special-purpose programs for hardening concrete structures. The first case corresponds to infinitely stiff subgrade, while in the second case the subgrade stiffness is totally neglected. In both cases the horizontal frictional forces between foundation and subgrade are neglected. To check the validity of the simplifications, full 3D analyses with the same subgrade stiffness have been performed.

To obtain more correct results, a more realistic description of the deformability of the ground has to be included. In DIANA this can be done by means of interface elements. These elements are quadratically interpolated. The "lower" nodes, ground nodes, are fixed in all directions, and the "upper" nodes are common nodes for the structure and interface element. In this work the stiffness is linear in compression, while the tension forces are neglected.

The stress development in the two points in the middle of the wall is presented in the fig(2). Fig(3) shows total calculated strains in the length direction of the wall compared to measured values.

Discussion of the results

The actual wall is relatively short (length/height=2.22), and it is placed on relatively stiff ground (20cm compacted gravel, and 5cm concrete blinding). It is seen that the results of full 3D analysis with realistic ground stiffness modelling are very close to the results of simplified analysis with free rotation assumption. Furthermore, the recorded strains are in reasonably good agreement with the calculated results for the upper part of the wall. For points close to the base, however, the difference between calculations and measurements is significant. Reasons of disagreement may be: slip in casting joint, deviation between measured and calculated temperatures, uncertainties in material modelling, uncertainties in strain measurements. The subject is thoroughly considered in [2].

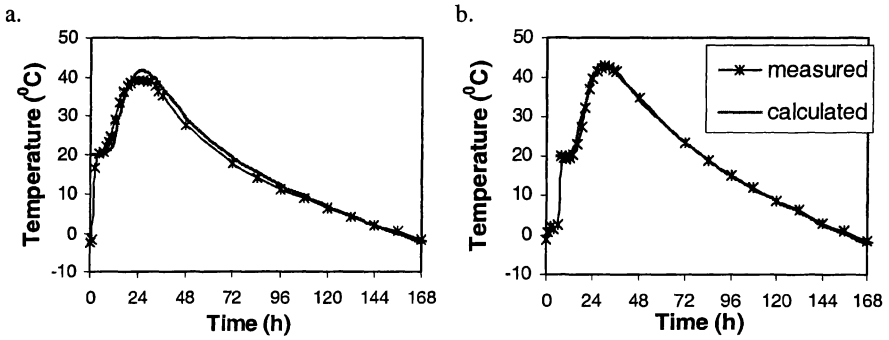

Figure 1. Measured and calculated temperature development in the middle of the wall at: a) 0.5 m from the base slab, b) 0.5 m from the top of the wall

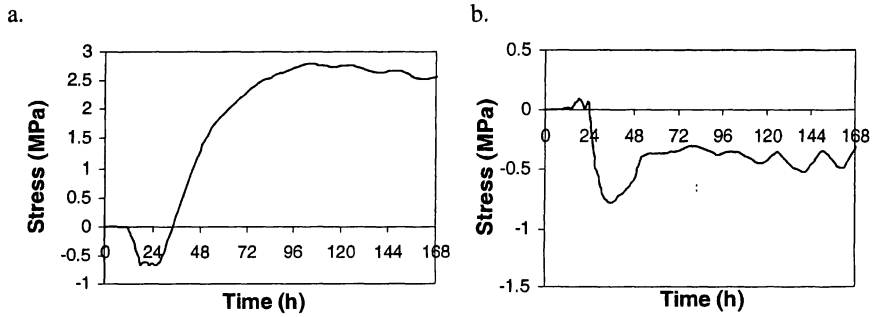

Figure 2. Stress development in the middle of the wall at: a) 0.5 m from the base slab, b) 0.5 m from the top of the wall

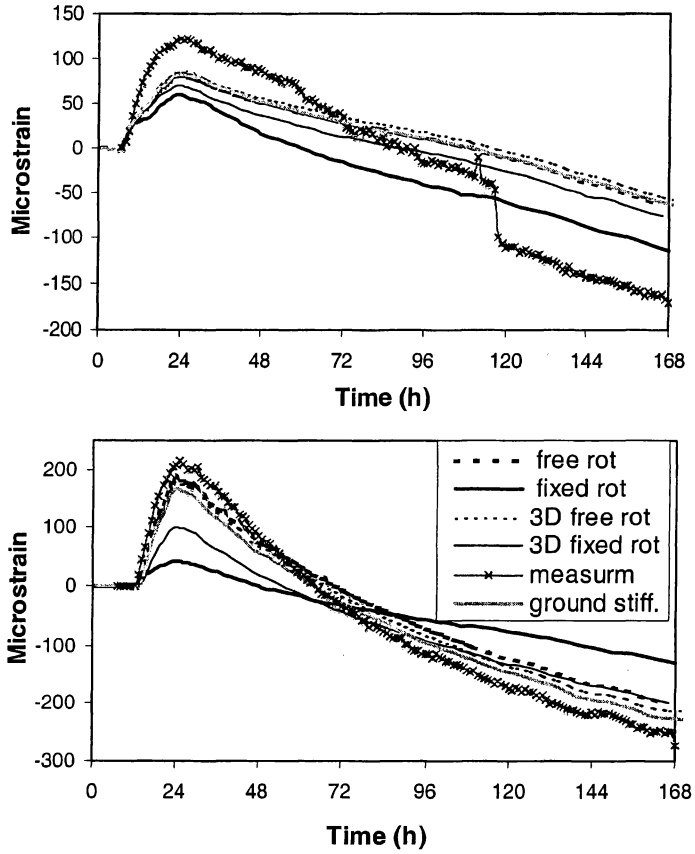

Figure 3. Strain development in the middle of the wall at 0.5 m from the base slab and 0.5 m from the top of the wall. Numerical results for different restraint conditions compared to the measured values

References

1. Heimdal, E., Kanstad, T. and Kompen, R., "Early age concrete field tests at the Maridal culvert. Project description and test results", NOR-IPACS Report STF22 A99763, Norway 1999
2. Bosnjak, D.,"Temperature induced cracking problems in hardening concrete structures", Doctoral thesis, NTNU, 2000
3. DIANA 7 User's Manual, 1998, TNO Building and Construction Research, The Netherlands
4. Bjøntegaard, Ø., "Thermal Dilation and Autogenous Deformation as Driving Forces to Self-Induced Stresses in High Performance Concrete", Doctoral thesis, NTNU, 1999

Finite Element Modeling of Prestressed Concrete Beams Strengthened with Carbon Fiber Reinforced Polymer Plates

Peter F. Takács and Terje Kanstad
Norwegian University of Science and Technology
Department of Structural Engineering
N-7491 Trondheim, Norway
Email: Peter.Takacs@bygg.ntnu.no and Terje.Kanstad@bygg.ntnu.no

Keywords: concrete, building technology, strengthening, Carbon Fiber Reinforced Polymer, full scale test, finite element modeling, cracking, Modified Compression Field Theory

1 Introduction

Strengthening old concrete structural elements with Carbon Fiber Reinforced Polymer plates has become a reasonable alternative to traditional techniques such as installing steel plates or external prestressing cables. They are relatively cheap, easy to handle and work with, effective and not subjected to corrosion.

When Isakveien Bridge in Oslo was demolished after 35 years in service two prefabricated prestressed concrete DT elements with in-situ concrete top-layer were preserved for testing. The two DT elements were cut half lengthwise, so eventually four T elements were obtained. Two beams of the four were tested to determine their actual flexural moment and shear capacity for reference. The other two beams were strengthened with longitudinal Carbon Fiber Reinforced Polymer (CFRP) plates (*SIKA CarboDur S*) in two different quantities, 108 mm^2 and 216 mm^2. The objective with the test series was to investigate the technology for future application mainly in the field of strengthening bridges similar than Isakveien Bridge was.

Simultaneously finite element modeling of the tests was carried out with general purpose finite element program system DIANA. The numerical investigation was based on a total strain based crack model which was developed at TNO Building and Construction Research [1] along the lines of the Modified Compression Field Theory originally proposed by Vecchio and Collins [2]. The main objectives with the finite element analysis were to provide reference data before the tests were executed, to investigate relevant finite element techniques with the main emphasis laid on smeared crack models and to compare the results of the tests, FE modeling and simplified design calculations.

2 Arrangement of the beams and testing

The length of the beams were 11.20 meter. Dimensions of the cross-section are shown in Figure 1. They were loaded symmetrically with two concentrated point loads. The span length and the arm of force varied from test to test in accordance with the intended failure mode which was moment failure for beam no.1 and no.3 and shear failure for beam no.2 and no.4.

The arrangement of the CFRP plates for beam no.3 and no.4 is illustrated in Figure 2.

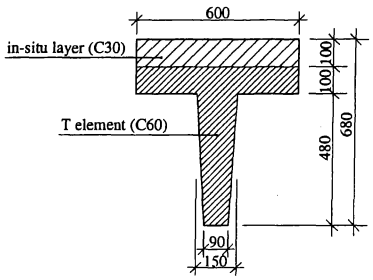

Figure 1 – Dimensions of the cross-section

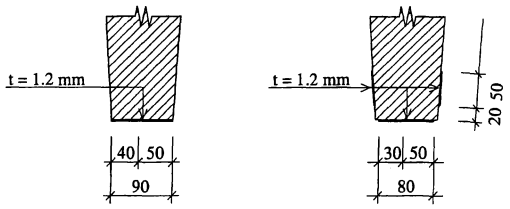

Figure 2 – Arrangement of the CFRP plates (beam no.3 and no.4)

3 Finite element modeling

Due to the low width-height ratio of the flange, uniform stress distribution can be assumed in the horizontal direction of the cross-section and so a two dimensional plane stress idealization is justified. Since the structure and loading scheme are symmetrical, it was sufficient to model only the left half of the beam. Eight-node plane stress elements with 3×2 Gauß integration scheme were used.

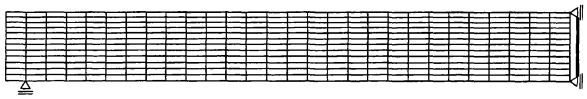

Figure 3 – Finite element mesh

Prestressing wires and the CFRP plates were modeled with embedded reinforcement elements assuming perfect bond between them and the concrete. Therefore the analyses were not intended to address localized failure modes where failure occurs between the concrete and the CFRP plates.

Cracking and crushing of the concrete and plasticity of the prestressing steel are the governing non-linear phenomena. A total strain based crack model implemented in DIANA and developed along the lines of the Modified Compression Field Theory was used to model concrete in both tension and compression. The constitutive model describes the stress as a function of the strain. The stress-strain relationships are evaluated in the principal directions of the strain vector which is known as the rotating crack concept.

In cracked concrete the principal compressive stress is a function not only of the principal compressive strain, ε_2, but also of the coexisting principal tensile strain, ε_1 [3]:

$$f_{2,max} = f_c \cdot \frac{1}{1+K_c} \le f_c \qquad K_c = 0.27 \cdot \left(-\frac{\varepsilon_1}{\varepsilon_{co}} - 0.37 \right)$$

where

$f_{2,max}$ *maximum compressive stress when the lateral principal tensile strain is* ε_1,
ε_{co} *compressive strain at maximum compressive stress (may be taken as -0.002).*

In the tension regime exponential softening curve was applied in the cracked concrete.

4 Evaluation and conclusions

Figure 4 compares calculated and measured load-deflection curves. In case of analysis 'A' material properties of the prestressing steel were taken with its given characteristic values while in case of analysis 'B' they were increased by 10 percent as a rough estimate for mean values. (Note that test no.1 and no.2 were terminated without reaching failure.)

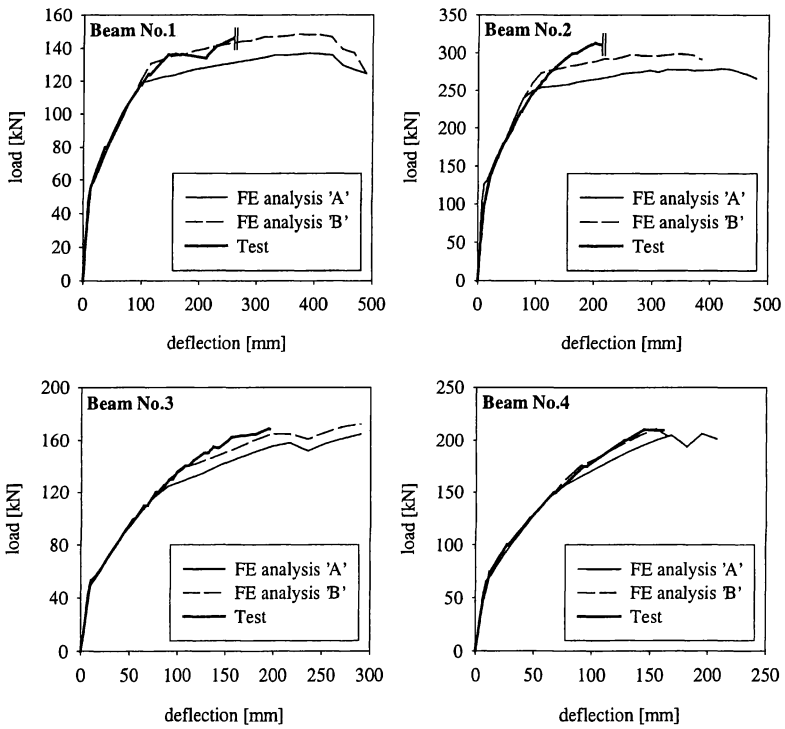

Figure 4 – Measured and calculated load-deflection curves (midspan)

Finite element analyses have given a fairly accurate prediction with respect to the maximum flexural moment and maximum shear force (Table 1 and Table 2), however, corresponding deformations were somewhat smaller than predicted. Finite element analysis has proved its advantage over simplified design methods particularly in case of shear failure where the conservative nature of the simplified shear design method is evident.

Table 1 – Maximum flexural moment (analysis vs. test)

	Maximum flexural moment [kNm]		
	NS 3473	*FE Analysis A/B*	*Test*
Beam No.1	*487*	*560 / 601*	*600*
Beam No.3	*679*	*734 / 765*	*751*

(NS 3473 – Norwegian Standard)

Table 2 – Maximum shear force (analysis vs. test)

	Maximum shear force [kN]		
	NS 3473	*FE Analysis A/B*	*Test*
Beam No.2	*159*	*291 / 312*	*324*
Beam No.4	*133*	*211 / 215*	*214*

The total strain based crack model has proved to be very well suited for modeling cracking with the smeared cracking approach and was found numerically stable which is often not the case with other crack models.

A comprehensive review of the project is given in a recent report [4] from the Norwegian University of Science and Technology, Department of Structural Engineering.

References

[1] de Witte, F. C. and Kikstra, W. P., DIANA Release 7.2 User's Manual, Nonlinear Analysis, TNO Building and Construction Research, Delft, The Netherlands, 1999

[2] Vecchio, F. J. and Collins, M. P., "The Modified Compression-Field Theory for reinforced concrete elements subjected to shear", ACI Journal, Proceedings V. 83, No. 2, Mar.-Apr. 1986, USA, pp. 219-231

[3] Vecchio, F. J. and Collins, M. P., "Compression Response of Cracked Reinforced Concrete", Journal of Structural Engineering, ASCE, 119, 1993

[4] Takács, P.F. and Kanstad T.: "Strengthening prestressed concrete beams with Carbon Fiber Reinforced Polymer plates", NTNU Report R-9-00, ISBN 82-7482-057-6, Trondheim, Norway, 2000

Crack Control of Hardening Concrete Structures - Verification of a Three-step Engineering Method

Jan Olofsson, Skanska Teknik AB, Gothenburg, Sweden
Daniela Bosnjak and Terje Kanstad, Division of Structural Engineering, NTNU, Norway

Background

Methods to prevent early-age cracking should be based on stress-strain based criterions and consider the many crucial factors involved; material properties as hydration heat development, thermal conductivity, mechanical properties, creep, autogenous shrinkage, thermal dilation, and external factors as ambient air temperature, wind speed, formwork-stripping, fresh concrete temperature, and finally, structural restraint from adjoining structures and subgrade. To obtain reliable calculation results, and to achieve an efficient methodology to prevent such cracking, are two major objectives by the Brite-EuRam Project IPACS (Improved Production of Advanced Concrete Structures) with partners from Sweden, Norway, The Netherlands, Germany and Italy (1997-2001).

Several specially designed finite element programs for analysing 2D temperature and 2D-2½D stress development in hardening concrete have been developed in recent years, e.g. Constre, HACON, 4CTemp&Stress and HEAT2.5D. In such programs only a slice (the cross section) of the structure is modelled, and while the temperature variations over the cross section can be quite accurately predicted, simplifications as the compensation plane method (infinitely long structure assumption), must be used to determine the principal stresses in the out of plane direction. Consequently, the adequate use of these programs requires knowledge of the total 3D structural response and the transformation into 2D-2½D models. Another drawback is the huge amount of time consuming calculations often needed to examine different casting situations due to variation of external conditions, position of embedded cooling pipes or heating cables etc for the studied structure.

Considering the problems mentioned above, it is important to find simplified models and methods to reduce the computational complexity. For the Öresund Bridge Project, Skanska Teknik developed a three-step engineering method for estimating early-age cracking. The 4CTemp&Stress program developed at DTI in Denmark, and its compensation plane method was used in the third and final step. As a part of the IPACS-project the engineering method is described and verified in two reports [1, 3].

Three-step engineering method

The method combines global linear elastic analysis and local time-dependent temperature and stress calculations of simplified structural models, representing the critical positions in the structure. It is divided into three steps as illustrated by Figure 1:

1. 2D (x, y) temperature and E-modulus analysis of cross section
1. 2D (y, z) or 3D linear elastic restraint analysis of total structure
1. 2½D (x, y, z) non-linear stress analysis of simplified model

In the first step the mean E-modulus during the heating (expanding) and cooling (contraction) phase are calculated for the hardening concrete. For the restraining structure the 28-days E-modulus must be used. The typical early-age crack problem structures usually consist of a hardening structural element cast against an already hardened structure (wall-foundation problem).

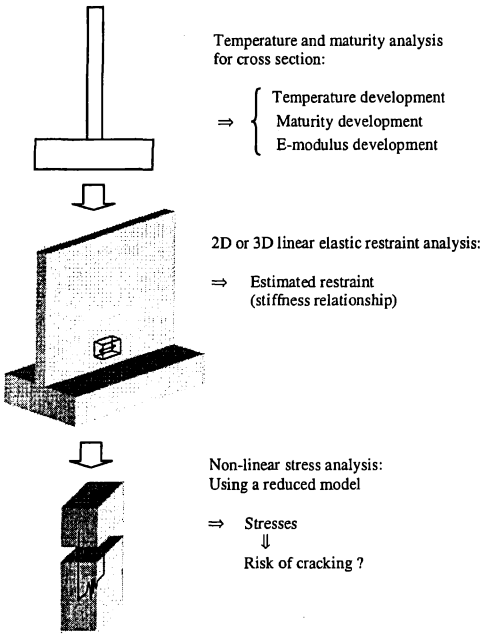

***Figure 1** Steps in proposed engineering method for crack risk estimation.* [1].

The structural restraint is estimated in two linear elastic analyses in the second step. The first simulation gives the average restraint during the expansion phase, and the second during the contraction phase. An arbitrary constant temperature load is applied on the hardening part of the structure in these analyses, resulting in restraint stresses. The main tensile stress, which in most cases is parallel to the structures length-axis and located in the lower central part of the hardening concrete, is then compared to the stress level for 100 % restraint, i.e. with no strain. A restraint factor R_z is then found by Eq. (1) for both the expansion and the contraction phases:

$$R_z = \frac{\sigma_{zz}}{\alpha_\theta \Delta T_{pre} E_{new}} \qquad (1)$$

σ_{zz} = Stress in the z-direction for the studied part [MPa]
α_θ = Thermal dilation coefficient [$°C^{-1}$]
ΔT_{pre} = Arbitrary prescribed temperature load [°C]
E_{new} = Elastic modulus of the hardening concrete used in the restraint analysis [MPa]

In the third step the relation of out of plane stiffness between the new and old concrete in the simplified model is used to model the restraint in the z-direction as:

$$\frac{A_{adj} E_{adj}}{A_{new} E_{new}} = \frac{R_z}{1 - R_z} \qquad (2)$$

The studied part is connected to a, from a restraint point of view, relevant part of the old adjoining structure in the expansion phase and with necessary adjustment of stiffness in the model also in the contraction phase. The model can be used to study effects of e.g. stripping of formwork, i.e. stresses in the cross section (x, y) from uneven temperature
distribution resulting in risk of surface cracking as well as risk of through cracking (z) due to restraint in the contraction phase.

Verification

In the IPACS-project, the finite element program DIANA has the role of a master-program, i.e. it shall amongst others in certain cases serve as a facit for simplified methods etc. The DIANA-IPACS version is currently being modified in accordance with the developments in material modelling [2]. The Engineering method is verified by full 3D-analyses of a series of walls cast on foundation similar to the walls of the Maridalen Culvert [3], where a comprehensive field test programme was performed by the Norwegian IPACS-partners; Selmer ASA, The Directorate of Roads and NTNU. Figure 2 presents calculated temperatures and stresses, and it is seen that both the calculated temperatures and stresses agree well. The main explanation of the deviations is due to the cooling effect from the slab on the critical position of the wall, which is estimated to be equal to one wall thickness above the foundation. This is difficult to handle by the engineering method. Based on the results achieved so far, it can be concluded that the deviation between the Engineering method and the full 3D-analyses in general is less than 10%. This is a rather small deviation compared to the influence of the general uncertainty in material properties and external conditions that is apparent for the early age cracking problems. For instance is the general experience from the evaluation of the field tests of the Maridalen Culvert that the deviation between calculated and measured temperatures is within ±5°C, while the corresponding deviation for strains probably is as large as ±50E-6. A very rough estimate of the corresponding stress deviation is ±0.8MPa.
The subject is more thoroughly considered in [2].

References

[1] Kjellman O. and Olofsson J., *3D Structural Analysis of Crack Risk in Hardening Concrete Structure.* IPACS-report TG4/N2, 1999.
[2] Bosnjak, D., *Temperature induced cracking problems in hardening concrete structures,* Doctoral Thesis, The Norwegian University of Science and Technology, Trondheim, Norway, 2000 (to be published).
[3] Kanstad, T., *Verification of Skanska's Engineering Method by Timedependent full 3D DIANA-analyses* . IPACS-report, October 2000
[4] Heimdal, E., Kanstad, T og Kompen, R. (1998) *Maridal culvert Field test,* IPACS, NOR-IPACS, and SINTEF report STF22 F98734. ISBN 82-14-01044-6.

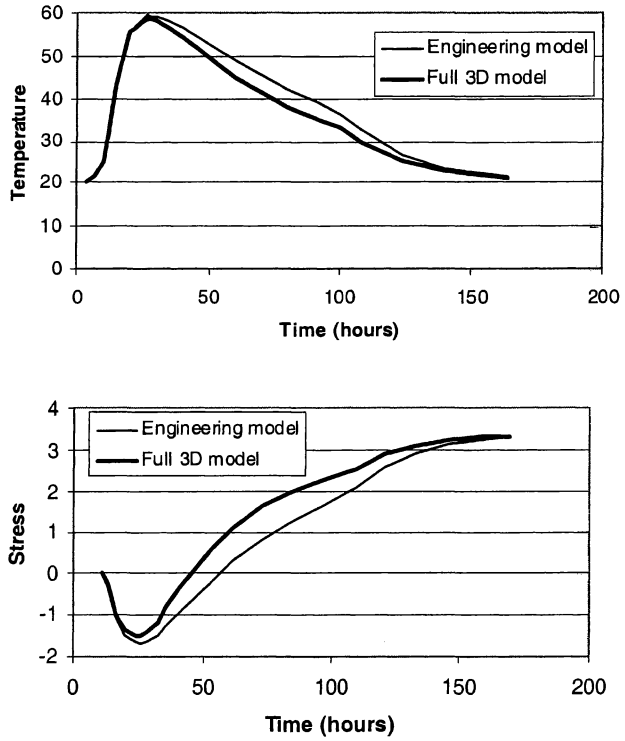

Figure 2. Calculated temperature and stress development in the critical position for through cracking, i.e. one wall thickness above the foundation.

The Rational Krylov Algorithm for Nonlinear Eigenvalue Problems

Patrik Hager
Department of Structural Mechanics,
Chalmers University of Technology, Göteborg, SE-41296 Sweden.
Email: patrikh@sm.chalmers.se

Introduction

Using a viscoelastic constitutive relation to describe the material behaviour in the equations of motion yields a nonlinear eigenproblem for the case of free vibrations. The equations of motion (nonlinear eigenproblem) are solved most conveniently by the displacement based Finite Element Method, FEM. To obtain accurate solutions it is often required a large number of unknowns in the FE equations, thus, the system matrices can be of large order. The resulting algebraic nonlinear eigenproblem can either be solved as an linear eigenproblem using a state-space formulation or it can be solved as it is, a nonlinear eigenproblem. The state-space formulation leads to matrices many times larger than the nonlinear formulation, and it is also cumbersome to establish the matrices of the state-space formulation. Little work has been devoted to the direct solution of the nonlinear eigenproblem.

The present paper deals with free vibration analysis of damped mechanical systems, where the damping effects are modelled by a viscoelastic constitutive relation. The equations of motion are solved approximately by the displacement based Finite Element Method, FEM. We study a method to solve the nonlinear eigenproblem by means of rational Krylov, formulated in the RKS ALGORITHM. The numerical examples show that rational Krylov can be used to find accurate solutions and that it is effective in terms of computational effort.

Viscoelastic Model

We employ a simple form of the linear standard viscoelastic model, it consists of a linear spring and a Maxwell unit combined in parallell. The material is assumed isotropic and we assume isothermal conditions. We also assume that the viscoelastic behaviour under conditions of so-called pure shear and pure dilation is similar, whereby we do not separate the stress and strain tensors into their deviatoric and spherical parts. The stress tensor, $\boldsymbol{\sigma}$, and the strain tensor, $\boldsymbol{\varepsilon}$, relationship can be expressed as:

$$\sigma_{ij}(t)+b\frac{d}{dt}\sigma_{ij}(t)=2G_{\infty}\varepsilon_{ij}(t)+L_{\infty}\delta_{ij}\varepsilon_{kk}(t)+b\frac{d}{dt}(2G\varepsilon_{ij}(t)+L\delta_{ij}\varepsilon_{kk}(t)) \qquad (1)$$

where G and L are the instantaneous Lamé's constants, G_{∞} and L_{∞} are the relaxed Lamé's constants and b is the relaxation constant with dimension time. The initial conditions to the constitutive relation differential equation is the elastic Hooke's law.

Variational Formulation

The governing equations are the equations of motion, the constitutive equations and the assumption of small displacements:

$$\sigma_{ji,j}=\rho\ddot{u}_i, \quad in\,\Omega \qquad (4)$$

$$\sigma_{ij}+b\dot{\sigma}_{ij}=2G_{\infty}\varepsilon_{ij}+L_{\infty}\delta_{ij}\varepsilon_{kk}+b(2G\dot{\varepsilon}_{ij}+L\delta_{ij}\dot{\varepsilon}_{kk}) \qquad (5)$$

and:

$$\varepsilon_{ij} = 1/2(u_{i,j} + u_{j,i}) \tag{6}$$

where body forces and surface tractions are zero.

We multiply the equations of motion, Equation (4), with the complex conjugate of functions $\hat{u}_i$ that is zero at and corresponding to the essential boundary conditions. Let the complex conjugate of a be denoted by $\overline{a}$. We integrate the resulting product over a part of the domain, Ω_m, that contains all the material with the relaxation constant $b = b_m$. By using the divergence theorem on the resulting integral we obtain:

$$\int_{\Omega_m} \sigma_{ij}\overline{\hat{\varepsilon}}_{ij}dx + \int_{\Omega_m} \rho\ddot{u}_i\overline{\hat{u}}_i dx = \int_{\Gamma_m} t_i\overline{\hat{u}}_i ds \tag{7}$$

where Γ_m is the boundary of Ω_m and $\mathbf{t}$ is the traction vector in the outward normal direction on Γ_m. Differentiating Equation (7) with respect to time and multipling with the relaxation constant b_m and adding the result to Equation (7) yields:

$$\int_{\Omega_m} (1+b_m D)\sigma_{ij}\overline{\hat{\varepsilon}}_{ij}dx + \int_{\Omega_m}(1+b_m D)\ddot{u}_i\overline{\hat{u}}_i dx = \int_{\Gamma_m}(1+b_m D)t_i\overline{\hat{u}}_i ds \tag{8}$$

where $D = \frac{d}{dt}$. We note that $(1+b_m D)\sigma$ corresponds to the left hand side of the constitutive relation, Equation (5), and thus we substitute it with the right hand side of the constitutive relation. We introduce the notation of scalar products where:

$$a_m(\mathbf{u},\hat{\mathbf{u}}) = \int_{\Omega_m}(2G\varepsilon_{ij} + L\delta_{ij}\varepsilon_{kk})\overline{\hat{\varepsilon}}_{ij}dx \tag{9}$$

is a strain-energy-type scalar product and:

$$c_m(\mathbf{u},\hat{\mathbf{u}}) = \int_{\Omega_m}\rho u_i\overline{\hat{u}}_i dx \tag{10}$$

is a kinetic-energy-type scalar product and we obtain:

$$a_m^{\infty}(\mathbf{u},\hat{\mathbf{u}}) + \mathrm{b}_m a_m(\dot{\mathbf{u}},\hat{\mathbf{u}}) + c_m(\ddot{\mathbf{u}},\hat{\mathbf{u}}) + \mathrm{b}_m c_m(\mathrm{D}\ddot{\mathbf{u}},\hat{\mathbf{u}}) = \int_{\Gamma_m}(1+b_m D)t_i\overline{\hat{u}}_i ds \tag{11}$$

where a_m^{∞} is the strain-energy-type scalar product using the relaxed Lamés constants. Consider the trial solution $\mathbf{u} = \mathbf{q}e^{\lambda t}$, by inserting the trial solution and dividing with the common time factor $e^{\lambda t}$ we have:

$$a_m^{\infty}(\mathbf{q},\hat{\mathbf{u}}) + \lambda b_m a_m(\mathbf{q},\hat{\mathbf{u}}) + (1+\lambda b_m)\lambda^2 c_m(\mathbf{q},\hat{\mathbf{u}}) = (1+\lambda b_m)\int_{\Gamma_m}\mathbf{t}_{\mathrm{q}}\cdot\overline{\hat{\mathbf{u}}}ds \tag{12}$$

where $\mathbf{t} = \mathbf{t}_{\mathrm{q}}e^{\lambda t}$. Add $a_m(\mathbf{q},\hat{\mathbf{u}}) - a_m(\mathbf{q},\hat{\mathbf{u}}) = 0$ to Equation (12) and let $a_m^{\Delta} = a_m - a_m^{\infty}$ and we have:

$$(1+\lambda b_m)\{a_m(\mathbf{q},\hat{\mathbf{u}}) + \lambda^2 c_m(\mathbf{q},\hat{\mathbf{u}})\} - \mathrm{a}_m^{\Delta}(\mathbf{q},\hat{\mathbf{u}}) = (1+\lambda b_m)\int_{\Gamma_m}\mathbf{t}_{\mathrm{q}}\cdot\overline{\hat{\mathbf{u}}}\mathrm{d}s \tag{13}$$

or, if we divide by the factor $(1+\lambda b_m)$:

$$\lambda^2 c_m(\mathbf{q},\hat{\mathbf{u}}) + a_m(\mathbf{q},\hat{\mathbf{u}}) - \frac{1}{1+b_m\lambda}a_m^{\Delta}(\mathbf{q},\hat{\mathbf{u}}) = \int_{\Gamma_m}\mathbf{t}_{\mathrm{q}}\cdot\overline{\hat{\mathbf{u}}}ds \tag{14}$$

Finally, we sum the integrals over all partitions Ω_m, $m = 1,\ldots,NMAT$ and invoke that we have zero surface tractions on the boundary of Ω to obtain the variational form of the equations of motion:

$$\lambda^2 c(\mathbf{q},\hat{\mathbf{u}}) + a(\mathbf{q},\hat{\mathbf{u}}) - \sum_{m=1}^{NMAT} \frac{1}{1+b_m\lambda} a_m^{\Delta}(\mathbf{q},\hat{\mathbf{u}}) = 0 \qquad (15)$$

where $c = \sum_{m=1}^{NMAT} c_m$ and $a = \sum_{m=1}^{NMAT} a_m$.

Finite Element Formulation

A displacement based FE formulation is employed. The assumed time-independent displacement field within an element is expressed in the form:

$$q^h = N^e x^e \qquad (16)$$

where N^e is the the element shape function matrix and x^e is the nodal displacement vector. The superscript h denotes the mesh size and indicates that the displacement field q^h is the FE solution not necessarily equal to q, the exact solution. Following the Galerkin method to obtain the FE equations we insert the assumed displacement field into the variational form of the equations of motion, Equation (15) and use the basis functions as test functions and we have the discretisized equations of motion:

$$(\lambda^2 M + K - \sum_{m=1}^{NMAT} (\frac{1}{1+b_m\lambda}\Delta K_m))x = 0 \qquad (17)$$

where M is the consistent mass matrix, K is the stiffness matrix with the instantaneous elastic material parameters used in Hooke's law, $\Delta K_m = \sum_{e=1}^{NEL(m)} K_{\Delta}^e$ where K_{Δ}^e is an element stiffness matrix with ΔG and ΔL used in Hooke's law and the summation is carried over the $NEL(m)$ elements with relaxation constant b_m.

Solution of Nonlinear Eigenproblem

We seek latent pairs, *i.e.* latent roots λ and corresponding latent vectors x, of the nonlinear eigenproblem:

$$A(\lambda)x = 0 \qquad (18)$$

In this paper the $n \times n$ matrix $A(\lambda)$ is complex and symmetric, explicitly written as:

$$A(\lambda) = \lambda^2 M + K - \sum_{m=1}^{NMAT} (\frac{1}{1+b_m\lambda}\Delta K_m) \qquad (19)$$

obtained from a FE discretisation, where n is the number of degrees of freedom. For simplicity we pose problems such that the matrices K and M are positive definite and the matrices ΔK_m are positive definite or positive semidefinite.

We aim to determine a few latent roots and vectors of the nonlinear eigenproblem by means of rational Krylov. Rational Krylov have been used to solve linear eigenproblems involving large sparse nonsymmetric matrices, [1], [2]. In that context, it is a generalisation of the shifted and inverted Arnoldi algorithm, where several factorisations with different shifts are used in one run. It computes an orthogonal basis and a small Hessenberg pencil.The rational Krylov approach in this paper can be viewed as nested Regula falsi and Arnoldi iterations.

We linearise the nonlinear eigenproblem $A(\lambda)x = 0$ by a Lagrange interpolation of $A(\lambda)$ between the two points σ and μ, thus:

$$A(\lambda) = \frac{\lambda-\sigma}{\mu-\sigma}A(\mu) + \frac{\mu-\lambda}{\mu-\sigma}A(\sigma) + \frac{(\lambda-\sigma)(\lambda-\mu)}{2}R \qquad (23)$$

where $\|R\| \leq \|A''(\xi)\|$ and ξ is in an interval if λ, μ, σ are in the interval. We keep σ fixed for several steps and iterate on μ, by neglecting the remainder in the Lagrange interpolation we have a Regula falsi method:

$$\left(B^j - \theta I\right)x = 0, \quad \theta = \frac{\mu_{j+1} - \mu_j}{\mu_{j+1} - \sigma}, \quad \mu_j \to \lambda \, as \, j \to \infty \tag{24}$$

which is a linear eigenproblem for each j where $B^j = A(\sigma)^{-1} A(\mu_j)$. The matrix B^j is in general complex and non-Hermitian.

To solve the linear eigenproblem that resulted from the Regula falsi it is possible to use Arnoldi. The Arnoldi iteration can simply be written:

$$B^j V_k = V_{k+1} H_{k+1,k} \tag{28}$$

where the $n \times k$ matrix $V_k = [v_1 v_2 \ldots v_k]$ is an orthonormal basis with a column, also called Arnoldi vector, added in each iteration step k and the $(k+1) \times k$ matrix $H_{k+1,k} = [h_1 h_2 \ldots h_k]$ is Hessenberg containing Gram-Schmidt orthogonalisation coefficients.

In rational Krylov we nest the two iterations, expressed as:

$$B^j V_j = V_{j+1} H^j_{j+1,j}, \quad H^j_{j,j} s = \tilde{\theta} s, \quad \theta \approx \tilde{\theta} \Rightarrow \mu_{j+1} \tag{29}$$

If we apply rational Krylov strictly as it is written in Equation (32) then the matrix $H^j_{j+1,j}$ of orthogonalisation coefficients must be computed by an expensive $H^j_{j+1,j} = V^H_{j+1} B^j V_j$ in each step j, and moreover, the matrix $H^j_{j+1,j}$ is not Hessenberg. In order to avoid an expensive computation of $H^j_{j+1,j}$ we update the matrix used in the previous step and let only the last column be true orthogonalisation coefficients, *i.e.* we use:

$$\tilde{H}^j_{j,j-1} = \frac{\mu_j - \sigma}{\mu_{j-1} - \sigma} \tilde{H}^{j-1}_{j,j-1} - \frac{\mu_j - \mu_{j-1}}{\mu_{j-1} - \sigma} I_{j,j-1} \tag{30}$$

References

[1] A. Ruhe, *The rational Krylov algorithm for nonsymmetric eigenvalue problems. III: complex shifts for real matrices*, BIT, Vol. 34, No. 1, 1994.

[2] A. Ruhe, *Rational Krylov: a practical algorithm for large sparse nonsymmetric matrix pencils*, SIAM J. Sci. Comput., Vol. 19, No. 5, pp 1535-1551, 1998.

ON NUMERICAL ALGORITHMS FOR DERIVATIVE NONLINEAR SCHRÖDINGER EQUATION

F.Ivanauskas
(Vilnius University, Institute of Mathematics and Informatics)
T.Meskauskas
(Vilnius University)

In this report we deal with the derivative nonlinear Schrödinger equation

$$\begin{aligned}\frac{\partial u}{\partial t} =& ia\frac{\partial^2 u}{\partial x^2} + b\frac{\partial u}{\partial x} + icu + id|u|^2 u + ik|u|^4 u + \\ & \alpha|u|^2\frac{\partial u}{\partial x} + \beta u\frac{\partial |u|^2}{\partial x},\end{aligned} \tag{1}$$

where $u = u(x,t)$ is unknown complex function, a, b, c, d, k, α, β – given real coefficients, $i = \sqrt{-1}$. This differential equation is studied for $t \in (0,T]$ and for x in some bounded interval $\Omega \subset \mathbf{R}$. For simplicity we let $\Omega = (0,1)$. ote that by rescaling a time variable t one coefficient can be set to 1 in equation (1). Therefore we further assume $a = 1$.

Hence the derivative nonlinear Schrödinger equation, or generalized nonlinear Schrödinger equation as it sometimes referred to in the literature, being a generalization of the nonlinear Schrödinger equation, is an abstract tool in many fields of modern science. The exhaustive information on the applications of the above models can be found in [1, 2].

We consider (1) together with initial and boundary conditions. Having defined the initial function

$$u(x,0) = u^{(0)}(x), \quad x \in \Omega, \tag{2}$$

we are going to justify a numerical analysis for the solution $u(x,t)$, satisfying one of the two different type conditions on the boundary. One of the popular ways in numerical modelling of the corresponding Cauchy problem is to truncate a solution outside of some given region Ω, i.e. zero Dirichlet boundary conditions

$$u(0,t) = u(1,t) = 0, \quad 0 \le t \le T. \tag{3}$$

Sometimes conditions (1) are already the part of the model. There also exists another approach caused by specific features of some modelled phenomena, namely, periodic boundary value problem

$$u(0,t) = \theta u(1,t), \quad \frac{\partial u}{\partial x}\Big|_{x=0} = \theta\frac{\partial u}{\partial x}\Big|_{x=1}, \quad 0 \le t \le T \tag{4}$$

with complex parameter (phase shift) θ, such that $|\theta| = 1$.

We assume at $t = 0$ initial function (2) satisfies boundary conditions (3) or (4), respectively.

The nonlinear Schrödinger equation (1) is one of the most generic soliton equations. Extended versions of the nonlinear Schrödinger equation with higher order nonlinearities have been proposed by various authors. It has been revealed that there exist "integrable"

cases even for extended equations. Among them, there are two celebrated equations with derivative type nonlinearities. One is the Chen-Lee-Liu equation

$$\frac{\partial u}{\partial t} = i\frac{\partial^2 u}{\partial x^2} - 2|u|^2\frac{\partial u}{\partial x},$$

and the other is the Kaup-Newell equation.

$$\frac{\partial u}{\partial t} = i\frac{\partial^2 u}{\partial x^2} - 2\frac{\partial}{\partial x}(|u|^2).$$

The pioneering inverse scattering transformation method [3] and its subsequent modifications made it possible to find analytic solutions to many well-known equations of mathematical physics. The analysis of the solitary waves appearing in different cases of derivative nonlinear Schrödinger models was done in [4, 5, 6, 7]. Recently there were computed new classes of symmetry reductions and associated exast solutions of two dimensional (with space variables x and y) derivative nonlinear Schrödinger equation [8].

Note though, that all known results in this field deal with the Cauchy problem. We examine the boundary problems, which require a different or adopted techniques. The techniques we apply is different from that used in [9, 10, 11, 12].

Another approach in numerical analysis is to apply finite elements methods [13, 14].

For initial boundary values problems of derivative nonlinear Schrödinger equation the numerical algorithm is proposed and its convergence and stability in C^1 norm is proved. There is no restrictions between space and time grid steps.

For periodic and mixed Dirichlet-von Neumann boundary problems of two nonlinear Schrödinger equations system the convergence and stability of Crank-Nicolson finite difference scheme in C norm is proved. There is no restrictions between space and time grid steps.

REFERENCES

1. A.C.Newell and J.V.Moloney, *Nonlinear Optics*, Addison-Wesley, Redwood City, California, 1991.
2. Zacharow V.E., Manakov S.V., Novikov S.P., Pytajevskij L.P. *Theory of soliton the inverse problem method*, [in Russian], Nauka, 1980.
3. M.J.Ablowitz and H.Sigur, *Solitons and Inverse Problem Method* [in Russian], Mir, Moscow, 1987.
4. G.Boling and W.Yaping, *Jornal of Differential Equations,* **123**, p. 35-55, 1995.
5. S.Kakei, N.Sasa and J.Satsuma, *J. Phys. Soc. Japan,* **64**(5), p. 1519–1523, 1995.
6. D.J.Kaup and A.C.Newell, *J. Math. Phys.,* **19**(4), p. 798–801, 1978.
7. W.van Saarloos and P.C.Hohenberg, *Physics D*, **56**, p. 303–367, 1992.
8. S.Hood, *J. Phys. A: Math. Gen.*, **31**, p. 9715–9727, 1998.
9. A.Domarkas and F.Ivanauskas, *Lietuvos Matematikos Rinkinys*, **27**(1), p. 48–57, 1987.
10. N.Hayashi, *Nonlinear Analysis. Theory , Methods & Application*, **20**(7), p. 823–833, 1993.
11. N.Hayashi and T.Ozawa, *Diff. Integral Eqs.*, **8**, p. 1061–1072, 1995.
12. N.Hayashi and E.I.Kaikina, *SUT J. of Math.*, **34**(2), p. 111–137, 1998.
13. Y.Tourigny, *IMA Journal of Numerical Analysis*, **11**, p.509-523, 1991.
14. Y.Tourigny,*Numerical Methods for Partial Differential equations*, **10**, p. 757-769, 1994.

A FAST MARCHING METHOD FOR 3D RESERVOIR SIMULATION

K. H. KARLSEN, K.-A. LIE, J. R. NATVIG, AND N. H. RISEBRO

1. Introduction

The motivation for doing reservoir simulation is to optimize the production of oil for different scenarios of enhanced recovery, such as water flooding, or polymer flooding. To give accurate predictions, one is faced with the problem of tracking the motion of the resident and injected fluid (i.e. oil and water). This motion is typically modelled by a coupled system of nonlinear equations in total pressure and fluid saturation; an elliptic equation for the pressure and a convection-diffusion equation for the saturation.

In many situations, the fluid motion from injection to production wells is dominated by convection. In such cases it is reasonable to neglect capillary pressure. The saturation equation then reduces to a nonlinear first order hyperbolic conservation law, which may develop discontinuous solutions even for smooth initial data. These discontinuities correspond to sharp interfaces between fluids, and are of great importance in determining how much and where the oil is in a reservoir. Moreover, exact predictions of water breakthrough in production wells are important to determine when separation equipment is needed.

In recent years, many methods have been devised to resolve these sharp fluid interfaces numerically. We present here the extension to three spatial dimensions of a novel method introduced by Karlsen, Lie and Risebro [1], based on the level set idea of Osher and Sethian [3] and the fast marching method of Sethian [4]. An important feature of the new method is that it has no inherent time step restriction; the length of each step can be chosen from accuracy considerations only.

2. The Mathematical Model

We consider a standard model for the flow of two immiscible fluids in a medium Ω with porosity ϕ and permeability K. Injection of one fluid and production of the other in different areas of the domain gives rise to a pressure gradient in the reservoir and a displacement of the two fluids. The relation between the flow rate and the pressure gradient in each phase is modelled by Darcy's law

$$v_i = -\lambda_i\big(\nabla P_i - \rho_i g \nabla D\big), \tag{1}$$

where i refers to the fluid phase (i.e., wetting $\mathbf{w}$ or non-wetting $\mathbf{n}$), g is the gravitational acceleration, D measures the vertical distance in the medium, P_i is the pressure, and ρ_i the mass density of phase i. The proportionality factor λ_i is called the mobility of phase i. In this paper, we assume that $P_{\mathbf{n}} = P_{\mathbf{w}} = P$, thereby neglecting capillary pressure. Furthermore, we assume incompressible medium and fluids. Conservation of mass for each fluid phase reads

$$\frac{\partial(\phi\rho_i S_i)}{\partial t} + \nabla\big(\rho_i v_i\big) = q_i, \tag{2}$$

where ϕ is the total available pore volume, S_i is the saturation of phase i, and q_i represents any sources or sinks for phase i. The saturation of phase i is the percentage of the available pore volume occupied by this phase, hence $S_n + S_w = 1$. Under these assumptions, the equation for the pressure reads

$$\nabla(\lambda_T \nabla P) + Q_T = \nabla\big[(\lambda_{\mathbf{n}}\rho_{\mathbf{n}} + \lambda_{\mathbf{w}}\rho_{\mathbf{w}})g\nabla D\big], \tag{3}$$

where $\lambda_T = \lambda_{\mathbf{n}} + \lambda_{\mathbf{w}}$ is the total mobility. In the following, we will neglect gravity. By introducing the fractional flow function f_i defined by $\lambda_i = f_i(\lambda_{\mathbf{n}} + \lambda_{\mathbf{w}})$, we get a hyperbolic equation for the saturation

$$\phi\frac{\partial S_{\mathbf{n}}}{\partial t} + v_T \nabla f_{\mathbf{n}}(S_{\mathbf{n}}) = -q_{\mathbf{n}}, \tag{4}$$

with total Darcy velocity given by $v_T = -\lambda_T \nabla P$. In the following we will drop the subscripts in the saturation equation.

We are mainly concerned with the initial value problem given by (3)–(4) and the initial data

$$S_0(\mathbf{x}) = \begin{cases} 1, & \text{if } |\mathbf{x} - \mathbf{x}_w| < r_w \text{ and } q_{\mathbf{n}}(\mathbf{x}_w) > 0, \\ 0, & \text{otherwise,} \end{cases} \tag{5}$$

Date: October 3, 2000.

Key words and phrases. oil reservoir simulation, level set method, fast marching method, numerical examples.

for $\mathbf{x} \in \Omega$ and $r_w > 0$. This corresponds to injection of water ($\mathbf{n}$) into a reservoir fully saturated with oil ($\mathbf{w}$). On the boundary $\partial\Omega$ we impose homogeneous Neumann boundary conditions both for the pressure equation (3) and the saturation equation (4). To make a well-posed method, we assume that the fractional flow function is S-shaped, i.e., non-decreasing with one inflection point and $f(0) = 0$, $f(1) = 1$.

3. The Numerical Method

3.1. Overall Strategy. To solve the coupled system of differential equations (3)–(4), we use a standard operator splitting scheme, commonly referred to as IMPES (IMplicit Pressure, Explicit Saturation). The overall strategy is to advance the solution (S, P) in steps Δt to a final time $t_f = N\Delta t$. Assume that the solution (S^n, P^n) at time $t_n = n\Delta t$ has been computed. To advance the solution to t_{n+1} we use the following splitting strategy. First we solve the pressure equation (3) with the saturation S^n held fixed,

$$\nabla(\lambda_T(S^n)\nabla P) + Q_T = 0,$$

using a standard finite element method. We then compute the total Darcy velocity v_T^{n+1} from P^{n+1} using (1). Finally we solve the saturation equation

$$\phi\frac{\partial S}{\partial t} + v_T^{n+1}\nabla f(S) = -q,$$

with fixed v_T^{n+1}. Starting with a suitable initial condition, this splitting will compute the solution to any prescribed time $t_f = N\Delta t$.

3.2. The Saturation Solver. Under the assumptions made in the IMPES strategy, the saturation equation (4) reduces to a hyperbolic conservation law

$$\phi(\mathbf{x})\frac{\partial u}{\partial t} + \mathbf{v}(\mathbf{x})\nabla f(u) = 0. \tag{6}$$

Here u is the unknown function (saturation), ϕ is the porosity of the medium and $\mathbf{v}$ is a divergence free vector field. We observe that for initial value problems of (6), the information only flows in certain directions, i.e., along what is commonly referred to as streamlines. To exploit this, we reformulate the evolution equation as a boundary value problem for a stationary Eikonal equation. This boundary value problem can be solved very rapidly by employing the *fast marching method* [4].

Consider now the isosurface corresponding to a constant value $u(\mathbf{x}, 0) = k$. This isosurface will evolve in time as the solution $u(\mathbf{x}, t)$ evolves according to (6). Let $\Xi_k(t)$ be a level set of the solution $u(\mathbf{x}, t)$ in the sense that

$$\Xi_k(t) = \{\mathbf{x} | u(\mathbf{x}, t) = k\},$$

that is, $\Xi_k(t)$ is the isosurface corresponding to $u(\mathbf{x}, t) = k$ at any time t. Now, assume that $\mathbf{y}_0 \in \Xi_k(0)$ and $\mathbf{y} \in \Xi_k(t)$ are points on the same characteristic curve $(\mathbf{x}(\tau), t(\tau))$ described by the characteristic equations

$$\dot{\mathbf{x}}(\tau) = \mathbf{v}(\mathbf{x})f'(u(\mathbf{x}, t)), \qquad \mathbf{x}(0) = \mathbf{y}_0, \tag{7}$$

$$\dot{t}(\tau) = \phi(\mathbf{x}), \qquad t(0) = 0. \tag{8}$$

We know that $u(\mathbf{x}(\tau), t(\tau)) = k$ is constant on the characteristic curve. Then there exists a $\tau(\mathbf{y})$ such that $\mathbf{y} = \mathbf{x}(\tau(\mathbf{y}))$. Since u is constant on $\Xi_k(t)$, (7)-(8) imply that the isosurface moves with a (particle) speed given by

$$\frac{d\mathbf{x}}{dt} = \frac{\dot{\mathbf{x}}(\tau)}{\dot{t}(\tau)} = \mathbf{v}(\mathbf{x})\frac{f'(k)}{\phi(\mathbf{x})}. \tag{9}$$

Then, from (7)-(9) we may compute

$$\phi(\mathbf{y}) = \frac{dt(\tau)}{d\tau} = \nabla_{\mathbf{y}}\tau(\mathbf{y}) \cdot \frac{d\mathbf{y}}{d\tau} = \nabla_{\mathbf{y}}\tau(\mathbf{y}) \cdot \frac{d\mathbf{x}(\tau)}{d\tau}|_{\mathbf{x}(\tau)=\mathbf{y}} = \nabla_{\mathbf{y}}\tau(\mathbf{y}) \cdot \mathbf{v}(\mathbf{y})f'(k). \tag{10}$$

Let $T_k(\mathbf{y}) = t(\tau(\mathbf{y}))$ be the time of arrival for the level set Ξ_k at $\mathbf{y}$. Then T_k is governed by (10). However, since $f'(k)$ is constant on the contour $\Xi_k(\cdot)$, we may as well solve the equation

$$\nabla T \cdot \mathbf{v}(\mathbf{x}) = \phi(\mathbf{x}). \tag{11}$$

Here we have defined $T = T_k f'(k)$. To supply the boundary conditions, we consider the initial data for the conservation law (6), i.e., $u_0(\mathbf{x}) = S_0(\mathbf{x})$. For the Eikonal equation this corresponds to boundary data of the form $\Xi_k(0) = \{\mathbf{x} | \, |\mathbf{x} - \mathbf{x}_w| = r_w, \, q_{\mathbf{n}}(\mathbf{x}_w) > 0\}$. In this case the solution of (6) is not smooth. We now

claim that the mapping $s = T(\mathbf{x})$ renders the initial value problem for (6) on a simpler one-dimensional Riemann problem. To see this, we set $w(s,t) = w(T(\mathbf{x}),t) = u(\mathbf{x},t)$ and compute, using (11)

$$\begin{aligned} &\frac{\partial}{\partial t}u(\mathbf{x},t) + \mathbf{v}\nabla f(u(\mathbf{x},t)) = \frac{\partial}{\partial t}w(s,t) + \frac{\partial}{\partial s}f(w(s,t)) = 0, \\ &u(\mathbf{x},0) = w(s,t) = \begin{cases} 1, & s < 0, \\ 0, & s \geq 0. \end{cases} \end{aligned} \tag{12}$$

Due to the form of f, the solution will consist of a shock $(0,\bar{v})$ and a rarefaction wave $(\bar{v},1)$, where $\bar{v}$ satisfies $f'(\bar{v})\bar{v} = f(\bar{v})$. We can now write down the solution of the (equivalent) problems (12) and (6):

$$w(s,t) = \begin{cases} (\tilde{f}')^{-1}(\frac{s}{t}), & \text{if } s < t\tilde{f}'(s/t), \\ 0, & \text{otherwise,} \end{cases} \quad \text{or} \quad u(\mathbf{x},t) = \begin{cases} (\tilde{f}')^{-1}(\frac{T(\mathbf{x})}{t}), & T(\mathbf{x}) \leq t\tilde{f}'(T(\mathbf{x})/t), \\ 0, & \text{otherwise.} \end{cases}$$

Here $\tilde{f}'$ is the derivative of the upper convex envelope of f and $(\tilde{f}')^{-1}$ is its inverse. This gives an implicit formulae for computing the saturation at an arbitrary point, given the time-of-flight. For a more complete description of this background, see Karlsen, Lie and Risebro [1].

3.2.1. *The fast marching method.* In order to solve the Eikonal equation (11), we use the fast marching method of Sethian [4]. The basic idea here is that information only flows in one direction, along the characteristics. Therefore, given a point $\mathbf{x}$, the solution at $\mathbf{x}$ only depends on the solution at points $\mathbf{y}$ in a neighbourhood of $\mathbf{x}$ with $T(\mathbf{y}) < T(\mathbf{x})$. The strategy in the fast marching method is to use this *causality* to arrange the nodes in increasing order, such that the solution can be computed *explicitly* using an upwind difference formula. This ordering cannot be known in advance, so it is constructed dynamically. To this end, we store a selection of nodes $\mathcal{N}$that are candidates for the next update. We label these nodes as *narrow-band* nodes, while nodes that have already been visited are *alive* nodes; the rest are *faraway* nodes. The set of alive nodes and faraway nodes are denoted $\mathcal{A}$ and $\mathcal{F}$, respectively.

Assume that the solution has been constructed for all alive nodes. Then the next step in the solution procedure is to pick the node $n \in \mathcal{N}$ with the smallest T. We update the arrival time for n and then the time for each of its neighbours. The solution at $\mathbf{x}_n$ has now been computed; to update the sets $\mathcal{A}$, $\mathcal{N}$ and $\mathcal{F}$, we label n as an alive node, and all n's neighbours that are faraway nodes are relabelled as narrow-band nodes. To compute the solution up to a time t_f, we continue this process until all nodes in $\mathcal{N}$ have $T \geq t_f f'(\bar{v})$ (recall definition of T). The solution is then computed on $\mathcal{A}$, while $T(\mathcal{N} \cup \mathcal{F})$ is arbitrarily set to $t_f f'(\bar{v})$. (We do not compute the complete solution since we only need to know arrival times $T \leq t_f f'(\bar{v})$.)

By storing $\mathcal{N}$ in a min-heap, the node with smallest time are extracted in $\mathcal{O}(1)$ operations and the faraway nodes are inserted in the heap in $\mathcal{O}(\log|\mathcal{N}|)$ operations. If the total number of nodes in the grid is m^3, then $|\mathcal{N}| = \mathcal{O}(m^2)$ and the solution of (11) is computed in $\mathcal{O}(m^3 \log m)$ operations.

3.2.2. *Restarting.* To apply the IMPES time stepping strategy, we need to be able to handle a time varying (piecewise constant) velocity field. In principle, the causality we based the fast marching method on is lost. However, since the total Darcy velocity is piecewise constant in the IMPES splitting, we are still able to apply the fast marching idea on each time step. When the velocity changes, we need to update the time-of-flight in the whole grid. To do this, we initialize several narrow bands corresponding to different level sets, and march each outwards, starting with the outermost band. This way, an approximate causality is maintained. Assuming the velocity field does not change much in each step, as is normally the case, the error introduced is small.

Therefore, assume that we have stopped the fast marching algorithm at time t_n. Then the largest time-of-flight in the domain is $t = t_n f'(\bar{v})$. We wish to restart the algorithm with a different velocity field. Let $t = N\delta$. For each $1 \leq j \leq N$, $j\delta$ corresponds to a level set Ξ_{k_j} with $j\delta = t_n f'(k_j)$. (Thus $k_N = \bar{v}$.) Initially, we construct N narrow bands $\mathcal{N}_j$, with corresponding sets $\mathcal{A}_j$ and $\mathcal{F}_j$, all of which are defined by

$$\begin{aligned} \mathcal{A}_j &= \{n : T(\mathbf{x}_n) < t_n f'(k_j)\}, \\ \mathcal{N}_j &= \{n : T(\mathbf{x}_n) > t_n f'(k_j),\ \mathcal{S}_n \cap \mathcal{A}_j \neq \emptyset\}, \end{aligned}$$

and $\mathcal{F}_j = \Omega_h - (\mathcal{A}_j \cup \mathcal{N}_j)$, where $\mathcal{S}_n$ is the set of neighbours of n. To construct the solution for times greater than t_n, we apply the fast marching algorithm to each narrow band $\mathcal{N}_j$ in turn, starting with $\mathcal{N}_N$, then $\mathcal{N}_{N-1}$, etc.

The remaining question is: how do we determine when to stop each band $\mathcal{N}_j$ to compute the solution at a later time t_{n+1}? Since each band corresponds to a different saturation value k_j, the characteristic

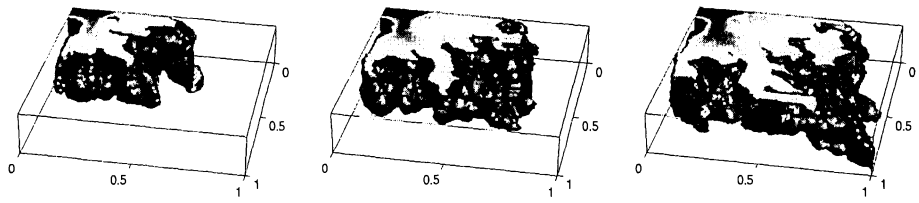

FIGURE 1. Example 1. Saturation component of the solution at time $t = 0.15$ (left), $t = 0.25$ (middle) and $t = 0.35$ (right). The level set (i.e. the front) in each figure is the actual oil-water front Ξ_0, while the shading on top show the saturation behind the oil-water interface.

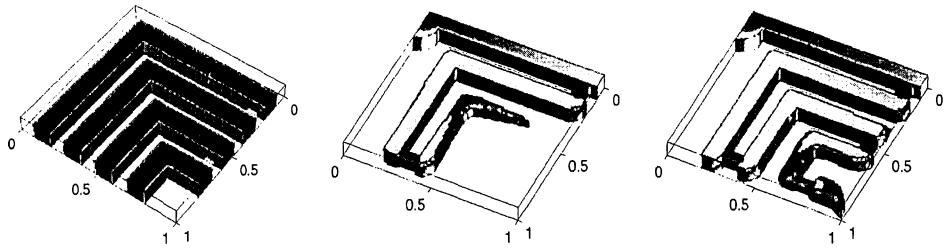

FIGURE 2. Example 2. The layered permeability field (left) and the saturation component of the solution of the artificial channel problem at time $t = 0.04$ (middle) and $t = 0.06$ (right).

speed $f'(k_j)$ is different for each band. Therefore it follows that the stopping time in the Eikonal equation (11) for band j is given by $t_{n+1}f'(k_j) = j\delta t_{n+1}/t_n$.

4. NUMERICAL EXAMPLES

4.1. Example 1: Inhomogeneous Quarter-Five-Spot. We consider a rectangular domain with dimensions $1.0 \times 1.0 \times 0.2$, partitioned uniformly in $100 \times 100 \times 20$ blocks. The mobilities of water and oil are $\lambda_w(S) = S^2$ and $\lambda_o(S) = 4(1-S)^2$ respectively; thus $f(S) = S^2/S^2 + 4(1-S)^2$.

Further, the permeability was generated with a log-normal distribution and subsequent smoothing. The result is a somewhat realistic-looking isotropic permeability field with $K_{11} = K_{22} = K_{33}$; the ratio between largest and smallest permeability is roughly 10^5.

The wells are vertical line sources; an injection well located at $(0, 0, \cdot)$ and a production well at $(1, 1, \cdot)$, both with intensities 0.2. The results are shown in Figure 1. We see that the structure of the oil-water interface, which is a shock, is well resolved.

4.2. Example 2: Channel Problem. The second test is an artificial channel problem. The case is designed to test how the method copes with water-oil fronts resulting from large jumps in the permeability. In reservoir simulation, such jumps occur in the presence of impermeable layers and faults.

The domain is rectangular with dimensions $1.0 \times 1.0 \times 0.1$. A series of Γ-shaped layers with low permeability are present in the slab, each having a small highly permeable "hole". In between these layers, the medium is highly permeable, see Figure 2. The ratio of the high and low permeabilities is 10^5 making the Γ-shaped regions virtually impermeable. The injector and productor are located at $(0, 0, \cdot)$ and $(1, 1, \cdot)$ respectively, with intensities 0.1. The available pore volume is $5.27 \cdot 10^{-2}$. Plot of saturation is given at two different times in Figure 2. The plots show that the fast marching method resolves the fluid interface accurately.

REFERENCES

[1] K. H. Karlsen, K.-A. Lie and H. H Risebro. A Fast Marching Method for Reservoir Simulation. To appear in *Computational Geosciences*.

[2] M. S. Espedal, K. H. Karlsen. Numerical solution of reservoir flow models based on large time step operator splitting algorithms. In A. Fasano and H. van Dujin, editors, *Filtration in Porous Media and Industrial Applications*, Lecture Notes in Mathematics, Springer. To appear.

[3] S. Osher, J. A. Sethian. Fronts propagating with curvature dependent speed: algorithms based on Hamilton-Jacobi formulations. J.Comput.Phys., 79(1):12-49, 1988.

[4] J. A. Sethian. Level Set Methods and Fast Marching Methods. 2. edition. Cambridge University Press,1999.

STATIC EQUATION OF AN ELEMENT (third part)
(A unified theory of the stiffness, mixed and flexibility methods)

Pentti Tuominen
Department of Civil Engineering
University of Oulu

Introduction

The purpose of this paper is to present how to generate static equation of an element for the stiffness, mixed and flexibility methods, when presumed shape functions are as starting point. At first there is a short repetition of the theory presented in NSCM - 11 and NSCM - 12 [1] and then two applications of the theory.

Theoretical part

The element considered in the paper is presented in Figure 1.

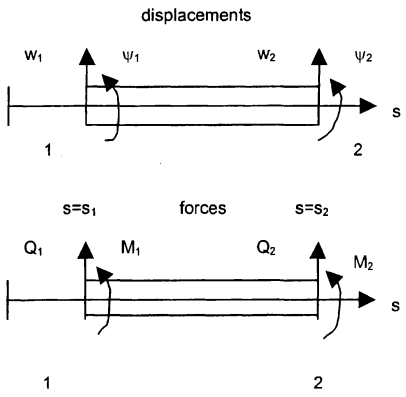

Figure 1. Element with positive displacements (w_i, ψ_i) and forces (Q_i, M_i) at nodes 1 and 2.

It was expected that an analytic solution of the governing differential equation was known. Expressions for displacement and forces of Figure 1 are thus known as functions of four integration constants $\mathbf{c}=\{c_1\ c_2\ c_3\ c_4\}$ and particular solution terms. The whole set of nodal quantities contains eight members (and similarly the set of nodal term equations). Two state vectors **a** and **b** contain both four quantities as components. They are called each others´ complements. Equations

$$\mathbf{a}=\mathbf{A}\mathbf{c}+\mathbf{a}_p \qquad (1)$$

and

$$\mathbf{b}=\mathbf{B}\mathbf{c}+\mathbf{b}_p \qquad (2)$$

can be written for the vectors. Here matrices **A** and **B** are coefficients matrices of integration constants **c** and vectors $\mathbf{a}_p$ and $\mathbf{b}_p$ contain a particular solution. **A** and **B** are each others´ complement matrices. Equation 1 gives the expression

$$\mathbf{c}=\mathbf{A}^{-1}\mathbf{a} - \mathbf{A}^{-1}\mathbf{a}_p. \qquad (3)$$

Substitution of result 3 into Equation 2 will produce Equation

$$\mathbf{b}=\mathbf{B}\mathbf{A}^{-1}\mathbf{a} + \mathbf{b}_p-\mathbf{B}\mathbf{A}^{-1}\mathbf{a}_p, \qquad (4)$$

which gives the dependence between state vectors **a** and **b.** Equation 4 is valid, if **A** is regular (its inverse exists). When **A** is singular matrices and vectors in Equation have to be reduced. Term $\mathbf{B}\mathbf{A}^{-1}$ in the equation is an interaction matrix between vectors **a** and **b.** Depending on the content of vectors it can be stiffness, flexibility, transfer or some other mixed matrix. The part $\mathbf{b}_p-\mathbf{B}\mathbf{A}^{-1}\mathbf{a}_p$ of Equation is a loading vector or more generally it can be called a source or forcing vector. Equation 4 has also an alternative form

$$\mathbf{b} = [\mathbf{B}\mathbf{A}^{-1}]\,\mathbf{I}^{-1}\mathbf{a} + \mathbf{b}_p - [\mathbf{B}\mathbf{A}^{-1}]\,\mathbf{I}^{-1}\mathbf{a}_p, \qquad (4a)$$

We can see that an interaction matrix has a complement, unit matrix **I**. When it is substituted into Equation 3 we will have the expression

$$\mathbf{c} = \mathbf{I}^{-1}\mathbf{a} - \mathbf{I}^{-1}\mathbf{a}_p = \mathbf{a} - \mathbf{a}_p \qquad (3a)$$

for integration constants **c** and we can interprete: Generation of a finite element is a procedure, where mathematical integration constants **c** are replaced with physical ones given in Equation 3a. See also Equations 48...57 in [3].

Then a question: We expected that an analytical solution of the problem is known. Are our Equations 3 and 4 valid or how they are used, when presumed shape functions are basis to an solution of our problem? In the next this problem is considered.

Applications

Equations 3 and 4 above seem to be valid also in connection of presumed shape functions. The way of using Equations is equalizing integration constants **c** with coefficients of shape functions, that is the use of Equation 3a.

Example of using shape functions

We are considering a two-noded beam element presented in Figure 1 and having a constant bending stiffness *EI* and length *L*. We assume the deflection

$$w(s) = w_1(1-3\xi^2+2\xi^3) + \psi_1\ L(\xi-2\xi^2+\xi^3) + w_2(3\xi^2-2\xi^3) + \psi_2 L(-\xi^2+\xi^3) \qquad (5)$$

where ξ=s/L and displacements w_i and ψ_i have the role of integration constants. For ψ(s) we obtain

$$\psi(s)=dw/ds=w_1/L(-6\xi+6\xi^2) + \psi_1(1-4\xi+3\xi^2) + w_2/L(6\xi-6\xi^2) + \psi_2(-2\xi+3\xi^2) \qquad (6)$$

For nodal displacements we will now have unit matrix **I** as the coefficient matrix. It is also presenting matrix **A** of Equation 4 when calculating the stiffness matrix.

Two more derivations and multiplying with *EI* will produce the wellknown expression

$$\begin{Bmatrix} Q_1 \\ M_1 \\ Q_2 \\ M_2 \end{Bmatrix} = \frac{EI}{L^3} \begin{bmatrix} 12 & 6L & -12 & 6L \\ 6L & 4L^2 & -6L & 2L^2 \\ -12 & -6L & 12 & -6L \\ 6L & 2L^2 & -6L & 4L^2 \end{bmatrix} \begin{Bmatrix} w_1 \\ \psi_1 \\ w_2 \\ \psi_2 \end{Bmatrix} \qquad (7)$$

for forces Q_i and M_i and the stiffness matrix. This is also matrix **B** of Equation 4.

If we are calculating the transfer matrix state vectors will be **a** =$\{w_1\ \psi_1\ Q_1\ M_1\}$ and **b** = $\{w_2\ \psi_2\ Q_2\ M_2\}$. Matrices **A** and **B** are now

$$A = \begin{bmatrix} 1 & 0 & 0 & 0 \\ 0 & 1 & 0 & 0 \\ 12EI/L^3 & 6EL/L^3 & -12EI/L^3 & 6EI/L^2 \\ 6EI/L^2 & 4EI/L & -6EI/L^2 & 2EI/L \end{bmatrix} \qquad (8)$$

and

$$B = \begin{bmatrix} 0 & 0 & 1 & 0 \\ 0 & 0 & 0 & 1 \\ -12EI/L^3 & -6EI/L^2 & 12EI/L^3 & -6EI/L^2 \\ 6EI/L^2 & 2EI/L & -6EI/L^2 & 4EI/L \end{bmatrix} \qquad (9)$$

Multiplication $\mathbf{BA}^{-1}$ will give the transfer matrix. Instead of the result we are presenting a generalization of the problem. We replace Equation 7 with Equation

$$\begin{Bmatrix} f_1 \\ f_2 \end{Bmatrix} = K \begin{Bmatrix} d_1 \\ d_2 \end{Bmatrix} + \begin{Bmatrix} r_1 \\ r_2 \end{Bmatrix} = \begin{bmatrix} C & D \\ F & G \end{bmatrix} \begin{bmatrix} I & 0 \\ 0 & I \end{bmatrix}^{-1} \begin{Bmatrix} d_1 \\ d_2 \end{Bmatrix} + \begin{Bmatrix} r_1 \\ r_2 \end{Bmatrix} \qquad (10)$$

where $\mathbf{f}_i$, $\mathbf{d}_i$ **and** $\mathbf{r}_i$ are force, displacement and nodal force vectors and matrices **C, D, F** and **G** are submatrices of the stiffness matrix **K**. As before we can shift over from the stiffness method to the transfer matrix method. For this purpose vectors **a** and **b** are

$$\mathbf{a} = \begin{bmatrix} I & 0 \\ C & D \end{bmatrix} \begin{Bmatrix} d_1 \\ d_2 \end{Bmatrix} + \begin{Bmatrix} 0 \\ r_1 \end{Bmatrix} \tag{11}$$

and

$$\mathbf{b} = \begin{bmatrix} 0 & I \\ F & G \end{bmatrix} \begin{Bmatrix} d_1 \\ d_2 \end{Bmatrix} + \begin{Bmatrix} 0 \\ r_2 \end{Bmatrix} \tag{12}$$

For the transfer matrix we will obtain

$$\mathbf{T} = \mathbf{B}\mathbf{A}^{-1} = \begin{bmatrix} 0 & I \\ F & G \end{bmatrix} \cdot \begin{bmatrix} I & 0 \\ C & D \end{bmatrix}^{-1} = \begin{bmatrix} 0 & I \\ F & G \end{bmatrix} \cdot \begin{bmatrix} I & 0 \\ -D^{-1}C & D^{-1} \end{bmatrix} = \begin{bmatrix} D^{-1}C & D^{-1} \\ F - GD^{-1}C & GD^{-1} \end{bmatrix}, \tag{13}$$

Equation 13 is given inter alia in Reference [2, p. 105]. This result is also valid when going back from the transfer matrix method to the stiffness one.

Then the question of using Equation 4 for generating a more-noded element for the stiffness method. Matrix **A** is regular and $\mathbf{A}^{-1}$ exists if shape functions of displacements fulfill geometrical boundary conditions. Also matrix **B** can be determined and forces at boundaries and inside the element can be calculated. An open question is the additional fiction of the finite element method. The forces have to be concentrated at the nodal points and one more integration is needed. Reference 4 highlights this problem.

ACKNOWLEDGEMENTS

The author wishes to express his gratitude to professor Eero-Matti Salonen for valuable discussions and cooperation.

REFERENCES

1. Tuominen, P. Static equation of an analytic element (A unified theory of the stiffness, mixed and flexibility methods). Proceedings of the NSCM-11: Nordic Seminar on Computational Mechanics, Anders Ericsson and Costin Pacoste (editors) Royal Institute of Technology, Department of Structural Engineering, pp. 171-174. Stockholm 1998.

2. Tesár, A. & Fillo, L'u: Transfer Matrix Method. Kluwer Academic Publishers, Dordrecht/Boston/London 1988.

3. Sekhon, G.S., Bhatia, R.S.: Generation of exact stiffness matrix for a spherical shell element. Computers and Structures 74 (2000) pp. 335-349.

4. Salonen, E-M.: The concept of fictitious loading. International Journal for Numerical Methods in Engineering, Vol. 14, 1653-1663 (1979).

A new accurate yet simple plate bending element with linear bending strains

Lars Damkilde
Department of Structural Engineering and Materials
Technical University of Denmark, DK-2800 Lyngby

Introduction

Plate bending elements have been and still are the subject of many papers. Zienkiewicz, see [1], has given a very good overview of the historical development dating back to around 1965. In this paper focus will entirely be on thin plate elements. Three main approaches have been used: a displacement based approach, a hybrid interpolation approach and finally a discrete Kirchhoff approach.
For the displacement based method there are great difficulties in establishing conforming elements. So far the only successful conforming element is the so-called Clough-Tocher element, [2]. The basis is a 10-degree of freedom triangular element which can be combined in either a triangular or a rectangular element. The triangular element consists of 3 basic elements with an interior node, which can be eliminated. This element has 12 degrees of freedom: 1 displacement and 2 rotations in each corner node and in each mid-side node a rotation parallel to the side. The element is relatively expensive but the accuracy is very high, see [3] where minor errors in the original paper have been corrected. Several almost conforming elements have been made, see e.g. [4]. These elements are less expensive but have a reduced accuracy. The aim of this paper is to propose a new non-conforming element which combines the high accuracy of the Clough-Tocher element and the simpler formulation of the other elements.
The hybrid or mixed formulations will not be discussed in detail here but the literature contains many examples, see. e.g. Felippa, [5] . The discrete Kirchhoff approach has been used in the well-known DKT-element, [6]. Another prominent example is the so-called SemiLoof element by Irons, [7]. The DKT-element has a reasonable accuracy and is relatively inexpensive, whereas the SemiLoof element has a better accuracy but a rather expensive formulation.

Formulation of the Element

The basic idea is to interpolate the displacement, w, as a polynomial of degree 3. In this way the element will have linear varying bending strains. A sufficient interpolation will demand 10 parameters corresponding to the functions $1, x, y, x^2, xy, y^2, x^3, x^2y, xy^2, y^3$. The 10 parameters could be chosen as 1 displacement and 2 rotations at each corner and a displacement in a central node. This element would not be conforming which demands C_1-continuity and it has also been shown that the so-called patch-test is not fulfilled. Any other choice of the 10th degree of freedom would loose the symmetry of the element.
An alternative solution is to choose the 10th degree of freedom as some quantity on the boundary. This can not be done in a way that preserves the symmetry in the triangular coordinates and therefore a slight modification of the so-called bubble function is made. This principle was first introduced by Specht, [4].
In the following area coordinates are used instead of $x-$ and $y-$coordinates. The idea is to write the bubble function, which is 0 at the boundary and maximum at the center, as:

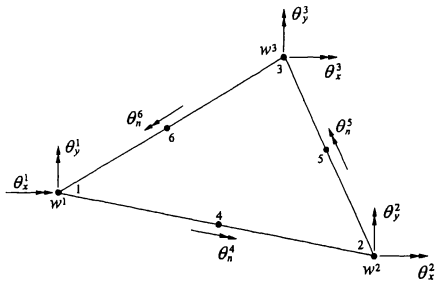

Figure 1: Nodal degrees of freedom for element

$$\lambda_1\lambda_2\lambda_3 = (\lambda_1 + \lambda_2 + \lambda_3)\lambda_1\lambda_2\lambda_3 \tag{1}$$

The bubble function is split into three parts which each is considered as an independent function. In this respect the interpolation of w contains both a full 3rd degree polynomial and some additional 4th degree terms. The nodal degrees of freedom at the 3 mid-side nodes are chosen as the rotations parallel to the sides. In Figure 1 the nodal degrees of freedom are shown. The element is non-conforming as C_1-continuity is lacking but the element fulfills the patch-test, see [4].
The shape functions can be expressed analytically and the result is given below. The geometric variables are given solemnly through the length of the 3 sides ℓ_1, ℓ_2 and ℓ_3 and the area of the triangle A.

$$\begin{aligned} \cot\Psi_1 &= \frac{1}{4A}\left(-{\ell_1}^2 + {\ell_2}^2 + {\ell_3}^2\right) \\ \mu_1 &= \frac{{\ell_2}^2 - {\ell_3}^2}{{\ell_1}^2} \end{aligned} \tag{2}$$

where Ψ_1 is the angle at node 1, and the parameter μ_1 expresses the skewness of node 1 in the triangular geometry. The parameters μ_2 and μ_3 are found by cyclic permutation of the indices. Node 1 is considered and the shape functions N_1, N_2 and N_3 refer to the vertical displacement in node 1, w^1, the rotation parallel to the opposite side of node 1, θ_b^1, and the rotation perpendicular to the opposite side of node 1, θ_v^1, respectively.

$$\begin{aligned} N_1 &= {\lambda_1}^2(3 - 2\lambda_1) + 3(2 + f_2){\lambda_1}^2\lambda_2\lambda_3 + 3f_1\lambda_1{\lambda_2}^2\lambda_3 - 3f_1\lambda_1\lambda_2{\lambda_3}^2 \\ N_2 &= \frac{2A}{\ell_1}\left({\lambda_1}^2(1 - \lambda_1) + (1 + \frac{1}{2}f_2){\lambda_1}^2\lambda_2\lambda_3 + \frac{1}{2}f_1\lambda_1\lambda_2\lambda_3(\lambda_2 - \lambda_3)\right) \\ N_3 &= \frac{2A}{\ell_1}\left({\lambda_1}^2(\cot\Psi_3\lambda_3 - \cot\Psi_2\lambda_2) + f_3{\lambda_1}^2\lambda_2\lambda_3 + f_4\lambda_1\lambda_2\lambda_3(\lambda_2 - \lambda_3)\right) \end{aligned} \tag{3}$$

where $f_1 = \mu_2 + \mu_3$, $f_2 = -\mu_2 + \mu_3$, $f_3 = (-\cot\Psi_2 + \cot\Psi_3 - \cot\Psi_3\mu_2 - \cot\Psi_2\mu_3)/2$ and $f_4 = (-5\cot\Psi_2 - 5\cot\Psi_3 + \cot\Psi_3\mu_2 - \cot\Psi_2\mu_3)/2$.
The shape function N_{10} for the rotation at the midside node between node 1 and 2 is given by:

$$N_{10} = \frac{8A}{\ell_3}\left(\lambda_1\lambda_2\lambda_3 - 2\lambda_1\lambda_2{\lambda_3}^2\right) \tag{4}$$

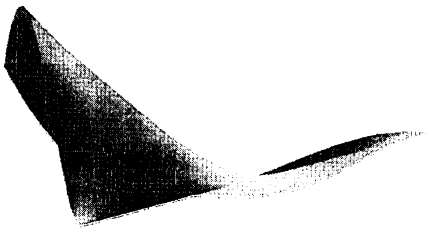

Figure 2: Shape function for N_3

The rest of the shape functions are found by cyclic permutation of the indices. In Figure 1 the shape function for a torsion of one of the corners is shown i.e. similar to N_3.
Based on the shapefunctions the stiffness matrix can be constructed and it is done numerically by full integration. For uniform loads the consistent load vector can be found analytically but no results will be given here.

Results

The element has been implemented in MatLab and tested on standard examples taken from the literature. The overall performance is very good, and below 2 tabels can be found which show the good convergence rate.
In Table 1 results for a quadratic plate with uniform load are presented. Only 1/4 of the plate is analysed due to symmetry and a uniform mesh with N subdivisions is used. The orientation of the mesh is either A or B, where A refers to the situation where the diagonals point to the center.

N	Simply supported		Clamped	
	A	B	A	B
1	1.0370	0.8828	0.4611	0.2670
2	1.0074	0.9821	0.9346	0.8780
3	1.0035	0.9947	0.9855	0.9677
4	1.0020	0.9980	0.9966	0.9888
5	1.0013	0.9991	0.9997	0.9955
6	1.0009	0.9996	1.0006	0.9980
7	1.0006	0.9998	1.0009	0.9992
8	1.0005	0.9999	1.0009	0.9997
9	1.0004	1.0000	1.0009	1.0000
10	1.0003	1.0000	1.0008	1.0001
16	1.0001	1.0000	1.0004	1.0002

Table 1: w/w_{exact} in central node for a uniform load

The results show a good convergence rate and high accuracy even for a coarse mesh. As the element is non-conforming the results are not necessarily to stiff. It is observed that the element is rather insensitive to the orientation. As expected $N = 1$ gives misleading results in the clamped case.
In Table 2 results for a quadratic plate with a point load in the center are shown. The element mesh is as in Table 1. The results show the same good convergence and accuracy as in Table 1.

N	Simply supported		Clamped	
	A	B	A	B
1	0.9102	0.7783	0.3283	0.3284
2	0.9774	0.9513	0.8746	0.8641
3	0.9914	0.9795	0.9616	0.9491
4	0.9959	0.9888	0.9837	0.9740
5	0.9977	0.9930	0.9918	0.9844
6	0.9987	0.9952	0.9955	0.9896
7	0.9992	0.9965	0.9973	0.9926
8	0.9994	0.9974	0.9983	0.9945
9	0.9996	0.9979	0.9989	0.9957
10	0.9997	0.9983	0.9993	0.9966
16	1.0000	0.9994	1.0000	0.9987

Table 2: w/w_{exact} in central node for a point load

Conclusion

A new plate element with linear bending strains has been proposed, and the linear tests show very good performance. The element is slightly more complicated than the simple elements of the DKT family but gives somewhat more accurate results. It is considerably less complicated than the Clough-Tocher element and the SemiLoof element but gives almost the same accuracy and for point loads somewhat better than the SemiLoof element. Work on the extension of the element to cover both stability and dynamic calculations is in progress.

References

[1] O. C. Zienkiewicz and R. L. Taylor. *The Finite Element Method*, volume 2. McGraw-Hill, 4 edition, 1992.

[2] R. W. Clough and J. L. Tocher. Finite element stiffness matrices for analysis of plates in bending. In *Proc. Conf. on Matrix Methods in Structural Mechanics*, Air Force Institute of Technology, Wright-Patterson A. F. Base, Ohio, 1965.

[3] P. N. Poulsen and L. Damkilde. A flat triangular shell element with loof nodes. *International Journal for Numerical Methods in Engineering*, 39:3867–3887, 1996.

[4] B. Specht. Modified shape functions for the three-node plate bending element passing the patch test. *International Journal for Numerical and Analytical Methods in Engineering*, 26:705–715, 1988.

[5] C. A. Felippa. Recent advances in finite element templates. In *Computational Mechanics for the Twenty-First Century*, Leuven, Belgium, 2000.

[6] J. A. Stricklin, W. E. Haisler, P. R. Tisdale, and R. Gunderson. A rapidly converging triangular plate element. *AIAA journal*, 7(1):180–181, 1969.

[7] B. M. Irons. The semiloof shell element. In D. G. Ashwell and R. H. Gallagher, editors, *Finite Elements for Thin Shells and Curved Members*, pages 197–222. Wiley, 1968.

An Analysis of the Approximation Properties of a Bilinear Reduced Strain Element in the Case of an Elliptic Shell

V. Havu, H. Hakula
Institute of Mathematics, Helsinki University of Technology
Helsinki, Finland

1 Introduction

By now it is well known that reliable numerical modeling of shells by traditional low-order finite element formulations is not an easy task. The most dramatic failure occurs when approximating nearly inextensional (or bending-dominated) deformations by standard low-order elements. In this case an asymptotic approximation failure, known as *shear-membrane locking*, occurs at the limit of zero shell thickness.

To avoid the locking in parameter dependent problems, it is customary to use elements that are based on some non-standard variational formulation of the problem. Among the (apparently many) possible technical variations within this approach, we choose to consider in our work the well known formulation by Bathe et al. [1] named MITC4.

2 The shell problem

We consider a dimensionally reduced shell model for a shell of thickness t arising from linear shell theory with homogeneous and isotropic material. We assume that the membrane, transverse shear and bending strains β_{ij}, ρ_i and κ_{ij} depend on the displacements (u, v, w) and on the rotations (θ, ψ) as follows:

$$\beta_{11} = \frac{\partial u}{\partial x} + aw, \quad \beta_{22} = \frac{\partial v}{\partial y} + bw, \quad \beta_{12} = \frac{1}{2}(\frac{\partial u}{\partial y} + \frac{\partial v}{\partial x}) + cw = \beta_{21}, \tag{1}$$

$$\kappa_{11} = \frac{\partial \theta}{\partial x}, \quad \kappa_{22} = \frac{\partial \psi}{\partial y}, \quad \kappa_{12} = \frac{1}{2}(\frac{\partial \theta}{\partial y} + \frac{\partial \psi}{\partial x}) = \kappa_{21}, \tag{2}$$

and

$$\rho_1 = \theta - \frac{\partial w}{\partial x} \qquad \rho_2 = \psi - \frac{\partial w}{\partial y}, \tag{3}$$

where we are assuming the shell to be *shallow* so that the parameters a, b and c defining the shell geometry can be taken constants. We consider only the case $ab - c^2 > 0$ s.t. the shell is elliptic. We will assume that the computational domain Ω (the shell midsurface) is of rectangular shape in the assumed coordinate system, so that $\Omega = \{(x, y) | 0 < x < L, 0 < y < H\}$ with $c^{-1} \leq \frac{L}{H} \leq c$ for some fixed constant c and with periodic boundary conditions at $y = 0, H$.

We are interested in the finite element approximation of *inextensional* displacement fields $\underline{u} = (u, v, w, \theta, \psi)$ in the energy space $\mathcal{U}$ satisfying

$$\beta_{11}(\underline{u}) = \beta_{12}(\underline{u}) = \beta_{22}(\underline{u}) = 0, \quad \rho_1(\underline{u}) = \rho_2(\underline{u}) = 0 \tag{4}$$

and denote the space of these fields by $\mathcal{U}_0$. We aim to expand the inextensional modes by the Fourier expansion

$$\underline{u} = \sum_{\lambda \in \Lambda} \varphi_\lambda(y) \underline{\phi}_\lambda(x), \quad \varphi_\lambda(y) = e^{i\lambda y}, \quad \Lambda = \{\lambda = \frac{2\pi\nu}{H},\ \nu \in Z\} \tag{5}$$

where, in view of (4), the first two components of $\underline{\phi}_\lambda = (u_\lambda, v_\lambda, w_\lambda, \theta_\lambda, \psi_\lambda)$ satisfy

$$\begin{pmatrix} v_\lambda \\ u_\lambda \end{pmatrix}' = i\lambda \begin{pmatrix} \frac{2c}{b} & -1 \\ \frac{a}{b} & 0 \end{pmatrix} \begin{pmatrix} v_\lambda \\ u_\lambda \end{pmatrix} = \lambda M \begin{pmatrix} v_\lambda \\ u_\lambda \end{pmatrix} \tag{6}$$

3 The reduced-strain FE scheme

To prevent the error amplification at small t, we need to consider some modification of the standard formulation. A natural approach is to modify the membrane and transverse stresses with suitable reduction operators. We assume that the mesh is uniform in the periodic direction and satisfies certain regularity conditions in the other direction. On this mesh we define the reduced membrane and shear strains as

$$\tilde{\beta}_{11} = \Pi_h^x \beta_{11}, \quad \tilde{\beta}_{22} = \Pi_h^y \beta_{22}, \quad \tilde{\beta}_{12} = \Pi_h^{xy} \beta_{12} = \tilde{\beta}_{21} \tag{7}$$

and

$$\tilde{\rho}_1 = \Pi_h^x \rho_1 \qquad \tilde{\rho}_2 = \Pi_h^y \rho_2, \tag{8}$$

where Π_h^x, Π_h^y and Π_h^{xy} are L^2-projection operators defined elementwise as projectors onto the global spaces $\mathcal{W}_h^x$, $\mathcal{W}_h^y$ and $\mathcal{W}_h^{xy}$, where $\mathcal{W}_h^x$ consists of functions that are constant in x and piecewise linear with respect to y on each element, $\mathcal{W}_h^y$ is defined analogously and $\mathcal{W}_h^{xy}$ consists of functions that are elementwise constants. The connection between our choice and the engineering tradition is given in [3].

Theorem 1. *Let $\mathcal{U}_{0,h} = \{\underline{u} \in \mathcal{U}_h \,|\, \tilde{\beta}_{ij}(\underline{u}) = \tilde{\rho}_i(\underline{u}) = 0\}$ where $\mathcal{U}_h$ is the bilinear finite element space and assume that the modified strains are further defined by (7) - (8). Then if $\underline{u} \in \mathcal{U}_0$, there exists a $\tilde{\underline{u}} \in \mathcal{U}_{0,h}$ such that*

$$|||\underline{u} - \tilde{\underline{u}}|||_h \leq Ch|\underline{u}|_2. \tag{9}$$

where $|||\cdot|||_h$ is the modified energy norm and h denotes maximal mesh spacing

Remark 1. *The main idea of the proof is to use the Fourier representation (5) and approximate then $\underline{u}$ by*

$$\tilde{\underline{u}} = \sum_{\lambda \in \Lambda : |\lambda| \leq \lambda_0} \tilde{\varphi}_\lambda(y) \tilde{\underline{\phi}}_\lambda(x), \tag{10}$$

where $\lambda_0 = \lambda_0(h)$ is a truncation frequency to be chosen, $\tilde{\varphi}_\lambda$ is the piecewise linear interpolant of φ_λ, and $\tilde{\underline{\phi}}_\lambda$ is a special approximation of $\underline{\phi}_\lambda$ to be found.

Proof of Theorem 1. Consider first a single Fourier mode. Since $\tilde{\varphi}_\lambda \tilde{\underline{\phi}}_\lambda \in \mathcal{U}_{0,h}$ it must satisfy the constraints $\tilde{\beta}_{ij}(\tilde{\varphi}_\lambda \tilde{\underline{\phi}}_\lambda) = \rho_i(\tilde{\varphi}_\lambda \tilde{\underline{\phi}}_\lambda) = 0$. Inspired by the form of $\varphi_\lambda \underline{\phi}_\lambda$ we seek a solution to these equations in the form $u_k^n = e^{i\lambda n h_y} U^k$, $v_k^n = e^{i\lambda n h_y} V^k$, $w_k^n = e^{i\lambda n h_y} W^k$, $\theta_k^n = e^{i\lambda n h_y} \Theta^k$ and $\psi_k^n = e^{i\lambda n h_y} \Psi^k$ where h_y is the uniform mesh spacing in the periodic y-direction. Substituting these expressions and simplifying we get that U^k and V^k satisfy

$$\begin{pmatrix} V \\ U \end{pmatrix}_{k+1} - \begin{pmatrix} V \\ U \end{pmatrix}_k = \delta_k M \left[\begin{pmatrix} V \\ U \end{pmatrix}_{k+1} + \begin{pmatrix} V \\ U \end{pmatrix}_k \right] \tag{11}$$

where $\delta_k = \frac{h_x^k}{h_y} \tan\left(\frac{1}{2}\lambda h_y\right) h_x^k$ being the local mesh spacing in the x-direction. Since u_λ and v_λ satisfy (6) we see that (11) is a finite difference approximation to (6) with a truncation error $\gamma_k \leq C(|\lambda|^3 (h_x^k)^3 + |\lambda|^3 h_y^2 h_x^k)$ for λ s.t. $|\lambda| h \leq c < \pi$. This leads also to optimal accuracy with respect to all other components giving finally

$$|||\tilde{\varphi}_\lambda \tilde{\underline{\phi}}_\lambda - \varphi_\lambda \underline{\phi}_\lambda|||_h^2 \leq C h^2 |\varphi_\lambda \underline{\phi}_\lambda|_2^2 \tag{12}$$

To obtain the final result, we note that the functions $\varphi_\lambda \underline{\phi}_\lambda$ and $\tilde{\varphi}_\lambda \tilde{\underline{\phi}}_\lambda$ are orthogonal on $\mathcal{U}$, write $\underline{u}$ as its Fourier-expansion $\underline{u} = \sum_{\lambda \in \Lambda} \varphi_\lambda(y) \underline{\phi}_\lambda(x)$ and let our approximation be $\tilde{\underline{u}} = \sum_{|\lambda| \leq \lambda_0} \tilde{\varphi}_\lambda(y) \tilde{\underline{\phi}}_\lambda(x)$ where $\tilde{\underline{\phi}}_\lambda(x)$ is defined as above. A direct calculation gives

$$|||\tilde{\underline{u}} - \underline{u}|||_h^2 = ||| \sum_{|\lambda| \leq \lambda_0} \tilde{\varphi}_\lambda \tilde{\underline{\phi}}_\lambda - \sum_{\lambda \in Z} \varphi_\lambda \underline{\phi}_\lambda |||_h^2 \leq \sum_{|\lambda| \leq \lambda_0} |||\tilde{\varphi}_\lambda \tilde{\underline{\phi}}_\lambda - \varphi_\lambda \underline{\phi}_\lambda|||_h^2 + \sum_{|\lambda| > \lambda_0} |||\varphi_\lambda \underline{\phi}_\lambda|||_h^2 \tag{13}$$

We can then set $\lambda_0 = \frac{C}{h}$ to obtain

$$|||\tilde{\underline{u}} - \underline{u}|||_h^2 \leq C h^2 \sum_{|\lambda| \leq \frac{C}{h}} |\varphi_\lambda \underline{\phi}_\lambda|_2^2 + C h^2 \sum_{|\lambda| > \frac{C}{h}} |||\lambda \varphi_\lambda \underline{\phi}_\lambda|||_h^2 \leq C h^2 |\underline{u}|_2^2 \tag{14}$$

□

4 Numerical example

As a numerical example on the performance of our reduced-strain formulation (7) – (8) we take the Morley hemispherical shell as in [2]. We parameterize the problem by the angles ϑ and ϕ and use a uniform rectangular mesh with respect to these parameters and let $R = 10$, $t = 0.04$, $\nu = 1/3$ to define the geometry and material. We measure the quality of the results by the magnitude of transverse deflection at the northern edge on the meridian of the load. The results are shown in Table 1 where the reference value is obtained using a p-version of FEM with $p = 6$. In this outset, which is favorable to the reduced-strain formulation, the classical formulation suffers from severe locking and produces essentially a zero solution. We note that the reduced-strain formulation is in this case comparable even to the p-version of FEM.

References

[1] Bathe, K. J. and Dvorkin, E. (1986): "A Formulation of General Shell Elements – The Use of Mixed Interpolation of Tensorial Components", *Int. J. Numer. Methods Eng.*, Vol 22, pp. 697-722

DOFs	deflection	absolute relative error
225	0.443469	0.3458
1425	0.653925	0.0331
3625	0.680617	0.0063
6825	0.689944	0.0201

Table 1: Deflection of the radial component for the Morley shell with the reduced-strain formulation. The reference value obtained with a p-version of FEM having roughly 112000 DOFs and $p = 6$ is 0.676345. All results were computed on a uniform mesh.

[2] MacNeal, R. H. (1994): *Finite elements: their design and performance*, Marcel Dekker

[3] Malinen M. (2000): "On geometrically incompatible bilinear shell elements and classical shell models.", *Helsinki University of Technology Laboratory for Mechanics of Materials Research Reports TKK-Lo-30*

CrossX - example of an efficient GUI for typical 2D FEM analyses

Lars Wollebæk and *Kolbein Bell*

Department of structural engineering
Norwegian University of Science and Technology, NTNU
7491 Trondheim

Introduction

CrossX™ [1] is a recently developed Windows-based, interactive program for computation of

a) section parameters and stiffnesses of, and

b) stress distributions on

arbitrary beam cross sections composed of one or more isotropic and linearly elastic materials.

The cross section is analyzed as a

- *massive* section, or as a
- *thin-walled* section.

The **massive** cross section is analyzed by a finite element method using a 6-noded 'linear strain' triangle considering only ST. VENANT torsion (with no warping restraint).

The **thin-walled** cross section is made up of a series of straight line segments (thin rectangles), with or without cells. Both ST. VENANT torsion and non-uniform, warping restrained torsion is considered.

CrossX offers a flexible set of tools for modelling complex cross sections, consisting of one or more materials. The discretization technique used by the program implies that all curved lines are approximated by a series of straight lines. For massive sections, symmetry properties may be exploited.

The computations carried out by the program are believed to be quite efficient and represent state-of the-art. However, they are based on published material and will therefore not be presented in any detail. The user interface, on the other hand, and particularly the presentation of computed results, is believed to contain some novel features that is applicable to 2D FEM analyses in general. The basic idea is to present 2D finite element results as *surfaces* in 3D space that can easily be manipulated (rotated).

While both massive and thin-walled models make use of the same principles, for both modelling and presentation of results, the thin-wall model is, strictly speaking, not a finite element model (although for most purposes it can be considered as a plane frame or truss model). Hence, this presentation focuses on the finite element analysis of the massive models.

Finite element analysis

Figure 1 shows a typical massive model. The mesh is generated automatically (by a mesh generator using DELAUNAY triangulation). The basic element used is a six-noded triangle with straight sides, the so-called *linear strain triangle*. The side nodes are located at mid-point.

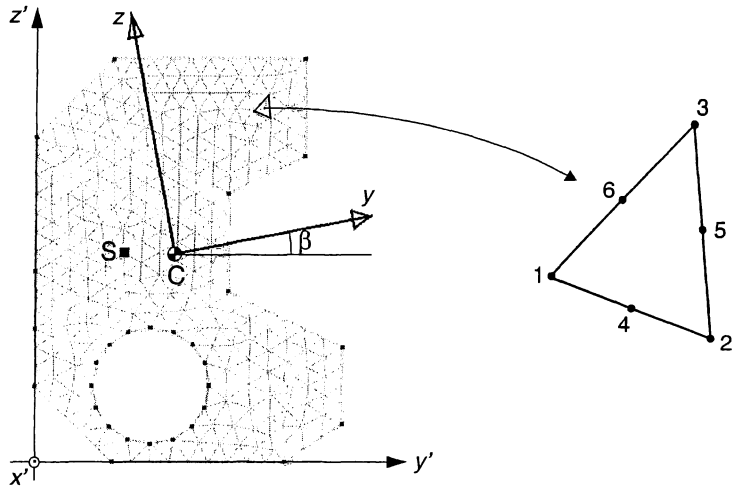

Figure 1 Typical finite element mesh and basic finite element

With this element all curved edges must be approximated by piece-wise straight (triangle) sides. It would of course have been possible to formulate the element as an *isoparametric* element with curved-edge capability. This would permit a better geometric representation, but only at the expense of a numerically more sensitive element and thus loss of robustness. It was therefore decided to stay with the straight edge version.

The section is referred to a reference system y' and z' (the x'-axis is parallel with the beam axis). Determination of the 'center of gravity' or area center, point C in Figure 1, and the orientation (angle β) of the principal axes, y and z, is straightforward. It should be noted that while the material properties are constant within a particular element, they may, in principle, vary from element to element. The center of area of the total cross section (C) is thus based on the 'axial stiffness' (E_iA_i) of each individual element, rather than the true area (A_i).

For the torsion problem **CrossX** uses a finite element solution, with respect to the warping function $\psi(y, z)$, that is similar to the procedure described by MEEK [2]. For the elastic shear analysis of prismatic beams, the purpose of which is to determine the shear stress distribution, the location of the shear center (S) and the shear deformation factors (κ_y and κ_z) for an arbitrary cross section subjected to shear forces V_y and V_z, the procedure described by MASON and HERRMANN [3] is used. This part also makes use of the warping function, but while the 'stiffness' matrix is the same as for the torsion analysis, the right-hand sides are different.

Stress results

In addition to all relevant cross sectional parameters and stiffnesses, **CrossX** also determines stresses and their distribution over the cross section due to prescribed section forces and moments (determined for instance by a separate beam or frame type analysis). The presentation of these stress components represents the essence of **CrossX** result visualization. As an example, Figure 2 shows 3D plots of the resulting shear stress (τ_r) due to a torsional moment (M_x) acting on a solid, rectangular cross section.

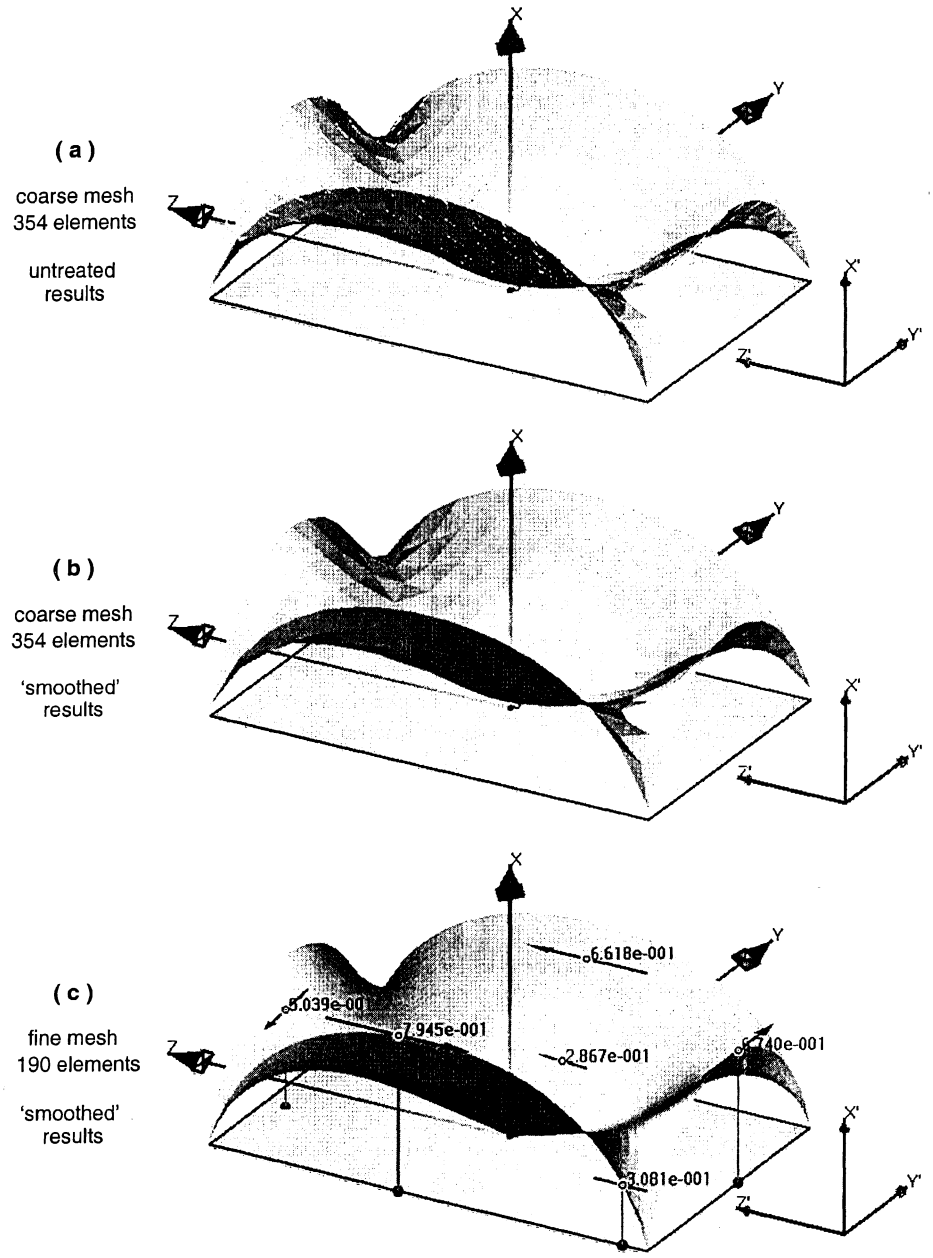

Figure 2 Resulting shear stress τ_r, due to M_x (torsional moment) on a rectangular section

Figure 2a shows the shear stress surface obtained by the program's default mesh (in this case 354 elements with 759 unknown parameters). The plot is based on values determined for each individual finite element. Hence the surface presents itself as a faceted surface with gaps between the triangular elements. Pushing the program's *smooth button* will produce the faceted surface in Figure 2b which has no gaps between the elements. This surface is based on the average nodal values at the corner nodes (straightforward nodal averaging with equal weight for each element is used). The problem is reanalyzed with a much finer mesh (4190 elements with 8555 unknown parameters). This mesh produces the stress surface in Figure 2c (after smoothing). This last figure also shows the values of the stress at some particular points (all of which coincide with a finite element corner node). If the stress component is a resulting shear stress, as it is here, a scaled line with an arrow indicates the direction and the magnitude of the shear stress at the selected points.

It is worth noting that the maximum stress value in the three cases shown i Figure 2 is: 0,9895 (a), 0,9880 (b) and 0,9901 (c). Assuming the fine mesh in 2c to be very close to the 'exact' result, the unsmoothed result obtained by the relatively coarse default mesh in 2a is off the mark by less than 0,1 per cent (in this particular case). Results (in the form of stress surfaces) for 15 different axial and shear stress components, including (von Mises) effective stress, are available.

The plots in Figure 2 may easily be rotated about all three axes, and various schemes are available with respect to color and 'texture' of the stress surface, including display of the mesh on the stress surface. It is possible to *clip* the stress surface by one or more horizontal and/or vertical planes and hide the part of the surface on one or the other side of any given clip plane. This feature is used to produce a contour like map, in 2 or 3D, of the stress surface. Coloring and lighting can be customized by the user, as can the number representation (format and number of digits). It is also possible to change (dynamically) between SI and US customary units.

The techniques of visualizing 2D finite element results developed in this program are believed to be quite effective and instructive, and they can be used for any kind of 2D problem. Some limited testing has shown that bending moments in plates are well suited to this type of presentation.

Acknowledgement

We would like to acknowledge the efforts of Oddmund V. Bleie in the early stages of the project development.

References

1. K. Bell, O. V. Bleie and L. Wollebæk: **CrossX** - a program for analysis of arbitrary beam cross sections. User's Manual. In preparation (will be made available on the Internet).
2. J. L. Meek: *Computer Methods in Structural Analysis*, E & FN SPON (Chapman & Hall), 1991.
3. W. E. Mason and L. R. Herrmann: Elastic Shear Analysis of General Prismatic Beams, *Journal of the Eng. Mech. Div.,* ASCE, August 1968 (pages 965-983).

PARALLEL COMPUTING OF WAVE PROPAGATION PROBLEMS

Torbjörn Ekevid, Nils-Erik Wiberg
Department of Structural Mechanics
Chalmers University of Technology
S-412 96 Göteborg, Sweden
email: torek@sm.chalmers.se

Introduction

During the last decade there has been an enormous development of computer hardware. More efficient communication buses and CPUs have been introduced in an accelerating manner. In the field of computer intensive applications as for example the finite element method, the advances in hardware technology have made it possible to solve problems that a few years ago were impossible to solve due to hardware limitations.

During the same period of time, parallel computers where many CPUs are connected through an extreme fast network have also become cheaper and easier to use. However, construction of programs for this type of computer generally requires careful consideration. In particular, care must be taken to maintain all the involved processors busy, performing useful computations and to minimize the overall communication between the processors.

In most programs for parallel computing, the MIMD (Multiple Instructions Multiple Data) model is used for engineering applications, due to its natural and intuitive approach. The concept of parallelization adopted here involves decomposition and distribution of data, such that each of the CPUs basically has to do the same amount of work. In finite element computation, partitioning of the computational grid on element level serves as the most natural data decomposition, even though decomposition is possible to do on node level. Considering parallel implementation of time stepping algorithms, explicit time integration schemes appear to be the most natural and easy implemented method for semi-discretized finite element methods. Several synonymous formulations can be found for explicit time integration algorithm for structural dynamics, see for instance Belytschko[1] or, Dokainish[2].

In our first study, implementation aspects of a parallel version of the central difference method were investigated. Here MPI[3] - Message Passing Interface were used for initial distribution of decomposed domain as well as for exchange of data throughout the entire time stepping procedure. Since the combination of FORTRAN 90, where utilities as complex data structures and data encapsulation were used, and MPI seemed promising, forthcoming studies are likely based on this combination.

The present paper focus on implementation aspects for parallel computations for the explicit version of the DG(1) method.

Theory

The main idea in the Discontinuous Galerkin method is to use both displacements and velocities as primary unknowns and approximate them as a tensor product of piecewise functions in space and in time permitting them to be discontinuous at a finite number of discrete time levels, see Figure 1. The discretization of the space-time domain is done in a way that utilizes the structure of a conventional discretization in space where additional uniform linear elements are used in time. Consequently, the properties of the spatial discretization will be the same as those obtained from a conventional semi-discretization of (1).

$$\boldsymbol{M}\dot{\boldsymbol{v}} = \boldsymbol{f}^{ext} - \boldsymbol{f}^{int} - \boldsymbol{C}\dot{\boldsymbol{u}}\,, \qquad \dot{\boldsymbol{u}} - \boldsymbol{v} = \boldsymbol{0} \tag{1}$$

Additional notations have to be introduced since the unknown fields are permitted to be discontinuous at certain time-levels

$${}^{n}\boldsymbol{w}^{+} = \lim_{\varepsilon\to 0^{+}} \boldsymbol{w}(t_n + \varepsilon), \quad {}^{n}\boldsymbol{w}^{-} = \lim_{\varepsilon\to 0^{-}} \boldsymbol{w}(t_n + \varepsilon), \quad \left[{}^{n}\boldsymbol{w}\right] = {}^{n}\boldsymbol{w}^{+} - {}^{n}\boldsymbol{w}^{-} \tag{2}$$

We can construct the system of residual equations on each time step from (1) by introducing the local weighting functions $\boldsymbol{w}_d$, $\boldsymbol{w}_v$ in time for displacements and velocities according to:

$$\int_{I_n} \boldsymbol{w}_v \cdot \left(\boldsymbol{M}\dot{\boldsymbol{v}} + \boldsymbol{f}^{int} - \boldsymbol{f}^{ext}\right) dt + \int_{I_n} \boldsymbol{w}_d \cdot \boldsymbol{K}\left(\dot{\boldsymbol{d}} - \boldsymbol{v}\right) dt + {}^{n}\boldsymbol{w}_d \cdot \boldsymbol{K}\left[{}^{n}\boldsymbol{d}\right] + {}^{n}\boldsymbol{w}_v \cdot \boldsymbol{M}\left[{}^{n}\boldsymbol{v}\right] = \boldsymbol{0} \tag{3}$$

where $\boldsymbol{K}$ is the tangential stiffness matrix at time t_n. Equation (3) serve as a base for deriving a number of different time-stepping methods involving discontinuities at discrete time levels, but in the subsequent part of the section we limit the description to cover just linear approximation of the unknown fields inside each time step which result in the DG(1)-method.

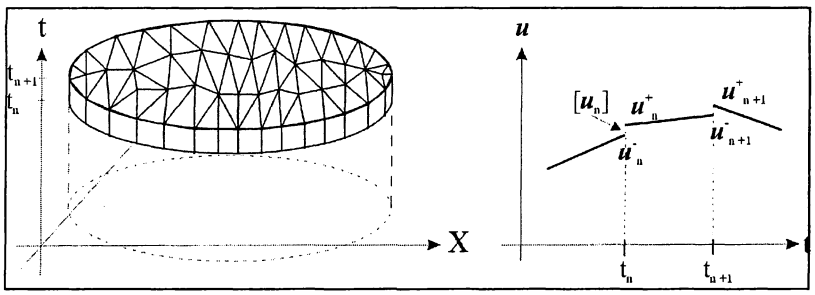

Figure 1. Illustration of the space-time DG finite element method

Further, vectors of displacements and velocities either from the previous time-step or if $n = 1$, from initial conditions are denoted $\tilde{\boldsymbol{d}}^{-}$ and $\tilde{\boldsymbol{v}}^{-}$. Let ${}^{n}\tilde{\boldsymbol{d}}, {}^{n}\tilde{\boldsymbol{v}}$ and ${}^{n+1}\tilde{\boldsymbol{d}}, {}^{n+1}\tilde{\boldsymbol{v}}$ serve as notation for the vectors of unknown displacements and velocities at t_n^{+} and t_{n+1}^{-}. Thus, displacements and velocities can be expressed in terms of linear basis functions ${}^{n}N$ and ${}^{n+1}N$ in time, at an arbitrary time t inside the current time step as:

$$\boldsymbol{d} = {}^{n}N^{t_n}\tilde{\boldsymbol{d}} + {}^{n+1}N^{t_{n+1}}\tilde{\boldsymbol{d}}, \quad \boldsymbol{v} = {}^{n}N^{t_n}\tilde{\boldsymbol{v}} + {}^{n+1}N^{t_{n+1}}\tilde{\boldsymbol{v}} \tag{4}$$

Inserting (4) and respective weighting functions into (3), performing integration in time explicitly, rearranging the equations by elementary row-operations yields a system of non-linear equations according to (5). The major difference between the central difference method and the DG(1) method is the iterative predictor-corrector phase of the two last equations in (5), which have to be done at each time-step in order to preserve the third order accuracy that the method originally has. Mostly this is achieved in only two corrector iterations[4].

$$\begin{cases} {}^{t_n}\tilde{\boldsymbol{d}}^{i} = \tilde{\boldsymbol{d}}^{-} + \frac{1}{6}\Delta t_n \left({}^{t_n}\tilde{\boldsymbol{v}}^{i} - {}^{t_{n+1}}\tilde{\boldsymbol{v}}^{i} \right) \\ {}^{t_{n+1}}\tilde{\boldsymbol{d}}^{i} = \tilde{\boldsymbol{d}}^{-} + \frac{1}{2}\Delta t_n \left({}^{t_n}\tilde{\boldsymbol{v}}^{i} + {}^{t_{n+1}}\tilde{\boldsymbol{v}}^{i} \right) \\ \boldsymbol{M}\,{}^{t_n}\tilde{\boldsymbol{v}}^{i+1} = \boldsymbol{M}\tilde{\boldsymbol{v}}^{-} + \frac{1}{6}\Delta t_n \left(\boldsymbol{F}^{ext}_{{}^{n}N} - \boldsymbol{F}^{ext}_{{}^{n+1}N} \right) - \frac{1}{6}\Delta t_n \left(\left(\boldsymbol{F}^{int}_{{}^{n}N} \right)^{i} - \left(\boldsymbol{F}^{int}_{{}^{n+1}N} \right)^{i} \right) \\ \boldsymbol{M}\,{}^{t_{n+1}}\tilde{\boldsymbol{v}}^{i+1} = \boldsymbol{M}\tilde{\boldsymbol{v}}^{-} + \frac{1}{2}\Delta t_n \left(\boldsymbol{F}^{ext}_{{}^{n}N} + \boldsymbol{F}^{ext}_{{}^{n+1}N} \right) - \frac{1}{2}\Delta t_n \left(\left(\boldsymbol{F}^{int}_{{}^{n}N} \right)^{i} + \left(\boldsymbol{F}^{int}_{{}^{n+1}N} \right)^{i} \right) \end{cases} \tag{5}$$

To fully take advantage of explicit formulations, the key is to avoid solution of linear system of equations. Thus in most explicit method, the main goal is to accomplish a diagonal (lumped) mass matrix and preserve the diagonal structure through the entire computation.

Parallel implementation aspects

During the time stepping procedure, exchange of data is unavoidable between processors sharing the same node. Even though tying to minimize the number of shared nodes, the remaining communication has to be done in an efficient way in order to achieve speed-up close to ideal.

The proposed method is based on collective communication assembling data for the shared nodes. For internal and external forces (the RHS), this collection have to take place every time step, while the entities in the diagonal mass matrix only are assembled once. Special treatment has to be carried out for concentrated external loads acting on the common nodes. Since repeated adding has to be avoided, these loads are added to the global right-hand side for shared nodes by just the master processor itself.

The overall algorithm for parallel implementation of the DG(1)-method is described in Figure 2 below.

Concluding remarks

As the size of engineering problem tends to grow in an accelerating manner, the possibility to utilize available parallel computers for speedup the computation becomes more attempting. From previous experience of the authors, communication packages as e.g. MPI provides a tool, which is efficient and rather easy to use and even if MPI is not a standard for FORTRAN 90, the combination seems to have a promising future for efficient software on scalable computing systems.

Experience from programming work also indicates that maintaining programs where the parallel and serial versions use the same procedures and are incorporated in the same program code are beneficial. In case that the program needs to be modified, it follows that only one version of the source code is necessary to maintain.

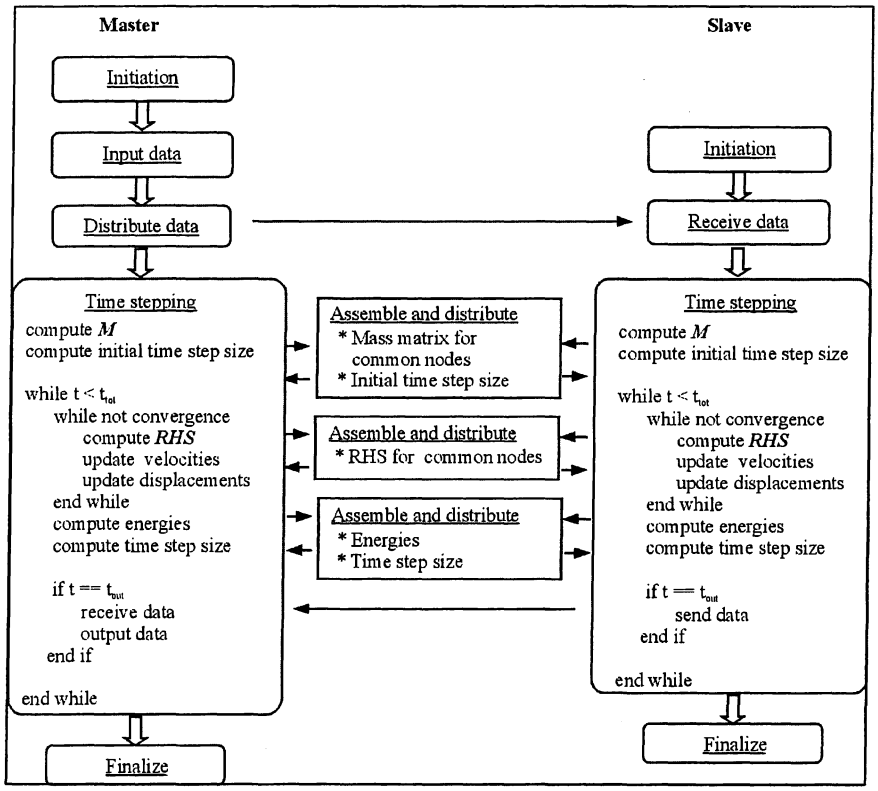

Figure 2. Overall parallel algorithm for the DG(1)-method.

References

[1] T. Belytschko and T.J.R. Hughes, *Computational methods in mechanics*, Elsevier, Amsterdam, (1983)

[2] M.A. Doainish and K. Subaraj, "A survey of direct time-integration methods in computational structural dynamics- I. Explicit methods". *Computers and Structures*, **32**(6), 1371-1386 (1989)

[3] MPI-2: Extension to the Message Passing Interface, University of Tennessee, Knoxville, Tennessee, (1997).

[4] N.-E. Wiberg and X.D. Li, "Adaptive finite element procedures for linear and non-linear dynamics", *Int. Journal of Numerical Methods in Engineering*, **46**, 1781-1802, (1999)

[5] K. Danielsson and R. R. Namburu, "Nonlinear dynamic finite element analysis on parallel computers using FORTRAN 90 and MPI", *Advances in Engineering software*, **29**(3-6), 179-186 (1998)

A METHOD TO ANALYSE THE NON-LINEAR DYNAMIC BEHAVIOUR OF CARBON-BLACK-FILLED RUBBER COMPONENTS USING STANDARD FE-CODES

PER-ERIK AUSTRELL, MARTIN JÖNSSON, ANDERS K OLSSON

Department of Mechanics and Materials, Division of Structural Mechanics, Lund University, P.O. Box 118, SE-221 00 Lund, Sweden

Abstract: For filled elastomers damping is caused by two different mechanisms at material level, resulting in viscous (rate dependent) and frictional (amplitude dependent) damping respectively [1] [3]. In the one-dimensional case this can be modelled with a rheological model consisting of a viscoelastic component coupled in parallel with an elastoplastic component according to figure 1.

Constitutive models for rubber used in standard FE-codes are usually either hyperelastic or viscoelastic. Elastoplastic models, needed to model the frictional damping, are also normally supplied in order to model the plastic behaviour of highly stressed metal.

The aim of this work is to propose a FE-procedure that is able to represent the dynamic behaviour of rubber materials including both rate and amplitude dependence as well as nonlinear elastic behaviour. The overlay method offers a method to obtain such a model using only the already implemented constitutive models in standard FE-codes. The result is a FE-model corresponding to the one-dimensional generalized rheological viscoplastic model discussed in section 1.

1 Introduction

Carbon black filled rubber consists of long polymer chains and a structure of microscopical carbon particles connected by weak crosslinks. Reorganization of the rubber network during periodic loading results in a viscous type of damping. The frictional damping is attributed to the filler structure and the breaking and reforming of the structure which take place during loading and unloading. The stresses obtained in a filled rubber material can thus be divided into a dominant elastic part, but also a viscous and a frictional part.

Combining the viscoelastic and the elastoplastic model in parallel yields a material model which sums the elastic, viscous and frictional stresses. A simple five-parameter model of this viscoplastic type is shown in figure 1. The model simulates the rate and amplitude dependence in a physically correct manner.

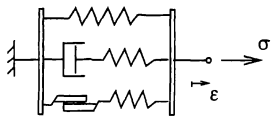

Figure 1: Mechanical analogy illustrating a simple viscoplastic material model resulting in a frequency and amplitude dependent dynamic modulus and damping.

Filled rubber materials subjected to harmonic loading show combined frequency and amplitude dependence of the dynamic modulus and phase angle. The behaviour of the material model in figure 1 in harmonic loading is illustrated in figure 2. The phase angle is a measure of the damping and thus also a measure of the hysteresis. I.e., a large phase angle yields a large difference between the loading and unloading curves. Values of

the modulus and phase angle, for which the amplitude and frequency results in a power output which exceeds a certain limit has been removed from the figure.

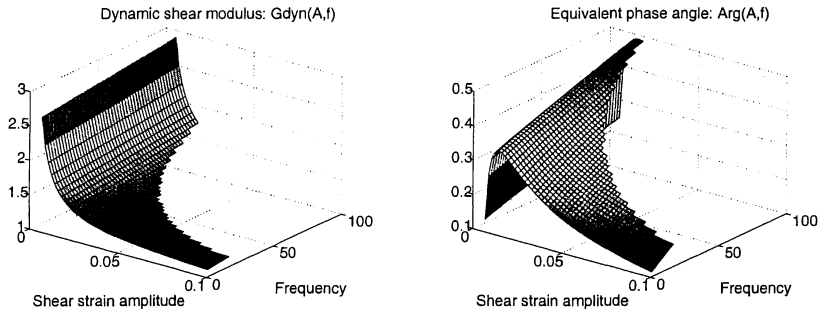

Figure 2: *One-dimensional viscoplastic material model. Amplitude and frequency dependence of the dynamic modulus and phase angle.*

The one-dimensional model shown in figure 1 can be generalized by adding more viscous and frictional elements in parallel. The model can then be given a quantitative better fit to experimental data. In section 2 this model is generalized into three dimensions for the purpose of finite element calculations.

2 The Overlay Method

According to the one-dimensional viscoplastic model shown in figure 1, the total stress is obtained by adding the elastic stress, the viscous, and the plastic stress. A direct generalization for a three dimensional stress state would be to add the elastic, plastic and viscous stress tensors. The total stress tensor $\boldsymbol{\sigma}$ is then given by

$$\boldsymbol{\sigma} = \boldsymbol{\sigma}^{e} + \boldsymbol{\sigma}^{ep} + \boldsymbol{\sigma}^{ve}$$

where the different stress tensors are obtained from a hyperelastic, a elastoplastic and a viscoelastic material model. The hyperelastic contribution is in this paper according to a model by Yeoh [5].

The elastoplastic part of the stress tensor is given by a summation

$$\boldsymbol{\sigma}^{ep} = \sum_{j=1}^{M} \boldsymbol{\sigma}_{j}^{ep}$$

where the terms are obtained from a non-hardening plasticity model, according to von Mises, implemented for large strains. The model used in this paper uses three terms in the summation above.

The viscoelastic stress contribution is also given by a summation according to

$$\boldsymbol{\sigma}^{ve} = \sum_{k=1}^{N} \boldsymbol{\sigma}_{k}^{ve}$$

where the terms are obtained from a visco-hyperelastic model, suitable for large strains.

2.1 Implementation of the overlay method

An easy way to obtain a model according to section 2 using standard FE-codes, without having to program a new constitutive model, is to use an overlay of FE-meshes. The basic approach using the overlay method, is to create one hyperelastic, one viscoelastic and one elastoplastic FE-model, all with identical element meshes. Assembling the nodes of these models according to figure 3, yields a finite element model that corresponds to the five-parameter model discussed earlier. In order to create a model corresponding to the generalized viscoplastic rheological model one simply add a suitable number of viscoelastic or elastoplastic FE-models.

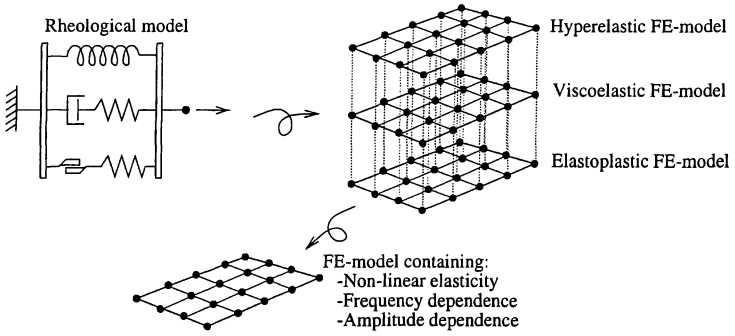

Figure 3: *Basic idea of the overlay method. The different basic FE-models are assembled into one model containing both frequency and amplitude dependent properties as well as non-linear elastic characteristics.*

Preliminary investigations indicate that the material parameters needed for the finite elements models can simply be copied from the one-dimensional model which have been fitted to experimental data.

The reason why the one-dimensional rheological model seems to be easily generalized into three-dimensions has not been thoroughly investigated. However, one reasonable explanation for this behaviour is that the isotropic and incompressible characteristics of rubber provides a constraint that reduces the degrees of freedom in the three-dimensional model.

3 Cylindric rubber bushing

A cylindric component according to figure 4 has been studied in [2]. The component is submitted to large amplitudes at low frequencies. The very slow load rate makes it possible to neglect the viscous contribution. Hence, the material model used in this paper contains only the hyperelastic and the elastoplastic stress contributions. The component has been submitted to a variety of different load cases. Only the radial load case is presented in this abstract.

Figure 4 shows the cylindric component submitted to a radial loading. The load case is displacement controlled and cyclic, with gradually increasing amplitude. The graph shows the relation between the radial force P, obtained from the finite element analysis, and the radial displacement. The graph also shows the influence of the non-linear elastic stress

contribution on the hysteretic response. The sharp corners of the hysteretic response is characteristic for the behaviour of highly filled rubber materials. If only the viscous damping was modelled the shape of the hysteretic response would be almost elliptic.

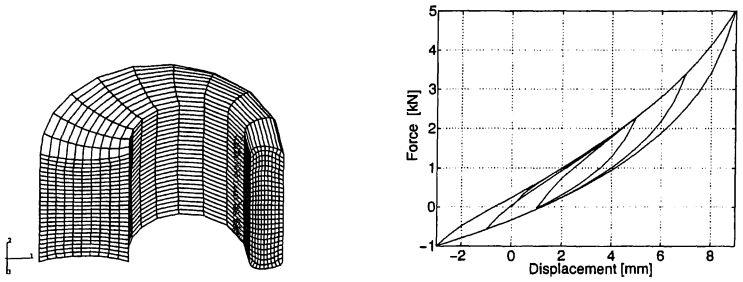

Figure 4: *Amplitude dependent dynamic stiffness. Analysis of the cylindric component submitted to a radial cyclic load.*

References

[1] P-E. Austrell
Modeling of Elasticity and Damping for Filled Elastomers
Lund University, Lund Institute of Technology, Division of Structural Mechanics, Sweden 1997, Report TVSM-1009

[2] P-E. Austrell, M. Jönsson
Analys av några axialsymmetriska gummikomponenter
Lund University, Lund Institute of Technology, Division of Structural Mechanics, Sweden 1999, Report TVSM–99/7129–SE (1-42)

[3] M. Kaliske, H Rothert
Constitutive Approach to Rate independent Properties of Filled Elastomers
Int. J. Solids Structures Vol. 35, No. 17, pp. 2057-2071, 1998

[4] J. C. Simo
On a Fully Three-Dimensional Finite-Strain Viscoelastic Damage Model: Formulation and Computational Aspects
Computer Methods in Applied Mechanics and Engineering, Vol. 60, pp. 153-173, 1987

[5] O. H. Yeoh
Characterization of Elastic Properties of Carbon-black-filled Rubber Vulcanizates
Rubber Chemistry and Technology, Vol. 66,pp. 754-772, 1993

OPTIMIZATION OF STEPPED SPHERICAL SHELLS OF VON MISES MATERIAL

J. Lellep and E. Tungel

Institute of Applied Mathematics,
Tartu University
46 Vanemuise str., Tartu 51014, ESTONIA

Abstract

An optimization procedure is developed for ideal rigid-pastic spherical shells pierced with a central hole. Outer edge of the shell is simply supported whereas the inner edge is absolutely free.

1. INTRODUCTION

Different approaches to optimization of non-elastic structural elements have been developed by G. Rozvany (1976), M. Save (1972), J. Lellep (1991). Axisymmetric plates and shallow spherical shells of minimum weight are studied by J. Lellep, H. Hein (1993, 1994) assuming that the thickness is piece-wise constant and that the material obeys Tresca yield condition. Deep spherical shells of Tresca material have been studied by J. Lellep and E. Tungel (1998).

It is somewhat surprising that relatively less attention has been paid to the optimization of plates and shells material of which obeys von Mises yield condition.

2. FORMULATION OF THE PROBLEM AND BASIC EQUATIONS

Let us consider a spherical shell of radius A subjected to the uniformly distributed transverse pressure of intensity P. Assume that the external edge of the shell (the circle corresponding to $\varphi = \beta$) is simply supported and the inner edge at $\varphi = \alpha$ is absolutely free.

Let the shell wall be of piece-wise constant thickness (Fig. 1), e.g.

$$h = h_j, \quad \varphi \in (\alpha_j, \alpha_{j+1}) \tag{1}$$

where $\alpha_0 = \alpha$, $\alpha_{n+1} = \beta$ and $j = 0, ..., n$. The number n and angles α, β are considered as given constants whereas h_j $(j = 0, ..., n)$ and α_j $(j = 1, ..., n)$ are to be defined so that the load carrying capacity P_0 attains the maximal value for given weight or material volume of the shell.

In the case of a sandwich spherical shell the material volume of a car-

rying layer can be presented as

$$V = \sum_{j=0}^{n} h_j(\cos\alpha_j - \cos\alpha_{j+1}). \tag{2}$$

We are looking for the minimum of the cost function

$$J_1 = -P_0 \tag{3}$$

under the condition that $V = V_0$ and that there exists a statically admissible stress field corresponding to the external loading $P = P_0$. In other words, we are using the lower bound approach to the load carrying capacity. According to the lower bound theorem of limit analysis actual limit load corresponds to the maximum of the load factor associated with a statically admissible stress field.

The equilibrium equations of a spherical shell element can be presented as (here the configuration changes of the shell are neglected)

$$\begin{aligned} (N_\varphi \sin\varphi)' - N_\Theta \cos\varphi &= S\sin\varphi, \\ (N_\varphi + N_\Theta + PA)\sin\varphi &= -(S\sin\varphi)' \\ (M_\varphi \sin\varphi)' - M_\Theta \cos\varphi &= -AS\sin\varphi. \end{aligned} \tag{4}$$

In (4) and henceforth primes denote differentiation with respect to current angle φ.

For the sake of convenience the following non-dimensional quantities will be used

$$\begin{aligned} &\gamma_j = \frac{h_j}{h_*}, \quad k = \frac{t}{2A}, \quad p = \frac{PA}{N_*}, \quad \gamma = \frac{h}{h_*}, \\ &n_{1,2} = \frac{N_{\varphi,\Theta}}{N_*}, \quad m_{1,2} = \frac{M_{\varphi,\Theta}}{M_*}, \quad s = \frac{S}{N_*}, \quad v = \frac{V}{h_*}. \end{aligned} \tag{5}$$

Here h_* stands for the thickness of layers of the reference shell of constant thickness. The quantities M_* and N_* stand for the yield moment and yield force for the reference shell, respectively. Thus $N_* = 2\sigma_0 h_*$, $M_* = \sigma_0 h_* t$, σ_0 being the yield stress of the material of carrying layers.

Material of the shell (of carrying layers) is assumed to be an ideal rigid-plastic material obeying von Mises yield condition. In its original form the yield condition suggested by von Mises can be presented as

$$\sigma_1^2 - \sigma_1\sigma_2 + \sigma_2^2 \le \sigma_0^2 \tag{6}$$

σ_1, σ_2 being principal stresses.

In the present paper the yield surface

$$\frac{1}{N_0^2}(N_\varphi^2 - N_\varphi N_\Theta + N_\Theta^2) + \frac{1}{M_0^2}(M_\varphi^2 - M_\varphi M_\Theta + M_\Theta^2) = 1 \tag{7}$$

will be used. Here M_0, N_0 stand for the yield moment and yield force, respectively, for the current section of the shell, e.g. $M_0 = \sigma_0 th$, $N_0 = 2\sigma_0 h$.

Making use of (5) equilibrium equations (4) can be presented as

$$\begin{aligned} (n_1 \sin\varphi)' - n_2 \cos\varphi &= s \sin\varphi, \\ (n_1 + n_2 + p)\sin\varphi &= -(s\sin\varphi)' \\ k[(m_1 \sin\varphi)' - m_2 \cos\varphi] &= s \sin\varphi. \end{aligned} \tag{8}$$

3. SOLUTION OF THE PROBLEM

The problem set up above will be considered as a particular problem of optimal control with the objective function (3), state equations (8) and additional contraints (9), (10). Variables n_1, m_1, s will be treated as state variables and n_2, m_2 as controls (Lellep, 1991). However, it appears that the variable s can be eliminated from the set (8).

The set of equations (8) takes the form

$$\begin{aligned} n_1' &= (n_2 - n_1)\cot\varphi - \left(n_1 + \frac{p}{2}\right)\tan\varphi + \frac{p}{2}\frac{\sin^2\alpha}{\sin\varphi\cos\varphi}, \\ m_1' &= (m_2 - m_1)\cot\varphi - \frac{1}{k}\left(n_1 + \frac{p}{2}\right)\tan\varphi + \frac{p}{2k}\frac{\sin^2\alpha}{\sin\varphi\cos\varphi}, \\ p' &= 0 \end{aligned} \tag{9}$$

It can be shown that the adjoint equations have the form

$$\begin{aligned} \Psi_1' &= \Psi_1(\tan\varphi + \cot\varphi) + \frac{\Psi_2}{k}\tan\varphi + \nu_j(2n_1 - n_2), \\ \Psi_2' &= \Psi_2 \cot\varphi + \nu_j(2m_1 - m_2), \\ \Psi_3' &= \frac{1}{2}\left(\tan\varphi - \frac{\sin^2\alpha}{\sin\varphi\cos\varphi}\right)\left(\Psi_1 + \frac{\Psi_2}{k}\right) \end{aligned} \tag{10}$$

for $\varphi \in D_j$ $(j = 0, ..., n)$.

The non-linear boundary value problem with equations (9) and (10) is solved numerically making use of different computer codes. It is worthwhile to mention that due to discontinuities of variables m_2 and n_2 one has to integrate the sets (9) and (10) in regions $D_j (j = 0, ..., n)$ separately. Satisfying the appropriate boundary and jump conditions for state and adjoint variables one obtains the full optimal solution.

The results of calculations are presented in the case $n = 1$ in Table 1. Here p stands for the maximal load factor whereas p_* is the limit load for the reference shell of constant thickness. The coefficient e in Table 1 shows the efficiency of the design established above.

Table 1: Optimal design for $k = 0.02$ and $\gamma_0 = 1.5$

α_0	α_2	α_1	γ_1	p	p_*	e
0,8	1,0	0,929	0,159	1,399	1,033	35%
0,6	1,0	0,834	0,417	1,557	1,205	29%
0,4	0,6	0,525	0,303	1,429	1,290	11%
0,4	0,8	0,624	0,523	1,663	1,351	23%

REFERENCES

1. Lellep, J. (1991). Optimization of Plastic Structures. Tartu Univ. Press, Tartu.

2. Lellep, J. and Hein, H. (1993). Optimization of rigid-plastic shallow shells of piece wise constant thickness. Struct. Optim., 6, 2, 134-141.

3. Lellep, J. and Hein, H. (1994). Optimization of clamped rigid-plastic shallow shells of piece wise constant thickness. Int. J. Non-Linear Mech., 29, 4, 625-636.

4. Lellep, J. and Tungel, E. (1998). Optimization of plastic spherical shells of piece wise constant thickness. Proc. Estonian Acad. Sci. Phys. Math., 47, 4, 260-269.

5. Rozvany, G.I.N. (1976). Optimal Design of Flexural Systems: Beams, Grillages, Slabs, Plates, Shells. Pergamon Press, Oxford.

6. Save, M.A. (1972). A unified formulation of the theory of optimal plastic design with convex cost functions. J. Struct. Mech. 1, 2, 267-276.

On Optimization of laminated plates with prestress: Using topology optimization

Niels L. Pedersen
Department of Solid Mechanics
Technical University of Denmark, Building 404, DK–2800 Lyngby, Denmark

1. Introduction

In this paper we investigate the possibilities of optimizing laminated plates with prestress. Topology optimization of prestressed plates has already been performed in Pedersen (2000) but in that paper the plate was assumed to be made from one homogeneous material with the same overall prestress throughout the plate. In the present paper the plate will be considered to be a laminate with different prestress levels in the different layers, see figure 1.

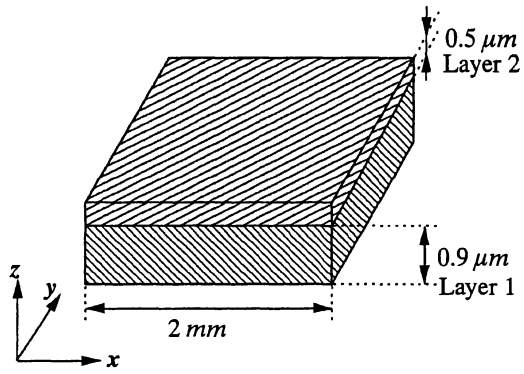

Figure 1. The laminate presently used

We will use topology optimization with a material distribution concept and mathematical programming. For an overview of topology optimization see Bendsøe (1995) and references therein. The focus of this paper is on laminated plates with different prestress in the individual layers. The object of the optimization is the distribution of the material in the plate since the prestress is given apriori from manufacturing. Because the prestress levels are in magnitude up to 400 MPa there will be a stiffening effect on the plate, this stiffening is accounted for by adding an initial stress stiffness matrix to the structural stiffness matrix (see Cook (1989) for further details). In addition to the initial stress stiffness matrix the prestress also gives a contribution to the force on the structure. When working with only one layer as in Pedersen (2000) or using symmetrical laminates the deformation due to the prestress will only be in–plane. In contradiction to this, the deformation of unsymmetrical laminates will also be out–of–plane.

2. Sensitivity analysis

The optimizations are performed using mathematical programming. The sensitivities (preferable analytical) of the different objectives and constraints are therefore needed. The fact that we are working with laminated plates with high levels of prestress will complicate the derivation of the sensitivities; and the calculations of the sensitivities are therefore shown. Before giving the derivation of the sensitivities it is shown how the prestress is added to the analysis of the structure.

2.1. Prestress

The prestressing of the structure introduces a force on the structure which is given by

$$\{F_\sigma\} = \sum_{e=1}^{NE} \{f_\sigma\}_e \qquad \{f_\sigma\}_e = -\int_v [B]_e^T \{\sigma_0\}_e \, dv \tag{1}$$

where $[B]_e^T$ is the usual matrix in finite elements that relates strain to displacements of element e and $\{\sigma_0\}_e$ is the prestress. The prestressing of the plates will also results in an initial stress stiffness matrix $[K_\sigma]$ see e.g. Cook (1989). The initial stress stiffness matrix is given by

$$[K_\sigma] = \sum_{e=1}^{NE} [k_\sigma]_e \qquad [k_\sigma]_e = \int_v [G]^T [S][G] dv \tag{2}$$

The matrix $[G]$ consists of derivatives of the finite element shape functions while the matrix $[S]$ contains the stress level of the element due to the prestressing. The stress level of the structure depends on the boundary conditions and has to be found by an initial static stress analysis. The force displacement relation corresponding to the prestress is given by

$$([K] + [K_\sigma])\{D_\sigma\} = \{F_\sigma\} \tag{3}$$

where $[K]$ is the original stiffness matrix and $\{D_\sigma\}$ is the displacement due to the prestress. The prestress may be expressed in prestrain, $\{\sigma_0\}_e = [E]\{\epsilon_0\}_e$. Using this, the stress level of the structure due to the prestressing is

$$\{\sigma_i\}_e = [E](\{\epsilon\}_e - \{\epsilon_0\}_e) = [E]([B]\{D_\sigma\}_e - \{\epsilon_0\}_e) \tag{4}$$

where $\{\epsilon\}_e$ is the resulting strain of element e . With the stress level given in (4) the initial stress stiffness matrix (2) can be calculated, and we see directly that the initial stress stiffness matrix is a function of the deformation resulting from the prestress. It should be noted that we may not find the pre–displacement using $[K]\{D_\sigma\} = \{F_\sigma\}$ as was the case in Pedersen (2000) were only one layer where considered. From (4) one should also note that the initial stress stiffness matrix is a function of the displacement due to the prestress, it is therefore necessary to perform a Newton–Raphson iteration to fulfil the equation

$$\{\Phi\} = ([K] + [K_\sigma(\{D_\sigma\})])\{D_\sigma\} - \{F_\sigma\} = \{0\} \tag{5}$$

When performing the Newton–Raphson iteration on (5) we will need the inverse of the derivative with respect to pre–displacement this matrix is given by

$$[K] + [K_\sigma] + \frac{\partial([K_\sigma]\{\overline{D_\sigma}\})}{\partial\{D_\sigma\}} \tag{6}$$

with the bar over quantities indicating that the quantity is regarded as a constant in the differentiation. For later reasons it is important to note that the last part of (6) is unsymmetric, which leads to an unsymmetric total matrix.

2.2 Sensitivity of compliance (work of external force)

Including the initial stress stiffness matrix, the force displacement relation for the structure is

$$([K] + [K_\sigma])\{D\} = \{F\} \tag{7}$$

where $\{F\}$ is the total force on the structure and $\{D\}$ is the total displacement. The force $\{F\}$ and the displacement $\{D\}$ may be split in two parts: the part coming from the prestress and the part coming from the external forces.

$$\{F\} = \{F_{ex}\} + \{F_\sigma\} \tag{8}$$

$$\{D\} = \{D_{ex}\} + \{D_\sigma\} \tag{9}$$

The objective of the optimization is not to minimize the total compliance or elastic energy of the structure but only the part that relates to the external force. This can be achieved by minimizing the work done by the external forces

$$W = \frac{1}{2}\{F_{ex}\}^T\{D_{ex}\} = \frac{1}{2}\{F_{ex}\}^T(\{D\} - \{D_\sigma\}) \tag{10}$$

We now need to take the derivative of (10) with respect to the design parameters. When using topology optimization and the SIMP method the design variables are the relative densities of the individual element in our finite element formulation. As was the case in Pedersen (2000) it is not preferable to take the derivative of the compliance directly since this expression will involve the derivatives $d\{D\}/d\rho_e$ and $d\{D_\sigma\}/d\rho_e$ where ρ_e is the design parameter, the relative density of element e. These derivatives could be found from differentiating equations (3) and (7) the computational cost is however too large. The two equations are instead augmented to the objective function resulting in the objective

$$\begin{aligned} W = {} & \frac{1}{2}\{F_{ex}\}^T(\{D\} - \{D_\sigma\}) + \{\lambda_1\}^T(\{F\} - ([K] + [K_\sigma])\{D\}) \\ & + \{\lambda_2\}^T(\{F_\sigma\} - ([K] + [K_\sigma])\{D_\sigma\}) \end{aligned} \tag{11}$$

The augmented objective is in principle identical to the original objective since we have only added zero quantities. At the same time we are free to chose the values of the multiplier vectors $\{\lambda_1\}$ and $\{\lambda_2\}$. The above method where we augment the objective is known as the adjoint variable method see Tortorelli and Michaleris (1994). Taking the derivative of (11) with respect to the design parameter gives

$$\begin{aligned} \frac{dW}{d\rho_e} = {} & \frac{1}{2}\{F_{ex}\}^T\left(\frac{d\{D\}}{d\rho_e} - \frac{d\{D_\sigma\}}{d\rho_e}\right) \\ & + \{\lambda_1\}^T\left(\frac{d\{F\}}{d\rho_e} - ([K] + [K_\sigma])\frac{d\{D\}}{d\rho_e} - \left(\frac{d[K]}{d\rho_e} + \frac{d[K_\sigma]}{d\rho_e}\right)\{D\}\right) \\ & + \{\lambda_2\}^T\left(\frac{d\{F_\sigma\}}{d\rho_e} - ([K] + [K_\sigma])\frac{d\{D_\sigma\}}{d\rho_e} - \left(\frac{d[K]}{d\rho_e} + \frac{d[K_\sigma]}{d\rho_e}\right)\{D_\sigma\}\right) \end{aligned} \tag{12}$$

From (12) we see that the unwanted derivatives of the displacement and the pre–displacement can be removed by choosing specific values of the multipliers. Although we are able to remove some derivatives we have also introduced some new derivatives. The use of the adjoint variable method is only applicable if the introduced terms are simple to achieve (computationally cheap). The derivative of the initial stress stiffness matrix can not be easily found, but we can avoid the problem by splitting the terms involving the derivative in two parts as

$$\{\lambda_1\}^T\frac{d[K_\sigma]}{d\rho_e}\{D\} = \{D\}^T\frac{\partial(\{\lambda_1\}^T[K_\sigma])}{\partial\{D_\sigma\}}\frac{d\{D_\sigma\}}{d\rho_e} + \frac{\partial(\{\lambda_1\}^T[K_\sigma])}{\partial\rho_e}\{D\} \tag{13}$$

By using (13) and the fact that the design parameter is a local quantity defined on an element level the final scheme for calculating the sensitivities becomes; we calculate the two Lagrange multiplier vectors.

$$([K] + [K_\sigma])\{\lambda_1\} = \frac{1}{2}\{F_{ex}\} \tag{14}$$

$$([K] + [K_\sigma] + \frac{\partial([K_\sigma]\{\overline{D_\sigma}\})}{\partial\{D_\sigma\}^T})^T\{\lambda_2\} = -(\frac{1}{2}\{F_{ex}\} + \frac{\partial([K_\sigma]\{\lambda_1\})}{\partial\{D_\sigma\}^T}\{D\}) \tag{15}$$

From this we can now calculate the sensitivities

$$\begin{aligned} \frac{dW}{d\rho_e} = {} & \{\lambda_1\}_e^T\left(\frac{d\{F_\sigma\}_e}{d\rho_e} - \frac{d[K]_e}{d\rho_e}\{D\}_e - \frac{\partial[K_\sigma]_e}{\partial\rho_e}\{D\}_e\right) \\ & + \{\lambda_2\}_e^T\left(\frac{d\{F_\sigma\}_e}{d\rho_e} - \frac{d[K]_e}{d\rho_e}\{D_\sigma\}_e - \frac{\partial[K_\sigma]_e}{\partial\rho_e}\{D_\sigma\}_e\right) \end{aligned} \tag{16}$$

where again e refers to element number.

3. Examples

There is defined a passive area at the center of plate with a radius of $0.8mm$. The material data are.

$$E_1 = 80{\cdot}10^9\, N/m^2 \qquad \nu_1 = 0.1987 \qquad \hat{\rho}_1 = 1725\, kg/m^3$$

$$E_2 = 110{\cdot}10^9\, N/m^2 \qquad \nu_2 = 0.1987 \qquad \hat{\rho}_2 = 1725\, kg/m^3$$

The plate is clamped at all four edges. In the example we only model one quarter because of symmetry and this part is discretizised by 40×40 elements. The prestress is thought to be a result of temperature change so that two principal stresses are identical while the rest of the stresses are zero.

$$\sigma_{xx} = \sigma_{yy} \qquad \sigma_{zz} = \sigma_{xy} = \sigma_{xz} = \sigma_{yz} = 0 \tag{17}$$

The prestress level in the plate is different in the two layers in layer 1 the prestress is $\sigma_{xx} = \sigma_{yy} = 400\, MPa$ while the prestress in layer 2 is $\sigma_{xx} = \sigma_{yy} = -50\, MPa$. In figure 2 the maximum deflection of the plate due to the prestress ($(d_\sigma)_{\max} = \| \{D_\sigma\} \|_\infty$) is also given.

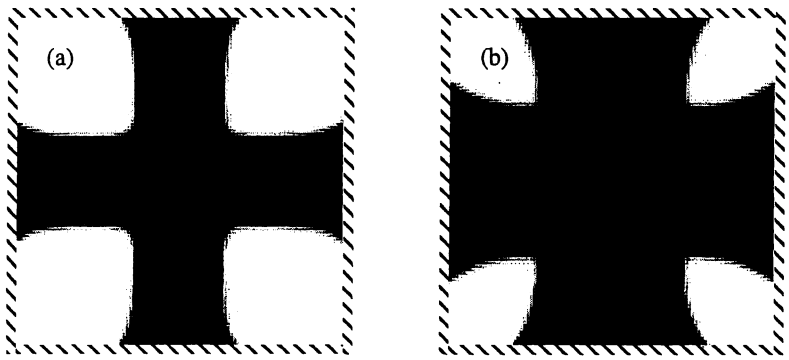

Figure 2. Optimization of compliance. The structure is loaded with an evenly distributed force on a circular part at the center and the plate is clamped at the four edges. (a) 50% material and (b) 75% material.

Acknowledgments

The author wishes to thank Pauli Pedersen, Ole Sigmund and the rest of the TOPOPT group, at the Technical University of Denmark, for fruitful discussions. This work was supported by the Danish Technical Research Council through the THOR–programme (Technology for Highly Oriented Research): "Systematic design of MEMS". This support is highly appreciated.

References

Bendsøe, M. P. (1995) "Optimization of Structural Topology, Shape and Material". Springer

Cook, R. D., Malkus, D. S. and Plesha, M. E. (1989) "Concepts and Applications of Finite Element Analysis". John Wiley & Sons, Inc.

Pedersen, N. L. (2000) "On Topology Optimization of Plates with Prestress" *Int. J. Numer. Met. Engng.* (accepted)

Tortorelli, D. A. and Michaleris, P. (1994) "Design Sensitivity Analysis: Overview and Review". *Inverse problems in Engineering* **1**, 71–105

PAPERBOARD PACKAGES EXPOSED TO STATIC LOADS; FINITE ELEMENT MODELING AND EXPERIMENTS

L. Beldie†, G. Sandberg†, P. A. Wernberg† and L. Sandberg*

†Department of Mechanics and Materials, Division of Structural Mechanics, Lund University, P.O. Box 118, SE-221 00 Lund, Sweden e-mail: bmlb@byggmek.lth.se, home page: http://byggmek.lth.se/

*Stora Enso Research, P.O. Box 9090, SE-650 09 Karlstad, Sweden e-mail: lars.sandberg@storaenso.com

1 INTRODUCTION

Paperboard packages represent a large and constantly growing part within the food-packaging industry due to their advantages compared with more traditional packaging methods. Continuous improvements, concerning both material and package design, have led to better products and increased usage of paperboard packages.
Meanwhile, problems can arise during transportation due to the combination of static and dynamic loads to which the packages are subjected, which can lead to damage. The static loads within a stack of packages are a result of the internal pressure and pressure from the surrounding packages. Dynamic loads arise due to vertical and horizontal acceleration. During transport, roughness and holes in the road give rise to vertical forces while sudden breaking leads to horizontal forces.
Understanding how a paperboard package performs under static loads is an important step in the process of designing better packages. In this paper, the study of paperboard panels and a single paperboard package subjected to static compressive loads is presented. Experiments and finite element analysis for each study are conducted. In the finite element simulations, the paperboard is modeled as an orthotropic linear elasto-plastic laminate. The study utilizes a non-linear finite element analysis based on the plasticity of the material and large displacements, and was performed on panels of various size and a paperboard package of the dimensions $0.085 \times 0.125 \times 0.246\ m^2$.

2 EXPERIMENTS

The experiments were performed at Stora Enso Research in Karlstad, Sweden. Three types of static tests were made. In the first set of experiments, one side was cut out of the package and subjected to edge compressive loading. Second, the package was divided into three parts and each part was individually loaded in compression. Third, the whole package was loaded in compression.

2.1 Compression of panels

The testing setup used in this experiment consists of three beams mounted in a vertical U-shape. The beams are provided with tracks in which the paperboard can glide. A fourth beam compresses the panels, as showed in Figure 1. Panels of $0.075\ m$ width and varying height can be compressed using this setup. Three panels of different dimensions were

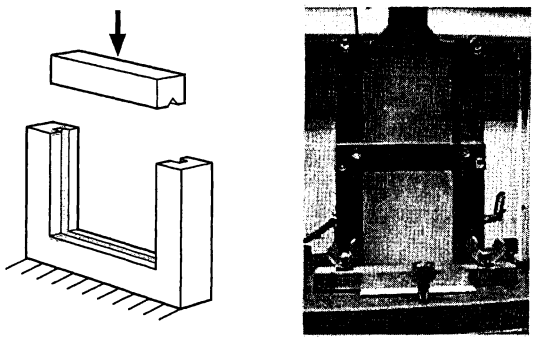

Figure 1: *Testing instrument for compression of a panel.*

subjected to edge compressive loading and the results are presented as force-displacement diagrams in Section 4.1. The test results were used as a verification of the finite element model of the material.

3 THE FINITE ELEMENT MODEL

In the finite element analysis ABAQUS/Standard 5.8 was used, while the pre-processing was performed with MSC/Patran 9.0. Compression of one package is a highly nonlinear problem, including large displacements and material nonlinearity.
The paperboard package was modeled with shell elements S4R5, which are 4-node doubly curved shells, using five degrees of freedom per node and reduced integration. The average element size was 4 *mm*. In reality, the package is folded and glued on the top and bottom so that three sheets of paperboard are in contact with each other in these areas. For this reason, a triple thickness was applied for the shell elements on the top and bottom of the package model. All six sides of the package were free to rotate around the corner axes in the finite element model. This is an approximation since, in reality, some bending stiffness exists in the corners. This approach was, however, assumed to be closer to reality then if the sides were entirely locked.
The paperboard was finite element modeled as an orthotropic linear elasto-plastic laminate material. The elasto-plastic material model for the paperboard was implemented by means of the ABAQUS linear kinematic hardening material model for a Hill yield surface.

4 COMPARISON OF FINITE ELEMENT SIMULATIONS AND EXPERIMENTS

4.1 Panels

Three paperboard panels of different dimensions were modeled with elements of type S4R5 and boundary conditions according to the conditions in the testing device used. The bulging of the panels was measured before the tests and this was applied as an initial imperfection, together with two higher eigenmodes obtained from an eigenvalue analysis. The results for a panel of dimensions 0.075×0.150 m^2 are presented in Figure 2.

The results presented in Figure 2 show good agreement between the finite element

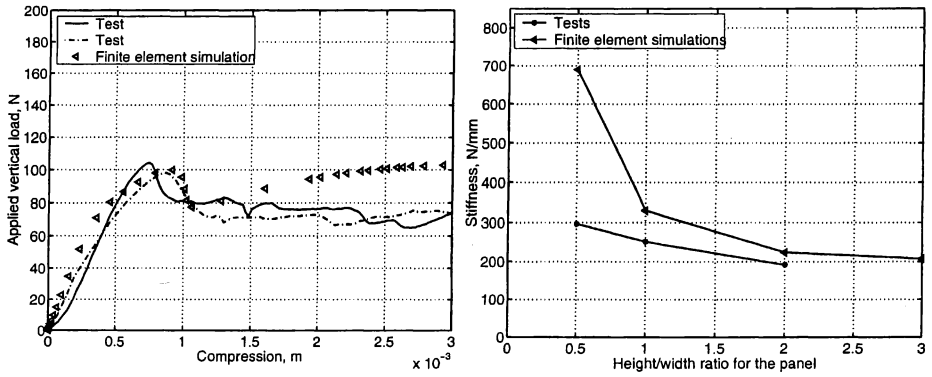

Figure 2: *On the left, compression of a panel of dimensions 0.075×0.150 m^2. On the right, variation of stiffness with the height:width ratio of the panel. Tests and FEM simulations.*

compression simulation and the test of a panel of dimensions $0.075 \times 0.150\ m^2$, that is, for a panel with a height:width ratio of 2. For the vertical walls of the package studied, this ratio is of 2 and 2.9 for the adjacent sides of the box. The agreement between the simulations and the tests tends to deteriorate as the height of the panel decreases. According to the test results, the stiffness of the panels does not change significantly as the height is varied, while the simulations show an increased stiffness for shorter panels. This can be explained by the fact that the upper and lower edge of the tested panels are not geometrically perfect, they might not be perfectly parallel and present irregularities due to the cutting process. This will lead to an uneven crushing of the edges in the compression tests. These phenomena become more dominant for shorter panels, preventing the stiffness of the panels to increase at the same rate as for the finite element simulations. The variation in stiffness with the height:width ratio can be seen in Figure 2. This diagram shows that there is good agreement between tests and simulations for panels with a height:width ratio of 2 or more.

4.2 The whole package

The package was modeled with 9550 elements of type S4R5. Two types of imperfection were applied. First, an eigenvalue analysis was conducted and two eigenmodes were imposed as initial imperfections. The largest imposed displacement was 6.24 *mm*, i.e. 10 times the paperboard thickness. The model was then compressed 1 *mm* and the deformed model was then used as an imperfection in a new compression simulation. The stresses in the model are concentrated at the upper corners, which is in agreement with the experimental results. Even the deformation of the model is in agreement with that seen in the experiments. The deformed package after a compression simulation is shown in Figure 3. The comparison of the stiffness results for a whole package was poor and it was concluded that a better model for the creases is needed. In Figure 3, a section of a crease is shown.

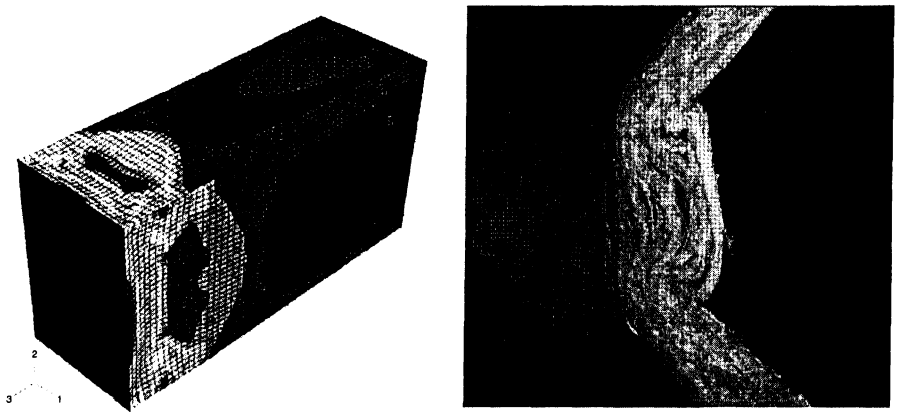

Figure 3: *On the left, von Mises' stress for the finite element model of the whole package subjected to compression. On the right, a section of a crease.*

5 CONCLUSIONS.

The numerical computations for a paperboard panel are in good agreement with the test results for a panel with a height:width ratio of 2 or higher. The agreement between the simulations and the tests tends to decrease as the height of the panel decreases. This leads to poor agreement between simulations and tests for the upper/lower parts of the package. The tests show that the middle part of the package exhibits a higher stiffness than the whole package, which leads to the conclusion that the low initial stiffness of the package is a consequence of the low stiffness of the upper/lower corners. The corners in the model were allowed to rotate and two types of imperfection were applied in the model of the whole package. The results show that the stiffness of a paperboard package is dictated mostly by the creases at the corners, and a more accurate model of the creases would improve the results.

References

[1] GRANGÅRD H., *Some Aspects of the Compressive Strength of Cartons*, Svensk papperstidning, (1972).

[2] GRANGÅRD H., KUBAT J., *Compression of Board Cartons*, Svensk papperstidning, (1973).

[3] WÅGSÄTER T., PALENRYD A., *FE-simuleringar och experimentella försök på kartongförpackningar*, Department of Structural Mechanics, Lund University, Sweden, (1998).

[4] HIBBITT, KARLSSON & SORENSEN , *Inc., ABAQUS Users Guide, Version 5.8*, Pawtucket, RI, USA, (1973).

Comment on a Recent Hardware Benchmark for Lunarc

G. Sandberg and K. Persson, Structural Mechanics

Per-Anders Wernberg, Lunarc

B. Jönsson and M. Kahn, Theoretical Chemistry

September 28, 2000

Abstract

This paper discusses a recently performed benchmark for high performance computing. Comparison are made between "off-the-shelf" PC-based solutions, including standard components as the AMD Thunderbird processor and the Alpha 21264 processor, and systems from conventional UNIX vendors. The comparison is based on both in-house Monte Carlo, quantum mechanic and finite element codes and on general, third party, finite element software. The background for the benchmark is to form the basis for the decision of building a Beowulf system.

Background

Traditionally, research utilising high performance computing have been relying on expensive computer systems. The history for Lunarc, the Centre for Scientific and Technical Computing at Lund University, is certainly a proof of this. The last couple of years new types of computer systems, e.g. Beowulf systems, which relies on cheap standard processors like the Intel-, AMD- or Alpha-processors have been gaining interest. Scientific and technical computing however has not yet developed deep experience in using such systems. The benchmark, reported in this paper, has been part of a basis for the decision to introduce such a system for the Lunarc groups.

Introduction

Lunarc was established November 26, 1996. It is an organisation within Lund University for cooperation in the field of scientific/technical computing. Collaborating units are the Divisions of Theoretical Chemistry, Physical Chemistry 2, and Structural Mechanics.

The core mission for Lunarc is to initiate and support activities and cooperation in research and education concerning scientific/technical computing, particularly efforts that demand high performance computers. Among the tasks for Lunarc are

[1]This paper was presented at the 13th Nordic Seminar on Computational Mechanics in Oslo, October 20-21, 2000

[2]The benchmark was performed during one week in september 2000

- acting for long term competence development within the field,
- attracting external resources for education, research, and equipment,
- acting as the University contact towards external organisations both nationally and internationally,
- cooperating with other research groups and organisations in the field of scientific/technical computing both nationally and internationally.

Lunarc Hardware History

Lunarc as a centre with a key responsibility within the area of scientific and technical computing was established in November 1996, ten years after the first event launched by the core groups of Lunarc. November 20, 1986 the first computer used by the groups, an IBM 3090-150/VF was inaugurated. The installation of the system, named Helios, was possible due to a study contract from IBM. At that time this was the largest IBM study contract in Europe, a recognition of the work and ambition of the researchers within the three groups.

In 1988 the computer, expanded to an IBM 3090-170/VF, was bought from IBM by funds mainly from the SE Bank. The system was in production until January 1991, when it was replaced by a network of workstations, IBM RS6000, of various sizes. The network was gradually enlarged by new computers up until 1996. The largest single addition was the installation of an eight-node parallel machine, an IBM SP2, in 1992. For a short moment, some ten weeks, it was the largest university computer in Sweden.

By the end of 1995 the capacity of the system had become a serious bottle neck for the research at the three departments, and a total revision was necessary. At the same time the group felt that the knowledge within the area of high performance computing and the network the group had established within this community should be put to work to the benefit of other research groups at Lund University. The groups proposed to Lund University that the collaboration between the groups should be transferred to a centre for scientific and technical computing.

In June 1997 Lunarc was granted 15 MSEK from the Knut and Alice Wallenberg Foundation and in September the same year Lunarc issued a request for proposals regarding a new parallel system for Lunarc. February 22, 1998 Lunarc signed a contract with Silicon Graphics that included a parallel system of 46 processors R10000, 250 MHz, a graphical visualization system ONYX2. Included in the contract was the upgrade to a 116 processor machine, R120000, 300 MHz processors, by June 1999.

Looking back on this period of fourteen years of utilization of computers for Lunarc: it is astonishing to note that the system installed in 1986 had a peak capacity of 20 Mflops for scalar calculations and 110 Mflops for computations performed in the vector processor. The 116-processor machine today has a peak capacity of close to 60.000 Mflops!

Benchmark software

The software used in the benchmark are MOLCAS, StatMech, some special purpose finite element routines and the general purpose finite element code Abaqus. Molcas is a quantum mechanical software, see also http://www.teokem.lu.se/molcas/about.html. StatMech is a statistical mechanical, Monte Carlo software, for simulating molecular systems. Below are listed some keywords for the various runs.

TC1 – TC3: CPU intensive statistical mechanical simulation, minimum memory demands, approximately 8 Mb, and no I/O.

Seward: The build up of integrals in a quantum mechanical problem, solving the Scrödinger Equation, medium memory demand and limited I/O.

SCE: Reading of the integral set generated by Seward, and diagonalisation based on an iterativ scheme.

The following three runs uses the general finite element software Abaqus.

Def: A two-dimensional nonlinear material mechanics analysis consisting of 5 014 degrees-of-freedom. An elastic-plastic material model is used and contact between the body and a rigid surface is defined. Since high friction is applied the problem will be unsymmetric. Memory requirement: 13 Mb, highly IO-dependent.

Dyn: A three-dimensional dynamic steady-state analysis of accoustic wave transmission through a floor consisting of 57 120 degrees-of-freedom. Memory requirement: 152 Mb.

Lin: A three-dimensional linear-elastic analysis of a wood microstructure consisting of 304 996 degrees-of-freedom. Memory requirement: 184 Mb.

Gen: Geometry and finite element mesh generation of a three-dimensional structure containing 1 044 936 degrees-of-freedom. Memory requirement: 105 Mb.

Fem1: Analysis of a temperature problem using a sparse-iterative solver. The model consists of 60 000 degrees-of-freedom. Memory requirement: 97 Mb.

Result of the comparison of SGI, Alpha and AMD

The following computer systems used as single processors where compared

Embla: SGI/Cray origin system, R12000 300 MHz, 256 Mb of CPU memory, five striped disks, SGI FORTRAN (and C) version 7.2.

UP1100: 600 MHz EV6, 256 Mb. COMPAQ FORTRAN (and C) for Alpha linux

AMD[1]: 1 GHz, 256 Mb. Portland group FORTRAN for i386 Linux.

It can be noted from Table 1 that both the Alpha processor and the AMD processor have far better performance than Embla. The speed-up-factor is between 20% and 100%. Also to be noted is that AMD is slightly faster than the Alpa.

Table 2 show that also for standard commercial finite element software the AMD processor perform better than the Embla system. The speed-up- factor is over two in one case. Still however the I/O performance slows down the overall performance but not to the extent that it questions the advantage of the AMD system.

[1]AMD is also available in a 1.1 GHz version

Table 1: *Timing in seconds for the benchmark running various in-house codes*

	Embla	UP1100	AMD running Linux
TC1	467	268	266
TC2	207	126	97
TC3	86	59	63
Seward	65	37	34
SCF	46	29	21
Gen	39	20	24
Fem1	62	51	54

Table 2: *Timing in seconds for the benchmark runs using Abaqus*

	Embla		AMD running NT4	
	user	real	user	real
Def	380	413	174	395
Dyn	294	326	211	290
Lin	226	314	144	237

Conclusion

The benchmark clearly shows that for single processor jobs, cheap standard processors compete very well with more advanced and expensive systems. The price relationship for the investigated systems AMD : UP1100 : Embla is approximately 1 : 1,5 : 10. Taking into account the performance for the benchmark runs the price-performance ratio is 1 : 1,6 : 17. Communication between processors is still a bottleneck. The implementation of a Gbit network between processors will close to double the cost for an AMD system. Also the utilization of the memory is of course easier for the standard Unix system. However, it can be concluded that the introduction of standard PC components will fundamentally cut costs for high performance computing.

Finally, the availability, the "of-the-shelf"-character, of the equipment like the one tested in this benchmark is another great advantage compared to general systems for high performance computing[2].

[2]The AMD system was bought, built and initiated during the first day. The day after the benchmark was conducted.

FROM TROLL TO FORUM

Use of offshore methods in the analyses and postprocessing of tall concrete buildings

Dan-Evert Brekke, Jasna B. Jakobsen, Roar Lie and Brynjar Sandvik

Troll A gas platform

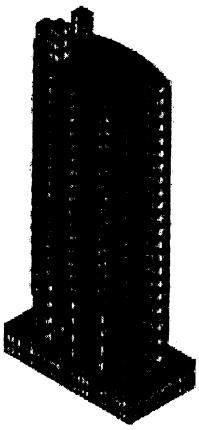

Forum hotel, FE model

For tall buildings accurate design calculations are necessary to satisfy specified safety and economical requirements. Multiconsult has recently been involved in the design of two such tall buildings, Forum hotel in Stavanger and an office building in Oslo. Our experience is that the calculation methods applied on many of the large offshore concrete structures for the North Sea, also represent an adequate approach for the design of such buildings.

Introduction and Background

During the last years Multiconsult has been responsible for the design of two rather tall buildings with a height of about 70 meters. One is the Forum hotel, formed as an ellipse, in Stavanger, and the other an office building at Sørkedalsveien 6 in Oslo.

The design of tall buildings includes various problems of different nature. In this article focus is put on the force distribution, design of concrete, and response to the wind load.

For most building structures, an effective, economic and secure design may generally be obtained without the use of a complex FEA. Based on a relatively simple structural model, the governing force distribution and design can in such cases be performed by help of long hand calculations and various stand alone program packages. Often the structure is not highly utilized, also explaining why one can accept a somewhat lower accuracy in the design calculations.

For the present tall buildings with 20 floors, the wind load and its response within the structure would apparently be governing for many structural parts, first of all the stiffening walls. With the architects need for open spaces in the lower floors, many walls could not continuously enter the ground, but had to be stopped or partly stopped in these regions. Such irregularities would of course have a great influence on both the stiffness and the load-bearing capacity of these structures. One of the buildings (Sørkedalsveien 6) had to be founded on piles down to the rock, due to very bad soil conditions. Both project teams concluded that the complexity of their buildings would require a more advanced design

calculation procedure than commonly used for more ordinary and lower buildings. We decided to give our FEA and postprocessor/design technology originally developed for offshore structures, a chance to go onshore.

Since the present buildings have relatively low frequencies and are located in urban areas, their dynamic response to gusty wind also had to be checked. This implies obtaining wind load effects including dynamic amplification factors (DAF's), and checking for possible large accelerations at the top of the buildings. The latter calculation is performed as a separate calculation, i. e. a stochastic calculation of the standard deviation of accelerations.

Calculation Procedure

For each of the two buildings the analyses were based on two models, one coarse model for modal dynamic analysis, and one finer model for the force response and design of the concrete structures. Each building was first modelled with geometric areas and lines. This made it easy to mesh the two models from the same basis.

The coarse model was used to find the eigenfrequencies and corresponding mode shapes and modal masses. This model included masses of the building applied at appropriate locations. Wind load effects including DAF's, are found on the basis of eigenfrequencies and mode shapes. These load effects were then included in the finer model to obtain the load response for design of the concrete structures.

In the stochastic calculation of the standard deviation of acceleration the eigenfrequencies and corresponding mode shapes and modal masses from the coarse analysis are used.

Finite Element Analyses

The analyses were performed by using the program ANSYS. For the static analysis a linear frontal solver with reuse of the stiffness matrix for each load case was adopted. The superposition of load responses was performed in the postprocessor. The dynamic analysis was based on the subspace iteration technique, which internally uses the generalized Jacobi iteration algorithm. It is highly accurate because it involves the full [K] and [M] matrices.

The analyses were performed on a PC, Intel Pentium II 266MHz with 20GB Disc and 256MB RAM, running Windows 98.

The static analyses required finer models than the dynamic analyses, since the static analyses were to be used for design. The model size for the Forum hotel in Stavanger is tabulated below.

	Static analysis	Dynamic analysis:
Nodes	69.011	3.930
Shell elements	68.467	4.156
Beam elements	1.232	342
Degrees of freedom	412.914	23.316

As the numbers show the static analysis became very large. The size of the triangularized file was about 8.0 GB, and about 5.0 GB of results was obtained. Windows 98 was not able to handle these large files. By trails and errors we managed to get around the disc problem. A file split option in ANSYS, allowed us to keep the size of each result file below 1.0 GB. A maximum of 5 right hand sides for each retracking run was then found. Several retracking runs had then to be performed for solving all load cases specified.

Another problem was to fit the large analysis into the RAM space available and to achieve a reasonable run time for the analysis. By using the different elementreordering options available in ANSYS, a matrix wavefront suitable for the computer memory and speed was obtained. The run time of the analysis on this relatively modest PC was about 24 hours for the reduction run and 12 hours for each backward substitution.

Very few simplifications were made in the model. The columns and beams were meshed with 2-noded beam elements. For the plates and walls the 4-noded shell elements have been adopted. Both types of elements have 6 degrees of freedom at each node. The elements have been based on appropriate material properties and dimensions to simulate the structure as properly as possible. All major block outs in both walls and plates have been included.

By connecting vertical beams with horizontal shell elements, singularity problems arise in the shell elements. These problems have been dealt with and passed in the postprocessor.

Postprocessing

During the 1980's and first half of the 1990's, Multiconsult was highly involved in the detail design of several offshore concrete platform structures for the North Sea. Among these was the TROLL A GBS (gas) platform, the worlds largest of its kind with a height of about 370 meters. To perform an economic and safe design of such complex structures, huge linear finite element analyses (FEA) had to be taken into use. With the help of advanced postprocessors, such as CONPOST (now named MultiCon) partly developed by Multiconsult, the FEA-results in terms of volume element stresses were integrated, transformed and combined to find the governing loadresponse throughout the complete shell structure. Finally, the concrete compression capacity was checked and required reinforcement amounts calculated through an enormous design code iteration process /1/.

What would be the best analysis and design strategy for the present tall buildings? Would it be reasonable to apply our advanced analysis and design tools within a rather small "calculation budget"? Should we try to model and design the whole building within one complete FEA, or should we rather only base the design of the walls and columns on one analysis, and the design of the floors on a separate local analysis? We decided to choose the former alternative, as a kind of pilot project.

Our experiences from the use of this integrated FEA/postprocessor tool (ANSYS/MultiCon) for design of tall concrete buildings are summarized as follows:

Global accuracy requirements: When modelling the total building with a correct structural geometry, the stiffness and the global force distribution of the building will be very accurate.

Detail accuracy requirements: In order to use the analysis results for further postprocessing and design, the element mesh must be regular, and of a certain fineness. For instance, in the riegel area of a wall, at least 4 elements are required across the height in order to catch a possible stressvariation in this area. Thus, 8 – 10 elements are required across the height from one floor to another. In the horizontal direction, the number of elements may vary, but from one span to another, at least 5 elements are recommended.

Loads and load combinations: With a postprocessor tool as MultiCon, the load combination work is effectively taken care of by the postprocessor itself. Thus, only unit load cases are run within the FEA program, reducing the required number of load cases to a minimum.

Complete design code check: A complete concrete design can successfully be performed for the walls in all sections from top to bottom. These code check calculations include capacity checks of the concrete in compression together with an updating of all required reinforcement amounts due to both ultimate limit state (ULS) and serviceability limit state (SLS) requirements. All design results in terms of required reinforcement amounts and corresponding utilization ratios are visualized by plotting directly on the

element model, both ensuring the quality of the analysis and design work and in addition yielding a very efficient design process.

Traceability: To avoid any kind of "black box" design, our postprocessor and design program MultiCon includes features which give the engineer the possibility to trace the complete load and code check history for all calculated design results.

Material amounts and economy: Simplified hand calculation methods are most often conservative compared to a FEA where the load-bearing capacity of the complete structure is utilized. Thus, the required amounts of concrete and reinforcements can be reduced to a minimum by the use of FEA, and hence contribute to low cost.

Security: For complex structures, there is seldom easy to foresee the correct force distribution only by use of knowledge, skills and simplified methods. However, in both our two tall building projects, the FEAs helped us to reveal unexpected response in critical structural elements.

Time consumption: With the severe environmental conditions in the North Sea, the required FEA's were not only very complex, but also very time consuming. It is still a challenge to adopt an optimal design approach, when introducing such program tools into the onshore market, where the structural calculation part of a total project normally is rather small.

Human response to building vibrations in gusty wind

Possible large accelerations at the top of a building would cause discomfort for the users. References. /2/and /3/ give guidelines for an acceptable standard deviation of the horizontal acceleration. They consider human response to infrequently induced low-frequency horizontal building vibrations caused by storms, i. e. intrusion, alarm and fear. In buildings used for general purposes, the criterion is that probably not more that 2 % of those occupying the parts of the building where the motion is greatest, comments adversely about the motion caused by the peak 10 min of the worst wind storm with a return period of 5 years or more.

The excitation of the building has been calculated according to the theory of wind loading and structural response, developed by Davenport in the sixties, presented in e.g. Refs. /4/, /5/ and /6/.

The wind speed is described as the sum of a constant mean wind and a gusty wind.

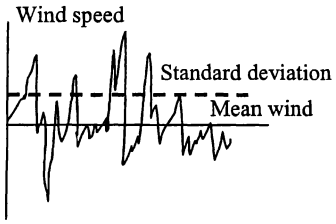

The mean wind speed as the function of the height was defined by a logarithmic function for urban areas. The gusty wind is described in terms of turbulence intensity, power spectral density and the normalized co-spectrum. Power spectral density defines the distribution of the wind energy at a single point, at different frequencies. The co-spectrum adds the information on the spatial structure of the wind.

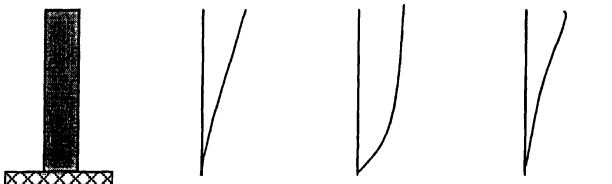

Modal wind forces were thus calculated taking into account that the gusty wind is not correlated over the building area normal to the mean wind. Vibration shapes and modal masses for the lowest frequencies were obtained from the FEA.

Standard deviation of the acceleration in the along-wind direction was calculated for the two lowest modes.

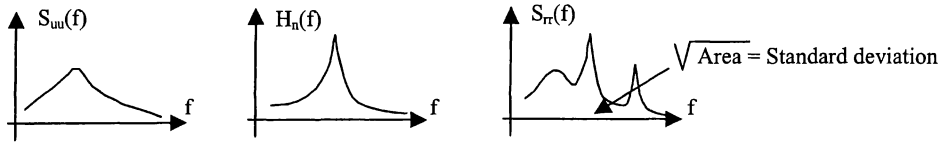

Normalized wind spectrum

Structural admittance for mode n

Response spectrum (two modes included)

For a narrow banded response, which is the case for the acceleration spectra, the response for the two lowest frequencies can be calculated separately.

As already mentioned the standard deviation of the acceleration was calculated by taking into account that the gusty wind is not correlated both vertically and horizontally across the building. In addition the acceleration was calculated also by assuming that fluctuating wind velocities are perfectly correlated in the horizontal direction across the 30 meter wide building. An example for Sørkedalsveien 6 is given in the table below.

Mode	Eigen-frequency [Hz]	Modal Mass [kg]	Standard deviation acceleration One dimensional [m/s^2]	Standard deviation acceleration Two dimensional [m/s^2]
1	0.424	4052821	0.0395	0.0203
2	1.604	8517283	0.0080	0.0023

For a frequency of 0.4 Hz, a limit of 0.04 m/s^2 is given by Ref. /2/. For the one dimensional calculation the values are at the limit of acceptable, while taking into account the that the gusty wind is not correlated across the building gives a standard deviation well within what is acceptable.

References

/1/ Brekke, D.–E., Åldstedt, E., Grosch, H.; Design of Offshore Concrete Structures Based on Postprocessing of Results from Finite Element Analysis. Proceedings of the Fourth International Offshore and Polar Engineering Conference. Osaka, Japan 1994.

/2/ ISO 6897 - 1984 (E), Guidelines for the evaluation of the response of occupants of fixed structures, especially buildings and off-shore structures, to low-frequency horizontal motion (0.063 to 1 Hz).

/3/ NS 4931, Veiledning for bedømmelse av menneskers reaksjoner på lavfrekvente horisontale bevegelser (0.063 til 1 Hz) i faste konstruksjoner, særlig bygninger og installasjoner til havs. 1985. (In accordance with ISO 6897 – 1984. In Norwegian).

/4/ Davenport, A. G., "Wind Structure and Wind Climate" and "The Prediction of the Response of Structures to Gusty Wind" [in] "Safety of Structures under Dynamic Loading", ed. by Holand et al., Tapir Publishers, Trondheim, 1978.

/5/ Hjorth-Hansen, E., "Fluctuating Drag Loading by Wind; Wind Engineering; Lecture Note 1", The Norwegian Institute of Technology, Trondheim, 1989.

/6/ Dyrbye, Cl. & Hansen, S.O., "Wind Loads on Structures", John Wiley & Sons, 1996.

Load capacity of tap bolted connections in tension

Lennart Østergaard, Henrik Stang and Lars Damkilde
Department of Structural Engineering and Materials
Technical University of Denmark, DK-2800, Kgs. Lyngby

Introduction

Tap bolted connections are used in space structures as the joint between spherical nodes and trusses, see figure 1. The connection consists of a bolt which is screwed into a threaded hole tapped in the spherical node, as shown on the figure. The bolt itself is mounted on the truss. This connection is different from a connection between a bolt and a nut because of the large outer diameter of the spherical node.

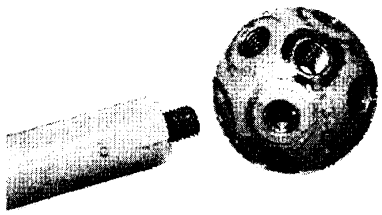

Figure 1: Spherical node and truss

Analytical methods to determine the load carrying capacity of tap bolted connections are difficult to establish. In [1] a simplified solution of the failure of the nut thread is derived.

Some experimental results can be found in [2]. The authors concluded that a linear relationship between the failure load and the length of the thread in engagement was valid until failure load of the bolt itself was reached. The Swedish building code SMS 1964, [3], tabulates required lengths of thread in engagement as a function of the strength of the bolt and nut materials.

This paper explains how to model tap bolted connections numerically as a contact problem between the nut and bolt thread. The obtained results are compared to a proposed analytical model and experimental observations.

Modelling

Three different failure modes must be considered, see figure 2. These are (a) tearing off the nut thread, (b) tearing off the bolt thread and finally (c) failure of the bolt itself. Derivation of the load capacity of failure mode (a) and (b) follows the same scheme.

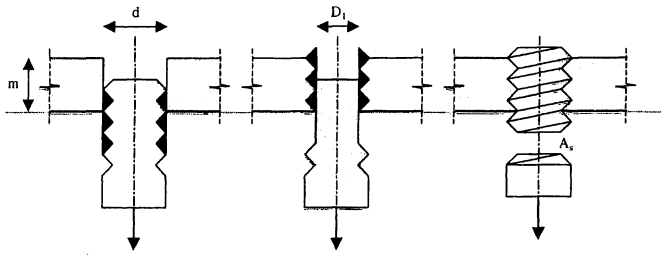

Figure 2: Failure modes

The connection was modelled in COSMOS as a plane strain contact problem using contact elements. Note that due to the axisymmetric geometry of the connection this model is a simplification of the system but the errors introduced are relatively small. The contact elements allow for the modelling of movements of two surfaces parallel and perpendicular to each other. It is thereby possible to model the normal and shear forces generated on the contact surfaces. The mesh which proved to give results with a sufficient precision is shown on figure 3a. The wide black line on the figure denotes the line of contact between the threads.

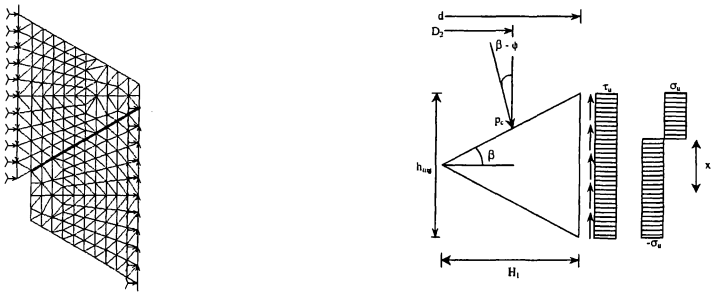

Figure 3: FEM-mesh (a) and simplified model of threads used in the analytical model (b)

Triangular elements with 3 nodes were used to model the threads. Thereby, only corner nodes are present on the contact surface. This proved important during the modelling. Contact elements are placed at every node on the contact surface. Choosing correct boundary conditions were difficult since the movements on the contact surfaces had to be in accordance with the real system and since numerical problems were encountered. Horizontally, the threads are supported on the outer vertical borders as shown. This is an approximation which is acceptable due to the large outer diameter that results in a good horizontal confinement of the threads. However, this boundary condition makes modelling of friction impossible. Therefore, the model can only be applied if the angle of friction is low. This is the case if the threads are in good condition e.g. greased with oil. Otherwise, a more complex boundary condition horizontally must be chosen that allows for movements in this direction. The threads are free to move vertically. The load is applied at the outer vertical boundaries. It is linear varying with maximum at the middle and zero at the top and bottom. This distribution was shown to yield an acceptable precision [4]. The threads were defined with real material properties determined from uniaxial tension tests.

Loading the threads in small steps allows for determination of the nonlinear constitutive condition between the nut and the bolt until failure. The load at failure is defined as the level where the von Mises stresses in a given vertical section approach the ultimate stress limit. The constitutive condition is then implemented in the connection itself as nonlinear springs combining the bolt and the nut materials. The latter model is axisymmetric and the stiffness of each spring is chosen in accordance with the radius of placement of the spring and the fineness of the mesh. Failure in this model is defined as the load level where the first spring reach the maximum allowable load determined in the contact model.

The results obtained from the numerical model are compared to experimental results and a proposed analytical model. Derivation of the analytical model is shortly explained in the following.

Determination of the load capacity for a given connection is based on figure 3b which shows a simplified version of the thread geometry with all necessary parameters included. The nominal bolt diameter is denoted by d, D_2 denotes the mean diameter of thread, β is the semi-angle of thread, ϕ the friction angle, H_1 the horizontal width of the contact surface, h_{mg} height of the thread at the section of failure, p_c resultant of contact pressure, τ_u shear stress at failure and σ_u normal stress at failure.

The length x and the stresses at failure, τ_u and σ_u may be determined by the equations of equilibrium. The latter two are then combined using von Mises yield criteria. The load capacity is then found by integration over the entire length of thread in engagement. Since it is assumed that the entire thread in engagement reach τ_u and σ_u at failure, this integration yields the area of the section which fails. Note that the assumption is only valid for small values of thread in engagement, m$\leqq$2d, where m denotes the length of the connection parallel to bolt axial direction. The solution is given by:

$$P = \frac{\cos(\beta - \phi)}{\lambda_{mg}} f_u \, \eta m \pi d \tag{1}$$

in which:

$$\lambda_{mg} = \sqrt{3 - 4\chi\psi\frac{H_1}{h_{mg}} + 2\psi^2\frac{H_1^2}{h_{mg}^2} + 2\frac{h_{mg}\chi - H_1\psi}{h_{mg}^2}\sqrt{(h_{mg}\chi - H_1\psi)^2 + h_{mg}^2\chi^2}} \tag{2}$$

$$\begin{aligned} \eta &= 1 - \tfrac{\sqrt{3}}{8}\tan\beta \\ \chi &= \sin(\beta - \phi) \\ \psi &= \cos(\beta - \phi) + \tan\beta \ \sin(\beta - \phi) \end{aligned} \tag{3}$$

The solution (1) - (3) is valid for failure in the nut thread (failure mode (a), see figure 2). A similar expression may be derived in the case of failure in the bolt thread.

Experiments were performed with a set-up developed in [2]. The set-up has been tested and it gives reproducible results. Figure 4 shows experimental results together with analytical and numerical results. As the figure shows, a good correlation with experimental results has been obtained.

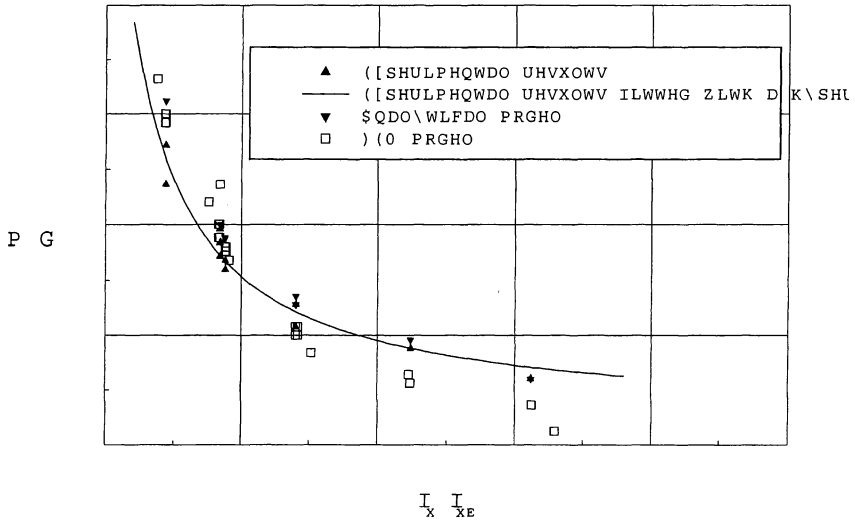

Figure 4: Comparison of results

Conclusion

It is concluded that the proposed mathematical models are able to describe the behavior of tap bolted connections with a good precision. The numerical model is suited to describe the behavior from start of loading to failure, and may be used for any value of m. However, the systematically error due to the 2D-modelling is a limitation in the model (see figure 4). To overcome this error, the problem must be regarded as a 3D or an axisymmetric problem. The analytical model can be used to determine the load capacity for any moderate value of m ($m \leqq 2d$). Experiments have confirmed the mathematical results.

References

[1] J. Rasmussen. *Maskinelementer I [in danish].* Afdelingen for Maskinelementer, Technical University of Denmark, 1982.

[2] H. Wiegand, K. H. Illgner, and P. Strigens. Einfluß der Gewindesteigung auf die Haltbarkeit von Schraubenverbindungen bei zügiger Beanspruchung (in german). *Industrie-Anzeiger*, 38:869–874, 1969.

[3] Sveriges Standardiseringskommision. Skruvar och muttrar. Gängade bottenhål. Metriska gängor och unifiedgängor. Grov stigning (in swedish). *SMS 1964*, Reg 17.051 UDK 621.882.1, Utgåva 2 1969.06.20.

[4] L. Østergaard. Tap bolted connections in tension (in danish). Master's thesis, Technical University of Denmark, DTU, Department of Structural Engineering and Materials, 1999.

13th Nordic Seminar on Computational Mechanics
20-21 October, 2000, University of Oslo, Oslo, Norway

Buckling analysis of beam-columns using an incremental perturbation method

EIVIND STEEN AND TOM K. ØSTVOLD
Marine Technology and Production Centre, Det Norske Veritas, Norway

1. Introduction

In the present work a multi-span beam-column, subjected to a simultaneously acting axial load and uniform lateral pressure, is analysed. The beam-column has an open asymmetric I-profile cross-section, which make it representative for the most common profiles used for stiffening bottom plates in steel ships.

The method of analysis is based on an incremental form of the virtual work principle in combination with an incremental perturbation method for stepping along the equilibrium path. The discretization follows a Raleigh-Ritz expansion in terms of harmonic functions.

The stress-distribution across the column cross-section and along the column axis is evaluated using a very fine grid of integration points located in the middle-planes of each component plate. The column cross-section is assumed to be solid and thus local buckling effects and twisting of the thin-walled component plates in the cross-section is not considered.

2. Method and assumptions

This paper gives only a very brief description of the theoretical assumptions and methods applied. Background theory and an application of the numerical perturbation method on an elastic mode interaction model for stiffened plates can be found in Steen (1998) and Steen (1999) respectively. Details of the present model is documented in Steen and Andreassen (1995-I, 1995-II).

Under the Bernoulli-Euler hypothesis of plane sections remaining plane and normal to the deformed reference surface, the first order expansion of the virtual work equation takes the following form

$$\int_V \dot{\bar{\sigma}}_{11}\, \delta\bar{\varepsilon}_{11} dV + \int_V \bar{\sigma}_{11}\, \delta\dot{\bar{\varepsilon}}_{11} dV = \delta\dot{E} \tag{1}$$

In Eq.(1) the external work has been given the symbol E. Second order expansion of the virtual work equation gives

$$\int_V \ddot{\bar{\sigma}}_{11}\, \delta\bar{\varepsilon}_{11} dV + 2\int_V \dot{\bar{\sigma}}_{11}\, \delta\dot{\bar{\varepsilon}}_{11} dV + \int_V \bar{\sigma}_{11}\, \delta\ddot{\bar{\varepsilon}}_{11} dV = \delta\ddot{E} \tag{2}$$

Applying a perturbation procedure implies that the rates of change (derivatives) of state variables such as strain, stress, external loads and deflections, with respect to a continuously increasing perturbation parameter emerge as variables. Thus in a proper formulated

perturbation scheme all variables may be considered to be continuos single valued functions of an always increasing perturbation parameter say η. First order rates and second order rates, with respect to this parameter, is given the notation of a single dot and double dot above the variable, respectively.

The kinematic relations is taken from Marguerre's plate theory, which accounts for the unavoidable out of straightness of the stiffener axis typically resulting from production and welding procedures. The constraint condition of prescribing a constant axial load along the column axis is used. This enables the elimination of the axial in-plane deflection u, and only discretization of the lateral deflection w is necessary. The continuos material model of Needleman-Tvergaard is used. This model can simulate stress-strain curves typical for aluminium as well as steel. In the present application elastic unloading effects are neglected.

The only geometrical boundary condition prescribed is that of zero lateral deflections at supports (spaced at a distance L), i.e. no geometrical rotational restraints are prescribed. The external lateral pressure has a uniform value along the column axis over all bays and thus symmetric as well as asymmetric deflection modes are considered.

The discretization of the lateral deflection w follows a standard Raleigh-Ritz formulation in terms of a harmonic Fourier development, i.e. it is assumed that

$$w(x_1) = q_i \, f_i(x_1) \qquad i = 1,2,\ldots,R \qquad (3)$$

where R is the total number of degrees of freedom.

The solution of the present beam-column problem would normally be written in the form

$$q_i = q_i(P, p) \qquad i = 1, 2,\ldots,R \qquad (4)$$

where P is the axial load and p is the lateral pressure. The simultaneously acting axial load P and lateral pressure p are related to the load parameter Λ in a multi-linear stepwise pattern. This multi-linearization can approximate any arbitrary continuos defined load history in load space (P, p) and provides for a single parameter representation of the actual external load system.

Within each linear load sequence of the multi-linear load history, the solution may be written as a function of a single continuously increasing perturbation parameter η. The expanded perturbation solution around a known state I_s takes the form

$$\begin{aligned} q_i &= q_{i,s} + \dot{q}_i(\eta - \eta_s) + \frac{1}{2!}\ddot{q}_i(\eta - \eta_s)^2 + \cdots \\ \Lambda &= \Lambda_s + \dot{\Lambda}(\eta - \eta_s) + \frac{1}{2!}\ddot{\Lambda}(\eta - \eta_s) + \cdots \end{aligned} \qquad i = 1, 2,\ldots,R \qquad (5)$$

A subscript s indicates that the property is known and evaluated at state I_s. In order to provide a parameter that always increases along the prescribed load path, it was demonstrated in Steen (1998) and Steen (1999) that the arc length along the equilibrium path in the solution space (Λ, q_i), was an appropriate parameter. Thus the definition of the perturbation parameter is taken to be the arc length along the tangent to the equilibrium path at a known point, i.e. the perturbation parameter η is defined as

$$\eta - \eta_s = \dot{q}_i(q_i - q_{i,s}) + \dot{\Lambda}(\Lambda - \Lambda_s) \qquad i = 1, 2,...,R \qquad (6)$$

This choice of perturbation parameter means that the unit tangent vector $\mathbf{t}_s$ to the equilibrium path in solution space (Λ, q_i) in state I_s, represent the first order solution to be found. From the first order incremental virtual work equation, Eq.(1) and Eq.(6), the first order perturbation problem is formulated as the following set of R linear equations and one second order equation.

$$G_i\dot{\Lambda} + H_{ij}\dot{q}_j = 0 \qquad i, j = 1,2,...,R \qquad (7)$$

$$1 = \dot{q}_1^{\,2} + \dot{q}_2^{\,2} + \cdots + \dot{q}_R^{\,2} + \dot{\Lambda}^2 \qquad (8)$$

The G_i and H_{ij} are state dependent coefficients. By using a maximum smoothness type of criterion, selecting the minimum angle between the known tangent $\mathbf{t}_{s-1}$ vector in state I_{s-1} and the sought tangent vector $\mathbf{t}_s$ for the current state I_s, the continuos equilibrium path is identified.

From the second order incremental virtual work equation, Eq.(3), the second order perturbation problem is formulated as the following set of R+1 linear equations

$$G_i\ddot{\Lambda} + H_{ij}\ddot{q}_j + K_i = 0 \qquad i, j = 1,2,...,R \qquad (9)$$

$$0 = \ddot{q}_1\dot{q}_1 + \ddot{q}_2\dot{q}_2 + \cdots + \ddot{q}_R\dot{q}_R + \ddot{\Lambda}\dot{\Lambda} \qquad (10)$$

In the present application of the incremental perturbation approach, solutions up to second order is used. This means that the tangent and curvature of the equilibrium path in state I_s are used for finding the next equilibrium state I_{s+1}. Moreover, by using the curvature of the equilibrium state in state I_{s-1} as a measure for selecting the size of the incremental value of the perturbation parameter $\Delta\eta = (\eta - \eta_s)$, the equilibrium path can be followed very accurately without equilibrium control. This has been shown to be the case for many examples by comparisons with other published solutions and analysis programs. This type of documentation on specific examples can be found in Steen and Engelsen (1997).

3. Results

As an illustration, the present procedure has been used for analysing an asymmetric I profile column subjected to pure axial compression. The column had a slenderness of 0.903, which gives a very unstable post-collapse response. Two imperfection levels have been included corresponding to a near perfect and typically fabricated column respectively. The results are given in Fig.1.

Acknowledgements
The continuos support from dr. S. Valsgård, G. Holtsmark, DNV and professor J. Hellesland, University of Oslo, is very much appreciated. Special thanks to E. Andreassen at DNV for his patient programming and testing work and to dr. G. Skeie, DNV for his verification of the theoretical basis.

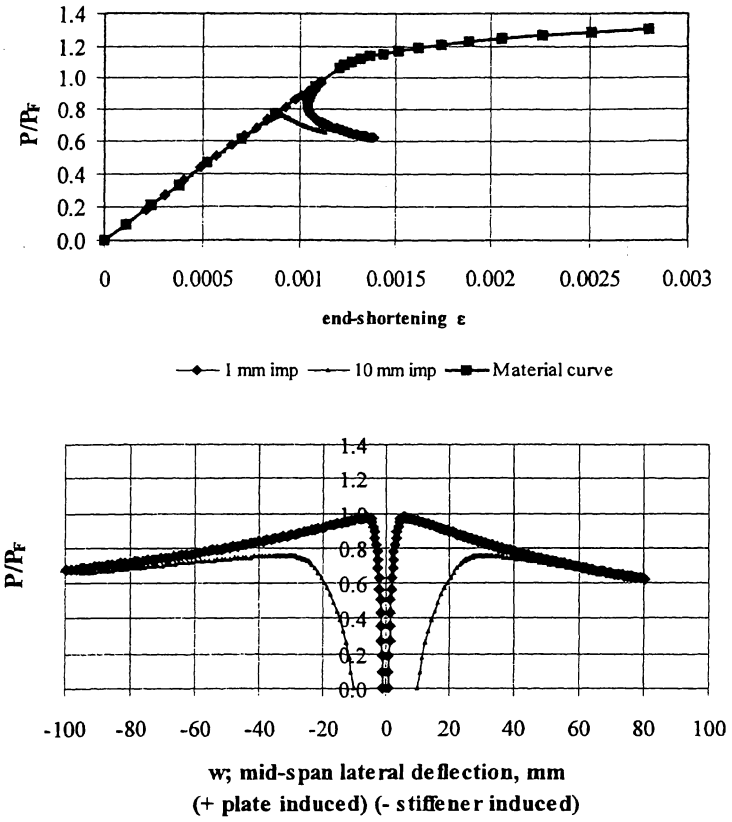

Fig.1. Axial load P/P_F – axial shortening ε curve and axial load P/P_F – lateral deflection w curves of an elastic-plastic column with asymmetric I profile cross-section. Axial load P scaled with squash load P_F. Cross-section: Plate 800 x 7.5 mm, Web 235 x 10 mm, Flange 90 x 15 mm, Column length L = 8000 mm. Needleman-Tvergaard material with n = 16, σ_F = 235 MPa and E = 206 000 MPa.

4. References

1. E. Steen, (1998). "Application of the Perturbation Method to Plate Buckling Problems", Research Report in Mechanics, No. 98-1, ISBN 82-553-1149-1, University of Oslo, Department of Mathematics, Mechanics Division.

2. E. Steen, (1999). "Buckling of Stiffened Plates using a Shanley Model Approach", Research Report in Mechanics, No. 99-1, ISBN 82-553-1182-3, University of Oslo, Department of Mathematics, Mechanics Division.

3. E. Steen and E. Andreassen, (1995-I). "Buckling of Stiffened Plates under Combined loads, PP2: Basic Theory development", DNV Report No. 95-0198.

4. E. Steen and E. Andreassen, (1995-II). "Buckling of Stiffened Plates under Combined loads, PP3: Detailed Theory development", DNV Report No. 95-0479.

5. E. Andreassen, (1996). "User's Guide to Computer Program for Buckling of Continuos Columns ver 1 (Colbuck1)", DNV Report No. 96-0182.

6. E. Steen and A.B. Engelsen, (1997). "ABAQUS analyses – Plate buckling/GL code", DNV Report No. 97-0506.

On linearizations in large-strain viscoelasticity

Bo Häggblad [a,b] *and Göran Paulsson* [a,b]
[a] *Dept. of Solid Mechanics, Royal Institute of Technology, S-100 44 Stockholm, Sweden*
[b] *ABB Corporate Research, S-721 78 Västerås, Sweden*

1. Introduction

We present models for finite viscoelasticity with nonlinear evolution laws that are not restricted to states near thermodynamic equilibrium. By suitable linearizations established models for finite linear viscoelasticity and small strain linear viscoelasticity are recovered. First, we study a common rheological model for a standard linear solid, shown in Fig. 1. The equilibrium back-ground response is given by the spring E_∞ and the evolution of the nonequilibrium over-stress is modeled by the spring E_v in series with a linear viscous element, characterized by the constant damping parameter η. The constitutive equations governing the response of this model can be derived from the isothermal Clausius-Duhem inequality (the second law of thermodynamics) by using the argumentation of Coleman and Gurtin [1]. Inserting the free energy on the form

$$\Psi\left(\varepsilon,\varepsilon_v\right)=\Psi_\infty\left(\varepsilon\right)+\Psi_v\left(\varepsilon-\varepsilon_v\right)=\frac{1}{2}E_\infty\varepsilon^2+\frac{1}{2}E_v\left(\varepsilon-\varepsilon_v\right)^2 \tag{1}$$

into the second law

$$-\dot{\Psi}+\sigma\dot{\varepsilon}\geq 0 \tag{2}$$

we obtain

$$\left(\sigma-\frac{\partial\Psi_\infty}{\partial\varepsilon}-\frac{\partial\Psi_v}{\partial\varepsilon}\right)\dot{\varepsilon}+\frac{\partial\Psi_v}{\partial\varepsilon_e}\dot{\varepsilon}_v\geq 0 \tag{3}$$

Sufficient conditions for the validity of the inequality (3) are the *constitutive relation*

$$\sigma=\frac{\partial\Psi_\infty}{\partial\varepsilon}+\frac{\partial\Psi_v}{\partial\varepsilon}=E_\infty\varepsilon+E_v\varepsilon_e \tag{4}$$

and the *residual dissipation inequality*

$$\frac{\partial\Psi_v}{\partial\varepsilon_e}\dot{\varepsilon}_v\geq 0 \tag{5}$$

It is clear that (5) is satisfied if we choose the *evolution law* to be as in linear viscoelasticity

$$\dot{\varepsilon}_v=\frac{1}{\eta}\frac{\partial\Psi_v}{\partial\varepsilon_e}=\frac{1}{\eta}E_v\varepsilon_e=\frac{1}{\eta}E_v\left(\varepsilon-\varepsilon_v\right) \tag{6}$$

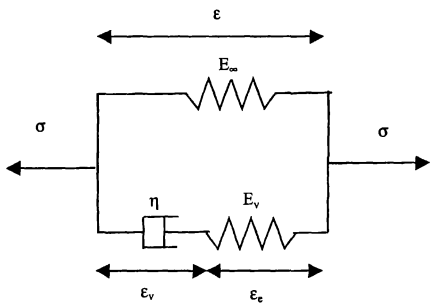

Figure 1. A rheological model for standard linear solid

2. Large strain viscoelasticity

In some situations (e.g. when modeling polymeric materials) it is necessary to consider large strains. In this context it is often assumed that the elastic response (the equilibrium back-ground response and the nonequilibrium over-stress) can be modeled by hyper-elastic networks ("springs"). To handle large elastic and inelastic deformations a multiplicative split of the deformation gradient (**F**) is introduced [2,3]. This defines an intermediate configuration $\mathcal{B}_v$ that would result upon an immediate (local) unloading of the actual overstress to the equilibrium state, see Fig. 2.

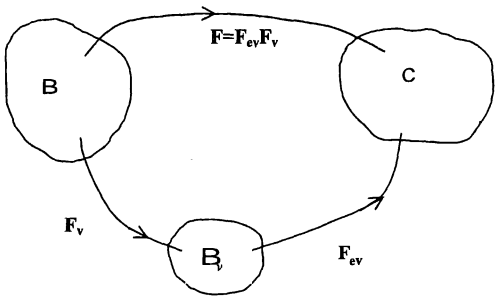

Figure 2. Multiplicative split of deformation gradient with intermediate configuration

Using the free energy

$$\Psi = \Psi(\mathbf{C},\mathbf{F}_v) = \Psi_\infty(\mathbf{C}) + \Psi_v(\mathbf{C}_{ev}) = \Psi_\infty(\mathbf{C}) + \Psi_v\left(\mathbf{F}_v^{-T}\mathbf{C}\mathbf{F}_v^{-1}\right) \tag{7}$$

in the finite counterpart of (2)

$$-\dot{\Psi} + \frac{1}{2}\mathbf{S} : \dot{\mathbf{C}} \geq 0 \tag{8}$$

and the argument of Coleman and Gurtin we obtain in place of (4) and (5)

$$\begin{aligned} &\mathbf{S} = 2\frac{\partial \Psi_\infty}{\partial \mathbf{C}} + 2\mathbf{F}_v^{-1}\frac{\partial \Psi_v}{\partial \mathbf{C}_{ev}}\mathbf{F}_v^{-T} \\ &-\frac{\partial \Psi_v}{\partial \mathbf{F}_v} : \dot{\mathbf{F}}_v \geq 0 \end{aligned} \tag{9}$$

where $\mathbf{S}$, $\mathbf{C}$ and $\mathbf{C}_{ev}$ are the second Piola-Kirchhoff stress tensor and right Cauchy-Green deformation tensors, respectively. Equation $(9)_1$ shows that it is necessary to consider the reference configurations for the response of different components when summing stress contributions. In $(9)_1$ the local spring force is pulled back to the undeformed (material) configuration before summing. Fig. 3 shows a possible nonlinear rheolocigal model.

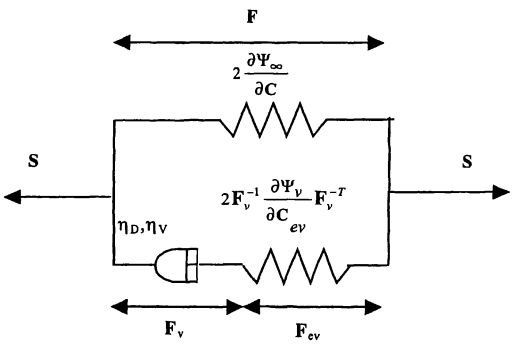

Figure 3. A nonlinear rheological model

Assuming isotropy, the relations in (9) can be expressed entirely in the current (spatial) configuration C avoiding deformation gradients

$$\boldsymbol{\tau} = 2\frac{\partial \Psi_\infty}{\partial \mathbf{b}}\mathbf{b} + 2\frac{\partial \Psi_v}{\partial \mathbf{b}_{ev}}\mathbf{b}_{ev} = \boldsymbol{\tau}_\infty + \boldsymbol{\tau}_{ev}$$
$$-2\frac{\partial \Psi_v}{\partial \mathbf{b}_{ev}}\mathbf{b}_{ev} : \frac{1}{2}\mathsf{L}_v\left(\mathbf{b}_{ev}\right)\mathbf{b}_{ev}^{-1} = -\boldsymbol{\tau}_{ev} : \frac{1}{2}\mathsf{L}_v\left(\mathbf{b}_{ev}\right)\mathbf{b}_{ev}^{-1} \geq 0 \tag{10}$$

where L_v denotes a Lie derivative and $\boldsymbol{\tau}, \boldsymbol{\tau}_\infty$ and $\boldsymbol{\tau}_{ev}$ are Kirchhoff stress tensors and $\mathbf{b}$ and $\mathbf{b}_{ev}$ left Cauchy-Green deformation tensors, respectively. The form (10) is convenient for the introduction of different linearizations. The simplest evolution law that satisfies $(10)_2$ is

$$-\frac{1}{2}\mathsf{L}_v\left(\mathbf{b}_{ev}\right)\mathbf{b}_{ev}^{-1} = \mathsf{V}^{-1} : \boldsymbol{\tau}_{ev} \tag{11}$$

where V^{-1} is a positive definite rank four viscosity tensor (assumed to be isotropic). It should be noted that even if V^{-1} is a constant tensor the evolution equation (11) is still highly nonlinear. In particular, if V^{-1} is linear and isotropic we can write [4]

$$\mathsf{V}^{-1} = \frac{1}{2\eta_D}\left[\mathbf{I} - \frac{1}{3}\mathbf{1}\otimes\mathbf{1}\right] + \frac{1}{9\eta_V}\mathbf{1}\otimes\mathbf{1} \tag{12}$$

where η_D and η_V are deviatoric and volumetric viscosities that may be deformation dependent.

3. Linearizations

For polymers the parameters η_D and η_V often depends on the free volume [5] (i.e. on the hydrostatic part of the stress tensor) and the age of the material (i.e. the time for the ongoing consolidating process towards thermodynamic equilibrium). Thus, starting from a theory for *finite viscoelasticity* with a nonlinear evolution law that considers aging effects and is applicable far from the elastic equilibrium, we discuss possible linearizations.

Linearization around thermodynamic equilibrium ($\mathbf{b}_{ev} = \mathbf{I}$)

This produces *finite linear viscoelasticity* theories [6] where large strains are permitted but are restricted to small perturbations around thermodynamic equilibrium (i.e. $\mathbf{b}_{ev} \approx \mathbf{I}$, see Fig. 4).

Although models based on these theories (see e.g. [7]) can be made computationally very efficient and appear in many commercial codes, the limited applicability to e.g. problems with large initial creep/relaxation should be noticed. In general, the models based on the fully nonlinear theory give faster relaxation to elastic equilibrium at higher strains [8 ,9 ,10]. On the other hand, several models based on finite linear viscoelasticity have important engineering applications in the analysis of superposed, small-amplitude vibrations around static, large strain equilibrium states, see e.g. [11,12].

By linearizing both sides of relation (10) we show for example how it is possible to obtain the evolution law of the finite linear viscoelasticity theory of Lubliner [3]:

$$\dot{\mathbf{C}}_v = \frac{1}{2\tau}\left(\mathbf{C} - \mathbf{C}_v\right) \tag{13}$$

where τ is the common deviatoric and volumetric relaxation time that is valid near thermodynamic equilibrium.

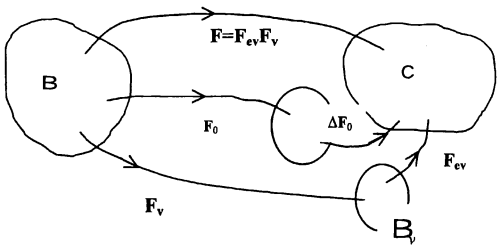

Figure 4. Linearization around $\mathbf{b}_{ev} = \mathbf{I}$

Linearization around undeformed reference configuration ($\mathbf{b} = \mathbf{I}$)
By linearizing both sides of relation (11) around the undeformed configuration we naturally recover an evolution law of type (6) that is valid for small deformations and small deviations away from thermodynamic equilibrium.

4. Illustration

We illustrate the differences between the studied viscoelastic theories by (FE-)computations on simple prototype problems that will be presented at the seminar.

5. References

[1] B.D. Coleman and M.E. Gurtin, Thermodynamics with internal state variables, J. Chemistry and Physics 47 (1967) 597-613
[2] F. Sidoroff, Une modele viscoelasticite non lineaire avec configurations intermediaire, J. de Mechanique, Vol. 13 (1974) 679-713
[3] J. Lubliner, A model of rubber elasticity, Mech. Res. Comm. Vol. 12 (1985) 93-99
[4] M.E.Gurtin, An Introduction to Continuum Mechanics, (1981) Academic Press, New York
[5] U.L Giancarlo and W.G. Knauss, Free volume theory and nonlinear thermoviscoelasticity, Polym. Eng. Sci. 32 (19992) 542-557
[6] B.D.Coleman and W.Noll, Foundations of linear viscoelasticity, Rev.Mod.Phys. 33 (1961) 239-249 Erratum ibid. 36, 1103 (1964)
[7] J.C.Simo, On a fully three-dimensional finite-strain viscoelastic damage model: formulation and computational aspects, Comput. Methods Appl. Mech. Engrg. 60 (1987) 153-173
[8] A. Lion, A physically based method to represent the thermo-mechanical behaiour of elastomers, Acta Mechanica 123 (1997) 1-25
[9] S. Govindjee and S. Reese, A presentation and comparison of two large deformation viscoelastic models, J. Eng. Materials and Technology Vol. 119 (1997) 251-255
[10] S.Reese and S. Govindjee, A theory of finite viscoelasticity and numerical aspects, Int.J.Solids Structures, Vol. 35, Nos 26-27 (1998) 3455-3482
[11] K.N.Morman and J.C.Nagtegaal, Finite element analysis of sinusoidal small-amplitude vibrations in deformed viscoelastic solids. Part 1: Theoretical development, Int.J.Num.Meth.Engng 19 (1983)1079-1103
[12] A.Lion, Thixotropic behaviour of rubber under dynamic loading histories: experiments and theory, J.mech:Phys.Solids, Vol. 46 No. 5 (1998) 895-930

An new approach to mechanism synthesis

John M. Hansen
Department of Solid Mechanics, Nils Koppels Allé, Building 404
Technical University of Denmark, DK-2800 Kgs. Lyngby, Denmark

Abstract. Many methods of performing mechanism synthesis relies on an attempt to redefine the dimensions of the system in such a way that a deviation from the desired behavior is minimized by the use of optimization methods. During the optimization process the optimizer may, however, suggest values of the dimensions, or design variables, that lead to infeasible designs, i.e. dimensions for which the mechanism cannot be assembled in one or more positions.

With the method proposed her, this problem is overcome by allowing the dimensions to vary *during* the motion of the system and subsequently minimizing the deviation of each variable dimension over a cycle. That is, for each time step the dimensions are allowed to change in order to obtain assembly *as well* as a desired kinematic behavior. This will lead to a variation of each dimension during a cycle of the mechanism, and this variation is the objective that is sought minimized. The minimization problem is solved using the optimality criterion.

1. Introduction

In recent years attempts have been made to implement general methods, based on optimization methods, [1]-[7], for performing dimensional synthesis of mechanisms. These methods are very powerful for many applications as they may be implemented generally, and it is possible to describe many different forms of synthesis goals through various objective functions. Also, it is possible to describe many forms of design restrictions as constraints, which may be added to the optimization problem, thus giving way for solution of a very broad class of mechanism design problems.

Often, these methods are based on minimizing an objective function, using a gradient based optimization method, where the design variables are updated according to the strategy used by the optimizer. In order for these methods to converge towards the desired solutions, it is however necessary to ensure that the design variables remain in a domain where the mechanism can assemble in all positions. For specific mechanisms, it is possible to include the assembly restrictions into the optimization formulation, as seen in [6]. There is, however, no general way of feeding the characteristics of the mechanism in question to the optimizer, and this will therefore sometimes suggest a new set of design variables, for which the mechanism cannot assemble in some or all configurations.

With the method proposed in this paper a way of handling the non-assembly problems is presented, in which the design variables are allowed to change during the motion of the mechanism in such a way that the mechanism can assemble at all times. It is obviously not the same mechanism that assembles at all these times, but as it is now guaranteed that it can assemble, the optimization effort can be put into minimizing the *deviation* from a mean value of the design variables.

In order to allow the design variables to change during the motion, it is necessary to reformulate the underlying analysis procedure to allow for this. For this purpose the joint coordinate method, as developed in [7] and specialized to planar kinematics in [8], has been adopted.

2. The optimization problem

With an general analysis method as e.g. the joint method, it is possible to perform a kinematic analysis for a given mechanism, and it is hence possible to e.g. determine the path of a given tracer point P on a body by determining the position vector for that point, $\mathbf{r}_n^P$, at a

number of discrete times, t_n. To design a mechanism so that the tracer point passes through a series of precision points, $\mathbf{r}_n^G$, we solve the optimization problem

$$\min_{\mathbf{b}} \sum_{n=1}^{N_S} \tfrac{1}{2}\left(\mathbf{r}_n^P - \mathbf{r}_n^G\right)^2 \tag{1}$$

where $\mathbf{b}$ is the vector of design variables, which are the dimensions that are allowed to change and N_S is the number of time steps.

While this method may be efficient and often will lead to good results, as seen in e.g. [1]-[5], it will sometimes encounter difficulties as the optimizer used may come up with dimensions that will not allow the mechanism to assemble in one or more positions. For a specific mechanism it is possible to set up constraints for the dimensions that will ensure that the mechanism will be assembled in all positions, but it is a much more difficult task to formulate this for a general mechanism. Therefore, an alternative approach is suggested here.

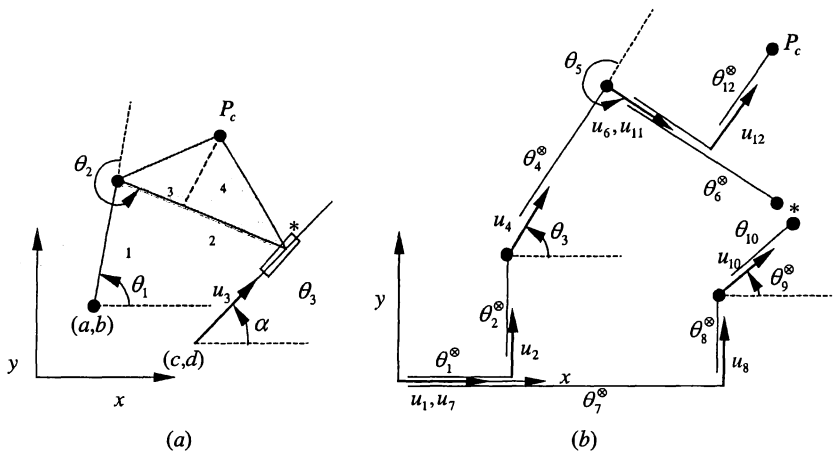

Figure 1. A slider-crank mechanism with nine design variables (a,b,c,d,ℓ_1,ℓ_2,α,ℓ_3,ℓ_4), and the corresponding mechanism where the design variables have been replaced by joints and joint variables, marked by ⊗.

The first step in this approach is to change the topology of the mechanism into a similar mechanism in which each dimension that is allowed to change is replaced by a corresponding joint. That is, if a length or a distance between two points in a body is allowed to change, the body is cut into two parts and a translational joint is inserted between the parts. Similarly, if an angle of a translational joint in a body is allowed to change, the body is cut and joined together by a revolute joint. The new joint variables describe the length and the angle, respectively. For a slider-crank mechanism, which has nine design variables, eight of which are length dimensions and one which is the angle of the translational joint, the original and the modified mechanism are as shown in Fig. 1.

For the modified system, at each time step, the mechanism is assembled in such a way that the assembly constraints $\mathbf{\Psi}(\boldsymbol{\theta}(t_n),t_n)$, see [8], are satisfied *and* the desired kinematic behavior is achieved. For example for the case described above, the set

$$\tilde{\mathbf{\Psi}}(\boldsymbol{\theta}(t_n),t_n) = \begin{Bmatrix} \mathbf{\Psi}(\boldsymbol{\theta}(t_n),t_n) \\ \mathbf{r}_n^P - \mathbf{r}_n^G \end{Bmatrix} = \mathbf{0} \tag{2}$$

must be solved, where $\boldsymbol{\theta}$ includes the newly added joint variables.

Solving this set of equations will in general involve a larger number of joint variables than the number of equations, and it will therefore yield more or less random numbers for some of

the joint variables. Also, the results will vary for each time step, thus allowing for time varying design variables.

Therefore, instead of solving Eq. (2) directly, a minimization problem is formulated, in which it is attempted to minimize the *deviation* from a mean value for all the design variables, while Eq. (2) is satisfied. That is, the problem to solve is

$$\min_{\boldsymbol{\theta}} \beta = \sum_{\theta_k \in \boldsymbol{\theta}_{DV}} \frac{1}{2}\left(\theta_k - \bar{\theta}_k\right)^2$$
$$s.t. \tag{3}$$
$$\tilde{\boldsymbol{\Psi}}(\boldsymbol{\theta}(t_n), t_n) = \mathbf{0}$$

where $\boldsymbol{\theta}_{DV}$ is the subset of $\boldsymbol{\theta}$ that corresponds to the design variables, and $\bar{\theta}_k$ is the mean value of θ_k over one cycle. Notice that this is stated for one discrete time step t_n, i.e. the optimization problem can be solved for each time step separately.

3. An example

The method has been tested on a number of different mechanisms. Below, the results are shown for a slider crank mechanism for which it has been desired that the tracer point passes through six point on a straight line. In figure 2, the initial as well as the final mechanism is shown, together with the values of the design variables in the two designs.

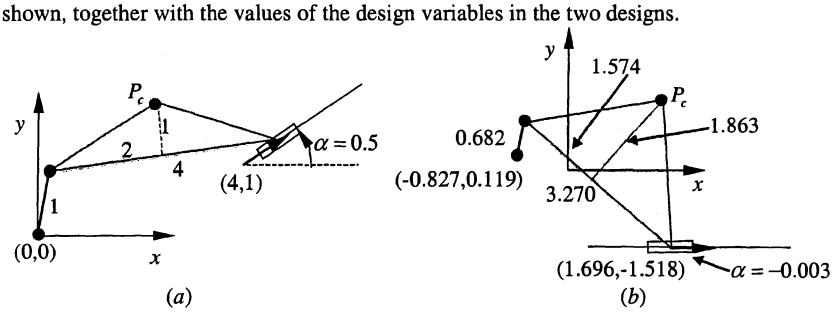

Figure 2. (*a*) The initial guess for the slider-crank mechanism, and (*b*) the resulting mechanism.

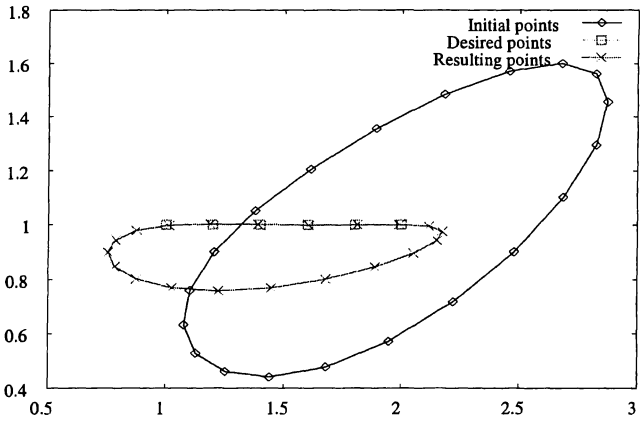

Figure 3. The desired precision points, the points generated by the initial guess, and the resulting points for the slider-crank mechanism.

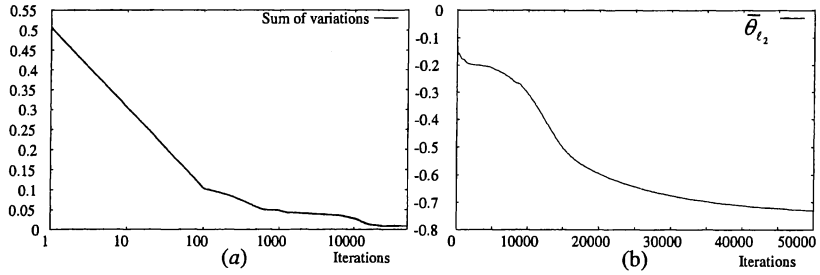

Figure 4. (*a*)The convergence of the objective function (logarithmic scale), (*b*) the convergence of the mean values of the joint variables for the joint variable corresponding to ℓ_2.

4. Discussion

In this paper a new method has been developed which can handle the non-assembly problem for synthesis of general mechanisms. By allowing the dimensions of the system that are treated as design variables to vary during the motion of the mechanism, it can be guaranteed that the system can assemble at all configurations. The synthesis problem is then solved by attempting to minimize the deviation of the design variables during a cycle.

As seen from the results, the method has a very slow convergence rate. For examples not shown here, the number of iterations has been in the order of a million, but also for these examples has the goal function shown a monotonic decrease, and the method has proved very stable for all the examples tested. This is, however, an area where future work should be concentrated.

Above, only results for which precision points were considered are presented. The method has, however, also been applied to problems where the tracer point is required to follow given curves.

References

[1] Haug, E.J., Sohoni, V.N., Design Sensitivity Analysis and Optimization of Kinematically Driven Systems. In: E.J. Haug (ed.), Computer Aided Analysis and Optimization of Mechanical System Dynamics, Vol. F9 of NATO ASI, 1984, pp. 499-554.

[2] Hansen, M.R., A General Procedure for Dimensional Synthesis of Mechanisms, *Mechanism Design and Synthesis* **46** (1992) 67-71.

[3] Bruns, T., Design of Planar, Kinematic, Rigid Body Mechanisms. Master's thesis, University of Illinois at Urbana-Champaign, Urbana, IL, USA, 1992.

[4] Hansen, J.M., Tortorelli, D.A., An Efficient Method for Synthesis of Mechanisms. In: Beste, D., Schiehlen (eds.), Optimization of Mechanical Systems, IUTAM symposium, Stuttgart, Germany, 1995, 129-138.

[5] Hansen, M.R., Hansen, J.M., An Efficient Method for Synthesis of Planar Multibody Systems including Shapes of Bodies as Design Variables, *Multibody System Dynamics* **2** (1998) 115-143.

[6] Paradis, M.J., Willmert, K.D, Optimal Mechanism Design using the Gauss Constrained Method. *Journal of Mechanisms, Transmissions, and Automation in Design* **105** (1983), 187-196

[7] Nikravesh, P.E., Gim, G., Systematic Construction of the Equations of Motion for Multibody Systems Containing Closed Kinematic Loops, *ASME Journal of Mechanical Design* **115** (1993) 143-149.

[8] Hansen, J.M., Analysis and Synthesis of Mechanisms. In: Esping B., Course on structural optimization, Östersund, Sweden (1994) chap. 8.

[9] Arora, J.S., Introduction to Optimum Design, McGraw-Hill, 1989.

Plastic zone growth in macro-microcrack interaction

S. Tarasovs, V. Tamuzs
Institute of Polymer Mechanics, Riga, Latvia
E-mail: tarasov@pmi.lv

Introduction

Several papers during the last years were devoted to the problem of plastic zone growth for collinear cracks [1]. In this work more general case was studied: plastic zone creation in isotropic, homogeneous elastic-perfectly plastic infinite plate containing crack and several microcracks near its tip. The macrocrack is subjected to a normal loading, acting at the infinity. The Dugdale model was used for plastic zones growing from the tips of macrocrack, microcracks are assumed to be elastic. The plastic zone length and crack opening displacement are found from finite element solution and compared with simple analytical solution.

Numerical analysis

Finite element method was used to solve the problem. Plastic zones are modelled by introducing non-linear interface elements along the line of supposed plastic zone growth. The interface elements have user defined traction-opening relationship (constant traction equal to the yield stress of the material in the case of perfect plasticity).

Analytical solution

Simple approximate solution of this problem is proposed in the work. It is based on the solution of the problem of micro-macrocrack interaction, which was derived by Romalis and Tamuzs [2]. Let an isotropic elastic-perfectly plastic plate contain a macrocrack and N microcracks of length $2a_k$. It will be assumed that all microcracks have the same length a. The main crack consist form an open zone $[-b, b]$ and two plastic zones created at the vicinities of the crack tips $-b$ and b such that the full length of the main crack is considered to be $2a_0$. In the case of symmetric location of microcracks the plastic zones at both ends of main crack have equal length $|a_0-b|$, which is still unknown.

The stress intensity factor for the main crack tips can be written in the form of power series with respect to the microcrack-macrocrack length ratio

$$K_I = k_0 + \lambda^2 \sum_i k_i, \quad \lambda = a / a_0 \qquad (1)$$

The first term in equation (1) is the SIF in the absence of microcracks and is equal to the classical Dugdale solution. The sum is the superposition of all microcracks influences. Assuming that plastic zones are sufficiently small, their influence on the microcracks can be neglected, and, as a first approximation, the elastic solution by Romalis and Tamuzs [2] can be used for calculation of the microcracks influences. If the K_I is determined, the length of the unknown plastic zones will be calculated from the condition $K_I = 0$, which means that the crack faces are closed smoothly,

$$\left[\frac{\sigma_\infty}{\sigma_y} - \frac{2}{\pi}\arccos b\right] + \frac{\lambda^2}{\sigma_y}\sum_{i=1}^{N} k_i = 0 \qquad (2)$$

where σ_∞ and σ_y are tensile stress applied at infinity and yield stress of material respectively.

Crack opening displacement (COD) is calculated in similar way.

Results

The geometry of the problem is presented in Figure 1. The distances between microcracks and macrocrack were changed. In Figure 2 the ratio of plastic zone length to nominal plastic zone without microcracks and similarly normalised crack opening displacement are exposed. The analytical results are compared with finite element solution.

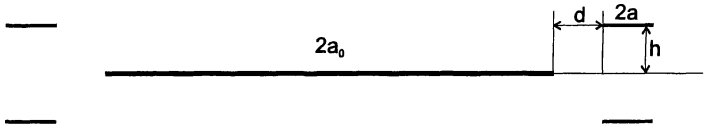

Figure 1. Geometry of the problem.

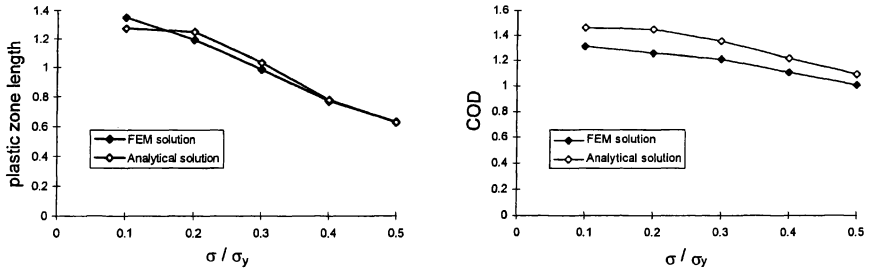

Figure 2. Normalised plastic zone length and crack opening displacement (d=a, h=2a).

Conclusion

It is seen that the pair of microcracks ahead of the crack tip increases the COD comparably with COD of a single crack whereas the plastic zone diminishes when it approaches to microcracks. So the defects ahead of the crack tip can enlarge the brittleness of material.

References

1. Theocaris P.S. Dugdale model for two collinear unequal cracks. *Engineering Fracture Mechanics*, Vol.18, 1983, pp. 545-559.
2. Romalis N., Tamuzh V. Propagation of a main crack in a body with distributed microcracks. *Mechanics of Composite Materials*, 20(1), 1984, pp. 35-43.

Efficient numerical simulation of nonlinear response of thin shells

B.Skallerud', L.I.Myklebust', and B.Haugen"
'Div.Applied Mechanics, The Norwegian University of Science and Technology, N-7491, Trondheim, Norway, "FEDEM Technology a.s., N-7030 Trondheim, Norway

INTRODUCTION

Many structural applications require nonlinear finite element analyses in order to assess response and capacity. Plastic deformations may be accounted for by means of thickness integration or stress resultants. The stress resultant model employed herein is based on Ilyushins' linear yield criterion for thin shells. The corners present with this criterion are circumvented by means of a simplification, hence, there is no need for multi-surface stress resultant updates[1-3]. A backward Euler difference is employed in the stress resultant update, and a consistent tangent is used in the Newton-Raphson iterations on the global equilibrium. Limit points are traversed by means of an orthogonal trajectory method. In collapse response of slender structures, the straining of the material may be moderate, but the motion may be governed by large rigid body translations and rotations. A way of accounting for this by means of the co-rotated approach is presented[4,5]. Triangular high-performance facet shell elements are employed[6].

THEORY

The global coordinate system is represented by unit vectors $\mathbf{I_1}$, $\mathbf{I_2}$ and $\mathbf{I_3}$. The co-rotated element coordinate system shared by shadow configuration C_{0n} and configuration C_n is represented by unit vectors $\mathbf{i_1^n}$, $\mathbf{i_2^n}$ and $\mathbf{i_3^n}$. Vectors given in the local co-rotated element coordinate system are marked with a tilde($\tilde{}$). A vector $\mathbf{x}$ in global coordinates is transformed into a vector $\tilde{\mathbf{x}}$ in the local coordinate system *0* by

$$\tilde{\mathbf{x}} = \mathbf{T_0 x} \qquad \mathbf{T_0^T} = (\mathbf{i_1^0}, \mathbf{i_2^0}, \mathbf{i_3^0}) \tag{1}$$

$\mathbf{T_0}$ is orthonormal. The rigid body rotation of $\mathbf{i_i^0}$ to $\mathbf{i_i^n}$ is given by

$$\mathbf{i_1^n} = \mathbf{R_{0n} i_1^0} \qquad \mathbf{R_{0n}} = \mathbf{T_n^T T_0} \tag{2}$$

where $\mathbf{R_{0n}}$ is the rigid body rotation matrix from position *0* to position *n*. The Rodrigues representation of the rotation matrix is used. Rotation of a vector $\mathbf{r_0}$ into $\mathbf{r}$ through an angle θ about an axis defined by the unit vector $\mathbf{n}$ is obtained by $\mathbf{r} = \mathbf{R r_0}$. The displacement vector is split into a deformational displacement vector and a rigid body displacement vector.

$$\mathbf{u} = \mathbf{u_r} + \mathbf{u_d} \qquad \mathbf{u_r} = \mathbf{r^{0n}} - \mathbf{r^0} \qquad \mathbf{u_d} = \mathbf{r^n} - \mathbf{r^{0n}} \tag{3}$$

The rotation of an element node as it moves from the initial configuration C_0 to the deformed configuration C_n is described by the rotation matrix $\mathbf{R}$. The rotation matrix is split into a rigid body rotation tensor $\mathbf{R_{0n}}$ and a deformational rotation matrix $\mathbf{R_d}$.

$$\mathbf{R} = \mathbf{R_d R_{0n}} \qquad \mathbf{R_d} = \mathbf{R R_{0n}^T} = \mathbf{R T_0^T T_n} \tag{4}$$

Balance in virtual work reads

$$\delta_R \tilde{\mathbf{v}}_d^T \tilde{\mathbf{f}}_e - \delta \mathbf{v}^T \mathbf{f}_{ext} = \delta \mathbf{v^T} ((\frac{\partial_R \mathbf{v_d}}{\partial \mathbf{v}})^\mathbf{T} \mathbf{f_e} - \mathbf{f_{ext}} = \mathbf{0} \Rightarrow \mathbf{f_e} = \mathbf{T^T \tilde{P}^T \tilde{H}^T \tilde{f}_e} = \mathbf{f_{ext}} \tag{5}$$

The transformations are matrices that provide the large rotation effects, see [2] for details. The consistent tangent stiffness is obtained by the variation of the internal force vector $\mathbf{f}_e$ with respect to the visible degrees of freedom, $\mathbf{v}$:

$$\begin{aligned} \delta\mathbf{f} &= \delta\mathbf{T}^{\mathbf{T}}\tilde{\mathbf{P}}^{\mathbf{T}}\tilde{\mathbf{H}}^{\mathbf{T}}\tilde{\mathbf{f}}_{\mathbf{e}} + \mathbf{T}^{\mathbf{T}}\delta_{\mathbf{R}}\tilde{\mathbf{P}}^{\mathbf{T}}\tilde{\mathbf{H}}^{\mathbf{T}}\tilde{\mathbf{f}}_{\mathbf{e}} + \mathbf{T}^{\mathbf{T}}\tilde{\mathbf{P}}^{\mathbf{T}}\delta_{\mathbf{R}}\tilde{\mathbf{H}}^{\mathbf{T}}\tilde{\mathbf{f}}_{\mathbf{e}} + \mathbf{T}^{\mathbf{T}}\tilde{\mathbf{P}}^{\mathbf{T}}\tilde{\mathbf{H}}^{\mathbf{T}}\delta\tilde{\mathbf{f}}_{\mathbf{e}} \\ &= (\mathbf{K_{GR}} + \mathbf{K_{GP}} + \mathbf{K_{GM}} + \mathbf{K_{MG}})\,\delta\mathbf{v} = \mathbf{K_T}\delta\mathbf{v} \end{aligned} \tag{6}$$

$\mathbf{K_{MG}} = \mathbf{T}^{\mathbf{T}}\tilde{\mathbf{P}}^{\mathbf{T}}\tilde{\mathbf{H}}^{\mathbf{T}}\tilde{\mathbf{K}}_{\mathbf{e}}\tilde{\mathbf{H}}\tilde{\mathbf{P}}\mathbf{T}.\tilde{\mathbf{K}}_{\mathbf{e}}$ represents the material stiffness for the element, and may include plasticity effects. It connects the local deformational dof increment with the local force increment: $\delta\tilde{\mathbf{f}}_e = \tilde{\mathbf{K}}_e\delta_R\tilde{\mathbf{v}}_d$.

Denoting the integration point stress resultant vector by $\boldsymbol{\sigma} = [\tilde{n}, \tilde{m}]^T$, the linear version of Ilyushin's stress resultant yield condition may be written in quadratic form[7,8]:$f = \boldsymbol{\sigma}^T\boldsymbol{A}\boldsymbol{\sigma} - (1 + \frac{H\epsilon_p}{\sigma_y})^2 = 0$. The off-diagonal submatrices in $\boldsymbol{A}$ lead to corners in the yield surface. Assuming $s = 0$, a hyperellipse is obtained as yield surface. In the elastic predictor plastic corrector approach applied herein, the stress update is obtained by

$$\boldsymbol{\sigma}_{n+1} = \boldsymbol{\sigma}_{trial} - \boldsymbol{C}\Delta\epsilon_{p,n+1} = \bar{\boldsymbol{Q}}^{-1}\boldsymbol{\sigma}_{trial} \qquad \bar{\boldsymbol{Q}} = [\boldsymbol{I} + 2\Delta\lambda\boldsymbol{C}\boldsymbol{A}] \tag{7}$$

The consistent material tangent for an integration point in the plane reads:

$$d\boldsymbol{\sigma} = [\boldsymbol{H} - \frac{\boldsymbol{H}\boldsymbol{g}\boldsymbol{g}^T\boldsymbol{H}}{\boldsymbol{g}^T\boldsymbol{H}\boldsymbol{g} + \beta}]d\boldsymbol{\epsilon} = \boldsymbol{C}_t d\boldsymbol{\epsilon} \qquad \boldsymbol{H}^{-1} = \boldsymbol{C}^{-1} + 2\Delta\lambda\boldsymbol{A} \qquad \boldsymbol{g} = 2\boldsymbol{A}\boldsymbol{\sigma} \tag{8}$$

The update of the global displacement and rotation is obtained as follows; displacements:$\mathbf{v} := \mathbf{v} + \Delta\mathbf{v}$, rotations: $\mathbf{R} := \mathbf{R}(\Delta\omega)\mathbf{R}$.

NUMERICAL SIMULATIONS

In the following, some cases are analysed in order to check the performance of the simplified plasticity model. Other numerical studies with the present formulation may be found in Refs.[1,2].

Torsion of a rectangular plate with a hole

The present case was first presented in [9]. A rectangular plate is fully constrained with respect to in-plane displacement at two opposite edges (the two other edges are free). Then one end of the plate is subjected to a large torsional rotation. Fig.1a shows the deformed mesh for a rotation of 180 degrees. Fig.1b shows the corresponding applied end rotation and corresponding torsion moment. The agreement between the present simulation and the one by Basar and Itskov is very good.

Shear buckling of plate girders

The following simulations are compared to the test results determined in [10]. Steel plate girders with/without longitudinal stiffeners were tested in three-point bending. Fig.1c shows geometry of deformed unstiffened specimen. The length to thickness ratio for the unstiffened web panel is about 385. Fig.1d illustrates the total load versus midpoint deflection of the girder for the test and the two simulations. Some deviation in elastic initial stiffness is observed. This is very typical when comparing numerical simulations with tests; the boundary conditions in the test are usually difficult to achieve exactly in the numerical models. The ABAQUS simulation diverged prematurely. The stress resultant approach simulation corresponds quite well to the test result, both with respect to limit load and post-collapse behaviour.

Considering the stiffened girder, Figs.1e and f depict the test result and simulations. Interestingly, the present formulation captures the correct (unsymmetric) collapse shape, whereas ABAQUS reaches a symmetric collapse mode. This is the reason for the deviation between ABAQUS simulation and test (Fig.1f). The present formulation yields good correspondence with the test. It should be noted that exactly the same finite element mesh was employed in the two simulations.

CONCLUDING REMARKS

The present investigation gives further insight into the performance of simplified plasticity modelling by means of stress resultants combined with high-performance thin shell finite elements. For materials with a relatively sharp transition from elastic to plastic behaviour and linear hardening, the simplified model works well. If the simplified plasticity model is employed for compression loaded components and structures of critical importance, the simulations should be supplemented with simulations accounting for gradual plastification over thickness. Furthermore, if there are significant uncertainties related to the loads/ boundary conditions/ material properties/ structural geometry, the simplified material model has a model bias that may be acceptable in the overall perspective.

REFERENCES

1. B.Skallerud and B.Haugen. Simplified stress resultant plasticity modelling in collapse analysis of thin shells. In 1. European Conference on Computational Mechanics ECCM'99, Munchen, 1999.
2. B.Skallerud and B.Haugen. Collapse of thin shell structures - Stress resultant plasticity modelling within a co-rotated ANDES finite element formulation. *Int.J.Numerical Meth. Engng*, **36**, 1999, 1961-1986.
3. J. C. Simo and J.G. Kennedy. On a stress resultant geometrically exact shell model. Part V Nonlinear plasticity: formulation and integration algorithm. *Comp. Meth. Applied Mech. Engng*; 1992, **96**: 133-171.
4. P. G. Bergan and M. K. Nygård. Nonlinear shell analysis using Free Formulation finite elements. In *Finite Element Methods for Nonlinear Problems*, Springer Verlag, Berlin, 1989, 317-338.
5. B.Haugen. *Buckling and stability problems for thin shell structures using high performance finite elements.* Ph.D.thesis, Univ. Colorado, Dept. Aerospace Engng, 1994.
6. C. A. Felippa and C. Militello. Membrane triangles with corner drilling freedoms: II. The ANDES element. *Finite Elements in Analysis & Design*; 1992, **12**: 189-201.
7. A. Ibrahimbegivic and F. Frey. Stress resultant elasto-plastic analysis of plates and shallow shells. COMPLAS-3, Barcelona, 1992, 2047-2059.
8. H. Matthies. A decomposition method for integration of elastic-plastic rate problem. *Int. J. Numerical Meth. Engng*; 1989, **28**: 1-11.
9. Y.Basar and M.Itskov. Constitutive model and finite element formulation for large strain elasto-plastic analysis of shells. *Comput.Mech.*,**23**, 1999, 466-481.
10. K.H.Tang and H.R.Evans. Transverse stiffeners for plate girder webs - and experimental study. *J. Construct. Steel Research*, 1984.

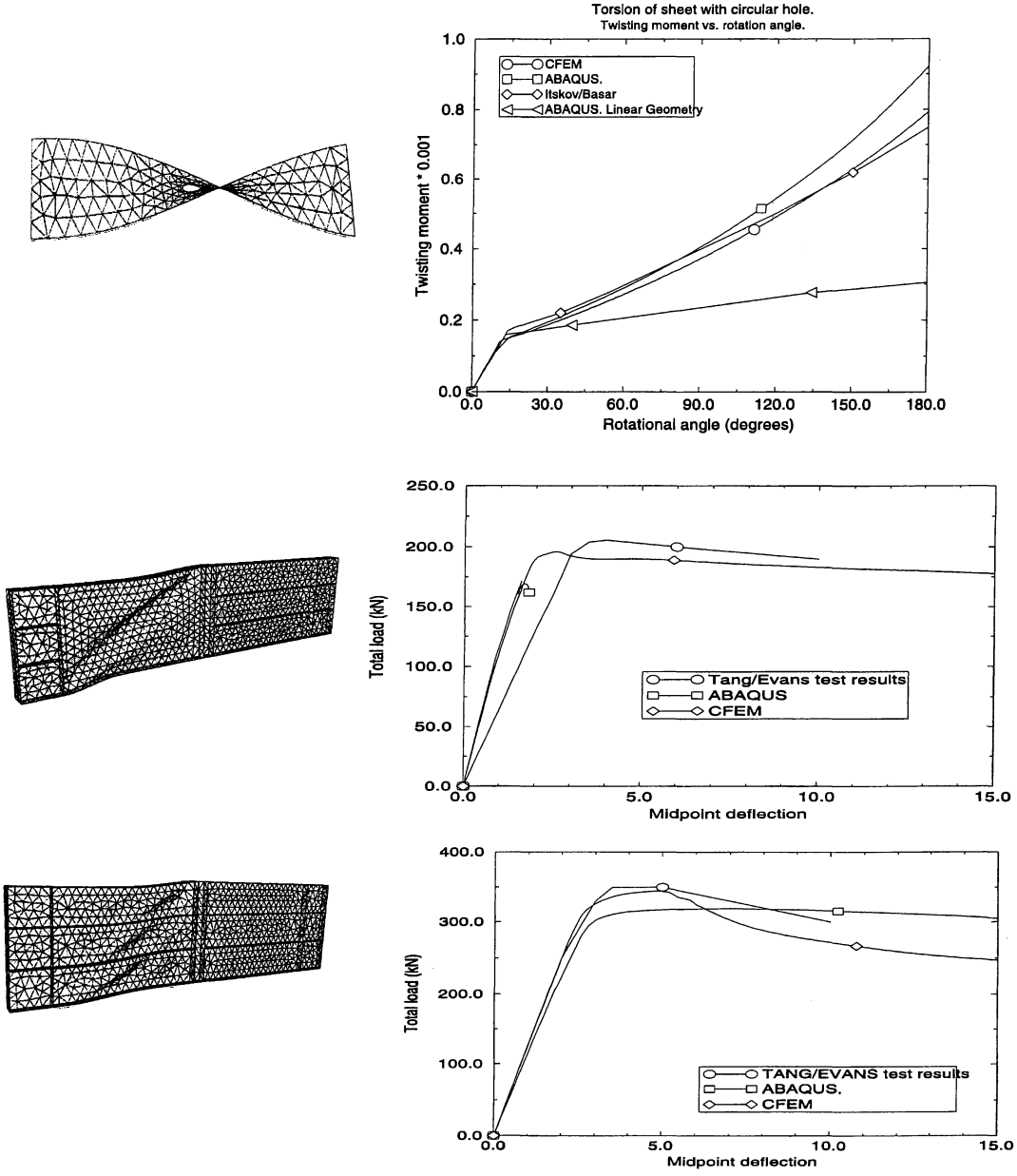

Figure 1: a) Deformed mesh at 180 degrees end rotation, b) Torsion response, c) deformed mesh unstiffened web, d) load versus midpoint deflection, e) deformed mesh stiffened web, f) load versus midpoint deflection.

Strength Analysis of Buckled Thin-Walled Composite Structure

Janis Brauns
Professor of Civil Engineering, Dr. Habil. Sc. Eng.

Department of Structural Engineering, LUA
19 Academia St., Jelgava, LV-3001, LATVIA
E-mail: braun@acad.latnet.lv

An investigation of the forms of shell buckling has been the subject of many experimental and theoretical studies [1-4]. On the basis of analysing of the forms of equilibrium it is possible to determine the stability of a shell on the whole, especially if a statistical analysis is used [5]. The purpose of this study is to analyse the stress state of orthotropic glass-fiber reinforced cylindrical shell in the case of short-time loading by means of displacement function. The radial displacement field of shells during loading was investigated and characterised by the sum of the harmonics of a Fourier series.

The analysis is intended to be used in the development of the inner structure of the shell material. For strength related properties, a phenomenological failure criterion can supply the feedback in material permutations and provide guidance in the fabrication process of composite structures. Failure is interpreted here as the occurrence of discontinuity in the material.

The length of the shell is L, the radius – R, and the thickness – h; axes x_1, x_2, x_3 are directed along the generatrix, the circumference, and the normal to the center of curvature. Using the Kirchhoff-Love hypothesis, the total strains and stresses are determined as the sum of the strains and stresses in the middle surface and of the flexural strains and stresses:

$$\varepsilon_{\alpha\beta}(x_1,x_2,x_3)=\varepsilon^0_{\alpha\beta}(x_1,x_2)+x_3[\kappa_{\alpha\beta}(x_1,x_2)-\kappa_{0\alpha\beta}(x_1,x_2)]; \tag{1}$$

$$\sigma_{\alpha\beta}(x_1,x_2,x_3)=\sigma^0_{\alpha\beta}(x_1,x_2)+x_3A_{\alpha\beta\gamma\delta}[\kappa_{\gamma\delta}(x_1,x_2)-\kappa_{0\gamma\delta}(x_1,x_2)]\ . \tag{2}$$

Here $\varepsilon^0_{\alpha\beta}$, $\sigma^0_{\alpha\beta}$ are membrane strain and stress; $\kappa_{0\,\alpha\beta}$, $\kappa_{\alpha\beta}$ are the distortion tensor of initial geometrical imperfection and deformation of the shell; $A_{\alpha\beta\gamma\delta}$ is the stiffness tensor of the material. The Airy stress function $\Phi(x_1, x_2)$ is related uniquely with the displacement function $w(x_1, x_2)$ by the equation of strain compatibility and is determined on the basis of strain compatibility equation for cylindrical shell by using compliance components S_{ijkl}:

$$S_{1111}\frac{\partial^4\Phi(x_1,x_2)}{\partial y^4}+S_{2222}\frac{\partial^4\Phi(x_1,x_2)}{\partial x^4}+(2S_{1122}+4S_{1212})\frac{\partial^4\Phi(x_1,x_2)}{\partial x^2\partial y^2}=$$
$$=-\frac{1}{R}\frac{\partial^2 w(x_1,x_2)}{\partial x^2}. \tag{3}$$

The solution of (3) is given by expressing the function of radial deflection $w(x_1, x_2)$ and the stress function $\Phi(x_1, x_2)$ by complex double Fourier series taking into account load q:

$$w(x_1,x_2)=\sum_{m=-M}^{M}\sum_{n=-N}^{N}[\alpha_{mn}-\alpha_{0mn}]\Psi_{mn}(x_1,x_2); \tag{4}$$

$$\Phi(x_1,x_2)=\sum_{m=-M}^{M}\sum_{n=-N}^{N}\varphi_{mn}\Psi_{mn}(x_1,x_2)-\frac{qRx_1^2}{2h}-\frac{qRx_2^2}{4h}, \tag{5}$$

where $\Psi_{mn}(x_1,x_2) = e^{i(\frac{m\pi x_1}{L}+\frac{nx_2}{R})}$ (i – imaginary unit).

Here m and n are the numbers of half-waves along the generatrix and the number of waves along the circumference, respectively. According to the experimental data obtained the maximum number of harmonics of the series along the generatrix M = 4 and along the circumference N = 6. Here and bellow α_{mn} and $\alpha_{0\,mn}$ are the coefficients of displacement and imperfection function.

The membrane stresses in the middle surface were determined as

$$\sigma_{11}^0(x_1,x_2) = \frac{\partial\Phi(x_1,x_2)}{\partial x_2^2};\ \sigma_{22}^0(x_1,x_2) = \frac{\partial\Phi(x_1,x_2)}{\partial x_1^2};\ \sigma_{12}^0(x_1,x_2) = -\frac{\partial\Phi(x_1,x_2)}{\partial x_1\partial x_2}. \quad (6)$$

By using stiffness tensor A_{ijkl} the flexural stresses for $x_3 = \pm h/2$ were expressed in the form

$$\sigma_{11}^f(x_1,x_2) = \pm A_{1111}\frac{\pi^2 h}{2L^2}\sum_{m=-M}^{M}\sum_{n=-N}^{N}(\alpha_{mn}-\alpha_{0mn})m^2\Psi_{mn}(x_1,x_2)\pm$$
$$\pm A_{1122}\frac{h}{2R^2}\sum_{m=-M}^{M}\sum_{n=-N}^{N}(\alpha_{mn}-\alpha_{0mn})n^2\Psi_{mn}(x_1,x_2); \quad (7)$$

$$\sigma_{22}^f(x_1,x_2) = \pm A_{2222}\frac{h}{2R^2}\sum_{m=-M}^{M}\sum_{n=-N}^{N}(\alpha_{mn}-\alpha_{0mn})n^2\Psi_{mn}(x_1,x_2)\pm$$
$$\pm A_{1122}\frac{\pi^2 h}{2L^2}\sum_{m=-M}^{M}\sum_{n=-N}^{N}(\alpha_{mn}-\alpha_{0mn})m^2\Psi_{mn}(x_1,x_2); \quad (8)$$

$$\sigma_{12}^f(x_1,x_2) = \pm A_{1212}\frac{\pi h}{LR}\sum_{m=-M}^{M}\sum_{n=-N}^{N}(\alpha_{mn}-\alpha_{0mn})mn\Psi_{mn}(x_1,x_2). \quad (9)$$

Fig. 1 shows a scan of a part of the shell surface with lines of the level of stresses σ_{22} and σ_{12}. The dashed lines indicate the sites of the fracture. At the sites of maximum compressive stress σ_{22} the shear stress is minimum, and vice versa but where the curvature $\kappa_{\alpha\beta}$ of the deformed surface changes sign, the level of the shear stress is high.

In order to take into account delamination process in buckling process of a shell, the interlayer shear stresses σ_{13} and σ_{23} were determined as

$$\sigma_{13}(x_1,x_2,x_3) = \frac{h^2-4x_3^2}{8}A_{1111}\frac{\pi^3}{L^3}\sum_{m=-M}^{M}\sum_{n=-N}^{N}(\alpha_{mn}-\alpha_{0mn})m^3 i\Psi_{mn}(x_1,x_2)+$$
$$+\frac{h^2-4x_3^2}{8}(A_{1111}\nu_{21}+2A_{1212})\frac{\pi}{LR^2}\sum_{m=-M}^{M}\sum_{n=-N}^{N}(\alpha_{mn}-\alpha_{0mn})mn^2 i\Psi_{mn}(x_1,x_2); \quad (10)$$

$$\sigma_{23}(x_1,x_2,x_3) = \frac{h^2-4x_3^2}{8}A_{2222}\frac{1}{R^3}\sum_{m=-M}^{M}\sum_{n=-N}^{N}(\alpha_{mn}-\alpha_{0mn})n^3 i\Psi_{mn}(x_1,x_2)+$$
$$+\frac{h^2-4x_3^2}{8}(A_{1111}\nu_{21}+2A_{1212})\frac{\pi^2}{L^2R}\sum_{m=-M}^{M}\sum_{n=-N}^{N}(\alpha_{mn}-\alpha_{0mn})m^2 ni\Psi_{mn}(x_1,x_2). \quad (11)$$

For characterising of the stress level in a shell depending on the co-ordinates the in-plane (membrane) stresses, couple stresses as well as transverse shear stresses were taken into

account. The description of the surface of strength by a quadratic polynomial usually is proposed. In a general form the equation is given in [6-8].

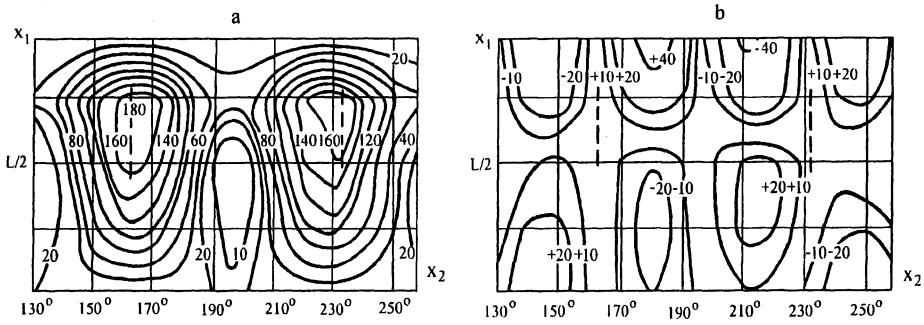

Fig. 1. Lines of constant level of stresses: a) $\sigma_{22}(x_1, x_2) = \text{const}$; b) $\sigma_{12}(x_1, x_2) = \text{const}$.

In the case of glass fabric reinforced plastic we consider the strength of the shell in the plane stress state. With retention of terms of the first and second order the strength criterion depicts the surface (ellipsoid) in three-dimensional space of stresses and takes the form

$$F_{11}\sigma_{11} + F_{22}\sigma_{22} + 2F_{12}\sigma_{12} + F_{1111}\sigma_{11}^2 + F_{2222}\sigma_{22}^2 + 4F_{1212}\sigma_{12}^2 + \\ + 2F_{1122}\sigma_{11}\sigma_{22} + 4F_{1112}\sigma_{11}\sigma_{12} + 4F_{2212}\sigma_{22}\sigma_{12} = 1. \tag{12}$$

The coefficients of (12) are components of tensors F_{ij} and F_{ijkl}. They are determined by the use of the strength tensor $R_{\alpha\beta\gamma}$, where $\alpha = 0, 11, \overline{11}$; $\beta = 0, 22, \overline{22}$; $\gamma = 0, 12, \overline{12}$. The index 0 denotes that the given stress component is absent; the bar over the index shows the presence of a compressive component. Using the strength values obtained experimentally, the coefficients are represented in the following form:

$$F_{11} = \frac{R_{\overline{1}100} - R_{1100}}{R_{1100}R_{\overline{1}100}}; \quad F_{22} = \frac{R_{0\overline{2}20} - R_{0220}}{R_{0220}R_{0\overline{2}20}}; \quad F_{1111} = \frac{1}{R_{1100}R_{\overline{1}100}}; \quad F_{2222} = \frac{1}{R_{0220}R_{0\overline{2}20}}; \\ 2F_{1122} = \frac{F_{11} - F_{22}}{R_{11\overline{2}\overline{2}0}} + F_{1111} + F_{2222} - \frac{1}{R^2_{11\overline{2}\overline{2}0}}; \quad 4F_{1212} = \frac{1}{R_{0012}R_{00\overline{1}\overline{2}}}. \tag{13}$$

The axes 1 and 2 of the ellipsoid are in the plane $\sigma_{11} \sim \sigma_{22}$ and axis 3 is parallel to axis σ_{12}. The components of the tensor of the strength surface F_{11} and F_{22} express the displacement of the center of ellipsoid in the direction of axes 1 and 2, respectively. The angle of rotation of the ellipsoid relative to axis 1 is a function of the component F_{1122}.

Substituting into (12) the coefficients of (13) a quadratic equation was obtained. Solving the equation, the theoretical values of the ultimate strength (surface of failure) were determined. The analysis was performed with consideration of the following experimental strength (MPa): $R_{1100} = 180$; $R_{\overline{1}100} = 170$; $R_{0220} = 300$; $R_{0\overline{2}20} = 230$; $R_{0012} = R_{00\overline{1}2} = 95$ and characteristics of rigidity of the material (MPa): $E_1 = 1.2 \times 10^4$, $E_2 = 1.9 \times 10^4$, $G_{12} = 0.25 \times 10^4$. Fig. 2 shows the lines of the constant stress level over the shell according to the criterion (12).

It is fixed that after buckling of glass fiber/epoxy shell made by winding method, the delamination of material took place. The influence of transverse shear stresses on the stress level is shown in Fig. 3.

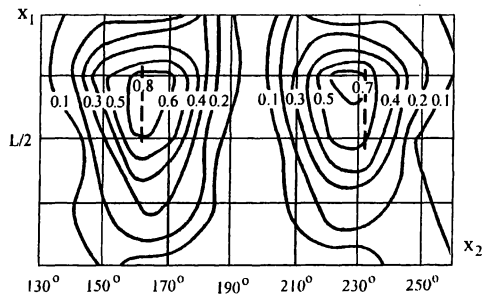

Fig. 2. Lines of constant level of stresses $f(\sigma_{ij}, \sigma_{kl})$ for glass fabric plastic shell.

The boundary surface, determined by the criterion (12), depends considerably on the loading rate. The strength characteristics of material are established on loading at a certain constant rate. The loading of shell was stepwise, since at each step of loading the form of buckling was measured for 3 min. Consequently, an additional study of fracture toughness of the shell with consideration of time factors is necessary.

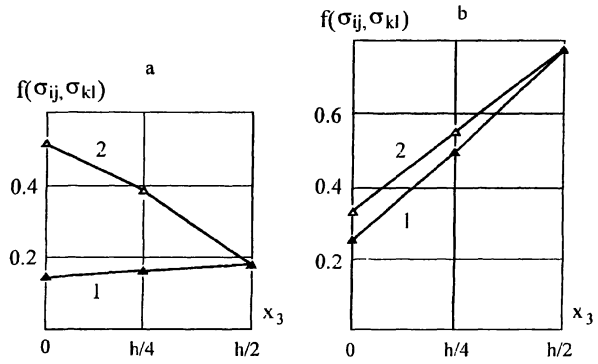

Fig. 3. Distribution of stress level $f(\sigma_{ij}, \sigma_{kl})$ for glass fiber/epoxy shell at the sites of maximum stress σ_{23} (a) and σ_{22} (b): without (1) and with (2) the effect of stress σ_{23}.

The method developed permits determination of stresses in a shell by means of an experimental deflection function. It is established that the fracture of glass fabric plastic shells occurs at maximum couple-stresses. For glass fiber/epoxy shells made by winding method the delamination took place under action of transverse shear stress. Failure criterion permits predicting the sites of fracture and maintenance of a shell upon loss of stability.

References

1. B.O. Almroth, A.M. Holmes and D.O. Brush, Exptl. Mech., No. 9 (1964) 69.
2. J.A. Brauns and R.B. Rikards, Polym. Mech., No. 4 (1972) 575.
3. P. Montague, Mech. Eng. Sci., 11 (1969) 103.
4. H. Showkati and P. Ansourian, J. Constr. Steel Res., No. 1 (1996) 53.
5. B.P. Makarov, Mech. Solids (in Russian), No. 1 (1970) 97.
6. I.I. Goldenblat and V.A.Kopnov, Polym. Mech., No. 2 (1965) 54.
7. A.K. Malmeister, Polym. Mech., No. 4 (1966) 324.
8. S.W. Tsai and E.M. Wu, J. Compos. Mater., 5 (1971) 58.

Dynamic plastic response of circular cylindrical shells to dynamic loads

Jaan Lellep and **Kadre Torn**
Institute of Applied Mathematics
Tartu University
Tartu 51014, Estonia

Abstract.

The dynamic response of a short cylindrical shell made of a rigid, perfectly plastic material is studied. The shell is subjected to initial impulsive loading. The transverse shear force is retained in the yield surface which is presented in the form of a cube in the space of generalized stresses.

1. Introduction

The dynamic plastic response of beams, plates and shells to large dynamic loads has studied by N. Jones [1], W. Stronge and T.X. Yu [7] and many others. The analysis based on the rigid-plastic idealization of a ductile material gives surprisingly accurate yet simple predictions for which a wide range of practical problems.

It was established by P.S. Symonds [8], T. Nonaka [6], N. Jones and J.G. Oliveira [2,3], N. Jones and B. Song [4], Q.M. Li and N. Jones [5] that shear forces can exercise an important influence on dynamic plastic behaviour of various structural members. In the case of circular cylindrical shells a cubic yield surface which retains the transverse shear force as well as the circumferential membrane force and the axial bending moment is used to control the plastic behaviour of shells.

2. Basic equations

Consider a circular cylindrical shell clamped at the left end and simply supported at the right hand end. Assume that the tube is subjected to the initial impulsive loading so that each point of the shell has the initial transverse velocity v_0.

The equations of motion of a shell element can be presented as

$$\begin{aligned} \frac{\partial M}{\partial x} &+ Q = 0, \\ \frac{\partial Q}{\partial x} &- \frac{N}{R} - \mu \frac{\partial^2 W}{\partial t^2} = 0 \end{aligned} \tag{1}$$

where Q stands for the shear force, M and N being the longitudinal moment and circumferential membrane force, respectively. In (1) μ stands for the mass per unit length of the shell and R is the radius of the middle surface of the shell.

Introducing the non-dimensional quantities

$$
\begin{aligned}
m &= \frac{M}{M_0}, \quad q = \frac{Q}{Q_0}, \quad n = \frac{N}{N_0}, \xi = \frac{x}{l}, \\
\nu &= \frac{Q_0 l}{M_0}, \quad \omega = \frac{N_0 l^2}{M_0 R}, \\
w &= \frac{M_0 W}{\mu v_0^2 l^2}, \quad \tau = \frac{M_0 t}{\mu v_0 l^2}
\end{aligned} \tag{2}
$$

one can present equations (1) as

$$
\begin{aligned}
m' &= -\nu q \\
\nu q' &= \ddot{w} + \omega n.
\end{aligned} \tag{3}
$$

Here primes denote the differentiation with respect to ξ and dots with respect to τ, respectively. In (2) M_0, N_0 and Q_0 stand for yield moment and yield forces, respectively.

Assume that the yield surface is presented by the cube with faces $m = \pm 1$, $n = \pm 1$, $q = \pm 1$. According to the associated flow law the strain rate vector $\dot{e} = (\dot{\kappa}, \dot{\varepsilon}, \dot{\gamma})$ is to be a subgradient for the this surface. As $\dot{\varepsilon} = \dot{w}$ and presumably $\dot{w} \geq 0$ the stress strain state of the shell corresponds to the face $n = 1$ of the yield surface. It can be shown that the transverse velocity is to be a piece wise linear function of the coordinate if the stress state corresponds to the faces $n = \pm 1$ of the yield surface.

3. Theoretical predictions of the dynamic response of a cylindrical shell

In the case of piece wise linear velocity fields the set (3) can be integrated twice with respect to the coordinate ξ using appropriate boundary conditions.

This leads to a system of ordinary differential equations which is integrated analytically or numerically.

The analysis shows that there exist five different cases of motion. For these cases the initial velocity patterns are presented in Fig.1-3.

In each case the motion takes place during different stages corresponding to different transverse velocity patterns. It is assumed that the case number i takes place for $\nu \in (\nu_i, \nu_{i+1})$ whereas ν_6 tends to infinity. Evidently, ν_i depends on the parameter ω. For instance, in the cse $\omega = 2$ we have $\nu_1 = 2.0$, $\nu_2 = 5.6166$, $\nu_3 = 6.4515$, $\nu_4 = 9,5626$, $\nu_5 = 15.154$. Maximal residual displacements are presented in Fig.4 for several values of the parameter ν.

Calculations carried out revealed interesting matters of dynamic behaviour of the shell. In the range of smaller values of the parameter ν residual deflections increase if parameter ν decreases. In this case the shear sliding of the material exercises more important role than the bending behaviour does. However, for greater values of ν the bending behaviour dominates over shear deformations.

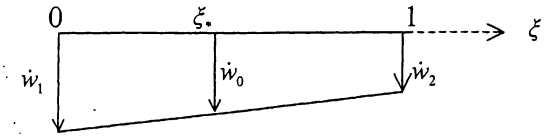

Fig. 1. Initial velocity field for the case I

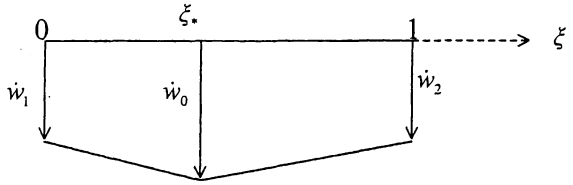

Fig. 2. Initial velocities for the cases II and III

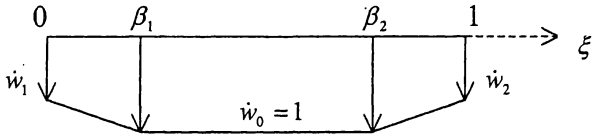

Fig. 3. Initial velocities for the cases IV and V

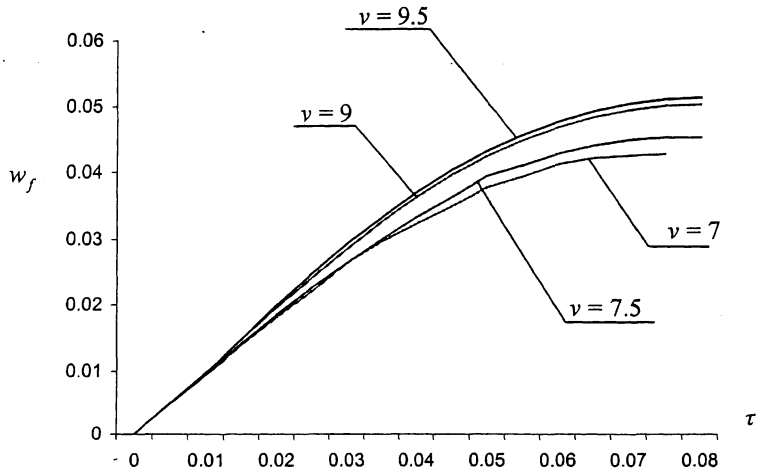

Fig. 4 Residual deflections

4. Conclusions

A theoretical study is presented herein which examines the influence of the transverse shear force on the dynamic plastic response of circular cylindrical shells with non-symmetric end conditions. It is shown that the dynamic response is governed by four different patterns of initial motion (five cases) which are defined by the parameters ν and ω. Generally, transverse shear effects predominate over bending response as ν decreases. However, at the initial stage of motion shear sliding takes place at the supports for wide range of values of the parameter ν. On the other hand the initial stage of motion is very short.

Acknowledgement. The support of Estonian Science Foundation through the Grant N^0 3380 is highly appreciated.

References

1. N. Jones, Structural Impact, CUP, Cambridge, 1989.

2. N. Jones and J.G. de Oliveira, Dynamic plastic response of circular plates with transverse shear and rotatory inertia. J. Appl. Mech. Trans. ASME, 1980, 47, N^0 1, 27-34.

3. N. Jones and J.G. de Oliveira, The influence of rotatory inertia and transverse shear on the dynamic plastic behaviour of beams. J. Appl. Mech. Trans. ASME, 1979, 46, N^0 2, 303-310.

4. N. Jones and B. Song, Shear and bending response of a rigid-plastic beam to partly distributed blast-type loading. J. Struct. Mech., 1986, 14, N^0 3, 275-320.

5. Q.M. Li and N. Jones, Blast loading of a "short" cylindrical shell with transverse shear effects. Int. J. Impact Eng., 1995, 16, N^0 2, 331-353.

6. T. Nonaka, Shear and bending response of a rigid-plastic beam to blast-type loading. Ing.-Arch., 1977, 46, 35-52.

7. W.J. Stronge and T.X. Yu, Dynamic Models for Structural Plasticity. Springer, 1993.

8. P.S. Symonds, Plastic shear deformations in dynamic load problems. In: Engineering Plasticity (eds J. Heyman and F.A. Leckie). Cambridge, 1968, 647-664.

13th Nordic Seminar on Computational Mechanics
October 20-21,2000 OSLO

Matti Lojander
Helsinki University of Technology
Department of Civil and Environmental Engineering
P.O. BOX 2100, FIN-02015 HUT, Finland
matti.lojander@hut.fi

PARAMETERS ON GEOTECHNICAL CALCULATIONS

Introduction

The real soil behaviour differs very much from the assumptions of simple elastic-perfectly plastic constitutive models. The reasons for the difference are nonlinear behaviour well below failure conditions, stress dependent stiffness, dilatancy, difference in behaviour for primary loading - reloading/unloading.../Schweiger 2000/.

The use of modern calculation programs is quite simple and easy for users. The use of higher order models for practical calculations may be problematic becauce of difficulties on determination of the soil parameters needed on the calculations.

Pre-consolidation pressure

For soft soils pre-consolidation pressure (σ_p) (or Over Consolidation Ratio, OCR) is one of the most important parameters. When the stresses are below the pre-consolidation pressure, the soil is overconsolidated (OC). When the stresses reach the pre-consolidation pressure plastic strains are developing and the soil is normally consolidated (NC). The modulus of deformation of of OC-soil is 10...100 times bigger than the modulus of NC-soil.

Oedometer tests are most common method for determination of the pre-consolidation pressure. Oedometer tests are anyway made on no horizontal strain conditions, and that is valid only if the loaded area is wide enough. Triaxial consolidation tests are also used for determining the pre-consolidation pressure. Triaxial tests are often carried out with different stress ratios and then it is possible to determine the shape of the initial yield surface. In these cases the anisotrophy of soft soil behaviour is always seen, and the observed shape of the yield surface is totally different from the assumed shape of the yield surface. The geotechnical engineer is then trying to deside which value he must use for his calculations. Is the correct value of the pre-consolidation pressure the one determined by oedometer tests on K_0-line (earth pressure at rest) or is it the one determined from the triaxial test on isotropic stress state or anisotropic stress state.

Poisson ratio

The value of Poisson ratio in drained state is dependent on stress and strain level. The determination of the Poisson ratio is based on the drained triaxial test results. Typical values for soils are 0,1...0,4. In most cases calculation programs use the elastic value of Poisson ratio, and then it must be determined from unloading or reloading cycle of the test results. If Poisson ratio is used for determining the value of K_0 ($K_0=\nu/(1-\nu)$) it is important that the results are checked with some practical formula, e.g. Jaky's formula ($K_0=1-\sin\varphi$).

Permeability

The coefficient of permeability of soil (k) differs very much: gravel 10^{-1}m/s...clay 10^{-11}m/s. Permeability of soft soil is also dependent on strains. Typically 20...25% deformation diminishes the permeability to 1/10 from the initial value. The value of permeability for soft soil is often derived indirectly from the results of oedometer tests. The cofficient of consolidation (c_v) is first derived and then the modulus of compression (M). The value of permeability is then calculated ($k=c_v\gamma_w/M$). This method is dangerous if the soil is lightly overconcolidated, because the permeability (and especially the coefficient of consolidation) on the overconsolidated range is bigger than in normally consolidated range. Better results are achieved if the calculation model accepts the decreasing value of permeability according to the strain or void ratio. Maybe the best method is direct measurement of the permeability with falling head permeameter test. This test is possible to combine to the oedometer test with small modification on the apparatus.

Stiffness

The stiffness modulus of soil is complicated, because the stress–strain–curve is non–linear even with very small stresses or strains. The traditional parameter is E_{50} which means that the secant modulus is calculated from the beginning of the test to 50% value of maximum shear stress. The determination of this modulus E_{50} is simple, especially from the results of isotropically consolidated triaxial tests. The structure of undisturbed soil sample is anyway heavily distroyed with isotropical consolidation. After K_0–consolidation the shape of the stress–strain–curve is totally different and the value of E_{50} is also different (and typically it contains much more plastic behaviour). The geotechnical engineer must first study his model and program, and then decide is the modulus needeed really elastic or plastic, and is it stress–dependent.

Conclusions

Some short comments presented here show that the choice of the parameters from the test results may be the most difficult task in geotechnical calculations. When using modern calculation methods he must have good

test results, typically triaxial test results. Then he must be capable for intrepretating the test result s according to the needs of the mechanical model and the calculation program used.

Effective System Properties in Random Vibration

F. Rüdinger and S. Krenk

Department of Structural Engineering and Materials
Technical University of Denmark, DK-2800 Lyngby, Denmark

Abstract. Parametric excitation of a structure may change the effective stiffness and damping. It is demonstrated how the effective system properties can be extracted and approximate solutions in terms of the probability density of the energy and the spectral density of the position can be obtained. The spectral density is obtained by an energy conditional formulation, where the spectrum at a particular energy level is assumed to be equal to the spectrum of a linear oscillator with damping corresponding to the energy level considered. Integration over all energy levels weighted by the probability density yields an unconditional spectral density.

1. Introduction

Environmental loads on structures may involve additive as well as parametric load components. While additive loads have been studied extensively, parametric excitation by stochastic loads is a less developed field. The parametric load components, typically modelled as white noise processes, can lead to changes in the system stiffness and damping properties, as described e.g. by Krenk et al. (2000). The present paper gives a brief outline of the effective properties, and the probability distribution and spectral density of the response.

2. Theory

A general form of the equation of motion of an oscillator excited by stationary white noise can be expressed as

$$\ddot{X} + f(X,\dot{X}) \;=\; b_j(X,\dot{X})W_j(t) \quad , \quad j = 1,2,... \tag{1}$$

If $b_j(X,\dot{X})$ is independent of X and $\dot{X}$ the excitation is termed additive or non-parametric, otherwise it is termed multiplicative or parametric. The white noise processes can be described in terms of their covariance functions as

$$R_{ij}(\tau) \;=\; E[W_i(t)W_j(t+\tau)] \;=\; 2\pi S_{ij}\delta(\tau) \tag{2}$$

where S_{ij} is the spectral density matrix. The excitation can be expressed in terms of a single unit white noise $W(t)$ multiplied by an amplitude. The equation of motion is written as a first order evolution equation of the state space vector $(X,\dot{X})$

$$\frac{d}{dt}\begin{bmatrix} X \\ \dot{X} \end{bmatrix} \;=\; \begin{bmatrix} \dot{X} \\ -f(X,\dot{X}) \end{bmatrix} + \begin{bmatrix} 0 \\ \sigma(X,\dot{X}) \end{bmatrix} W(t) \tag{3}$$

where $\sigma(X,\dot{X})$ is the amplitude of the combined load process, given by

$$\sigma(X,\dot{X})^2 \;=\; 2\pi S_{ij} b_i(X,\dot{X}) b_j(X,\dot{X}) \tag{4}$$

Equation (3) can be written as an Itô type stochastic differential equation, as

$$d\begin{bmatrix} X \\ \dot{X} \end{bmatrix} \;=\; \begin{bmatrix} \dot{X} \\ -f(X,\dot{X}) + \dfrac{1}{4}\dfrac{\partial \sigma(X,\dot{X})^2}{\partial \dot{X}} \end{bmatrix} dt + \begin{bmatrix} 0 \\ \sigma(X,\dot{X}) \end{bmatrix} dB(t) \tag{5}$$

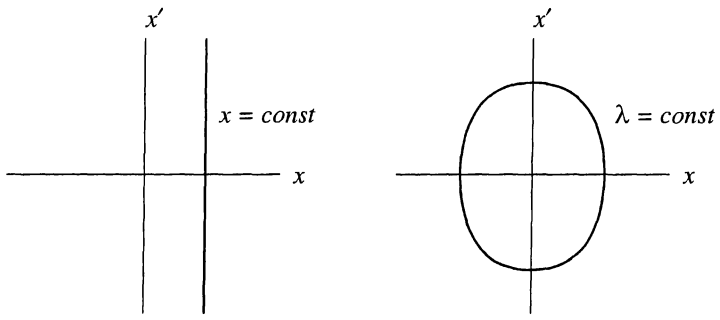

FIGURE 1. Conditional expectations: a) Potential force via $E[\ *\ |x]$, b) Exponent $\psi(\lambda)$ and damping via $E[\ *\ |\lambda]$.

The internal force function $f(X,\dot{X})$ is modified by the term $-\frac{1}{4}\partial\sigma^2/\partial\dot{X}$ accounting for the correlation between the force $\sigma(X,\dot{X})W(t)$ and the velocity $\dot{X}$. $dB(t)$ is the increment of a unit Wiener process, the formal derivative of which is a unit white noise. This formulation permits the derivation of a partial differential equation – the Fokker-Planck equation – for the joint probability density $p_{x,\dot{x}}(x,\dot{x})$ of $X,\dot{X}$.

2.1. **Probability density and effective stiffness.** Even in the stationary case it is in general difficult to obtain exact solutions for the joint probability density $p_{x,\dot{x}}(x,\dot{x})$. However, solutions can be approximated by

$$p_{x,\dot{x}}(x,\dot{x}) \;=\; C\exp(-\psi(\lambda)) \quad , \quad \lambda \;=\; \tfrac{1}{2}\dot{x}^2 + G(x) \;=\; \tfrac{1}{2}\dot{x}^2 + \int_0^x g(\eta)d\eta \tag{6}$$

where λ is the mechanical energy and $G(x)$ the elastic part of the energy. The effective stiffness $g(x)$ is determined as the expectation of the *modified* internal force function for a given position

$$g(x) \;=\; E\Big[f(x,\dot{X}) - \frac{1}{4}\frac{\partial\sigma(x,\dot{X})^2}{\partial\dot{X}}\;\Big|\;x\Big] \tag{7}$$

$E[*|x]$ corresponds to integration over all velocities for x constant with weight function $p_{x,\dot{x}}(x,\dot{x})$, as shown in figure 1a. The function $\psi(\lambda)$ is determined by

$$\frac{d\psi}{d\lambda} \;=\; \frac{E\left[f(X,\dot{X})\dot{X} + \dfrac{1}{4}\dfrac{\partial\sigma(X,\dot{X})^2}{\partial\dot{X}}\dot{X}\;|\;\lambda\right]}{E\left[\frac{1}{2}\sigma(X,\dot{X})^2\dot{X}^2\;|\;\lambda\right]} \tag{8}$$

$E[*|\lambda]$ corresponds to integration along the path shown in figure 1b. It is thus the expectation of the argument for X and $\dot{X}$ described by a free undamped vibration at energy level λ. Equations (6) and (8) yield an approximate solution in terms of the joint probability density $p_{x,\dot{x}}(x,\dot{x})$ of X and $\dot{X}$.

2.2. **Spectral density and effective damping.** The spectral density of the position can be determined by an approximate technique developed by Krenk & Roberts (1999). In the following only the case of a system with linear stiffness is considered. The spectral density of the position at a given energy level can in this case be approximated by

$$S_x(\omega|\lambda) \;=\; \frac{h_{eq}(\lambda)\lambda}{\pi}\left[\frac{2}{(\tilde{\omega}^2-\omega^2)^2 + h_{eq}(\lambda)^2\omega^2}\right] \tag{9}$$

Here $\tilde{\omega}^2 = g(x)/x$ is the effective stiffness evaluated from (7) and $h_{eq}(\lambda)$ is the equivalent damping at a given energy level

$$h_{eq}(\lambda) = \frac{1}{\lambda} E\left[\left(f(X,\dot{X}) - \frac{1}{4}\frac{\partial \sigma(X,\dot{X})^2}{\partial \dot{X}}\right)\dot{X} \mid \lambda\right] \tag{10}$$

corresponding to the expectation of the modified internal force function for a constant energy level as shown in figure 1b. The spectral density is now obtained by

$$S_x(\omega) = \int_0^\infty p_\lambda(\lambda) S_x(\omega|\lambda) d\lambda \tag{11}$$

which is a superposition of spectra at various energy levels, each weighted by the probability density for that energy level. A more detailed discussion of the technique is given by Krenk et al. (2000).

3. Example

A system governed by the following equation of motion is considered

$$\ddot{X} + \omega_0 \left(2\zeta + W_2(t)\right)\dot{X} + \omega_0^2 \left(1 + W_1(t)\right) X = W_0(t) \tag{12}$$

It is assumed that $S_{01} = S_{02} = 0$. The amplitude is then given by

$$\sigma(X,\dot{X})^2 = 2\pi\left(S_{00} + \omega_0^4 X^2 S_{11} + 2\omega_0^3 X\dot{X} S_{12} + \omega_0^2 \dot{X}^2 S_{22}\right) \tag{13}$$

The effective stiffness is evaluated from (7) as

$$g(x) = (\alpha\omega_0)^2 x \quad , \quad \alpha^2 = 1 - \pi\omega_0 S_{12} \tag{14}$$

The parameter α indicates a change in the effective natural frequency of the system, corresponding to a change in effective stiffness α^2.

The effective damping is evaluated from (10) as

$$h_{eq}(\lambda) = 2\zeta_e\omega_0 \quad , \quad \zeta_e = \zeta - \tfrac{1}{2}\pi\omega_0 S_{22} \tag{15}$$

where the last term in the expression for the effective damping ratio ζ_e originates from the additional term in (10).

The probability density of a non-dimensional energy variable $\xi = \lambda/\lambda_0$ then follows from (6) as

$$p_\xi(\xi) = \frac{\nu - 1}{(1+\xi)^\nu} \quad , \quad \xi = \frac{\lambda}{\lambda_0} \quad , \quad \nu > 1 \tag{16}$$

where the reference energy level λ_0 and the non-dimensional parameter ν are given by

$$\lambda_0 = \frac{2S_{00}}{\omega_0^2\alpha^{-2}S_{11} + 3\omega_0^2 S_{22}} \quad , \quad \nu = \frac{4\zeta + 2\pi\omega_0 S_{22}}{\pi\omega_0\alpha^{-2}S_{11} + 3\pi\omega_0 S_{22}} \tag{17}$$

The spectral density is obtained from (9) and (11) as

$$\frac{S_x(\omega)}{\sigma_x^2} = \frac{4\zeta_e}{\pi}\frac{(\alpha\omega_0)^3}{((\alpha\omega_0)^2 - \omega^2)^2 + 4\zeta_e^2\omega^2\omega_0^2} \quad , \quad \sigma_x^2 = \frac{\lambda_0}{(\alpha\omega_0)^2(\nu-2)} \tag{18}$$

The correlation coefficient is introduced as $\rho = S_{12}/\sqrt{S_{11}S_{22}}$. In figure 2 the probability density is given for two different parameter combinations both for $\rho = 0$ (no correlation) and for $\rho = 1$ (full positive correlation). The solid lines correspond to the theoretical results and the crosses and dots correspond to results obtained by numerical simulation. The results show excellent agreement. It is observed that the four cases shown in the two figures give practically the same results in terms of probability density. In figure 3

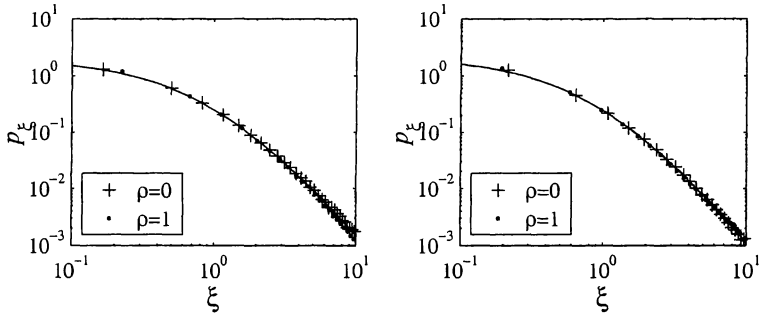

FIGURE 2. Probability density of non-dimensional energy, a) $\zeta = 0.05$, $\omega_0 S_{11} = \omega_0 S_{22} = 0.0064$, b) $\zeta = 0.1$, $\omega_0 S_{11} = \omega_0 S_{22} = 0.012$.

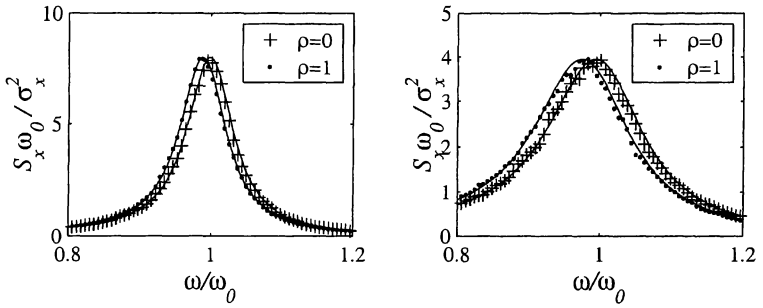

FIGURE 3. Auto spectral density of position, a) $\zeta_e = 0.04$, $\nu \simeq 3$, $\alpha_{\rho=1} = 0.99$, b) $\zeta_e = 0.08$, $\nu \simeq 3$, $\alpha_{\rho=1} = 0.98$.

the spectral densities corresponding to the same parameter values are shown. Again the theoretical results agree very well with the numerical results. The effect of the change of stiffness and damping is clearly seen from the four spectra.

4. CONCLUSION

It has been demonstrated how parametric excitation can change the effective stiffness and damping of a mechanical system. A method for obtaining an approximate expression for the probability density of the energy has been outlined. The spectral density at a given energy level is approximated by the expression for the linear system with an energy dependent damping function. Integration over all energy levels weighted by the probability density of the energy yields an approximate expression for the spectral density. The validity of the method has been demonstrated by comparison between theoretical results and results obtained by numerical simulation. The effective system properties are directly observable from the spectrum.

5. REFERENCES

Krenk, S., Lin, Y. K. and Rüdinger, F. (2000). Effective system properties and spectral density in random vibration with parametric excitation (to be published).

Krenk, S. and Roberts, J. B. (1999). Local similarity in nonlinear random vibration, *Journal of Applied Mechanics*, Vol. 66, pp. 225-235. 1375-1378.

THE INFLUENCE OF THE DIFFUSION SPACE GEOMETRY ON BEHAVIOR OF A BIOSENSOR

F. Ivanauskas and R. Baronas

Vilnius University, Naugarduko 24, 2600 Vilnius, Lithuania

Abstract

The reaction-diffusion equation was applied for modelling of amperometric biosensors based on a carbon paste electrode encrusted with a single inhomogeneous microreactor. The mathematical model of the biosensor operation is based on a system of nonstationary reaction-diffusion equations, containing a non-linear term given by Michaelis-Menten function. The finite-difference technique was used for discretisation of the model. Using the numerical solution of the problem, the influence of the size, shape and position of a microreactor was investigated.

1. Introduction

Recently, the amperometric biosensors based on carbon paste electrodes (CPEs) encrusted with a single microreactor (MR) have been constructed for the determination of glucose [4]. The MRs were prepared from CPC-silica carrier and were loaded with glucose oxidase (GO), mediator and acceptor. The goal of this paper is to present a model allowing us an effective digital simulation of the biosensor operation.

The reaction carried out by an enzyme can be represented by the following equation:

$$S \xrightarrow{E} P, \tag{1.1}$$

in which S is the substrate, P is the reaction product, and E is the enzyme. The rate (velocity) on the reaction (1.1) is the rate of appearence of P. In an enzyme catalyzed reaction, reaction velocity at various different concentrations, gives a curve, described as a rectangular hyperbola, and the equation of the curve is usually called the Michaelis-Menten equation [3]:

$$dv/dt = -du/dt = V_{max}u/(K_m + u). \tag{1.2}$$

Three variables in this equation are the concentration of substrate, u, the concentration of reaction product, v, and the time, t. V_{max} and K_m are two rate constants for the reaction (1.1). V_{max} is the maximal enzymatic rate, and K_m is the Michaelis constant.

Measurements of the product of the enzymatic reaction were made via amperometric sensing. Amperometric sensors are usually operated under limiting potential or small overpotential conditions. Under these conditions, the concentration of the reaction product at the electrode surface is zero.

Due to the technology of the construction of MR, the number and geometrical shape of the cells, which are filled with glucose oxidase, cannot be precisely defined. The problems in the modelling arise because of the possibility to solve analytically such type of equations. In the digital simulation, the inhomogeneous nature and the size of MR, the complexity of the boundary conditions and the overload of calculation are the main problems. Therefore, the model was reduced by the homogenization process [1].

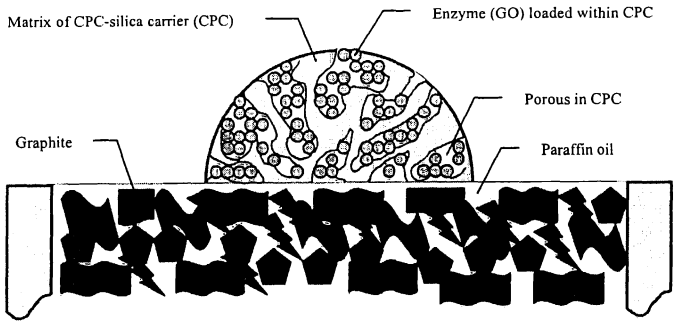

Fig. 2.1: A principal structure of a biosensor based on an inhomogeneous microreactor (MR). MR was constructed from CPC-silica carrier and was loaded with glucose oxidase. The average size of a cell which is filled with glucose oxidase is much less than the size of MR. The geometrical shapes of cells are not precisely defined. The figure is not to scale.

2. Detailed model

Let $\overline{\Omega}$ be the finite closed area of the container (buffer solution) which was filled with some substrate, and Ω_0 the area of MR ($\Omega_0 \subset \Omega$). Let Γ be the whole surface of the container ($\overline{\Omega} = \Omega \cup \Gamma$), and Γ_1 ($\Gamma_1 \subset \Gamma$) only the base of the container. Γ_1 also denotes the surface of the electrode.

Since the microreactor, announced in [4], was constructed from CPC-silica carrier (CPC) and was loaded with glucose oxidase (GO), let the whole MR area Ω_0 consist of two areas: Ω_{0C}, the CPC-carrier, and Ω_{0G}, the glucose oxidase ($\Omega_0 = \Omega_{0C} \cup \Omega_{0G}$) (figure 2.1).

The simplified operation of the biosensor includes heterogeneous enzymatic process (reaction) and diffusion. The stimulus of the reaction is MR, but the reaction performs only in the area Ω_{0G} of MR which was filled with glucose oxidase. The model consists of a system of the following non-stationary non-linear differential equations of reaction-diffusion type [2]:

$$\frac{\partial u}{\partial t} = \text{div}\,(D\ \text{grad}\ u) - f(u), \quad \frac{\partial v}{\partial t} = \text{div}\,(D\ \text{grad}\ v) + f(u), \tag{2.1}$$

$$D|_{\Omega_{0G}} = D|_{\Omega\setminus\Omega_0} = d, \quad D|_{\Omega_{0C}} = 0, \tag{2.2}$$

$$f|_{\Omega_{0G}} = V_{max}u/(K_m + u), \quad f|_{\Omega_{0C}} = f|_{\Omega\setminus\Omega_0} = 0, \tag{2.3}$$

where d is the constant diffusion rate of the substrate and reaction product, u, v, V_{max}, K_m and t mean the same as in (1.2). The initial conditions ($t = 0$) are

$$u|_{\Omega_0} = 0, \quad u|_{\overline{\Omega}\setminus\Omega_0} = u_0, \quad v|_{\overline{\Omega}} = 0. \tag{2.4}$$

When an electrode is polarised, the concentration of the reaction product at the electrode surface is being reduced to zero. This is used in the boundary conditions ($t > 0$) given by

$$\left.\frac{\partial u}{\partial \mathrm{n}}\right|_{\Gamma} = 0, \quad \left.\frac{\partial v}{\partial \mathrm{n}}\right|_{\Gamma\setminus\Gamma_1} = 0, \quad v|_{\Gamma_1} = 0, \tag{2.5}$$

where $\partial u/\partial \mathrm{n}|_\Gamma$ is a derivative of u with respect to the internal normal direction to the surface Γ.

Due to the technology of the construction of MR, the number of cells which are filled with glucose oxidase is very large, so an average size of a cell is much less than the size of MR. The number of the cells and the geometrical shape of the cells cannot be precisely defined. For that reason, it is hopeless to solve (2.1)-(2.5) analytically and even to design an effective algorithm for the numerical calculations.

3. Homogenized model

It was assumed that MR is a periodic medium, and the model (2.1)-(2.5) was reduced by the homogenization process [1]. Let c be the ratio of the volume of the glucose oxidase which fills the MR cells to the volume of entire MR (it is easy to calculate this ratio experimentally), i.e., $c = volume(\Omega_{0G})/volume(\Omega_0)$. By using the homogenization process, the definition of the non-linear term related to the enzymatic reaction was simplified and the model was reduced to

$$\frac{\partial \overline{u}}{\partial t} = \mathrm{div}\ (\overline{D}\ \mathrm{grad}\ \overline{u}) - cf(\overline{u}), \quad \frac{\partial \overline{v}}{\partial t} = \mathrm{div}\ (\overline{D}\ \mathrm{grad}\ \overline{v}) + cf(\overline{u}), \tag{3.1}$$

$$\overline{D}|_{\Omega\setminus\Omega_0} = d, \quad \overline{D}|_{\Omega_0} = \overline{d}, \tag{3.2}$$

$$f|_{\Omega_0} = V_{max}\overline{u}/(K_m + \overline{u}), \quad f|_{\Omega\setminus\Omega_0} = 0, \tag{3.3}$$

where $\overline{u} \approx u$, $\overline{v} \approx v$, and $\overline{d}$ is the average diffusion rate in the entire area of MR (Ω_0).

The initial conditions and the boundary conditions are the same as above ((2.4) and (2.5), respectively).

The value $\overline{d}$ of the diffusion rate in the area of MR (Ω_0) depends on the diffusion rate d, the geometry of MR, and the ratio c [1]. If d_{go} is a diffusion rate in enzyme (GO), and d_{cpc} is a diffusion rate in silica carrier, then the average diffusion rate $\overline{d}$ in the entire media can be chosen employing the following condition:

$$2d_{go}d_{cpc}/\left(d_{go} + d_{cpc}\right) \leq \overline{d} \leq \left(d_{go} + d_{cpc}\right)/2. \tag{3.4}$$

Because of (3.4) and assumption that $d_{go} = d, d_{cpc} = 0$, the average diffusion rate $\overline{d}$ must satisfy the condition $0 \leq \overline{d} \leq d/2$.

4. Simulation of the biosensor action

The model (3.1)-(3.3), (2.4), (2.5) was used for digital simulation of the real experiment [4]. The container (bulk, buffer solution) was modelled as a right cylinder with circles of radius R in bases and altitude of H. MR was modelled as a rotation figure. Particularly, MR was modelled as a hemisphere of radius R_0. MR was placed on the center of the base of the container (figure 2.1).

In such case, due to symmetry, the model (3.1)-(3.3), (2.4),(2.5) may be written in two cylindrical coordinates (r, z) with

$$\Omega = \{(r,z) : 0 < r < R, 0 < z < H\}, \quad \Omega_0 = \{(r,z) : r^2 + z^2 < R_0^2, z > 0\}. \tag{4.1}$$

The definition of Ω_0 in (4.1) depends on the shape of MR. Several other geometrical shapes of MR differing from the hemisphere were used in the investigation of the biosensor behavior.

Approximately, 60% of the volume of MR was loaded with the glucose oxidase (GO), and the rest part of MR was the CPC-silica carrier (CPC), i.e., the ratio $c = 0.6$ in (3.1). The value $d/2.7$ was chosen as the homogenized diffusion rate $\overline{d}$ in the area of MR to have the best fit between the experimental and numerical curves of the current.

The biosensor current density is proportional to the concentration gradient of the reaction product near the surface of the electrode as described by Faraday law. The total biosensor current $I(t)$ at time t can be expressed by integrating of the current density over the entire surface of the electrode (the base of the buffer solution):

$$I(t) = \iint_{\Gamma_1} nF\overline{D}\frac{\partial v}{\partial \mathrm{n}}\Big|_{\Gamma_1} d\Gamma_1. \tag{4.2}$$

where n is a number of electrons involved in transformation of the depolarizer, and F is Faraday constant.

The finite-diffence technique was used for discretisation of the model. In the all cases of simulation of the biosensor action, radius R_0 of the microreactor was much smaller than radius R of the model container ($R_0 \ll R$). Because of this a non-uniform discrete grid was introduced to avoid an overload of calculations. An exponentially increasing step of the grid was used in the space directions r and z for $r > R_0$, $z > 0$, while a constant step of the grid was employed in t direction.

Conclusions

The homogenization process [1] can be successfully used to reduce the mathematical model of the operation of a biosensor based on an inhomogeneous microreactor. The homogenized problem can be effectively solved by using finite-different technique.

The values of the current (including the maximal current) increase if the radius of a microreactor increases and this growth is non-linear.

The form of MR appears to be important for the current and it is especially important at the initial stage of the reaction. Here the current grows faster as the area of the base of MR increases. Later this importance decreases.

The current emerges with delay if MR is lifted up from the electrode. The time of delay depends on an altitude.

REFERENCES

1. Bakhvalov N. S. and Panasenko G. P., *Homogenisation of Processes in Periodic Medium*, [in Russian], *Nauka, Moskow*, 1984.
2. Baronas R., Ivanauskas F. and Kulys J., *Modelling a biosensor based on the heterogeneous microreactor*, *J. Math. Chem.*, **25**, p. 245-252, 1999.
3. Lide D. R., ed., *Handbook of Chemistry and Physics, 74th Edition*, CRC Press, Boca Raton, Ann Arbor, London, Tokyo, 1993-1994.
4. Kulys J., *Carbon paste electrode encrusted with a microreactor as a glucose biosensor, Biosens. Bioelectr.*, **14**, p. 473-479, 1999.
5. Samarskii A.A., *The theory of difference schemes*, [in Russian], *Nauka*, Moskow, 1989.

Author index